8-2005

Clinical Significance of Hip Separation in Metal on Polyethylene, Metal on Metal, and Ceramic on Ceramic THA Due to Resonant and Energy Dispersion Effects

Joseph Scott Bader
University of Tennessee - Knoxville

To the Graduate Council:

I am submitting herewith a thesis written by Joseph Scott Bader entitled "Clinical Significance of Hip Separation in Metal on Polyethylene, Metal on Metal, and Ceramic on Ceramic THA Due to Resonant and Energy Dispersion Effects." I have examined the final electronic copy of this thesis for form and content and recommend that it be accepted in partial fulfillment of the requirements for the degree of Master of Science, with a major in Mechanical Engineering.

Richard D. Komistek, Major Professor

We have read this thesis and recommend its acceptance:

Jack F. Wasserman, Mohamed R. Mahfouz

Accepted for the Council:
Carolyn R. Hodges

Vice Provost and Dean of the Graduate School

(Original signatures are on file with official student records.)

To the Graduate Council:

I am submitting herewith a thesis written by Joseph Scott Bader entitled "Clinical Significance of Hip Separation in Metal on Polyethylene, Metal on Metal, and Ceramic on Ceramic THA Due to Resonant and Energy Dispersion Effects." I have examined the final electronic copy of this thesis for form and content and recommend that it be accepted in partial fulfillment of the requirements for the degree of Master of Science, with a major in Mechanical Engineering.

Richard D. Komistek
Major Professor

We have read this thesis and recommend its acceptance:

Jack F. Wasserman

Mohamed R. Mahfouz

Acceptance for the Council:

Anne Mayhew

Vice Chancellor and Dean of Graduate Studies

(Original signatures on file with official student records)

CLINICAL SIGNIFICANCE OF HIP SEPARATION IN METAL ON POLYETHYLENE, METAL ON METAL, AND CERAMIC ON CERAMIC THA DUE TO RESONANT AND ENERGY DISPERSION EFFECTS

A Thesis
Presented for the
Master of Science
Degree
The University of Tennessee, Knoxville

Joseph Scott Bader
August 2005

DEDICATION

This thesis is dedicated to my parents, Carol Bader and Larry Bader. They taught me the value of higher education, and I would not have been nearly as motivated to continue my education in engineering if they hadn't instilled those values into me.

ACKNOWLEDGEMENTS

I am grateful to those who helped me to complete the requirements for my Master of Science Degree in Mechanical Engineering. I thank Dr. Komistek for his guidance and for procuring the funding for this project. I express gratitude to Dr. Wasserman who helped guide me through many of the technical aspects of this project. I also am also grateful for Dr. Mahfouz's serving on my committee. I also appreciate the time and expertise that Dr. Brian Haas lent during the course of this project. My thanks also goes out to Brandon Merkl who helped out on the data processing technique. In addition, I would like to thank Oak Ridge National Laboratory for their assistance and lending of resources for this project. I also appreciate and thank DePuy Orthopaedics Inc., a Johnson and Johnson Company, who funded this project.

Lastly, I am thankful for my friends, family and coworkers at the Center for Musculoskeletal Research for their help and support over the course of this project.

ABSTRACT

Femoral head sliding within the acetabular cup does occur in THA. Since it is known that impact conditions can lead to component ringing, the present study investigates the vibrational response of variable bearing surface materials. A further understanding of the physical response resulting from impact during femoral head sliding may lead to valuable insight pertaining to THA failure.

Accelerometers were mounted to synthetic bones which had been implanted with hip prostheses. Data was collected from these sensors as a machine impacted the femoral head into the acetabular cup. These tests were carried out for metal-metal, ceramic-ceramic, and metal-polyethylene bearing surfaces at varying loads.

Contrary to the non impact condition, when hip separation was simulated leading to impact conditions, the frequency magnitudes were significantly increased. The results from this study revealed that the amplitude and range of vibration is dramatically increased when the femoral head is separated from the acetabular cup under impact conditions. The ceramic-ceramic material experienced the largest magnitude of frequency. The vibration caused by the ringing of components in the THA system has the potential to damage both prosthetic components as well as the area of the bone in contact with them. If the dominant frequencies seen during the testing for this study were to coincide with the resonant frequency of the bone at the implant/bone interface, then damage and degradation becomes much more likely, with the ultimate possibility of loosening and failure.

TABLE OF CONTENTS

LIST OF TABLES

LIST OF FIGURES

NOMENCLATURE

MPa	megapascals
Hz	hertz
mV	millivolt
g	acceleration of gravity
pC	picocoulomb
N	Newton

Abbreviations:

BW	body weight
COC	ceramic on ceramic
DFT	discrete Fourier transform
FEM	finite element modeling
FFT	fast Fourier transform
FIR	finite impulse response
IIR	infinite impulse response
MOM	metal on metal
MOP	metal on polyethylene
PMMA	polymethylmethacrylate
RAM	random access memory
RMS	root mean squared
PSD	power spectral density
THA	total hip arthroplasty

CHAPTER I

INTRODUCTION

1.1 Problem:

In 1999, there were more than 200,000 THA's performed in the U.S. (AAOS, 2003). Since 1994, revisions have accounted for 17% of the THA's in the US (Wright et al., 2000). The average cost of the initial THA procedure is around $26,000 while the cost of a THA revision averages approximately $32,000. These factors combine for a total cost of $4.2 billion annually in the US. In addition to the cost, the average hospital stay for a primary THA is 5 days while a revision THA is 6.5 days (Fiedler, et al., 2003).

Many complications cause the need for a revision including infection, aseptic loosening, dislocation, osteolysis from loosening, and fracture (Fiedler, et al., 2003). The most serious of these common complications is loosening (Georgiou, et al., 2001). A 10 year, post surgery follow-up study reported that an estimated 0-7% of THA femoral components and 22-29% of acetabular components become loose (Georgiou, et al., 2001). The two primary types of implant loosening are septic loosening and aseptic loosening. Septic loosening is caused by an infection at the tissue surrounding the hip replacement. Aseptic loosening is caused by factors that aren't related to an infection.

Aseptic loosening in THA's is reportedly as high as 14% in the US (Sharp et al., 1985). Many reasons for this figure have been investigated including foreign body reaction to wear particles, body enzymes, and sensitivity to implant motions (Krischak et al., 2003). Implant stability is also dependent on the biomechanical properties of the

bone it to which it is affixed and the amount of bone in contact with the implant (Meredith et al., 1997). Other factors that may contribute to implant loosening are a lack of bony in-growth on the porous implant surfaces and possible surgeon error. One possible cause of aseptic loosening that has yet to be investigated in depth is vibration of the bones and implant components.

1.2 Proposed Investigation:

Dennis et al. (2001) reported that the femoral head separated from the acetabular cup during gait at least 1 mm through "In vivo" 3-D model fitting process. When these components come back together, it was hypothesized that an impulse was generated at impact. As with any impact, the energy is dissipated in one of a variety of ways. A primary way in which energy can be dissipated in an impact is through vibration. When a system undergoes free vibration, it will vibrate at a natural frequency. If the excitation frequency coincides with the natural frequency, large oscillations may develop. This condition is called resonance and can result in dangerously large oscillations (Thomson, 1988), which can result in damage to the system. The possibility exists that the vibration from component impact during gait could cause resonance within the THA and cause damage to either the implant components or to the bone. Therefore, it was the purpose of this study to investigate the natural frequencies of all the components of a THA system and to measure the vibration frequencies and magnitudes that occur in the system after impact during gait. These data can then be examined to determine whether vibration within the THA system from impact loading has the potential to cause aseptic loosening at the implant/bone interface.

CHAPTER II

BACKGROUND

2.1 Anatomy:

In order to understand the terminology in this thesis, the basic anatomy involved must be understood. For the purposes of this study, only bony landmarks on the pelvis (Figure 1) and femur (Figure 2) are needed.

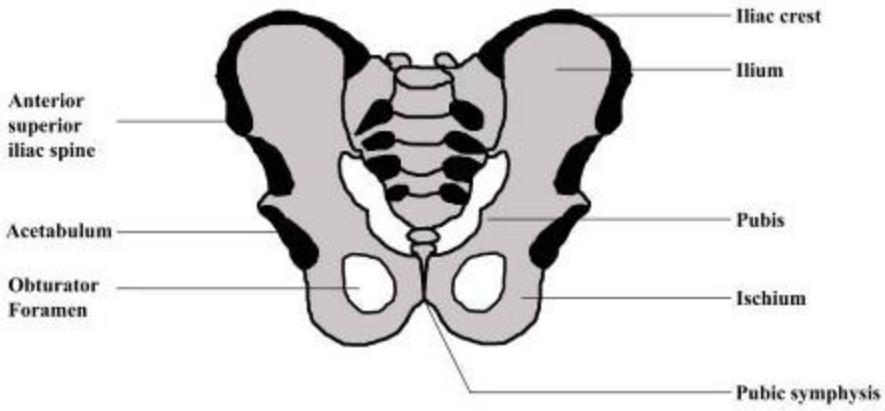

Figure 1. Anatomy of the Pelvis

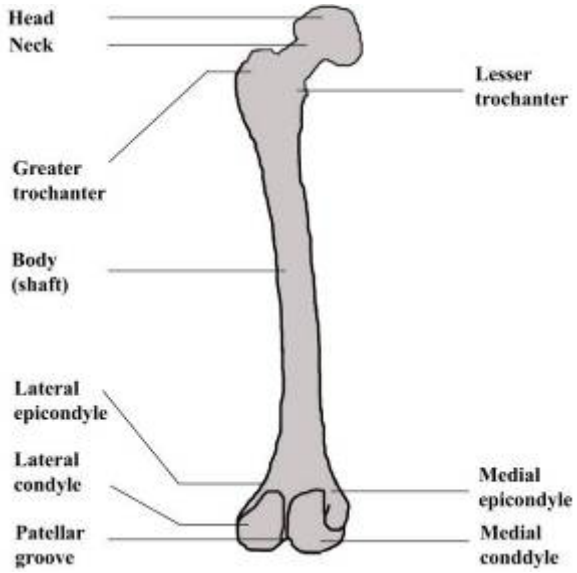

Figure 2. Anatomy of the Femur

2.2 Total Hip Arthroplasty:

Total hip arthroplasty is the name of the procedure undertaken when a natural hip is replaced by a synthetic prosthetic hip. THA is an invasive procedure which must be carefully considered before being undertaken. The main criteria used by physicians when determining if THA is appropriate for a particular patient follow (Fiedler, et al., 2003):

1. There should be radiographic evidence of joint damage.
2. There should be persistent pain causing a disability.
3. The persistent pain cannot be fixed by non-surgical treatments.
4. The goals after replacement are realistic and attainable.

Several techniques exist for this surgery including the posterior approach with an incision in the rear and the lateral approach with an incision on the side (Fiedler, et al., 2003). Overall for THA's, 90% of those who undergo the procedure report a decrease in limp,

become independent of assist devices and regain significant strength in their hip musculature (Towheed, et al., 1996).

The earliest known attempt at performing a THA came in 1822 (Klenerman, et al., 2002; Paavolainen, et al., 2002). In the 1950's PMMA was introduced as a cement for THA. Sir John Charnley was credited with inventing the low friction hip replacement in the early 1960's and developed many surgical techniques that paved the way for today's orthopedic surgeons. Modern THA techniques were introduced in the 1940's, and the use of modern THA materials dates back to the 1960's. Today, there are numerous types of hip implants on the market. For example, as of 1995 there were over 62 different types of hip prostheses made by 19 companies in England alone (Fiedler, et al., 2003). Most of these hip implants vary in design, size and material but contain the same components. An acetabular cup is placed in the acetabulum which has been reamed out by the surgeon. The acetabular cup is affixed by either bone cement or by notches or grooves which allow it to rest securely in the acetabulum. Within this cup is placed the acetabular liner. The liner is the bearing surface for the implant at the pelvis and can be made of a variety of materials, usually polyethylene, metal, or ceramic. The femoral stem is put inside the superior end of the femur where the femoral head has been cut off by the surgeon. This stem is affixed by either cement or by grooves like the acetabular cup. Attached to the stem on the femur is the femoral head which is the bearing surface of the femur in the hip. The femoral head is usually made of either ceramic or metal.

The criteria used when designing a hip implant include (Callaghan et al., 1995):

1. The implant must be able to provide appropriate control of joint movement.
2. The components must be capable of transferring large loads to the bones.

3. The implant must be capable of providing long term and permanent fixation.

While much time, effort, and money go into the design of these implants, they do not last indefinitely within the body. The material used for the implant, the size of the femoral head, and the overall design affect such factors as the surgical technique used, the amount of wear the implant undergoes, the likelihood of complication, and the survival rate of the implant itself.

At present, according to follow-up studies, metal on polyethylene (MOP) hip implants have been most successful of the THA implant materials currently in use. The MOP serves as the baseline for success of other materials (Fiedler et al., 2003). THA's have been made from ultra high molecular weight polyethylene (UHMWPE) for more than 30 years. Fatigue of the UHMWPE is a concern in the MOP prosthesis as well as the existence of wear particles that potentially could cause aseptic loosening (Fiedler et al., 2003). Overall the MOP implant has an 80%-90% survival rate after 25 to 30 years of use in older patients (Berry, et al., 2002a; Berry, et al., 2002b).

Metal on metal (MOM) implants have been in use the second longest next to MOP implants. MOM exhibits less wear than the MOP. However, some concerns of the MOM are metal-loosening, unknown carcinogenicity, and patient sensitivity to metal particles. MOM has an aseptic loosening rate of 0.9% to 11.9% per year and exhibits a 72% to 91% survival rate in 10 to 15 year follow-up studies (Fiedler, et al., 2003).

Ceramic on ceramic (COC) implants were introduced in the 1970's but were taken off the market due to unacceptably high wear rate and fracture risk (Fiedler, et al., 2003). A newer, more reliable version of the COC implant has been implemented in Europe since 1990 and gained FDA approval in the US in 2003. The COC fracture rate

before the introduction of the new implant was approximately 13.4% but was reduced to less than 1% afterward (Willmann, et al., 2000; Jazrawi, et al., 1998). More recent COC implant designs exhibit a wear rate of 0.003 mm/year, which is lower than MOP by a factor of ten.

2.3 Biomechanics of the Hip:

Published data on the forces occurring at the hip vary. Some researchers believe that the forces acting on the hip not only act vertically during gait but also in the lateral and ventral directions (Rydell, 1966). The direction of the force is also believed to change as the femur moves (Rydell, 1966), and some hip loci studies show that the position of the femoral head in the acetabular cup moves as well (Dennis, et al., 2001). Determination of the forces occurring at the hip can occur either through mathematical modeling or through the use of a telemetry prosthesis.

Two main approaches are used for modeling: (1) Optimization techniques that allow for more unknowns than equations of motion and (2) Reduction methods that ensure that the system of equations is determinant. The muscles can be included, the mechanical properties of the tissue in the joint can be varied and the mathematical method used to determine the value can vary. The primary methods of mathematical modeling of forces in the hip are FEM, classical Newtonian dynamics, and Kane's method of dynamics. Data from these various modeling methods range from 2.3 to 6.9 times body weight. (Brand, et al., 1982, 1994; Crowninshield, 1978; Hardt, 1978; Hurwitz, et al., 2003; Komistek, et al., 1998; Morrison, 1968, 1970; Paul, 1965, 1976; Seireg and Arvikar 1973).

Telemetry involves the use of placing instrumentation within a prosthesis such as accelerometers, force transducers, torque sensors or temperature sensing devices. The force values read by these prosthesis range from 2.3 to 3.2 times BW (Bergmann, et al., 1993, 1997, 2001; Davy et al., 1988; Kotzar et al., 1991; Rydell, 1966; Taylor, et al., 1994, 2001). Mathematical modeling tends to have larger magnitudes due to assumptions and various optimizations schemes.

The maximum force found for running varies between five times body weight and three times body weight (Rydell, 1966; Taylor, et al., 2001). Stair descending maximum forces vary between 2.6 and 3.1 times body weight (Taylor, et al., 2001; Bergmann, et al., 2001). In addition to the forces on the hip while the foot is in contact with the ground, Hodge et al. (1986) report an instrumented hip transducer reading of -0.13 MPa during swing phase. Based on the orientation of this transducer in the prosthesis and the negative value of the force reading, separation of the femoral head from the acetabular cup during swing phase is a strong possibility.

2.4 Detection of Loosening:

Some of the major factors that can influence the loosening of a hip implant are prosthesis design, skill of the surgeon, sex of the patient, and whether or not the patient has arthritis (Fiedler, et al., 2003). For cementless hip implant designs, signs of loosening can include thigh pain and the inability to lift the leg (Fiedler, et al., 2003). In order to prevent the trouble and pain associated with implant loosening, it is important to catch loosening early.

The most accurate method for determining prosthesis loosening is through pull and push out tests (Johansson, et al., 1987). However, this method requires sacrifice of the implant and is, therefore, of little diagnostic use. Digital subtraction, arthography, and scintography are also used. However, arthography, the most accurate of these methods, is invasive and poses a risk to the patient (Rosenstein, et al., 1989). Radiography is the most common method used for detecting implant loosening because it is accurate and non-invasive (Merideth, et al., 1997). The major drawback with radiography is that it can't measure changes in the bone structure, only relative changes in the marginal bone height (Merideth, et al., 1997). Researchers have shown that measuring the resonant frequency of the bone can be used to monitor the stability of an implant (Meredith, et al., 1996; Li, et al., 1996; Rasmusson, et al., 1999; Georgiou, et al., 2001). The method can be used to detect changes in the stiffness of an implant and the surrounding tissue. While still in its infancy, this method has proven to be 20% more sensitive to detecting implant loosening than the use of radiographs in situations where such tests are viable (Georgiou, et al., 2001).

2.5 Frequency Ranges:

Many studies have investigated the vibratory properties of long bones. A variety of methods have been used, yielding a variety of results for the resonance frequency. Of particular interest to this study are the resonant frequencies of the femur.

Campbell and Jurist (1971) used the shaker method to find the resonance of an excised human femur, after removal of a small wedge of bone from the neck, after removal of the femoral head, and after re-attachment of the femoral head. While the

reactance of the intact femur was the largest, all four of the tests had a peak somewhere between 750 and 800 Hz. Thomas et al. (1990) also used the shaker method with an excised human femur with both ends fixed. They found that when the end load was varied, the resonance of the femur varied between 138 and 177 Hz. They concluded that axial compression may affect the stiffness of bone and, thereby, affect the resonant frequency. They also reported when the femur was tested under THA conditions by removing the femoral head, reaming the shaft, and freeing the upper end, that no resonance peaks were visible. Based on this data, their conclusion was that there was no risk of inducing harmful resonances in bone during THA because the femur has no resonances. Khalil et al. (1981) used the impulse response method to find resonances in several vibrational modes of the femur. These frequencies varied between 250 and 879 Hz. Couteau et al. (1998a), Couteau et al. (1998b), compared their experimental femoral resonance frequencies found from impact hammer testing with a finite element model of the femur that they developed. These comparisons were carried out for both the normal femur and the implanted femur. The normal experimental results varied between 202 Hz and 932 Hz while the implanted experimental results varied between 278 Hz and 832 Hz. The normal numerical results varied between 288 Hz and 924 Hz while the implanted numerical results varied between 264 Hz and 780 Hz. The decrease in resonant frequency between non-implanted and implanted femurs is due to the increase in mass. Rosenstein et al. (1989) studied the resonances of normal femurs, securely implanted femurs, and loosely implanted femurs using the shaker method. They found the resonant frequency of the normal femur varied between 220 Hz and 375 Hz. The firmly implanted femur had a resonant frequency range of 230 Hz to 325 Hz. The loose

Table 1. Comparison of Femoral Resonance Frequencies from Different Studies

	Campbell	Thomas		Khalil	Couteau				Rosenstein		Taylor	
					Normal		Implanted					
	Exp.	Normal	For THA	Exp.	Exp.	FEM	Exp.	FEM	Normal	Implanted	Exp.	FEM
Mode 1 (or range)	138-177	750-800	None	250	301.6	287.8	278	264	220-375	230-325	285	285
Mode 2				315	353.3	364.2	330	324			317	324
Mode 3				825	886.6	819	758	693			521	489
Mode 4				879	961.6	931.9	832	780			777	710

implanted femur exhibited distorted signals and superimposed peaks within tens of Hz of the resonant frequency. Taylor et al. (2002) used modal analysis and a finite element model to determine femoral resonant frequencies. Their frequencies ranged from 285 Hz to 710 Hz. Overall, the reported values for the femur resonances vary significantly between the six studies (table 1).

2.6 Factors Influencing Frequency:

A number of physiological factors can affect resonant frequency measurements of long bones. When measuring fractured long bones over the duration of the healing period, the resonant frequency increases as the bone heals (Markey, et al., 1974; Shagaldi, et al, 1997). Osteoporosis and diabetes affect the resonant frequency of long bones by decreasing it (Jurist, 1970a; Jurist, et al., 1969). Age tends to by another factor influencing bone resonant frequency. Between the ages of 6 and 55, long bone resonant frequency decreases steadily in females (Jurist, 1970a).

The effect of skin, ligaments, tendons, and muscle on the resonant frequency measurement of long bones varies in the literature. Some scientists report that skin and other soft tissues can damp out long bone vibration (Nokes, et al., 1984; Nakatsuchi, et al., 1996). Other researchers say that skin has a modest effect on long bone frequencies

(Tsuchikane, et al., 1995). Yet some say that skin and soft tissue can affect the resonant frequency of a long bone but don't affect the ability to take acceleration measurements (Rosenstein, et al., 1989; Nokes, et al., 1988). Muscle mass affects resonant frequency (Denecker, 1968), and the resonant frequency of long bones gradually increases as muscles are removed from the joint (Tsuchikane, et al., 1995). Preloading the recording accelerometers in proportion to the soft tissue thickness allows soft tissue effects to be overcome (Nokes, et al., 1984; Nokes, et al., 1988; Nakatsuchi, et al., 1996). In one study the investigators claimed the measurement of some subjects was impossible due to constant muscular tension (Van Der Perre, et al., 1996).

Factors of the experiment itself can have an affect on the resonant frequency measurement. Measuring resonant frequency directly and by collecting the data and running an FFT give different frequency values (Nokes, et al., 1984). Slight changes in forearm and hand position created significantly different results in a study investigating the resonant frequency of the ulna (Jurist, et al., 1970b). In that same study, the researchers determined that accelerometer location and accelerometer tightness also affected the natural frequency measurement. They also determined that there was up to a 7% change in resonance frequency from day to day. In another study investigators dispute the idea that accelerometer placement has any effect (Christensen, 1982). Some researchers found significant differences in the resonant frequencies between different specimens (Rosenstein, et al., 1989).

The stiffness of the tissue surrounding the implant as well as the height of the implant left exposed also has an affect on the resonance (Nokes, et al., 1984; Shagaldi, et al, 1997; Lowet, et al., 1993). Along these same lines, loosening of an implant has a

significant effect on the frequency of the bone (Li, et al., 1996; Rosenstein, et al., 1989). In one study (Li, et al., 1996) there were never more than two resonances found. A significant change in natural frequency was exhibited for bones with and without implants (Rosenstein, et al., 1989; Couteau, et al., 1998). Chung et al. (1979) reported that there was a significant change in the resonant frequency of a bone during the curing of bone cement.

2.7 Methods of Measuring Vibration:

The first known use of vibration in orthopaedics came in 1932 when a doctor monitored the healing progress of fractured bones by tapping on them and listening to the response with a stethoscope (Nokes, et al., 1988; Lippmann, 1932). Since then, many methods of measuring the vibratory properties of bone have been developed both experimentally and theoretically.

Accelerometers can be used to measure vibration in through one of two main techniques . In one method, they are mounted on the object to be measured, and the object is then impacted. This is called the impulse response method, and the excited frequencies exhibited are called the natural frequencies (Christensen, et al., 1986; Nokes, et al., 1988, Couteau, et al., 1998a; Couteau et al., 1998b). The object can also be excited by a specific external frequency or set of frequencies. This concept is called bone resonance analysis, and the stimulus usually comes from a mechanical shaker, vibrator or speaker (Georgiou, et al., 2001; Campbell, et al., 1971; Thomas, et al., 1991; Nokes, et al., 1988). Sometimes, when a particular frequency range is of interest, a microphone can be used in these tests instead of an accelerometer (Lowet, et al., 1993). Overall, the

impulse response method requires less time and is simpler than the shaker method and is therefore preferable (Nakatsuchi, et al., 1996).

There are a wide variety of other experimental methods used to determine the vibratory properties of bone as well. In 1970 Brash and Skorecki determined that a traveling microscope could be used to establish resonance modes that were higher than the fundamental frequency because damping prevents high dynamic magnification. In another study, researchers concluded that the electric charge accompanying a stress in a bone can be detected by electromagnetic sensors due to bone's piezoelectric nature (Saha, et al., 1977). Strain gauges have also been used to measure vibratory properties (Pelker, et al., 1983). Changes in sonic wave propogation indicating resonant frequency have also been used via ultrasound testing (Van Der Perre, et al., 1996). One of the most accurate methods was carried out by Matthews et al.(Sonstegard, et al., 1976). They eliminated error due to soft tissue effects for in vivo measurements by placing an accelerometer directly on the bone using a needle. The obvious drawback to this method, however, is its invasive nature and finding subjects willing to undergo the procedure.

Experimental factors other than the method of determining resonance are also varied through the literature. Some experiments simulated soft tissue by wrapping the bone in wet cotton material (Thomas, et al., 1991). The location of the accelerometer placement also varied in many of those tests, varying from the femoral shaft to the greater trochanter (Thomas, et al., 1991). Some tests attempted to measure in vivo resonances by placing the accelerometer on a spot close to the bone such as can be found with the tibia at the medial malleolus (Markey, et al., 1974), while some measured with accelerometer directly on the skin, yet some just measured the vibration properties directly on the bone.

Some conditions on the bone such as loading and limiting mobility, attachment by pins, or resting the bone on a sponge were also a factor (Thomas, et al., 1991; Christensen, et al., 1986; Nokes, et al., 1988; Jurist, et al., 1973).

Many experimental results are found in order to verify the results of a theoretical model. There are many types of numerical ways to determine resonances in bone. Some of the earliest methods involve an oversimplification of the bone using a beam model to simulate its behavior (Lowet, et al., 1993). A slightly more advanced study modeled bone as a uniform cylindrical tube (Jurist, et al., 1973). The most advanced and accurate method of numerical modeling used to measure resonances is finite element modeling (FEM) (Orne, et al., 1976; Nokes, et al., 1984; Couteau, et al., 1998; Van Der Perre, et al., 1983). In this type of modeling, a model of the bone is created using CT images and placed into a FEM program for analysis (Couteau, et al., 1998). FEM analyses give similar results as those found in experimental methods and can have an error as low as 5% when compared to the experimental results. Numerical determination has advantages in that once a particular model is validated, testing and material parameters can be easily changed in order to simulate different situations. Also, if CT images are available for a large selection of subjects, many different analyses can be run without the need for actual human subject involvement.

2.8 Fourier Transform and the FFT:

When examining accelerometer data, the original data is captured with respect to time. While often useful, examining data in the frequency domain is usually necessary in order to achieve the best understanding of the acquired data. The Fast Fourier transform

is a means of converting data signals acquired in the time domain to the frequency domain so that additional information can be extracted from the given data. For discrete data, such as that acquired by a data acquisition card and stored on a computer for later analysis, there is a specific equation used to carry out the Fourier transform. The digital Fourier transform series is defined by (Inman, 2004):

$$x_k = x(t_k) = \frac{a_0}{2} + \sum_{i=1}^{N/2}\left(a_i \cos\frac{2\pi i t_k}{T} + b_i \sin\frac{2\pi i t_k}{T} \right) \qquad \text{k=1,2,…}N$$

The digital spectral coefficients are given by:

$$a_0 = \frac{1}{N}\sum_{k=1}^{N} x_k$$

$$a_i = \frac{1}{N}\sum_{k=1}^{N} x_k \cos\frac{2\pi i k}{N}$$

$$b_i = \frac{1}{N}\sum_{k=1}^{N} x_k \sin\frac{2\pi i k}{N}$$

2.9 Power Spectral Density and Periodogram Analysis:

In our analysis we used the periodogram method which used windowing and averaging to reduce the effect of noise in the analysis. The power spectral density is one of the methods that is used to average complex signals. There are two primary

approaches for estimating the power spectrum of a signal. The first of these approaches is the periodogram analysis that is used to find the PSD of a signal based on the Fourier Transform of the finite length signal. The second method which is a more advanced method and not used in this study involves estimating the auto-covariance sequence and then computing the Fourier Transform based on this auto-covariance sequence. The periodogram analysis is most appropriate for the purposes of this study because it based directly on the FFT of the sample. The values of the PSD at specific frequencies are given by (Oppenheim, 1999):

$$I(\omega_k) = \frac{1}{LU} |V[k]|^2$$

This equation means that in order to find the PSD at a particular frequency, ω_k, you must square the value of the discrete fourier transform (DFT) at that frequency, V[k], and then multiply by one over LU. L is the window length of the sample and U is a normalization constant used to remove bias in the spectral estimate. U=1 is maximum normalization but depending on the particular data window being used it can range anywhere between 0<U<1.

2.10 Data Filtering:

In digital signal processing, there are times when the researcher knows that certain frequencies are unwanted and/or the researcher is limited by the hardware that is used. For situations such as these, a digital filter is often very desirable. There are two types of digital filtering techniques, finite impulse response (FIR) and infinite impulse

response (IIR), both of which have unique advantages and disadvantages in a given application.

IIR filters can be more beneficial because they use less calculation and memory than a similar FIR filter. However IIR filters have a number of drawbacks compared to the FIR filter. They are more susceptible to noise and arithmetic error. IIR filters are slower to implement through the use of fixed point arithmetic. They don't offer the computational advantages that FIR filters do regarding decimation and interpolation.

FIR filters have a number of advantages over their IIR counterparts. FIR filters can easily be designed to be linear phase so that phase is not distorted. Implementation of an FIR filter is relatively simple and appropriate for use in situations involving decimation and interpolation. It is important to note that FIR filters are not feedback filters, so fewer mathematical problems arise in the design of an FIR filter and the coefficients of the FIR filter can be less than one.

The Butterworth filter is one of the most commonly used digital filters. The filter has the following transfer function (Roberts, 2004):

$$H(j\omega) = \frac{1}{\sqrt{1 + (\omega / \omega_c)^{2n}}}$$

Here, ω is the frequency of interest and ω_c is the cutoff frequency of the filter. The order of the filter is determined by the desired parameters for the filters and is represented by n in the above equation.

2.11 Aliasing:

Shifted versions of the original frequency spectrum that show up at integer multiples of the data sampling rate are called aliases because they look like the original spectrum but appear in a different place (Roberts, 2004). Aliasing is a problem that can occur when acquiring and analyzing data. Essentially, parts of frequencies higher than what is being analyzed show up as errant spikes in the FFT or PSD. This can cause problems because knowing which frequency peaks are caused by actual data and which are caused by aliasing can be difficult, if not impossible. Two precautions need to be taken in order to ensure that aliasing does not occur when acquiring data digitally. First of all, a hardware low-pass filter needs to be implemented into the system. The filter should block out all frequencies above the maximum frequency of interest or the Nyquist rate. This helps ensure that any data at frequencies larger than the Nyquist rate does not get recorded during data acquisition. Second, the data should be sampled at a sampling rate of at least twice the Nyquist rate or highest frequency of interest. If the highest frequency of interested was 10 kHz, then the data would have to be sampled at no less than 20,000 samples per second.

CHAPTER III
MATERIALS AND METHODS

3.1 Data Acquisition Setup:

The first step of carrying out this project was determining how vibration data would be collected and analyzed. A decision was made that acquiring vibration data in three dimensions would be most beneficial. Vibration characteristics at different places of the bone/implant system would have to be analyzed. It was finally decided that the number of locations to be analyzed would be four: on the acetabular cup, on the pubis directly behind the center of the acetabulum, on the femoral stem, and on the greater trochanter of the femur. Because tri-axial accelerometers were to be used, a data acquisition system allowing for acquisition of at least 12 channels would be necessary.

3.1.1 Accelerometers:

An accelerometer is an instrument used to convert mechanical motion into voltage. There are many types of accelerometers, and one of the most common types is piezoelectric (figure 3). A piezoelectric material is one which creates an electric charge when compressed or bent. Some of the most common piezoelectric materials are quartz and barium titanate (Thomson,1988). There are two main ways to quantify the sensitivity of a piezoelectric crystal, and they are to either measure the charge per g (pC/g) or voltage per g (mV/g). The accelerometers used for this study had a sensitivity of approximately 10 mV/g.

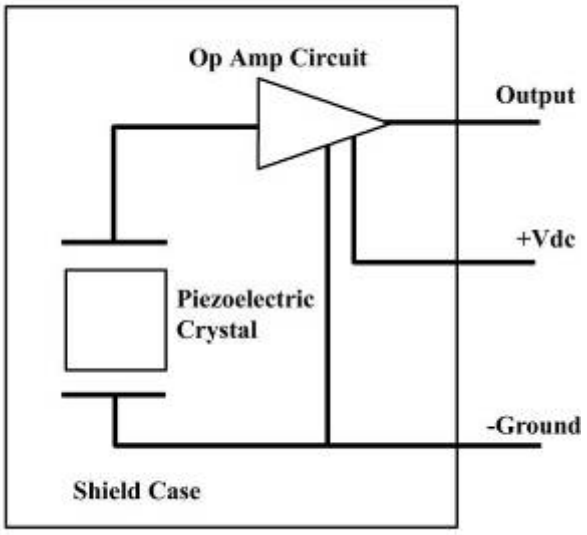

Figure 3. Schematic of Typical Piezoelectric Accelerometer

Accelerometers for this study had to meet several criteria. They had to be tri-axial, small enough to attach to the system without adversely affecting the system dynamics, and capable of measuring vibration up to 10,000 Hz. The accelerometers chosen were four PCB 356A11 piezoelectric tri-axial accelerometers (figure 4). These accelerometers measured from two to 7,000 Hz on the x-axis and from two to 10,000 Hz on the y and z axes. The size of the sensors was 0.25 inches cubed. After initial testing, two of these sensors wore out and had to be replaced. Due to the fact that the 356All was no longer made, they were replaced with two PCB HT356B11 piezoelectric tri-axial accelerometers. The specifications for the HT356B11 accelerometers were identical to that of the 356All accelerometers except the HT356B11 was capable of being used in environments of extreme temperature.

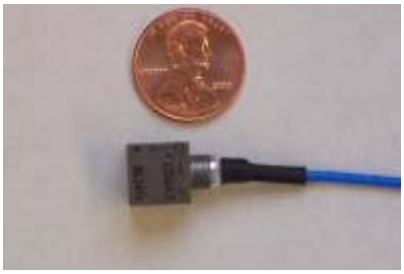

Figure 4. Tri-axial Accelerometer Used for Measurement, Compared with Penny to Demonstrate Scale

Each of the accelerometers had an integrated cable which ended in a ¼-28 four pin jack. A shielded cable was then connected to this jack (cable #: 034G05) which terminated with one female BNC connector for each of the three channels.

3.1.2 Signal Conditioner:

A PCB 583 series 16 channel signal conditioner was chosen to condition the signals from the accelerometers (figure 5). The signals could be input to the conditioner by using either BNC connectors for each channel or a single 37 pin cable. The BNC connectors from each accelerometer were connected directly to the signal conditioner. The same options existed for the output signal from the signal conditioner. It was decided that a 37 pin cable would be used for the output from the signal conditioner to the connector block. Therefore, a surplus female 37 pin cable was located and implanted. Since the output connector on the signal conditioner was female, a female to male adapter was used. Unfortunately, the cable was no longer mass produced and was, therefore, difficult to find.

Figure 5. PCB 583 16 Channel Signal Conditioner

3.1.3 Connector Block:

In order to connect the output of the signal conditioner to the data acquisition card, it was necessary to use a connector block. A National Instruments SCB-68 68-pin shielded connector block was chosen (figure 6). In order to connect the 37 pin cable to the connector block, some modifications had to be made. The 37 pin connector on the cable was removed and the insulation was stripped from the main cable and each of the smaller wires contained within it. The wire which corresponded to each pin had to be identified due to a lack of cable and instrumentation documentation. This was done by connecting one of the accelerometers to a PCB 394C06 calibration shaker along its z-axis. This shaker provided excitation at 1 g RMS at a frequency of 159.2 Hz. The wire corresponding to the z-axis was connected to the signal conditioner. All of the wires from the 37 pin cable were laid out on a counter surface and taped separately to the surface so that none of the wires touched. An oscilloscope was then used. A positive and a negative lead were touched to random wires on the counter until an oscillating wave corresponding to the shaker excitation appeared on the oscilloscope screen. The colors of

Figure 6. NI SCB-68 Block Connector Configuration Used in Testing

these wires were written down and then they were untaped from the counter and separated from the other wires. The channel on the signal conditioner to which the accelerometer was attached was then moved, and the process was repeated until it was known which wires corresponded to a particular channel. All remaining wires were considered ground wires and treated accordingly. The wires were connected to the block in a reference single ended configuration. Each channel had a positive, negative, and ground wire. Once all 16 channels of the signal conditioner had been connected to the connector block, the connector block was connected to the data acquisition card via ribbon cable.

3.1.4 Data Acquisition Card:

In order to help overcome the problem of aliasing, the minimum sampling rate required had to be at least twice the largest frequency of interest (the Nyquist frequency).

$$f_{sample} \geq 2 * f_{Nyquist}$$

The highest frequency that the chosen accelerometers could accurately measure was 10,000 Hz. Therefore, the Nyquist frequency was 10,000 Hz requiring the sampling rate to have been at least 20,000 samples per second per channel.

The data acquisition card chosen for this project was a National Instruments PCI-MIO-16E-1 card. The card had the capability of sampling at a rate of up to 1.25 Mega-samples/second. This translates to up to 78,000 samples per second per channel for a 16 channel system. This was well above the minimum sampling rate required for this study. Due to acquired data file size as well as questions regarding the ability of the computer to write data to disk quickly enough, it was decided that the sampling rate would remain at 20,000 Hz, knowing that the card was capable of handling such a load.

3.1.5 Computer:

The computer housing the data acquisition card was a Dell desktop. It had a 2.4 GHz Pentium 4 processor, 1,000 Megabytes of RAM and an 80 Gigabyte hard drive. This machine also had a DVD burner for the purposes of transferring large amounts of data quickly. The computer was used to control the data acquisition system as well as store the data (figure 7).

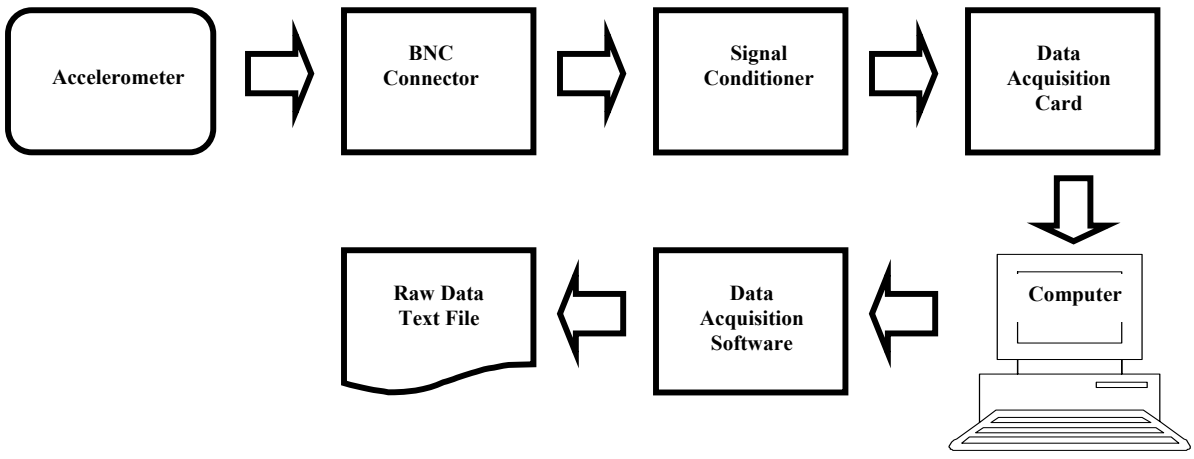

Figure 7. Block Diagram of Data Acquisition System

3.1.6 Initial Channel Setup:

Once the hardware was set up, the software had to be configured so that the data acquired would be accurate. The card was calibrated according to the specifications outlined in the instructions that came with it. Once calibration had been completed, the NI Measurement and Automation explorer was used to configure each channel coming into the card. The data coming into the card was from a SCB-68 68-pin shielded connector block and there were 16 channels. Sixteen channels were configured initially so that if another channel had to be used later, adding the device to the original twelve channels would be relatively simple. It was indicated that each of the channels was also in the referenced single ended configuration. Individual global channels were then set up for each channel. The setup specified that the incoming signals were from piezoelectric accelerometers, and the calibration data provided by the manufacturer for each accelerometer channel was input into the NI software. This included information such as measurement range and calibrated sensitivity. This process also meant that the acquired data was written to file in the appropriate units, and no conversion was needed from volts to acceleration.

3.1.7 Initial Channel Testing:

In order to observe the signals coming into the card, a simple program was written using Labview version 7.0 (National Instruments Corporation, Austin, TX). This program merely took the signals seen by the card and plotted them on a moving graph in real time like an oscilloscope. This program graphed all twelve accelerometer channels simultaneously. The accelerometers were then tapped on their different axes to make

sure that the signal corresponded to the appropriate channel. Once it was clear that tapping a specific accelerometer on a specific axis caused the signal on its corresponding channel to move, the signs of the channels had to be tested. A sign convention was established stating that the positive N3> axis was the direction pointing perpendicular to and away from the accelerometer mounting surface. The N1> and N2> axes were then chosen based on the right hand rule and the corresponding markings that existed on the accelerometer from the manufacturer where N1> corresponded with the x-axis and N2> corresponded with the y-axis. The accelerometers were tapped in the positive direction of a particular axis, and it was expected that the observed signal should be a positive spike. If the spike was negative, then the positive and negative wires were switched in the connector block, and the test was run again. The same test was carried out in the negative direction for each axis to make sure that the opposite case was also true. Once all the channels responded as anticipated, a simple impact test was developed to further test the setup.

3.1.8 Initial Impact Tests:

In order to further verify that the data acquisition setup was working properly, some early impact tests were conducted. In order to do this, another Labview program had to be created. This time, one of the sample programs that came with Labview was used and modified for the purposes of this project. This program allowed the user to establish which channels to acquire, the scanning rate for each channel, and the size of the cache so that the computer could store the information to hard disk, without error. The program wrote the data to disk in a tab delimited text file format in which each

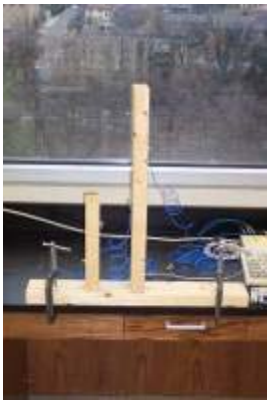

Figure 8. Testing apparatus used to verify accelerometer signals

channel was a separate column. For the purposes of this test, the 12 accelerometer channels were acquired at a rate of 20,000 Hz.

The actual initial impact test involved a simple device where the accelerometers were fixated to a piece of wood and impacted with a second wooden structure that was secured to the counter top (figure 8). Two accelerometers were placed on the piece of wood in the same orientation on opposite sides. The other two accelerometers were placed on the apparatus in the same orientation as the wood piece on opposite sides of the apparatus. Once the data acquisition program was running, the wood piece was used to tap the apparatus. Our intention was to ensure that the vertical axes of the wood piece and the apparatus have equal and opposite values.

3.2 Experimental Setup:

3.2.1 Bones:

Ideally this study would have been conducted with actual fresh cadaver bones in order to get a better idea of the vibratory properties of the implants and bones *in vivo*.

However, due to the impracticality of acquiring cadaver hips and using them in a timely fashion, it was decided that this study would be conducted using lifelike synthetic human bones. The bones chosen for this project were third generation composite bones (Sawbones®) (figure 9). These bones were created to be as mechanically similar to actual human bone as possible (table 2) and designed for biomechanical testing purposes (Heiner et. al., 2001). The size of the bones used for this project was large, and all bones were representative of the left side of the body.

3.2.2 Implants:

All of the implants for this study were donated by DePuy Orthapaedics, Inc., a Johnson and Johnson Company. In order to test the components under impact conditions as well as to test the individual components without any sort of loading, two sets of each type of hip system were needed. Six Pinnacle™ 100 54 mm acetabular cups, and 6 Summit™ cemented size 3 femoral stems were donated. Four 28 mm Articul/Eze™ metal on metal femoral heads, and two 28 mm Biolox® Delta Articul/Eze™ ceramic femoral heads were also given for the study. In addition, two 54 mm Biolox® Delta Ceramax™ ceramic acetabular cup inserts, two 54 mm Ultamet™ metal inserts, and two 54 mm Pinnacle™ Marathon™ polyethylene inserts were contributed. Besides the donated implants, one set of DePuy implants previously supplied for another study was used for testing the system in a trial implanted pelvis and femur.

Table 2. Mechanical Properties of Simulated Cortical Bone (E-glass-filled Epoxy) and Simulated Cancellous Bone (Rigid Polyurethane Bone) (Reproduced from www.sawbones.com)

Simulated Cortical Bone (E-glass-filled Epoxy)				
	Tensile		Compressive	
Density (g/cc)	Strength (MPa)	Modulus (MPa)	Strength (MPa)	Modulus (MPa)
1.7	90	12,400	120	7,600

Simulated Cancellous Bone (Rigid Polyurethane Bone)			
		Compressive	
	Density (g/cc)	Strength (MPa)	Modulus (MPa)
Solid	0.27	4.8	104
Cellular	0.32	5.4	137

Figure 9. Third Generation Composite Sawbones® used for impact testing

3.2.3 Implanting the Prosthetics:

The actual implanting of the prosthetics into the synthetic bones was carried out by an orthopaedic surgeon, Dr. Brian Haas (Colorado Joint Replacement, Denver, CO) and his operating staff. The procedure was carried out in an operating room at Rose Medical Center in Denver, CO that was available for use. Due to Dr. Haas's availability, the process was carried out over the course of a day, in steps, depending on when he was available to work on the project. The instruments and procedure used for implanting the prosthetics were as close as possible to those used during an authentic total hip arthroplasty in a living patient. The femoral head was severed from the femur using a reciprocating saw (figure 10a). A reamer was then used to create a hole in the cancellous bone large enough for the hip stem and bone cement to fit (figure 10b). The bits of synthetic cancellous bone that had been loosened were dumped out. Pieces of gauze were then stuffed into the hole that goes all the way through the femur along its vertical axis so that the bone cement to be put in later would remain in the reamed hole instead of flowing out of the bone. The Endurance™ bone cement was then prepared.

A. **B.**

Figure 10. A.) Using a Reciprocating Saw to Sever the Femoral Head from the Femur **B.)** Using a Reamer to Hollow Out the Inside of the Synthetic Femur

Figure 11. Applying Bone Cement Used to Affix Hip Stem within the Femur

This procedure was done by first opening the powder bag supplied in the kit with scissors and pouring the contents into the supplied mixing container. The top of the ampoule of bone cement liquid was then torn off, and the liquid was poured into the cement mixing container. The ingredients were combined in the mixing container for 45 seconds and then the mixing container was attached to the gun cartridge. After 2-2 ¼ minutes from the start of mixing, the cement was ready to be extruded. After being properly prepared, a large amount of bone cement was added to the reamed hole (figure 11), and the hip stem was then placed into the cement and adjusted until the orientation was correct to the best judgment of the physician. The implant was then allowed to set. This process was repeated three times. To make sure that all the implanted femurs were oriented in a similar fashion, the femoral head of each bone was cut off at an angle using the implant before it as a template (figure 12). The purpose was to make the angle of the cut close in all four femurs. Placing the femoral head was postponed until later because this procedure didn't need to be performed by the surgeon and the excess bone cement would need to be cleaned from the implant using some sort of sharp implement. The process

A. **B.**

Figure 12. A.) Marking a Femur Using a Previously Cut Femur as a Template **B.)** Cutting a Femur Using a Previously Cut Femur as a Template

used for implanting the acetabular cup into the synthetic pelvis was similar to that used for the femur. A set of DePuy acetabular reamers was used to gradually grind the cortical surface away from the pelvis (figure 13a), leaving the softer cancellous bone inside (figure 13b). In order to get the bone cement to adhere, small holes were drilled in the cancellous bone around the acetabulum. When the cement hardened inside these holes and around the implant itself, the holes would act as an anchor, keeping the implant from falling out under the conditions to which it would be subjected later. More bone cement was prepared and placed into the reamed hole; the acetabular shell was then placed into the hole and oriented to the position Dr. Haas desired (figures 13c-e). Like the femoral head, the placement of the acetabular cup insert was delayed until a later time because the surgeon's expertise was not needed and excess cement needed to be removed from the cup to ensure a tight and proper fit between the cup and insert (figure 13f).

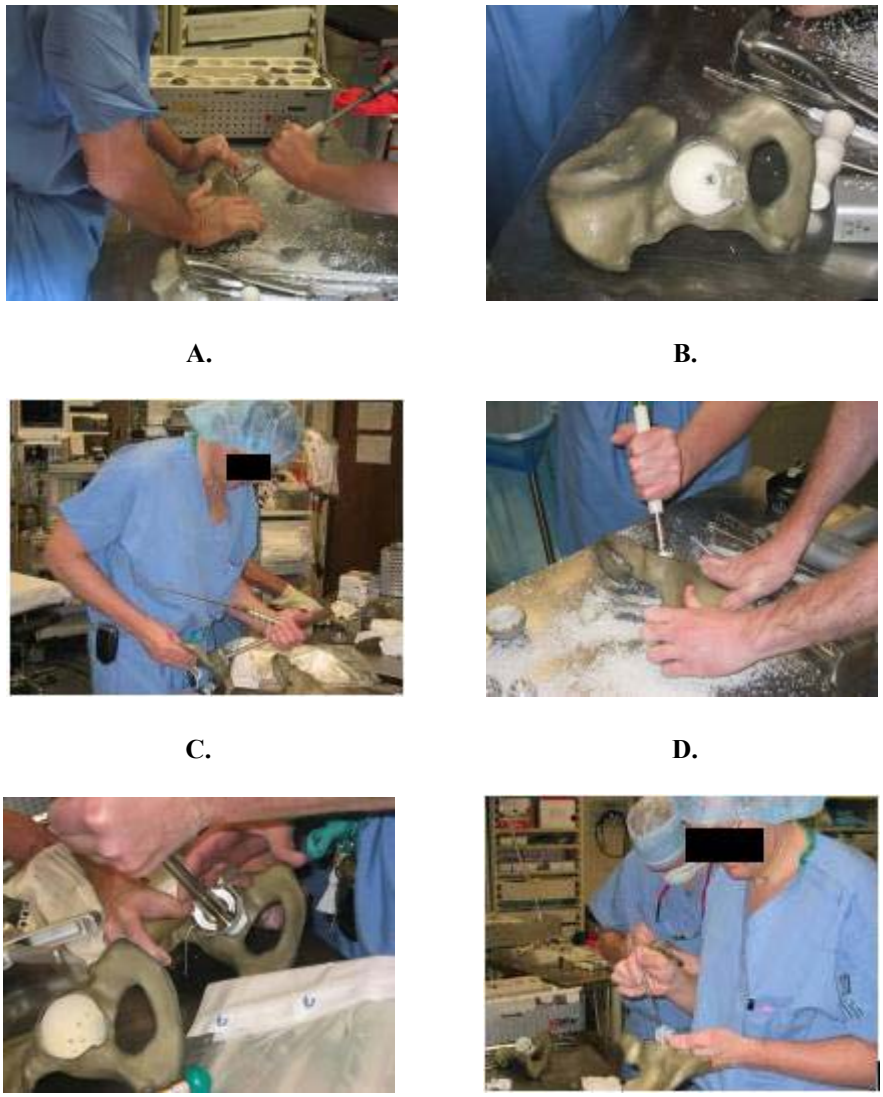

A. **B.**

C. **D.**

E. **F.**

Figure 13. A.) Reaming Out the Synthetic Pelvis **B.)** Reamed Out Pelvis **C.)** Positioning of Acetabular Cup **D.)** Securing Acetabular Cup **E.)** Placing Acetabular Cup (drilled holes in cancellous bone can be seen in the lower left) **F.)** Removing Excess Bone Cement

3.2.4 Accelerometer Orientation:

In order to understand mounting of the accelerometers and the analyses of the accelerometers, the importance of accelerometer orientation must be understood for all tests involved in this study. Kane's notation (Kane, et al., 2000) is used throughout this text in order to reduce confusion caused by the multiple sets of axes. For acetabular cup resonance tests, the cable for the accelerometer pointed toward the open end of the cup (Figure14). For the femoral stem, the cable pointed away from the femoral head 180° (figure 15). For the unimplanted femur, the accelerometers all faced approximately the same direction (figure 16). The orientation of the accelerometers in the unimplanted pelvis is the same as the implanted pelvis except for the third accelerometer which is mounted on the superior portion of the ilium (figure 17). All implanted component accelerometers are oriented the same as they are for the impact tests (figure 18).

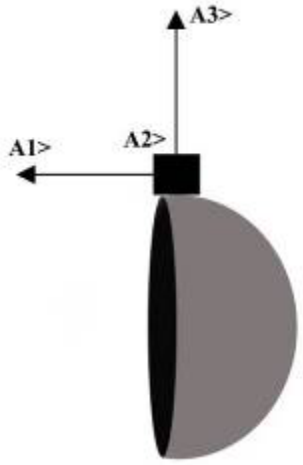

Figure 14. Orientation of the Acetabular Accelerometer

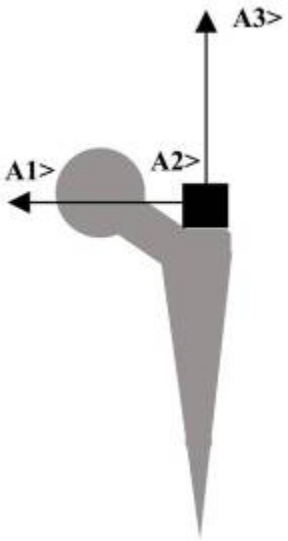

Figure 15. Orientation of the Femoral Stem Accelerometer

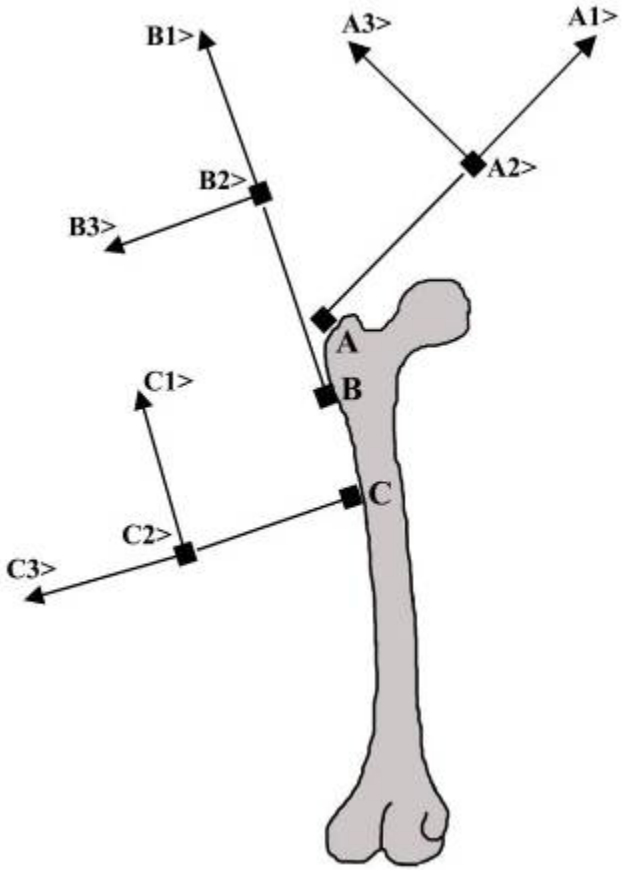

Figure 16. Orientation of Accelerometers During Normal Femur Testing

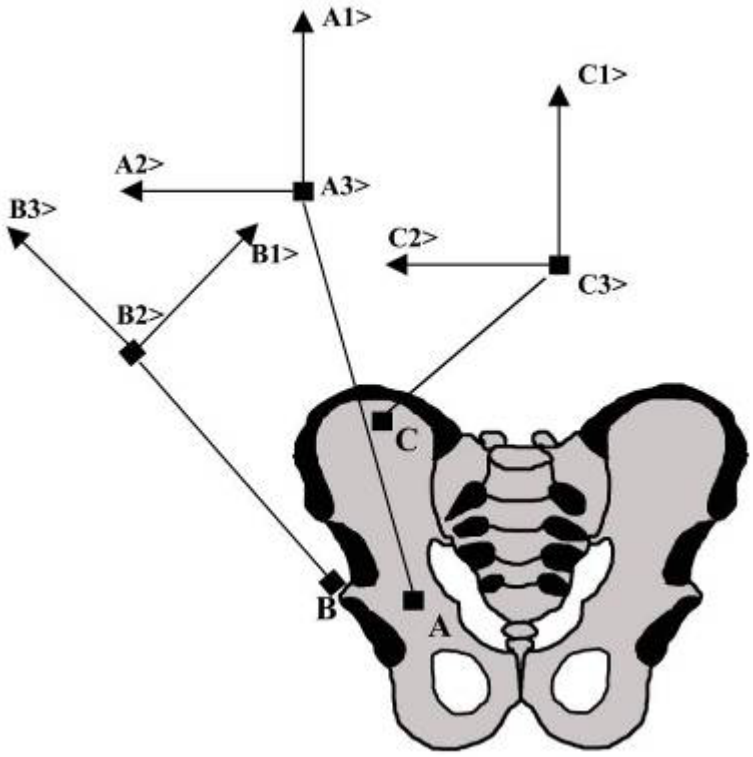

Figure 17. Orientation of Accelerometers During Normal Pelvis Testing

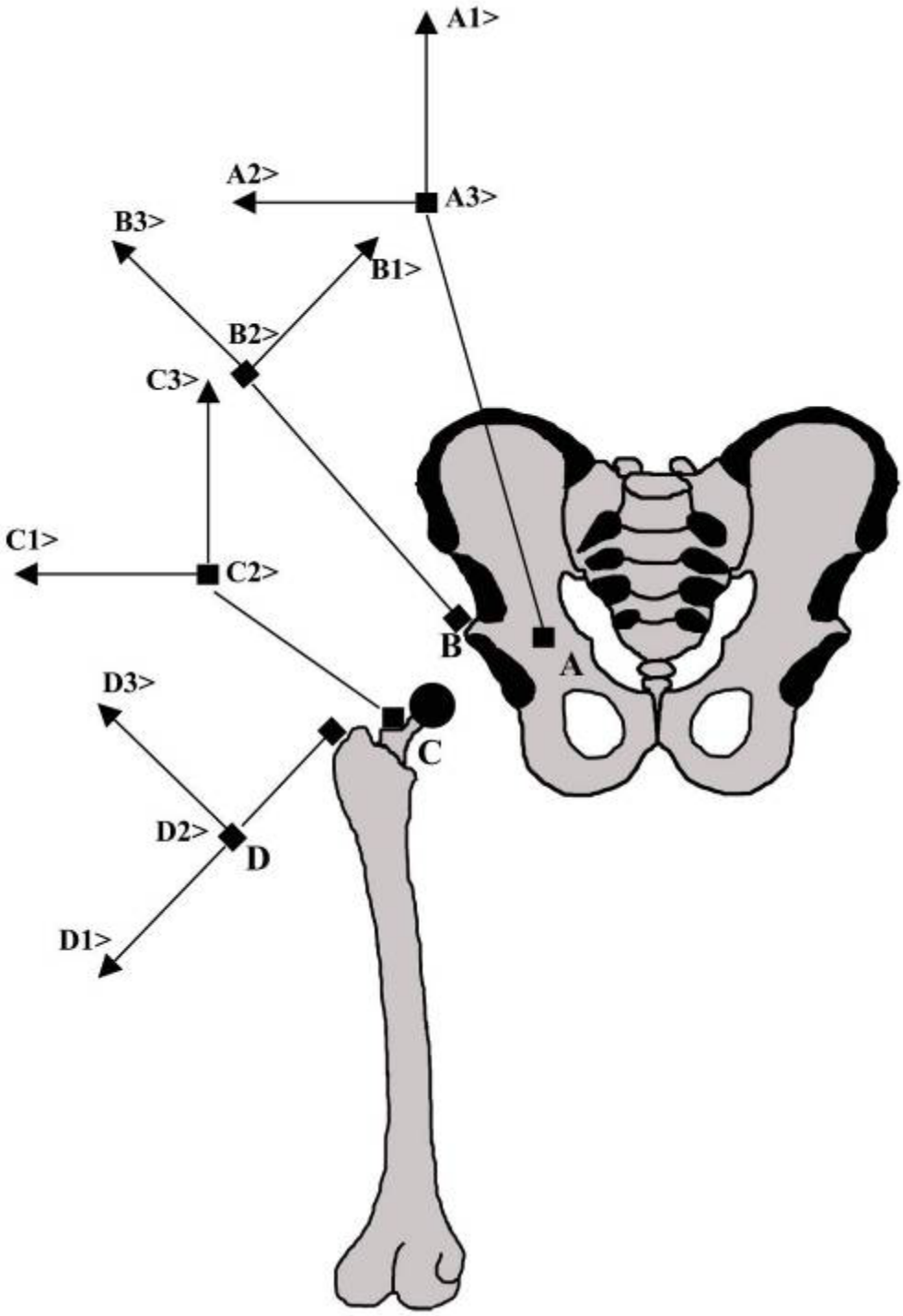

Figure 18. Orientation of Accelerometer Axes During MTS Machine Testing

3.2.5 Attaching the Accelerometers:

When conducting research with accelerometers, a variety of techniques exist for mounting them. It is generally considered that the more securely the accelerometer is attached to the mounting surface, the less interference and transient noise will be seen in the signal. Based on this assumption, it was decided that the best way to mount the accelerometers for this study was to use a hard mount. Mounting the sensors this way involved screwing them directly onto the surface of interest. The accelerometers are manufactured with a 5-40 threaded hole for the purpose of mounting. Therefore, the idea of mounting these involved securing a 5-40 threaded rod onto the mounting surface which allowed the accelerometer to be screwed onto the surface of interest.

Initially it was decided that the best option for attaching the metal rods to the bones was to screw them directly into the bones. A 0.101 inch hole was drilled and then a 5-40 tap was used to thread the hole. A metal stud was cut from a longer piece of 5-40 stock and screwed into the hole with the help of a pair of pliers. The accelerometer was then screwed onto the part of the metal stud that protruded from the bone. This procedure worked for the first few times the accelerometer was attached, but the strength of the cortical bone the screw was using as an anchor eventually gave way, and the mount became loose. Therefore, another method of fixation was necessary.

Due to the large amount of bone cement donated by DePuy, a decision was made to use bone cement to affix the accelerometers to the bones. Bone cement is designed in part to mimic the physical characteristics of bone, and, therefore, it was felt that using bone cement for such a purpose would not change the vibratory characteristics of the system in a significant manner. To prepare the bone, the same spot on all of the bones

was marked with a permanent marker. A ¼-inch diameter hole was then drilled through the cortical bone into the cancellous bone. A ½-inch piece of threaded stud was cut from a larger piece of threaded stock. The stud was screwed into the hole in the accelerometer until tight by using a pair of pliers. This process was done for three holes at a time. Once three accelerometers were ready to be mounted, a batch of Endurance™ bone cement was prepared using the same instructions indicated previously. The holes were filled with the cement, and then the accelerometers with the studs attached were placed in the cement. Care was taken to ensure the orientation for each accelerometer was the same. C-clamps were then used to tightly secure the accelerometer to the bone until the cement had completely set. The accelerometers were then unscrewed from the studs, and a bone with multiple hard mounts was left. The bones with multiple studs were to be used later for component analysis. Bones being used specifically for the impact testing received one hard mount, one on the greater trochanter for the femurs (figure 19b) and one on the pubis directly behind the center of the acetabulum for the hemi-pelvises (figure 19a).

A. **B.**

Figure 19. A.) Accelerometer Hard Mounted on Back of the Acetabulum **B.)** Accelerometer Hard Mounted on Greater Trochanter

Figure 20. Accelerometer Mount and Mounted Accelerometer on Acetabular Cup

Drilling a hole into the implant and tapping a hole was the initial idea used for attaching the implant accelerometers. For the non-implanted acetabular shells, a 0.101 inch was drilled into the top edge of the microsphere surface parallel to the opening of the cup. This hole was made as deep as possible without protruding into the inner surface of the cup itself. Overall, the holes were about 1/8" deep. These holes were then threaded using the 5-40 tap. A small 5-40 stud was screwed into the hole to make sure it was secure, and the accelerometer was then screwed onto the stud to make sure the length of the stud was correct. Then, a few drops of Loctite™ adhesive were placed into the hole, and the stud was allowed to set. The accelerometers were then screwed back into place to make sure everything was still tight and oriented correctly (figure 20).

For the stems, the hole was drilled on the bottom of the neck of the prosthesis near the trunion. However, it was determined after several failed attempts that drilling and tapping a hole into a piece of Cobalt-Chrome without special equipment was impossible. Therefore, bone cement was once again necessary for attaching the mounts. As before, a metal stud was cut from a larger piece of 5-40 stock and screwed into the accelerometer. A flat horizontal surface with notched a hole is located on the top of the Summit™ stems, before the neck begins to protrude. The purpose of this hole is to

Figure 21. Mounting Stud Placement on Femoral Stem

provide a place for the surgeon to apply instrumentation with the purpose of adjusting the location of the implant during surgery. Since there was no longer a need for this hole, it was convenient to fill it with bone cement, so it can be used as a mount anchor. Therefore, after the bone cement and accelerometer had been prepared, the hole was filled with bone cement, and the accelerometer was placed within the hole as far away from the neck as possible (figure 21). The accelerometer would have clearance when being screwed on and off of the implant. Pressure was applied with the thumb on the accelerometer until the cement had set. C-clamps couldn't be used because of the irregular shape of the femur and the location of the accelerometer. This procedure was carried out for both the implanted and non-implanted femoral stems.

Before attaching accelerometers to the implanted acetabular cup, some issues had to be addressed. The site chosen for attachment was the edge of the acetabular cup closest to the obturator foramen (the large hole that is present on each side of the pelvis). This site was chosen because the space created by the obturator foramen gave some degree of maneuverability to the drill and to the accelerometer which had to be twisted around in order to be secured. The edge of the cup was concealed by a small bit of the cortical shell which was removed by a Dremel® rotary tool. Once the shell was exposed, a 0.101 inch

hole was drilled, and the same procedure was carried out as described earlier with the non-implanted acetabular cups. Once the metal stud was in place for the first acetabular cup, it became apparent that the mounting approach would have to change. The space given by the obturator foramen was large enough for the accelerometer itself, but it didn't leave enough freedom to screw on the accelerometer because of the wire protruding from the side of the accelerometer. Therefore, it was necessary to carve out some space on either side of the stud into the superior pubic ramus and into the ischium.

Because of the awkward angle involved in affixing the accelerometer into the first implanted cup, it was decided to try using an industrial strength epoxy. In order to do this, the cortical bone still had to be removed at the point of fixation, and parts of superior pubic ramus and the ischium had to be carved out again. The accelerometers had come with smaller pre-made studs and a small hexagonal base with which to attach the stud and accelerometer. The option of using the base instead of gluing the accelerometer directly onto the cup was chosen because this choice would allow the sensor to be removed and affixed multiple times. If the accelerometer had been glued directly, the bond would have had to be broken when the accelerometer needed to be taken off and would have had to have been glued again for more tests to occur. The difference between the glued and hard mounted accelerometers was not expected to be noticeable. Once the inserts were placed in the cups, the decision was made to make the hard mounted pelvis the one with the polyethylene liner because it was expected to have the smallest magnitude of vibration. If there was any difference at all between the mounts, the extra security of the hard mount would help ensure that the least amount of vibration data was distorted.

3.2.6 Testing Machine:

Through collaboration with Oak Ridge National Laboratory (ORNL), the MTS 312.21hydraulic material tester was chosen as the testing device for this study. ORNL also granted use of their machine for the purposes of this study. This machine had a load range of 0 to 22,000 pounds. This particular apparatus performed testing on a single axis (the vertical axis). The height of the load frame was adjustable. This was important because it allowed the mechanism to accommodate the height of a full length femur and accompanying fixtures. A 1 inch 1-14 thread connector was the initial basis for connecting fixtures to this machine, but ORNL was also in possession of a collection of adapters allowing several choices of fixture mount size.

3.2.7 Fixtures:

Fixtures had to be designed for the impact tests which needed to meet several criteria, including:

1. Holding the pelvis and femur in correct anatomical position
2. Not moving during impact tests
3. Withstanding the maximum force of the impact tests
4. Showing minimal inhibition of the vibratory properties of the THA system
5. Fitting and working properly with the machine chosen for the impact tests
6. Demonstrating economically feasibility

The largest of these problems to overcome was the proper orientation of the femur with the pelvis during the tests. The human hip interface is not a one dimensional system. Gait applies movement and forces in multiple directions. For the purposes of this study

the femoral head had to be lined up with the acetabular cup. If the tests only involved one specific femur and one specific pelvis, the fixtures could have been designed around that one set. However, due to the slight differences in orientations of the implants, a pair of fixtures had to be designed that provided for an adjustable orientation. Adjustability would allow all of the implanted bone sets to be used in the same fixtures. Planning for adjustability would also save time on the design process because as long as the fixtures were adjustable over a range of dimensions, they wouldn't have to be designed for any specific test. After planning and talking with the machine shop, a final design was chosen for both fixtures.

3.2.8 Pelvis Fixture:

On the MTS machine, the piston is the bottom component which moves vertically. Therefore, to make the test visibly and physically accurate, the pelvis was chosen to be mounted to the static part of the machine that was to be impacted by the piston. Originally impact tests for this study were going to run as high as 1,000 lb and a fixture design capable of withstanding a 2,000 lb impulse was necessary for safety reasons. It was decided that the fixtures used in this study be designed, such that they could be used for future testing using much larger loads than those used in this study. To make the pelvis fixture as adjustable as possible, a ball joint was chosen to attach the pelvis fixture to the top of the machine. A ball end trailer hitch was used as the ball joint. A round metal plate, 4.5 inches in diameter, 0.75 inch thick with 3-5/16 inch screws was placed over the shaft of the trailer hitch and held in place by the ball. The next part of the fixture was a ½-inch thick 9x7 inch piece of steel. Another steel ring plate, identical in

size to the previous ring plate, except one half inch thicker was welded to this plate. The center of this thicker plate had been reamed out spherically to accommodate the ball joint. Three holes in the larger ring lined up with the three holes in the other ring. When screws connected the two plates, the result was a plate that was moveable from the horizontal to 80 degrees. When the screws were completely tightened down, the ball joint became immobile.

Once the rigid plate fixture had been created, a method of attaching the pelvis to the plate had to be devised. To distribute the impact forces of impact across the plate evenly, the pelvis had to lay on the plate using a material to fill the irregular gaps between the back of the pelvis and the plate, ensuring that unnecessary stresses were not applied to the synthetic bone. The best way do accomplish this task was determined to be through the creation of a mold to hold the pelvis. Conceptually, a mold with a flat bottom and with the contours of the back side of the pelvis on top was created. The pelvis would be placed in the mold, and the mold would be attached to the fixture plate. When struck, the entire plate would absorb the impact.

The material chosen for the mold was Bondo® auto body filler. This particular material was chosen because it was cheap, readily accessible, easy to work with, and fairly strong. While it was not certain that this material would be capable of withstanding the forces exerted under testing conditions, a decision was made to try it, and if it failed, replace it with something else. To create the mold, a plastic container with roughly the same dimensions of the pelvis was chosen. A large amount of Bondo® was mixed and poured into the container. A pelvis which had no implants was covered in Aluminum foil for protection and placed in the container. The pelvis was adjusted to the desired

orientation and angle. Excess Bondo® was quickly moved around the pelvis to fill in gaps. The mold was then allowed to set. Once ready, the mold was removed from the container, and a Dremel® rotary tool was used to cut the mold until the pelvis could be removed. The tool was then used to smooth the mold and eliminate any jagged edges as well as to loosen the mold slightly so that the pelvis could be easily placed and removed, yet not fall out. A large hole was bored into the back of the mold so that there would be no interference with the accelerometer that was positioned on the pubis directly behind the center of the acetabulum. From this hole, a large groove was cut so that the wire from the accelerometer could be placed without being pinched. Three ½-inch diameter holes were then drilled at three corners of the mold and then tapped. Holes corresponding to the holes in the mold were drilled into the ½-inch plate of the fixture 1.5 inches from the edge at three of the corners. Screws were then used to secure the mold to the fixture (figure 22).

Once the mold was attached, one of the pelvises was placed in the mold, and the fixture was held in the same orientation in which it would be during testing. It was decided that the angle of the incline was not steep enough and did not resemble the

Figure 22. Pelvis Resting Inside Pelvis Fixture

posture of the pelvis of a standing human closely enough. Therefore, a Dremel® tool with a cutting wheel was used to cut a wedge of the trailer hitch portion of the fixture. This cut allowed the rotating plate more room to maneuver and created a more lifelike pelvis position. Once the fixture was deemed to be adjustable enough, the threaded end of the ball joint (14 threads per inch) was screwed into the machine and tightened using two hexagonal nuts.

3.2.9 Femur Fixture:

Like the pelvis fixture, designing adjustability into the femur fixture was very important. The base of the fixture was a ½-inch piece of steel. On this plate was welded a piece of steel pipe which was threaded interiorly with a 14-1 tap. On top of the pieces of steel were mounted two precision sliding tracks designed for use in metal machine shops. On top of these tracks was mounted another ½-inch piece of steel which joined the two tracks and provided a surface for the bone to rest. When oriented anatomically, it was determined that the hollow shaft of the bone made a 5.5° angle with the horizontal. Therefore, a hole was drilled into the plate at a 5.5° angle and threaded. A threaded rod was screwed into this hole so that the femur could be mounted on it, reducing movement of the femur during testing. On the sides of the base plate were mounted vertical plates which were about as tall as the femur when it stood on end. Holes were drilled into these plates and threads were tapped. Threaded rods with knobs on one end and adjustable feet on the other were screwed into these holes and used as clamps to secure the femur (figure 23). Packing foam was placed between the feet and the femur in order to minimize any

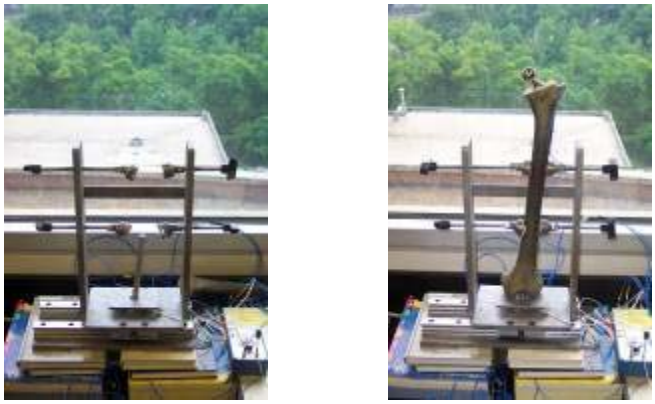

A. **B.**

Figure 23. A.) Femur Fixture **B.)** Femur Mounted Within Fixture

effect the fixture would have on vibration as well as to minimize any damage that might occur from the clamping.

Later it was decided that it was necessary to have a force transducer in the system other than the one mounted on the impact tester. Because the fixtures had already been made, altering the existing fixtures would be the best course of action. A 0.159 inch hole was drilled and tapped with 10-32 UNF-2B threads into the platform on top of the sliding tracks. This hole was used to mount the force transducer to the fixture. A smaller steel plate was then laid on top of the transducer. A screw was used to secure the plate to the top of the transducer. The femur was then placed on this plate instead of the plate mounted on top of the sliding tracks (figure 24).

Figure 24. Femur Mounted on Force Transducer

3.3 Testing:

3.3.1 Component Resonant Testing:

Each component and component configuration was tested to determine resonancy and excited frequencies. This testing was done by hanging the component, with accelerometer mounted, from a string and then tapping it with an instrumented impact hammer while the data acquisition system was running. Each component test was conducted six times in order to verify the repeatability of the frequencies seen in the test and because it was possible to conduct an unlimited number of tests unlike the situation presented at ORNL.

For the acetabular shells, a small 0.043" hole was drilled through the rim of the acetabular cup right above where the accelerometer stud was placed. A piece of string was tied through this hole and the implant was hung from this string. Impact occurred at the center of the shell or the center of the acetabular liner. Tests were carried out for the acetabular cup, acetabular cup with metal liner, acetabular cup with polyethylene liner,

and the acetabular cup with ceramic liner in this fashion. Cup tests were performed with one accelerometer mounted towards the mouth of the cup (figure 25).

A piece of thread was tied around the bottom of the trunion toward the top of the implant in order to hang the femoral stem. This process allowed the implant to hang securely. Impact for the stem tests occurred at the top of the trunion when no femoral head was present and on the top of the femoral head when present. Hip stem tests were carried out for the stem only, the stem with metal femoral head, and the stem with ceramic femoral head. Stem tests were performed with one accelerometer mounted on the top of the femoral stem (figure 26).

In order to test the bones, kite string had to be employed because the weight was too great for the sewing thread used in the implant tests to withstand. To test the femur, the string was tied around the femoral head. Impact occurred at the top of the natural and synthetic femoral head for femur tests. Tests were carried out on the natural bone, implanted stem, implanted stem with ceramic femoral head, and the implanted stem with metal femoral head. Femur tests were conducted with two mounted accelerometers, one on the stem (when available) and one on the greater trochanter of the femur (figure 27a). To test the pelvis, the string was tied around the obturator foramen in order to hang the bone. Impacts for the pelvis occurred at the center of the acetabulum when no implant was present and at the center of the acetabular cup or insert when implants were present.


Figure 25. Resonant Test Setup for Acetabular Cup and Liner


A. **B.**

Figure 26. A.) Resonant Test for Femoral Stem **B.)** Resonant Test for Femoral Stem with Head

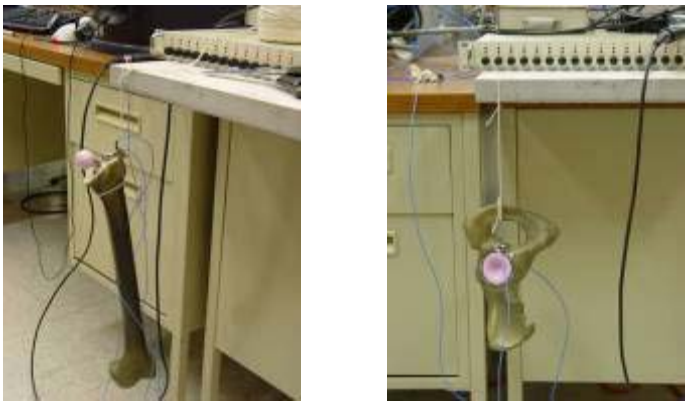

A. **B.**

Figure 27. Resonant Test Setups for **A.)** Implanted Femur and **B.)** Implanted Pelvis

Tests were carried out on the normal pelvis, pelvis with cup implanted, pelvis with cup and metal insert, pelvis with cup and ceramic insert, and pelvis with cup and polyethylene insert. Pelvis tests were conducted with accelerometers mounted on the cup and on the pubis directly behind the center of the acetabulum (figure 27b).

Tests were also conducted with the bones in the fixtures in order to investigate any possible effect the fixtures may have on the system. For the femur, the femoral fixture was set upright and a normal bone, bone with stem and ceramic femoral head, and bone with stem and metal femoral head were placed within it and secured (figure 28a). The impact hammer was used to strike the femur on the femoral head, and vibration was measured by accelerometers mounted on the greater trochanter and on the top of the stem. For the pelvis, the tests were conducted with the pelvis in the fixture which was laid on the ground. The impact hammer was used to strike the center of the acetabular liner or acetabulum for the normal pelvis, pelvis with acetabular cup with metal liner, pelvis with acetabular cup with polyethylene liner, and pelvis with acetabular cup with ceramic liner (figure 28b). Vibration for the mounted pelvis tests was measured by an

A. **B.**

Figure 28. Resonant Test for **A.)** Femur and **B.)** Pelvis in Corresponding Fixtures

accelerometer mounted on the rim of the acetabular cup and by an accelerometer mounted on the pubis directly behind the center of the acetabulum.

3.3.2 Tests with No Separation:

In order to compare the differences in the frequencies occurring due to vibration when sliding occurs and when it doesn't occur, some tests had to be run where no separation existed. To properly carry out these tests, a Force vs. Time measurement was taken several times using a three dimensional AMTI® force plate. The average times of these trials from heel strike to toe-off were taken to give a target time frame that the impact tester should use to reach the desired force and then let back off. The time determined necessary for the non separation load tests to emulate was 0.5 seconds (Figure 29). To carry out these tests, the fixtures were mounted onto the load frame of the MTS frame, and the implanted bones were then loaded into the fixtures (figure 30). During MTS testing, it was necessary to clamp the pelvis into the fixture in order to prevent it from falling out of the fixture.

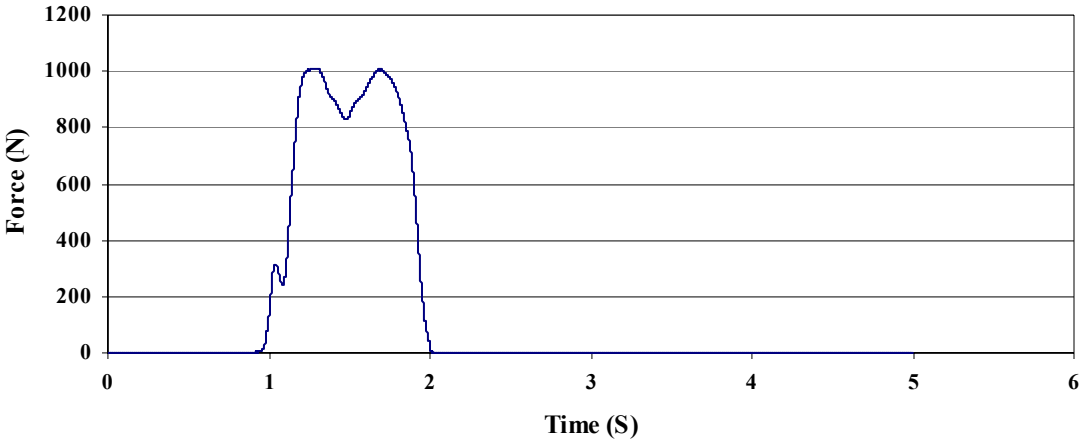

Figure 29. Example of Forceplate Curve Used to Determine Speed of Tests Without Separation

A. **B.**

Figure 30. A.) Orientation of Bones While in Fixtures During Testing **B.)** Fixtures in MTS Machine During Testing

The femur was moved up until a force registered on the controls (indicating contact) and then backed off till the force was just zero. This process meant that there was contact between the acetabular cup and the femoral head but no force being applied. A specific maximum load was input into the MTS machine controls. The machine was configured in such a way that once the maximum force had been reached, the machine would reverse and go back to the position in which it started. Based on the forceplate data, a specific speed was input into the controls as well. This decision meant that the maximum load would be reached in a predetermined amount of time in order to more closely resemble the load curve observed in actual gait movement. These tests were carried out at 222.5, 445, 667.5, 1112.5, 1335, and 1780 N. After each test, the load curve was observed (Figure 31) to ensure that it did follow a similar pattern to that of gait and that the desired force was reached. When necessary, the loading speed and maximum force were adjusted.

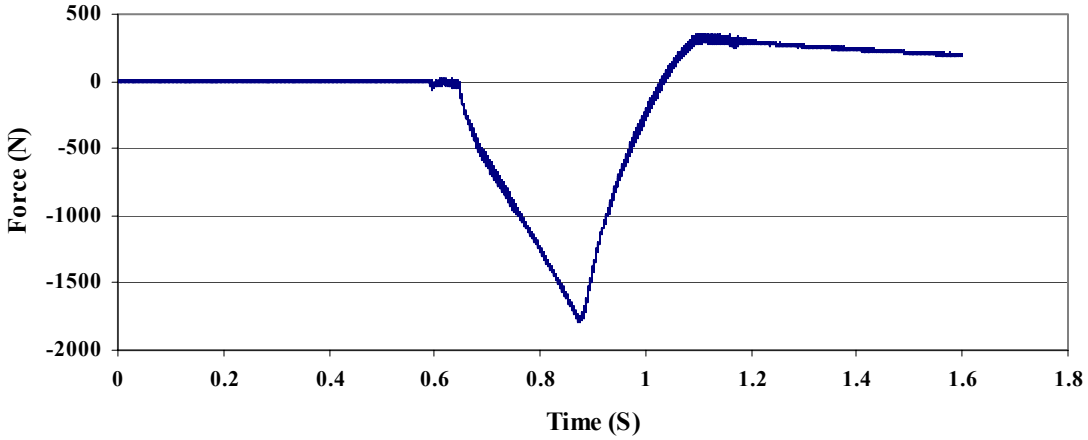

Figure 31. Force Curve of MTS Tests with no Separation

3.3.3 Tests with Separation:

In impact tests such as these, the actual physical separation between the femoral head and acetabular cup is of little consequence. The parameter distinguishing the amount of separation was velocity as related by the simple relation:

$$v = \sqrt{2ax}$$

In this case, v is the vertical velocity of the femur as it impacts the pelvis; x is the desired separation to simulate; and a is the acceleration of the femur into the pelvis that occurs in the body. In this situation, the acceleration of the pelvis's moving toward the femur (or vice versa) was considered to be the acceleration due to gravity or 9.81m/s^2. Acceleration was assumed to be constant. For a separation of 1mm, it was determined that the machine had to have a vertical velocity of 14 cm/s. Because this machine used English units, the equivalent of 5.6 inches was the speed desired to simulate the impact caused by a separation of 1mm. The vertical speed that the machine reached was found by calculating the derivative of the displacement curve using a simple program written in Matlab. The displacement data was output by an extensiometer which was in contact with the bottom of the femur fixture. The extensiometer was connected to the data acquisition system, and fixture displacement data was collected for all tests (figure 32). Ideally, the impact tests with separation would be carried out at identical loads as found in the tests with no separation. However, the machine being used for this study did not necessarily yield very repeatable results. Therefore, many tests had to be repeated, and much data were acquired over a variety of loads and simulated separations (table 3). The tests being compared in this study are grouped by their proximity to one another based on

Figure 32. Extensiometer and Load Cell on Test Setup

Table 3. Impact Test Groups Considered for Comparison

Material	Force (N)	Simulated Separation (mm)
MOP	679.03	1.5078
MOM	688.82	0.7964
COC	662.57	1.0569
MOP	1139.6	1.2245
MOM	1168.1	0.9289
COC	1132.9	1.1931
MOP	1280.6	1.1698
MOM	1270.8	1.1698
COC	1290.4	1.0642
MOP	1506.7	1.1468
MOM	1533.8	1.43
COC	1501.3	0.7964
MOP	1713.2	2.411
MOM	1739.4	1.3876
COC	1722.9	1.0277
MOP	1979.2	1.8014
MOM	1883.6	1.3048
COC	1851.1	1.1164

both load registered by the MTS load cell and by the separation calculated from the derivative of the displacement curve. The tests, actual force, and simulated separation can be found in Table 3.

3.4 Data Processing:

3.4.1 Preliminary Processing:

Once the data had been acquired, all post processing was carried out using Matlab (The Mathworks Inc., Natick, MA). To examine data characteristics after each test to determine if the test was actually what was desired, some smaller crude programs were developed. In order to determine if the velocity, and, thereby, the simulated separation, was accurate, the data obtained from the extensiometer were differentiated to get the velocity. The largest velocity on the plot was determined to be the max speed. In order to determine what was truly the maximum velocity, tests with smaller displacements often had a smaller step size on the differentiation than tests with larger displacements. The simple code used for this can be seen in the appendix. In addition to velocity measurements, unfiltered FFT's were taken from each channel and plotted for quick comparison in addition to simple plots of the raw acceleration signal produced from the impact for all acceleration channels.

3.4.2 Data Verification:

It was determined that an appropriate way to verify validity of both accelerometer data and force transducer data from the impact tests was to compare velocity with respect

to force. The force measured by the MTS load cell corresponded to the vertical force exhibited by the test. The most appropriate acceleration signal corresponding to this force was the z-axis on the accelerometer mounted on the femoral stem. Ideally, in a test such as this the velocity would be at a maximum just as the force began to rise at the instant impact began. To get the velocity curve in this case, the integral was found for the acceleration signal in question. Integration was carried out by using the cumulative sum of the signal and multiplying it by $1/F_s$. The plot of the velocity exhibited on the vertical axis of the femur accelerometer was then compared to a scaled and smoothed version of the force curve. Since the shapes were the only items being considered in this analysis, any change in magnitude caused by the smoothing filter on the force curve was inconsequential.

3.4.3 Final Data Processing:

After all preliminary processing had been completed, a definitive method of processing the large amount of data acquired needed to be developed. The method used needed to make the data as clear as possible for comparison while keeping the overall distortion from filtering and other manipulation to a minimum.

With an FIR filter, there are both poles and zeros to manipulate, making the filter more complex. Therefore, it was decided to use an IIR filter design technique to filter the acquired data. The method was implemented through the use of Matlab. The first step in implementing this IIR technique was determining the filter parameters. Because of noise and ambient vibration, it was decided to eliminate all frequencies below 10 Hz. Because not all of the accelerometer axes went past 7000 Hz, it was decided to filter out all signals

above 7000 Hz, thus creating a passband between 10 and 7000 Hz. The desired filter to use was a Butterworth filter. The order of the filter was determined by using the "`buttord`" command in Matlab. The desired cutoff frequencies and dB loss were input into the command parameters. The starting point of the filter was determined to be 5 Hz and the ending frequency was determined to be 8000 Hz. The maximum allowable loss through the passband was set at 3 dB and the minimum allowable loss through the stopband was set at 10 dB. The "`buttord`" command then determined that the proper order for a Butterworth filter meeting all of the stated criteria was 3. This information was then used to create a Butterworth filter using the "`butter`" command (figure 33).

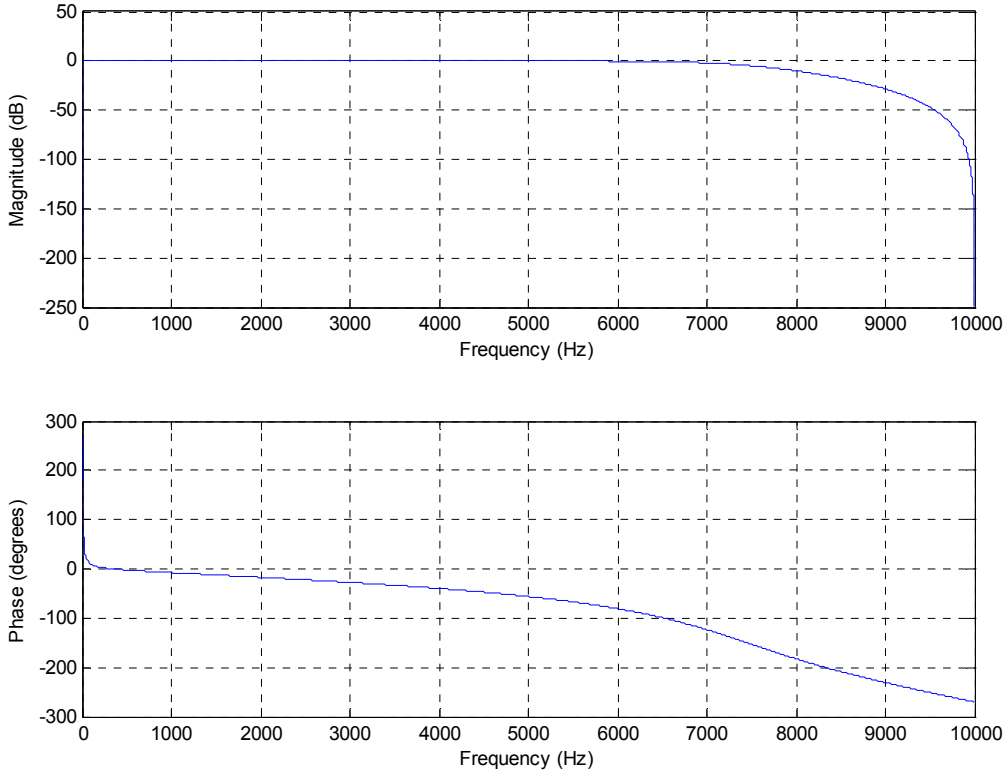

Figure 33. Magnitude and Phase of the Passband Filter

After reviewing the preliminary data, a spike in the 670 to 690 Hz range was exhibited in all impact tests. The spike was also present when the data acquisition program ran, but no impact test was conducted. Therefore, it was determined that the spike was due to some sort of noise in the system. In order to get rid of this noise, a stopband filter was necessary. Design of this filter was similar to the passband filter. The passband for this filter was set up to be 0-655 Hz and 685-7000 Hz. The maximum dB loss in the passband was set at 3 dB and the minimum dB loss in the stopband was set to 10 dB. Through use of the "`buttord`" command, it was determined that the order of this filter was 2. This information was then used to create a Butterworth filter using the "`butter`" command (figures 34 and 35).

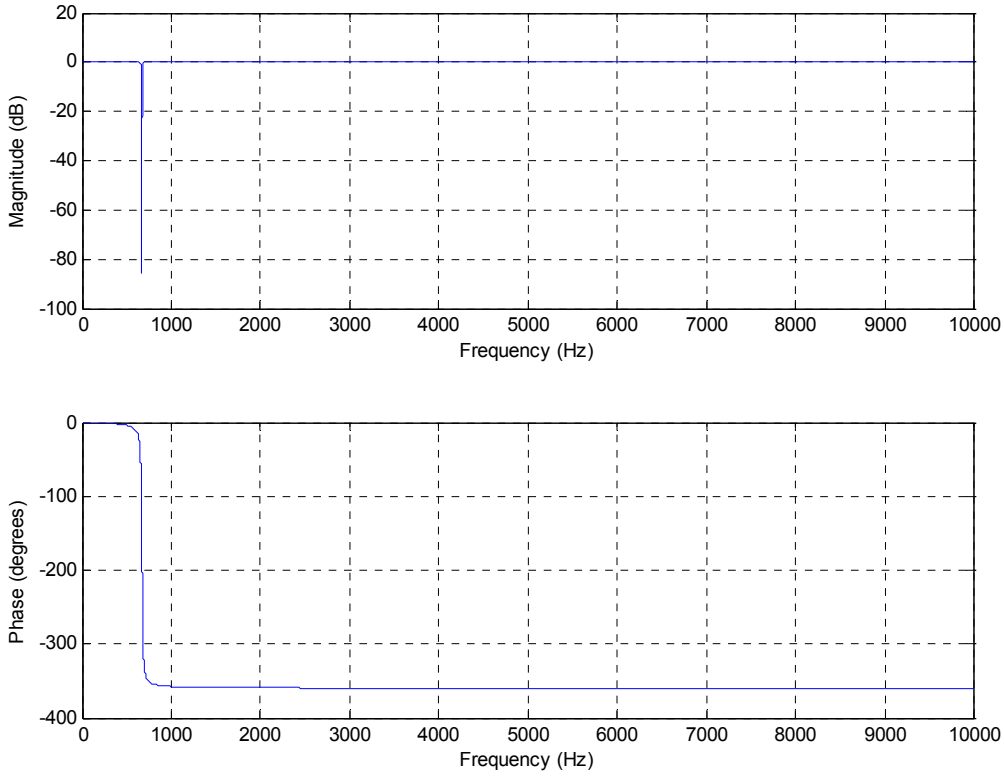

Figure 34. Magnitude and Phase of the Stopband Filter

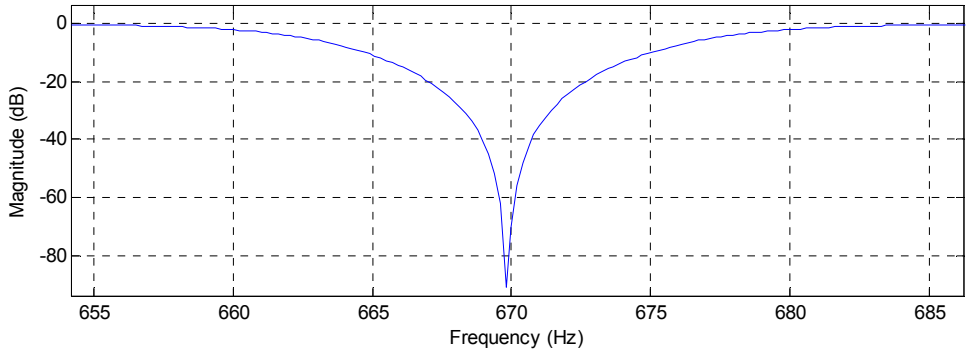

Figure 35. Close Up Magnitude of Stopband Filter

The data was processed using a hanning window that was overlapped 8 times within the width of the sample being used. This window was then used to find the PSD using Welch's method via the "`pwelch`" command in Matlab.

CHAPTER IV

RESULTS

Note: All results are for the accelerometer mounted on the femoral stem in the vertical direction (C3>) during an 1150 N test for COC, unless noted otherwise

4.1 Effects of Filtering:

The changes observed in the acceleration signal due to filtering are minimal (figure 36). However, when this signal is observed in the frequency domain, the change in magnitude and the elimination of unwanted signals is apparent (figure 37). A band pass filter was applied, effectively only allowing frequencies between 10 and 700 Hz. The effect of this filter can be seen by observing the sharp dropoff after 7,000 Hz compared to the unfiltered signal. A stop-band filter was also used to eliminate frequencies in the range of 655 Hz to 685 Hz. It was necessary to remove these signals because a spike in the PSD was present for this frequency, even if no impact was made. This indicates that the signal is some sort of noise in the system, possibly from the vibration of the MTS testing machine itself. Therefore, we assumed that this noise spike is from another machine that was in use during the impact testing machine tests we conducted involving natural frequency determination. The effect of this filter can be seen in the small negative spike on the filtered PSD around 670 Hz that is not present on the unfiltered PSD.

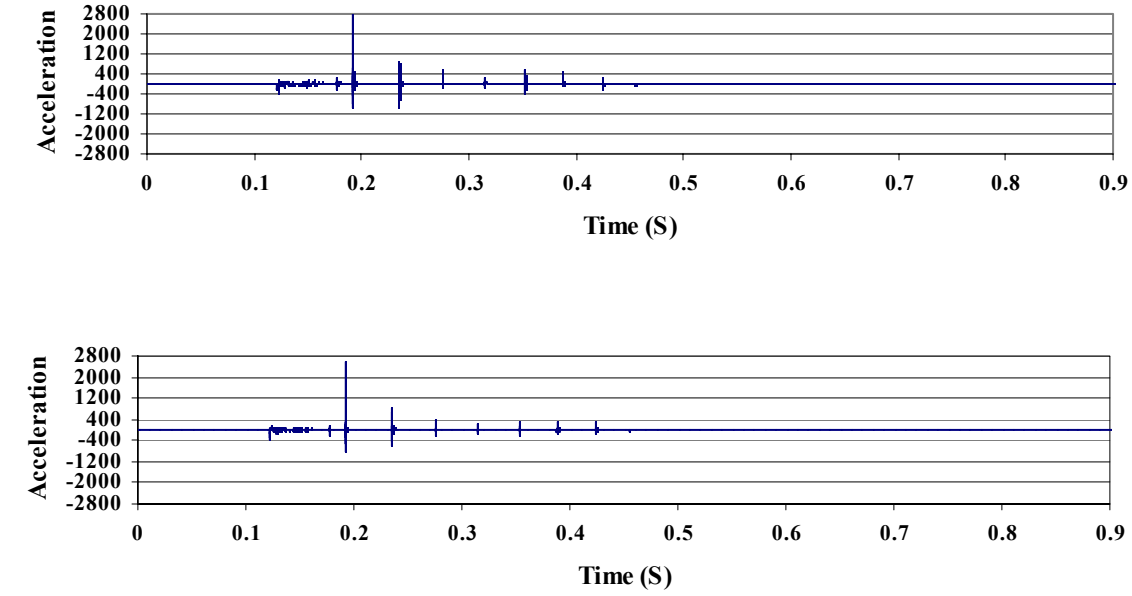

Figure 36. Comparison of Acceleration Signal Without Filtering (top) and with Filtering (bottom)

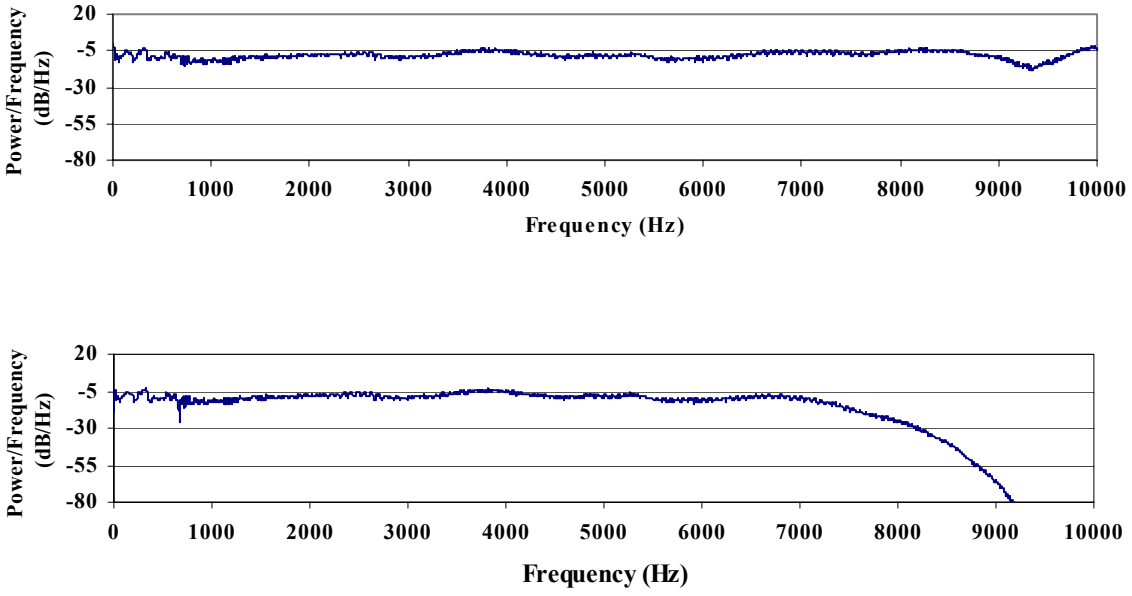

Figure 37. Comparison of PSD Signal Without Filtering (top) and with Filtering (bottom)

4.2 Data Correlation and Verification:

In order to help verify that the data acquired was logical, it was necessary to subject the data to some rudimentary preliminary tests. One of these tests was a comparison of the force signal registered by the force transducer and the velocity of the femur fixture as it moved upward in the C3> direction. The nature of this test suggests that the velocity of the femur fixture moving up will be at a maximum just before impact and then decrease. As the velocity decreases, the force should be at a maximum. In order to compare the force from the MTS transducer and the velocity derived from the acceleration signal, the data first had to be filtered so that the general shape of the curves could be examined more easily. A high-pass Butterworth filter with a cutoff frequency of 50 Hertz was created for this purpose. The smoothing filter makes observing the general behavior of the signal easier (figures 38-40). It is evident that the magnitude of the signals is changed when this filter is applied, but this change is of no consequence because the overall behavior of the signal is not changed. The relationship between the MTS load cell data and the velocity derived from the accelerometer signal verifies that the data acquired is logical for the test in question (figure 40). The maximum force does occur approximately when the velocity curve is at zero.

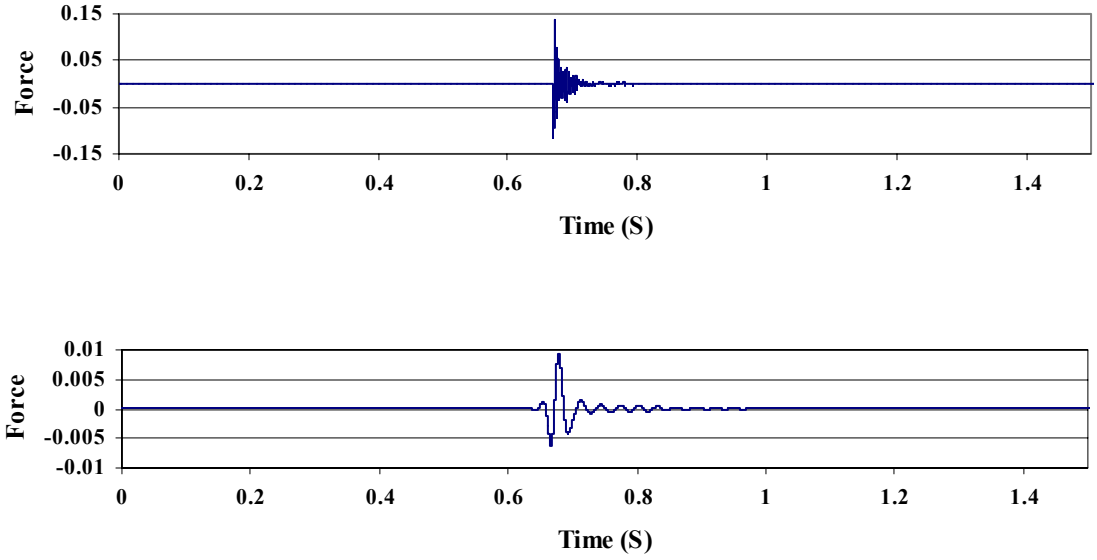

Figure 38. Comparison of Force Signal and Force Signal After a Smoothing Filter is Applied

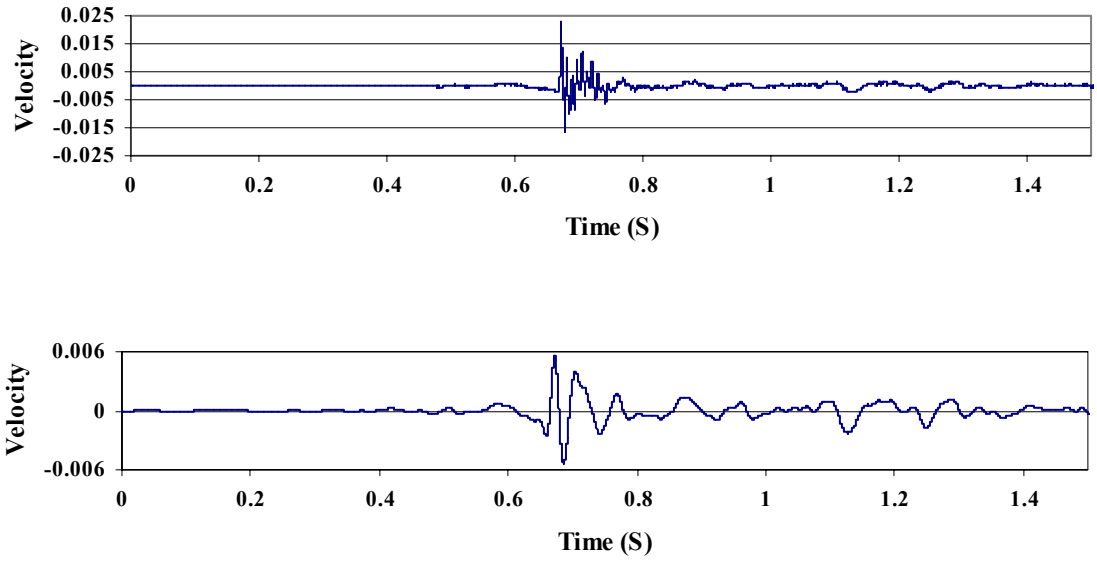

Figure 39. Comparison of Velocity Signal and Velocity Signal After a Smoothing Filter is Applied

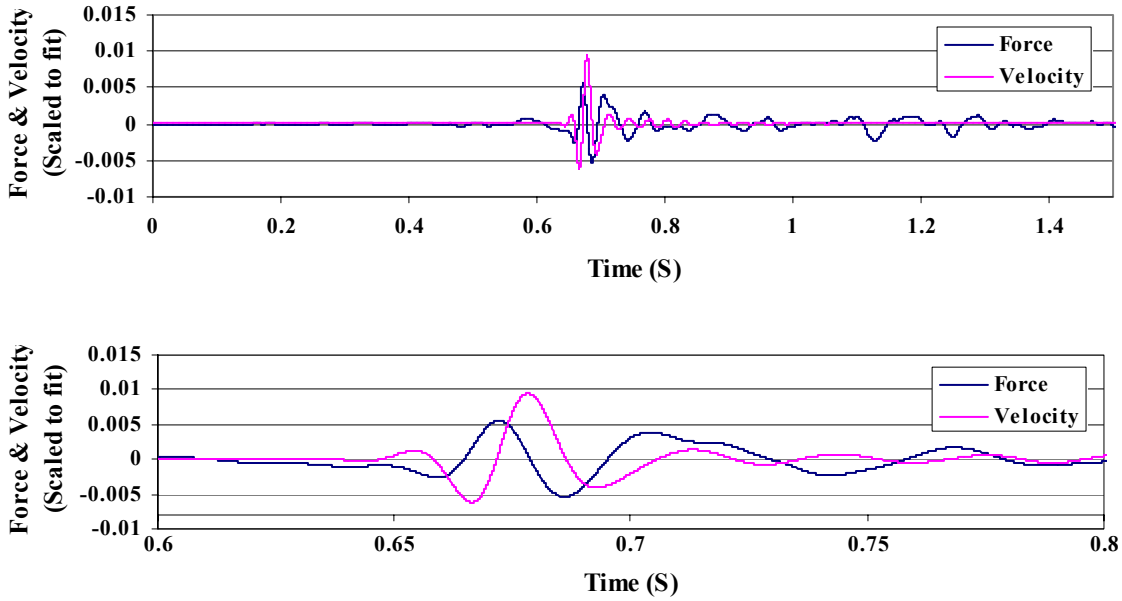

Figure 40. Comparison of Force and Velocity Curves to Verify Data Reliability. Entire Force Curve (top) and Blown Up Impulse Region to Demonstrate that the Force is at a Maximum Approximately when the Velocity is Zero (lower).

4.3 The Effect of Impact Force:

When a comparison of the acceleration signals under maximum and minimum load tests is made (figures 41-43), a noticeable difference can be observed in the magnitude of the acceleration. Both MOP tests and MOM tests show an increase in acceleration magnitude by more than a factor of ten when the maximum impact force is applied compared to the minimum impact force. The COC test however, does not exhibit this trait. This may be due to the different nature of the COC material or it may be due to an errant test.

The trend is similar for the PSD's of the maximum and minimum force acceleration signals (figures 44-46). The magnitude and range of frequencies was increased significantly between maximum and minimum impact loads for MOP tests and MOM tests. For the COC tests, the PSD magnitude actually decreased slightly for the

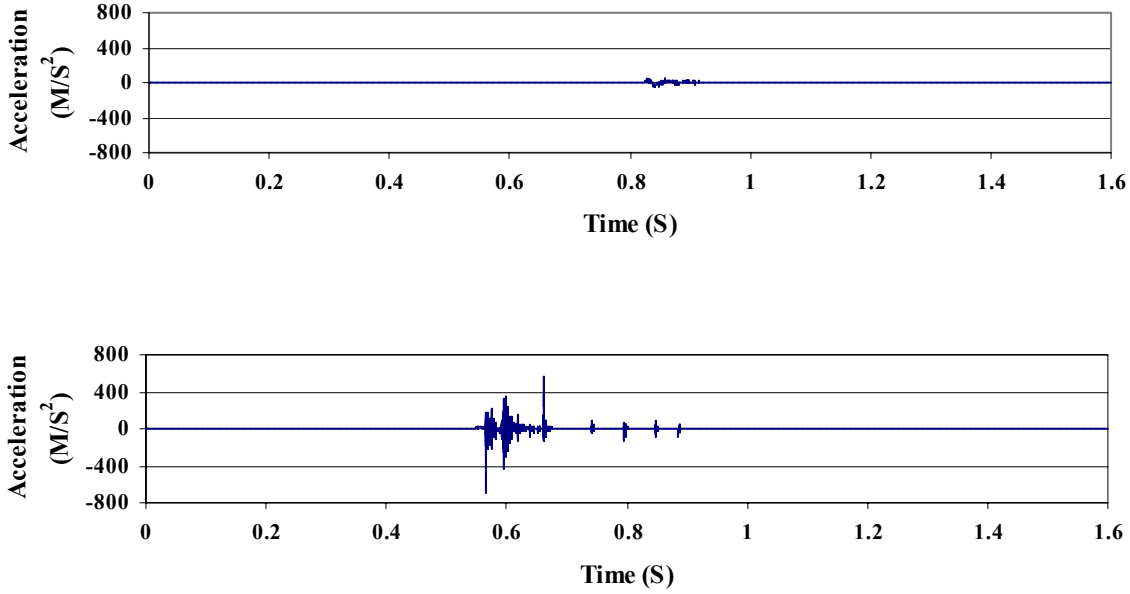

Figure 41. Comparison of Acceleration Signals for MOP at Minimum Test Load (top) and Maximum Test Load (lower).

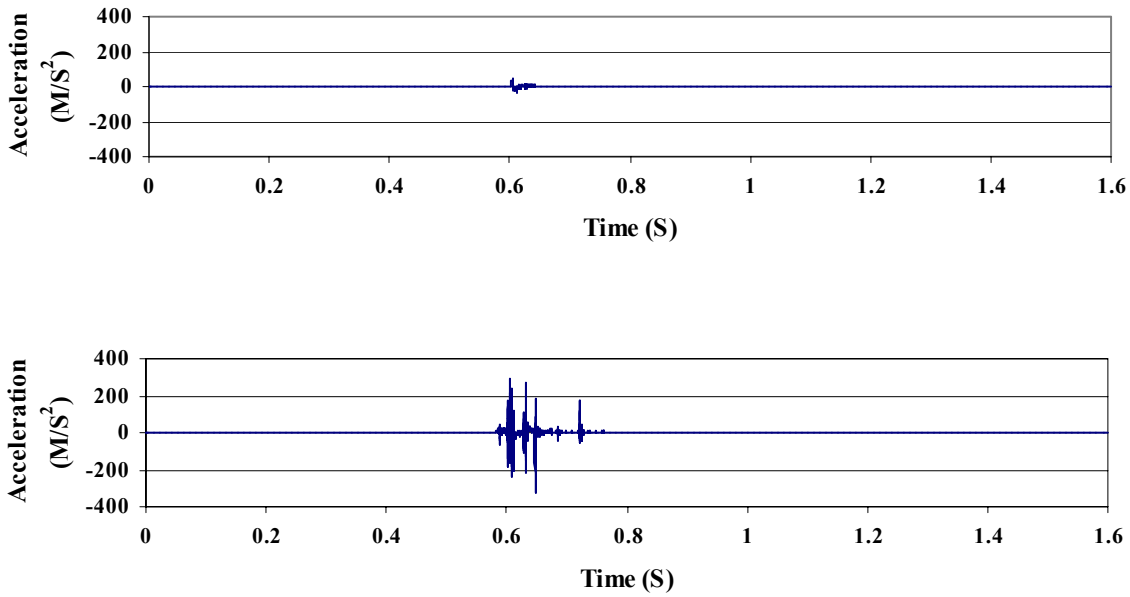

Figure 42. Comparison of Acceleration Signals for MOM at Minimum Test Load (top) and Maximum Test Load (lower).

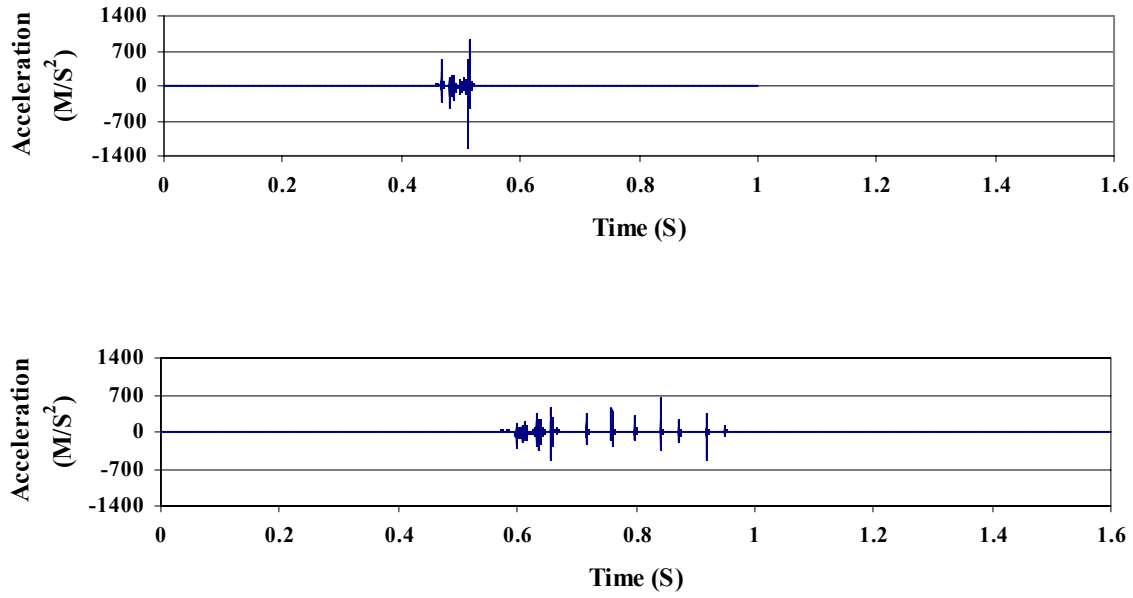

Figure 43. Comparison of Acceleration Signals for COC at Minimum Test Load (top) and Maximum Test Load (lower).

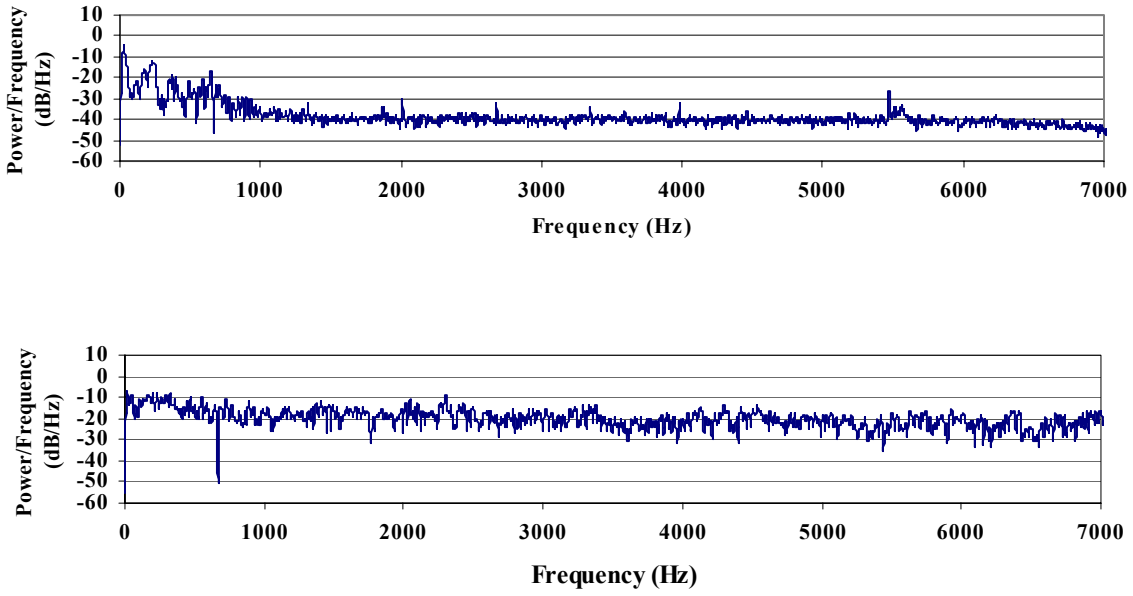

Figure 44. Comparison of PSD Signals for MOP at Minimum Test Load (top) and Maximum Test Load (lower).

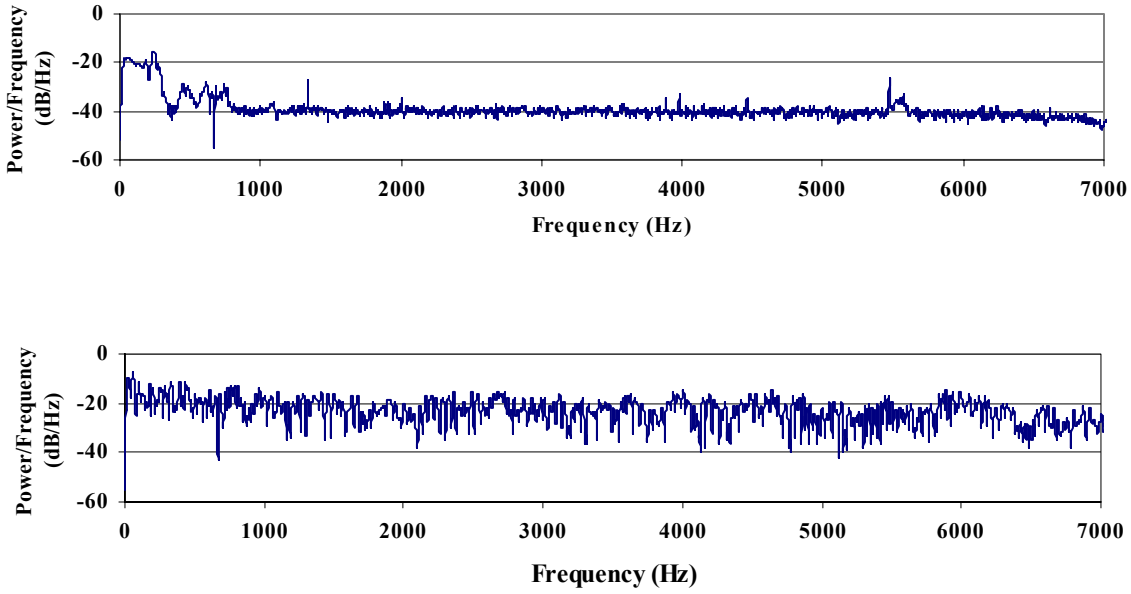

Figure 45. Comparison of PSD Signals for MOM at Minimum Test Load (top) and Maximum Test Load (lower).

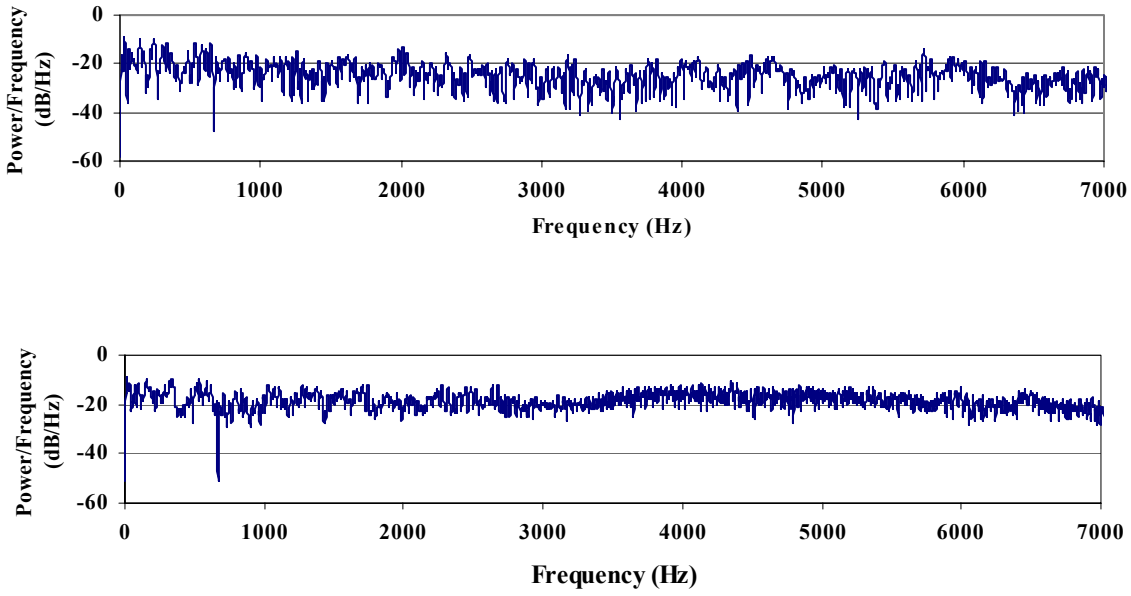

Figure 46. Comparison of PSD Signals for COC at Minimum Test Load (top) and Maximum Test Load (lower).

maximum force. However, the peak frequencies were not as clear for the maximum load test thereby indicating that the increased load could have added vibratory noise to the system, thereby making the signal more difficult to read.

4.4 Separation Vs. No Separation:

Comparing the vibratory behavior of implants under conditions involving separation and without separation is important. A test without separation would simulate the hip if it were a true ball and socket joint and the femoral head never left the acetabular cup. On the other hand, a test with separation would simulate the hip if the femoral head were to separate from the acetabular cup during gait. Hence, any significant difference between the two types of tests could be attributed directly to the fact that sliding occurs.

A comparison between tests of equal force with and without separation was made for MOP, MOM, and COC (figure 47). For the MOP and MOM tests, the dominant frequencies were much larger for the tests with separation, however the magnitude of the noise and lesser frequencies was in the same range. On the other hand, for the COC tests, tests with separation had a larger PSD magnitude by a factor of ten for most of the frequency range. This seems to indicate definite difference in vibration transmission properties for the ceramic THA when compared to the metal and polyethylene. This difference may be due to the increased hardness of the ceramic THA material. The metal and polyethylene THA's are softer and absorb a large portion of the impact through deformation. However, when the harder ceramic components impact each other, there is much less deformation and much more of the energy is transferred to the bone and surrounding tissues.

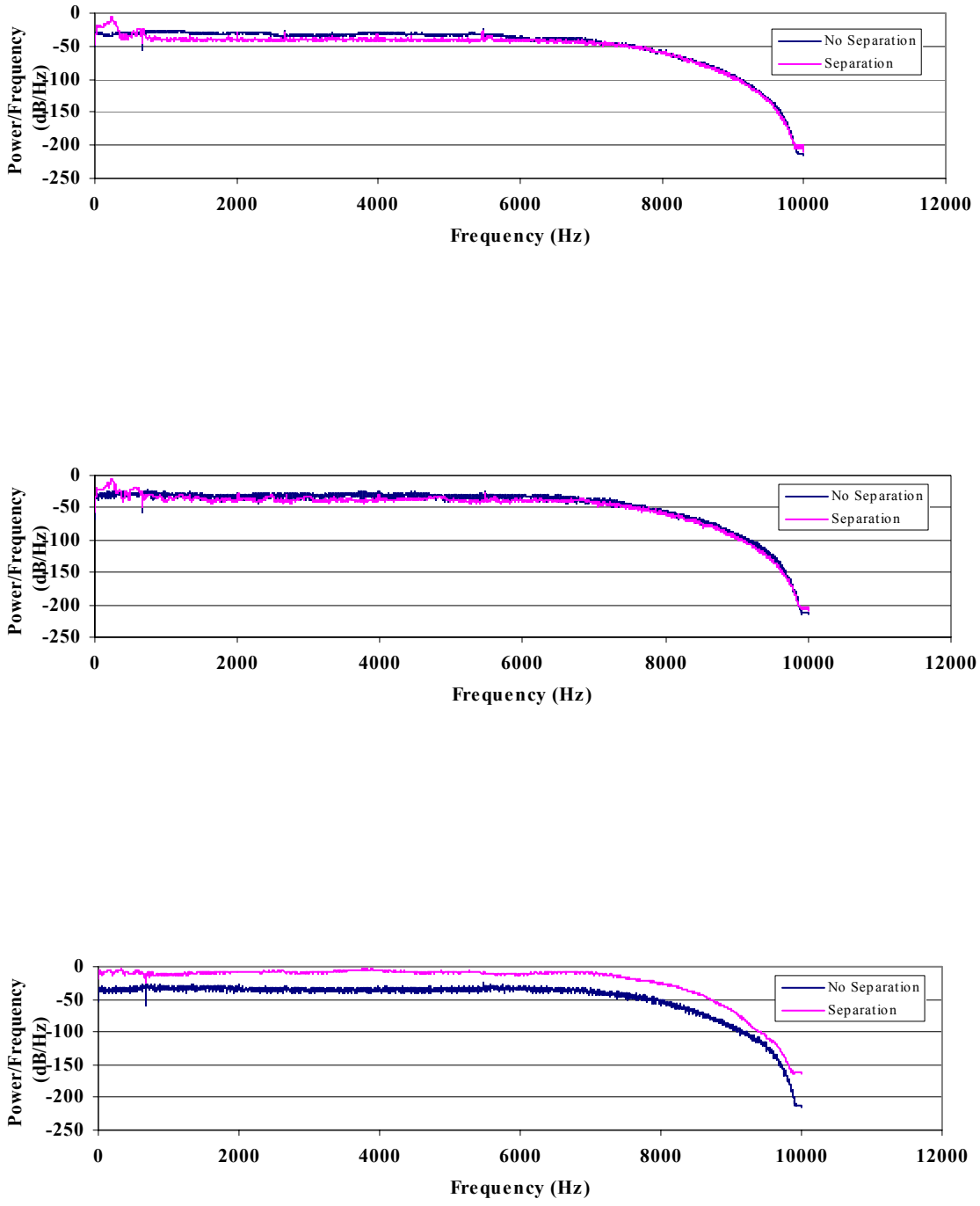

Figure 47. Comparison of PSD's for Tests with and without Separation for Metal on Polyethylene (top), Metal on Metal (middle), and Ceramic on Ceramic (lower).

4.5 Component Frequencies:

For each component or set of components, six tests were taken. If a frequency peak showed up in three or more of these tests, then that frequency was included in the component results (tables 4 and 5). A variety of different frequencies, magnitudes and patterns were exhibited among the various components (figures 48-55). The frequency range for the bones without implants (figures 48 and 49) seemed to vary between roughly 300 Hz and 2250 Hz. Implant components and their various configurations had higher frequency peaks in the range of 1800 Hz to 9600 Hz. The PSD's of the bones tended to exhibit clear peaks, but there were many of them. These multiple peaks can be attributed to the different vibratory modes of the bone and the bone's complex geometry. PSD's for the stem and the cup also exhibited pristine peaks, but fewer of them because the geometry of these components is more simple. PSD's for stem and cup tests with femoral heads and liners attached where more complex. For the implanted component tests, there was also a wide range of frequencies but the repeatability of the tests was just as good as the un-implanted components. There were still some clean peaks exhibited, however the trend seems to say that the more components added to a test (i.e. femoral head then implantation), the more complex the frequency spectrum became and therefore the more difficult to decipher. The possibility for an errant resonant peak is greater for these more complex systems because of the interference that the peaks have with one another.

Many of the frequencies found for the unimplanted femur (table 4) match up well with the resonant tests in previous studies. In all but two of the axes, there was a peak in the range of 310-330 Hz. Khalil, Couteau, Rosenstein, and Taylor (table 1) all had

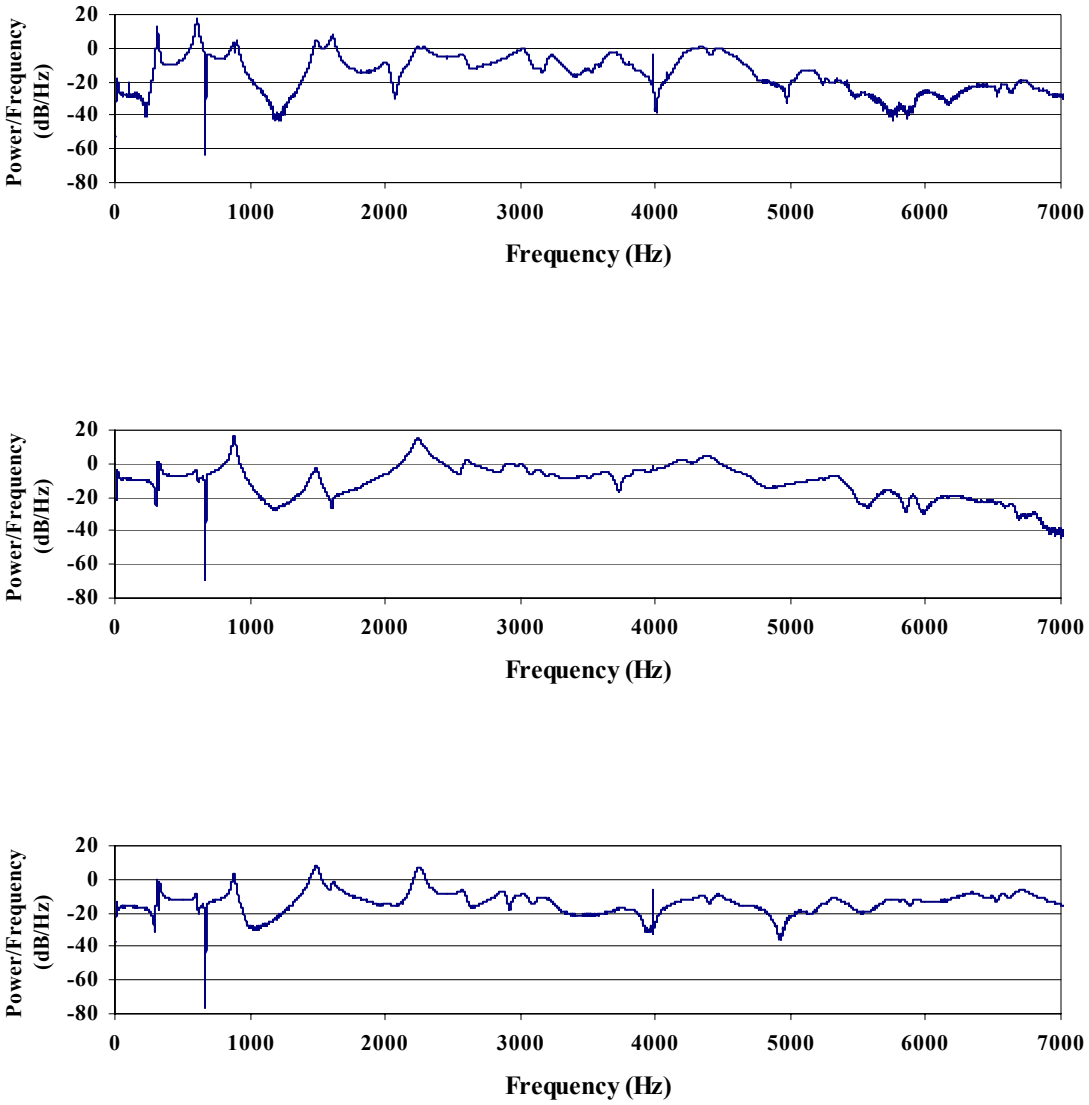

Figure 48. PSD Data for the Unimplanted Femur Resonance Test. The Accelerometer Shown Here was Mounted on the Greater Trochanter and the Signals are for the A1-axis (upper), A2-axis (middle), and the A3 -axis (lower).

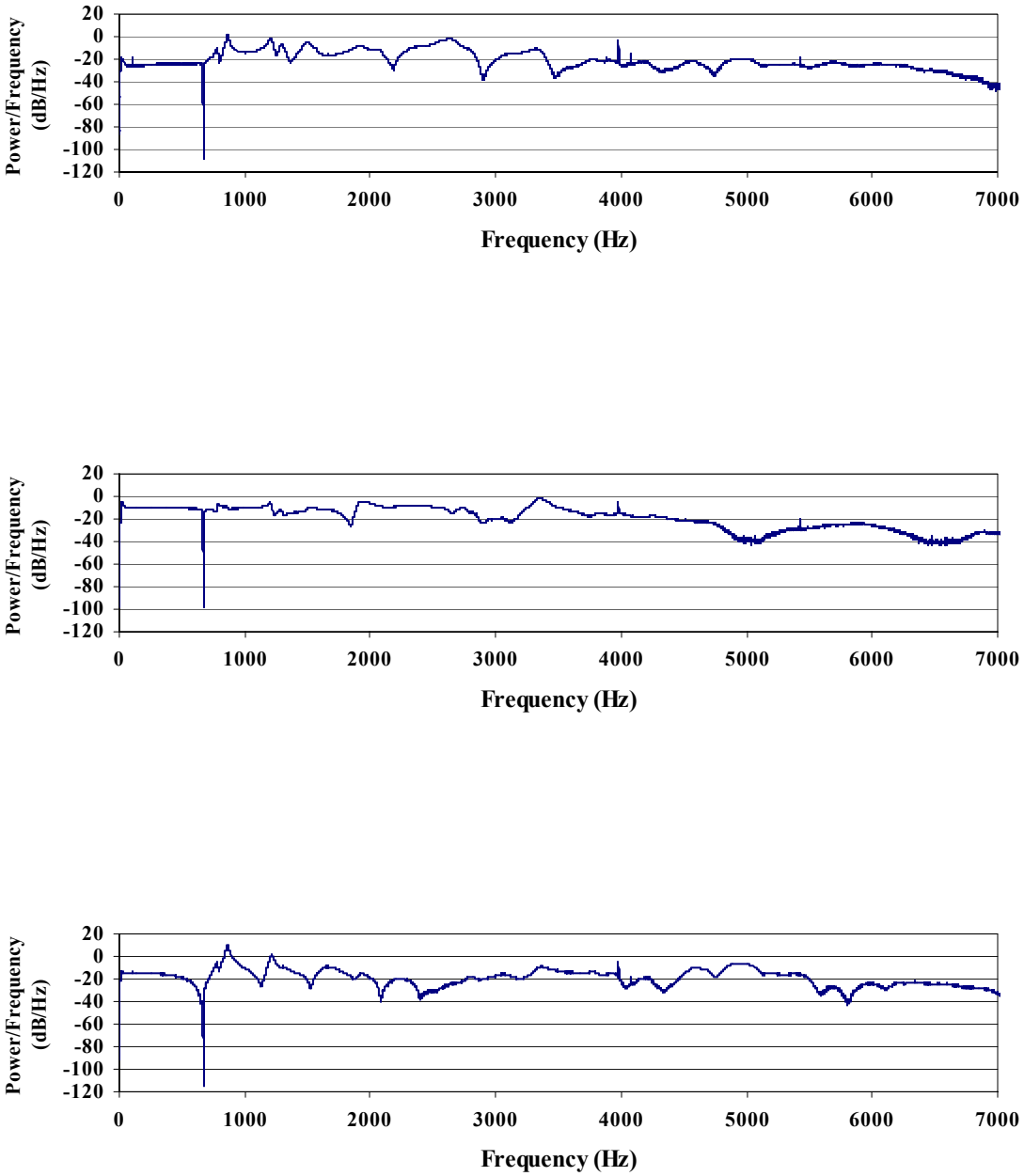

Figure 49. PSD Data for the Unimplanted Pelvis Resonance Test. The Accelerometer Shown Here was Mounted on the Pubis Directly Behind the Center of the Acetabulum and the Signals are for the A1-axis (upper), A2-axis (middle), and the A3 -axis (lower).

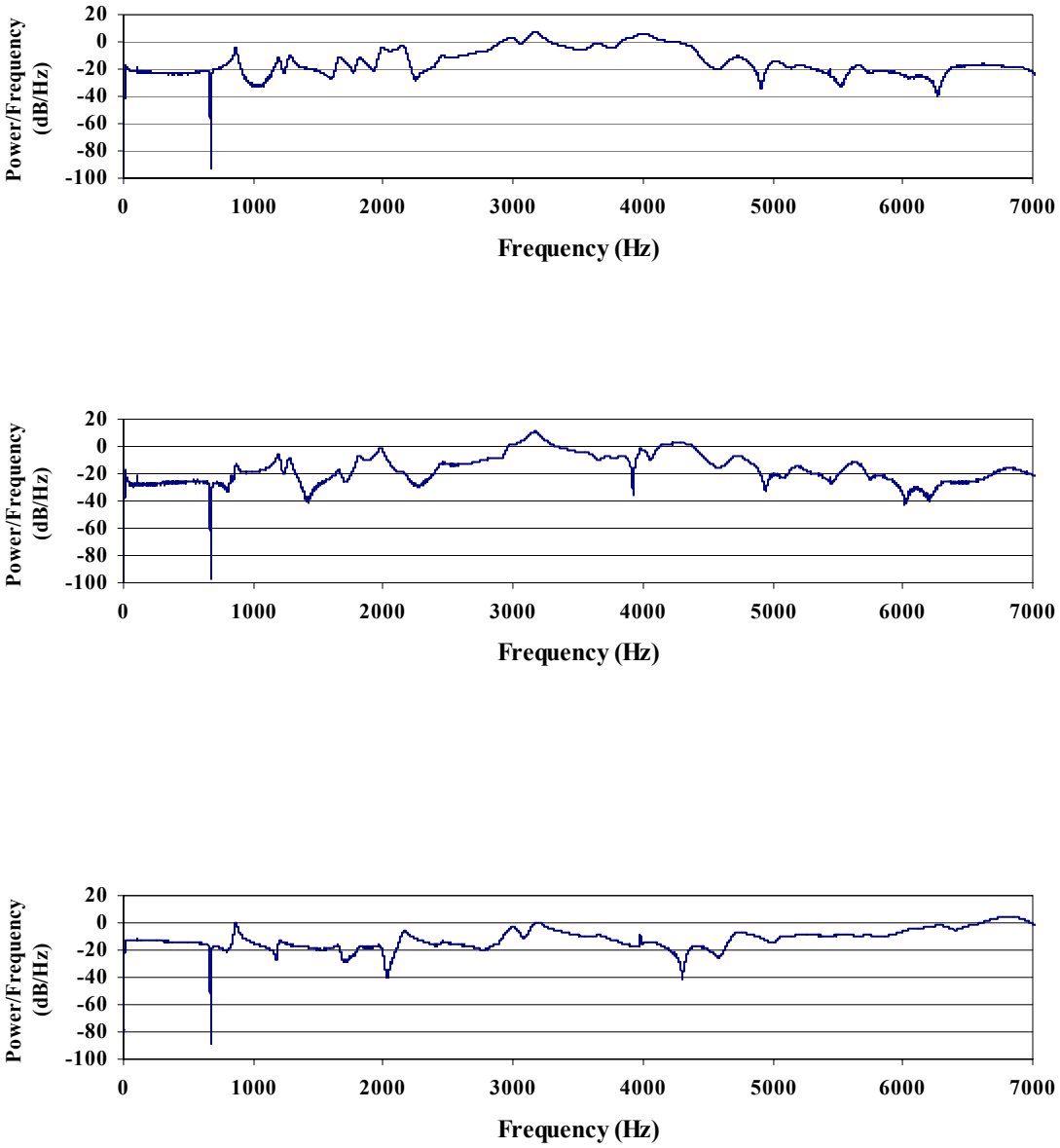

Figure 50. PSD Data for the Pelvis Implanted with a Cup and Metal Insert Resonance Test. The Accelerometer Shown Here was Mounted on the Cup Next to the Acetabulum and the Signals are for the A1-axis (upper), A2-axis (middle), and the A3 -axis (lower).

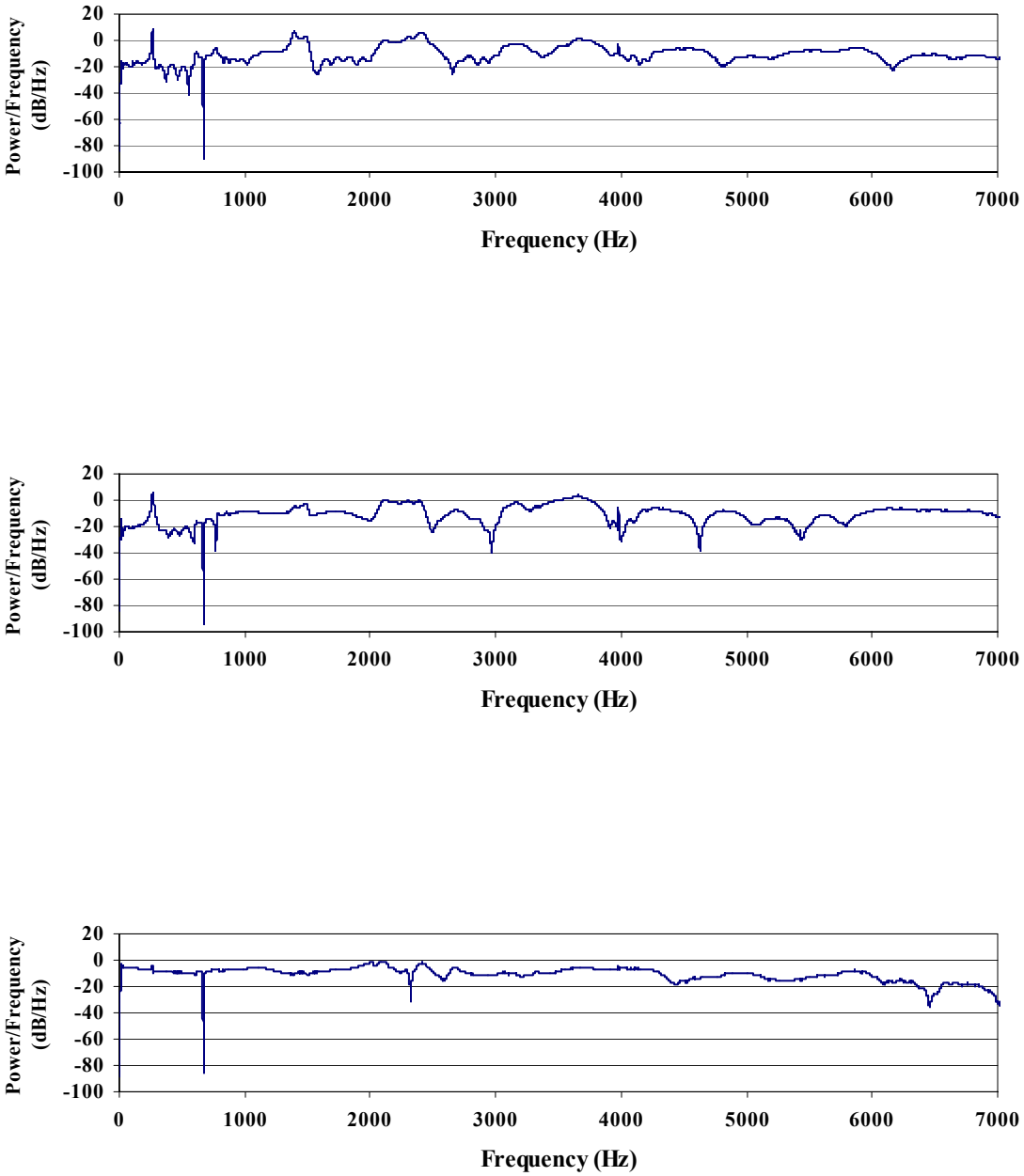

Figure 51. PSD Data for the Femur Implanted with a Stem and Metal Femoral Head Resonance Test. The Accelerometer Shown Here was Mounted on the Stem and the Signals are for the A1-axis (upper), A2-axis (middle), and the A3 -axis (lower).

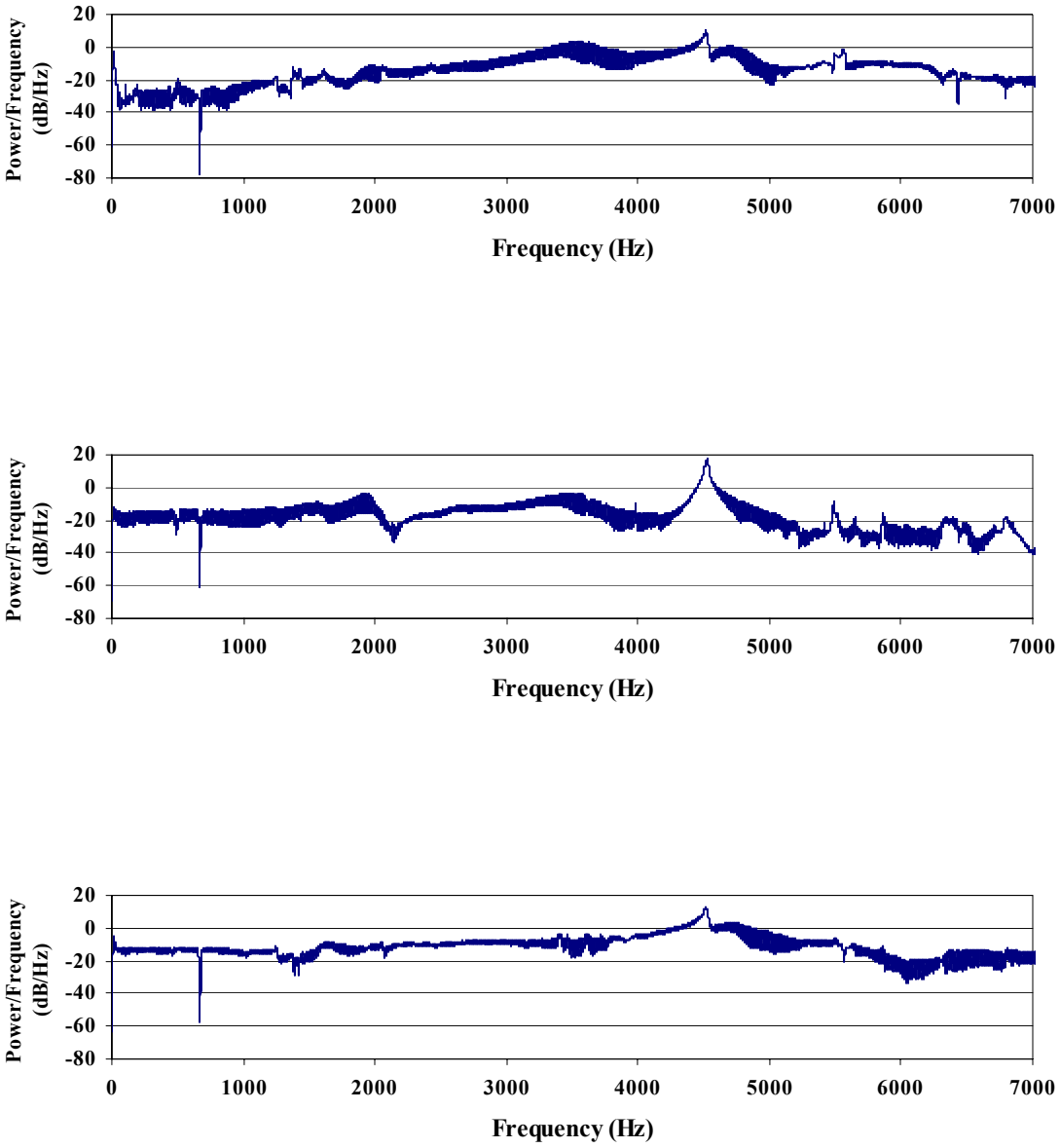

Figure 52. PSD Data for the Acetabular Shell Resonance Test. The Accelerometer Shown Here was Mounted on the Lip of the Shell and the Signals are for the A1-axis (upper), A2-axis (middle), and the A3 - axis (lower).

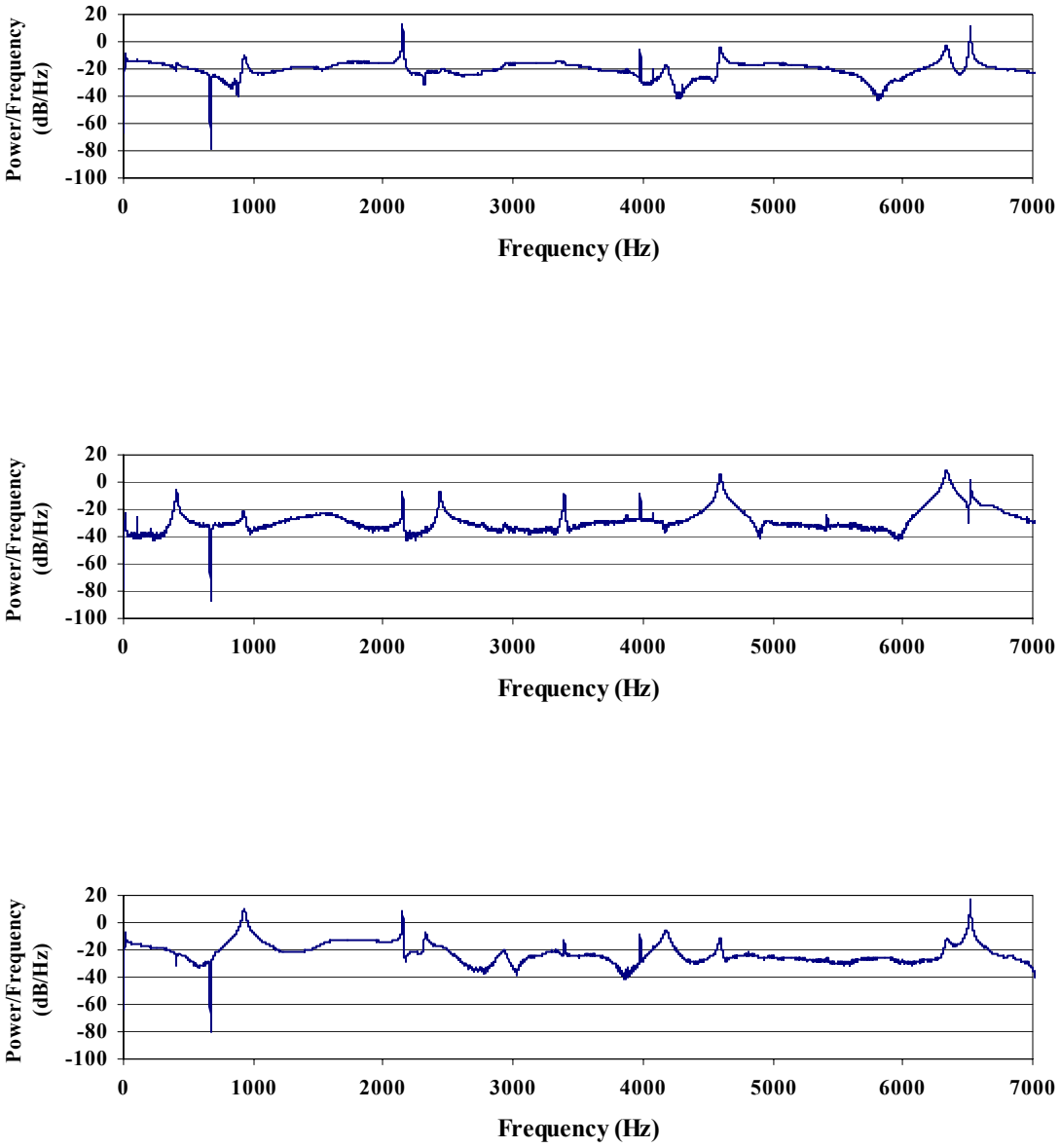

Figure 53. PSD Data for the Femoral Stem Resonance Test. The Accelerometer Shown Here was Mounted on the Top of the Stem and the Signals are for the A1-axis (upper), A2-axis (middle), and the A3 -axis (lower).

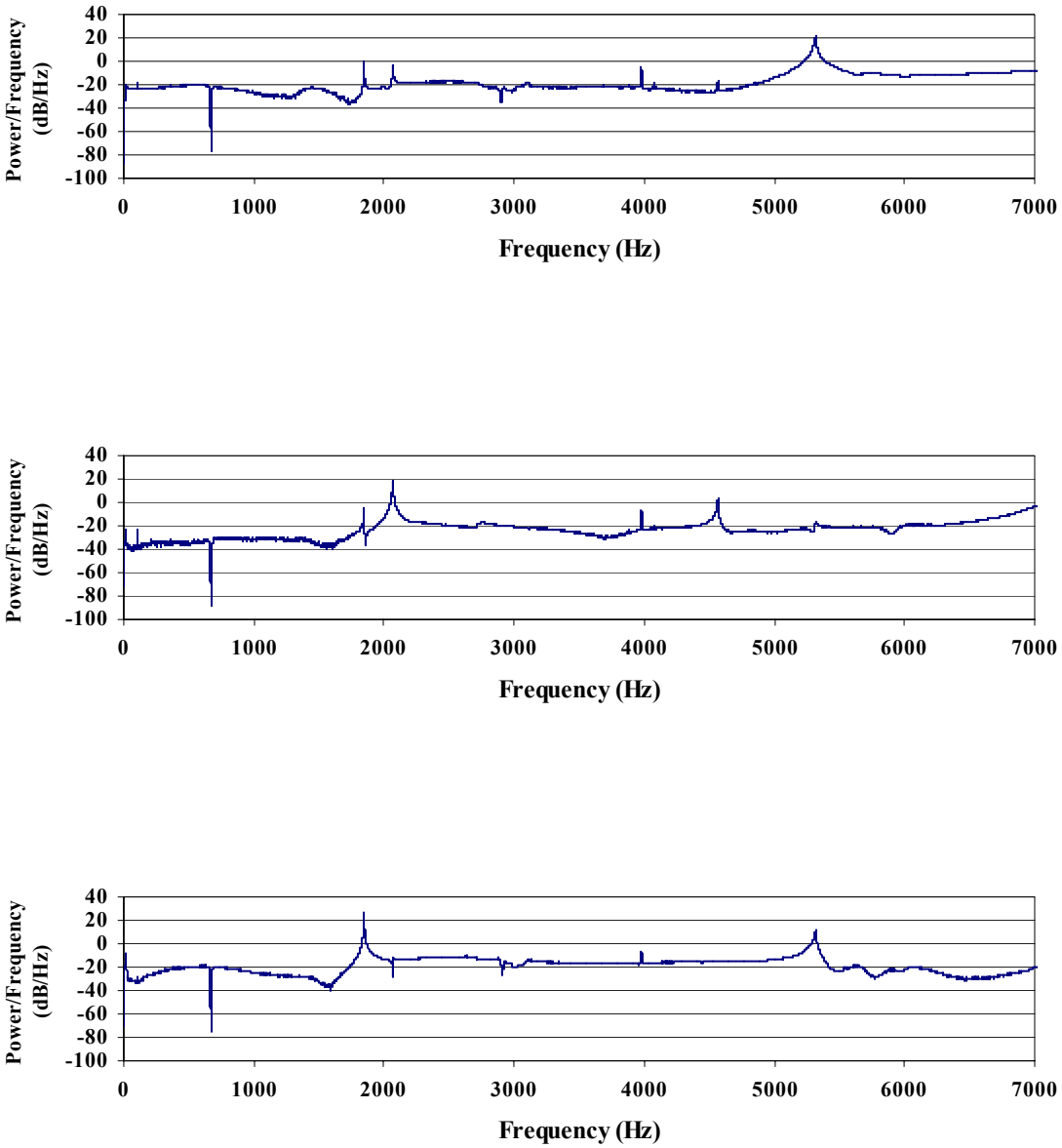

Figure 54. PSD Data for the Femoral Stem with Metal Head Attached Resonance Test. The Accelerometer Shown Here was Mounted on the Top of the Stem and the Signals are for the A1-axis (upper), A2-axis (middle), and the A3 -axis (lower).

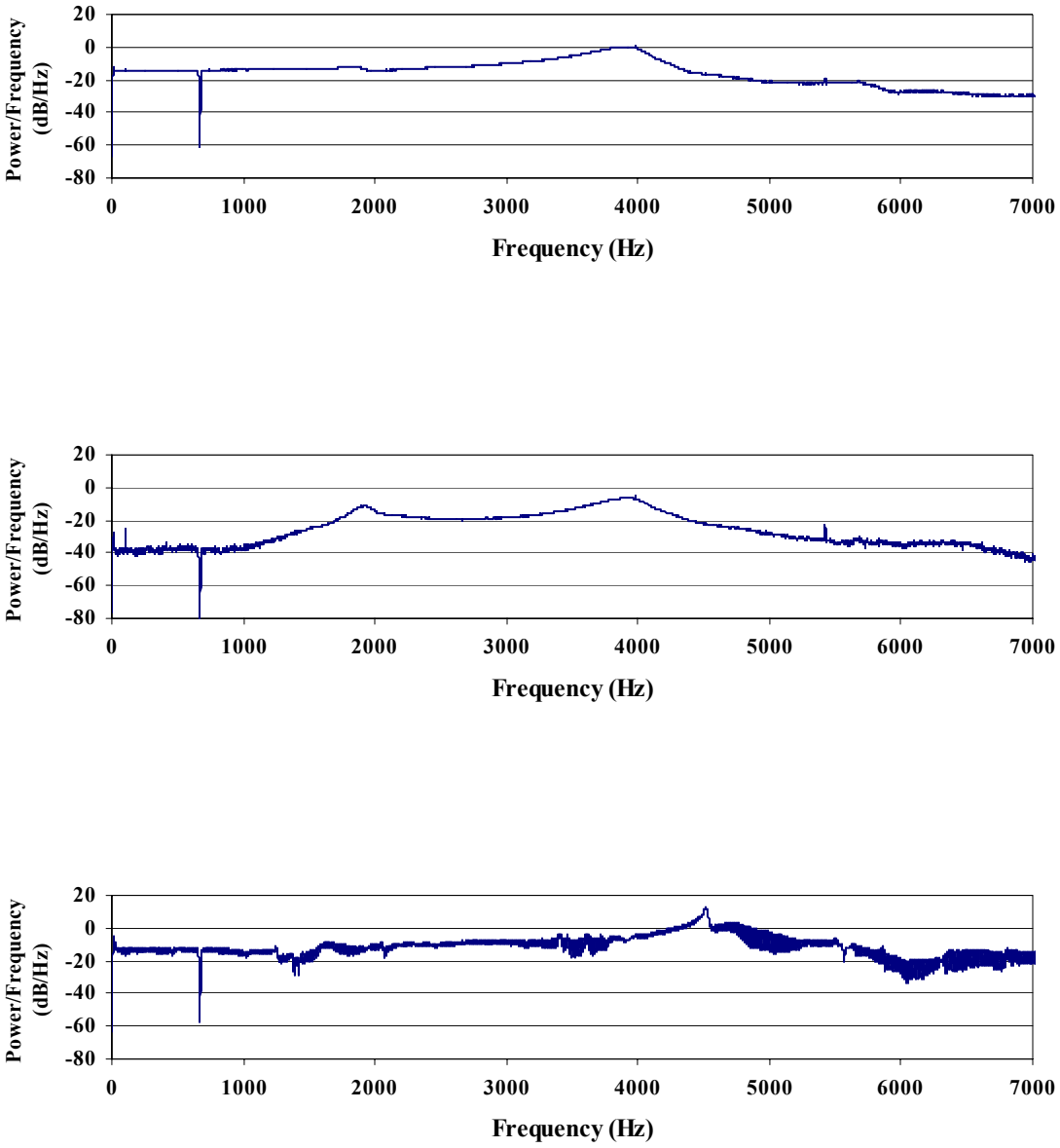

Figure 55. PSD Data for the Acetabular Cup with Metal Insert Resonance Test. The Accelerometer Shown Here was Mounted on the Lip of the Shell and the Signals are for the A1-axis (upper), A2-axis (middle), and the A3 -axis (lower).

Table 4. Dominant Frequencies Found in Synthetic Bones

Synthetic Bone Tests									
Test	**Accelerometer 1**			**Accelerometer 2**			**Accelerometer 3**		
Axis	**A1>**	**A2>**	**A3>**	**B1>**	**B2>**	**B3>**	**C1>**	**C2>**	**C3>**
Pelvis	862±1 1300±10 1490±10 2629±10	1934±10 2533±10	861±1 1205±10	862±1 1215±10 1495±2	862±2 1206±2 1295±3	862±1 1296±5	859±2 1208±3 1490±10 1930±10	861±1 1290±10 1490±1 1930±4	861±1
Femur	320±10 606±2 879±1 1493±1 1605±10	329±2 881±2 2232±10	315±10 881±1 1485±10 2240±10	330±2 607±1 881±1 1480±10 2240±5	606±3 1485±3 1611±2 2006±5	882±1 1492±3 2237±5	1490±2 2000±5 2248±10	313±1 607±1 1488±1 2012±4 2235±1	329±1 882±1 1488±3 2242±3

Table 5. Dominant Frequencies Found in Implant Components

Component Tests			
Axis	**A1>**	**A2>**	**A3>**
Shell	4516±10 3610±10	4516±10	4516±10 9900±10
Shell/Metal	3995±10 1870±10	3995±10 1910±10	3980±10
Shell/Poly	3100±10 1510±10	1570±10 3105±10	
Shell/Ceramic	3020±10	3000±10	3080±10
Stem	2149±1 6339±1 6519±1	2150±10 2437±1 3979±10 4593±1 6337±1 9595±10	927±1 2149±1 6520±1
Stem/Metal	1846 2067 3979 5315±10 7820±10 8790±10	1846 2067 3979 4564±10 8500±10	1846 5315±10
Stem/Ceramic	1937 2222±1 3979 5142±10 5703±1 8095±10	2222±1 5142±10 8085±10 9620±10	1937 5702±10 6068±10

resonant peaks within this range. Five of the nine channels have a peak near 881 Hz. Khalil determined that there was a peak at 879 Hz and Couteau determined that his experimental femur had a peak at 886.6 Hz. In addition, for the implanted femur with the metal head, all but one of the axes exhibited a peak near 270 Hz (table 6). Couteau was the only of the compared studies that included implanted femurs, but a peak was found at 278 Hz for the experimental method and at 264 Hz for the FEM method. None of the other studies examined femur resonance above 1000 Hz, so the correlation of the other peaks found here and their data is impossible to determine. However, the large number of peaks that correspond to peak values in other studies seems to validate the method and results of this study.

4.6 Impact Test Frequencies:

Because multiple tests of the same material and load were not taken during this study, repeatability of impact test results are not known. The trend of complicating the signal as more components were added to the test continued. Now that the fixture, extensiometer, and MTS machine were all introduced into the system, the number of peaks found in each test increased significantly. The major peaks were recorded and listed with the corresponding relative magnitude in order to demonstrate how dominant one peak was compared with the others (table 7). During the impact tests, a peak could be found in basically almost any frequency range along the spectrum.

Table 6. Dominant Frequencies Found in Implanted Bones

Implanted Component Tests						
Axis	**A1>**	**A2>**	**A3>**	**B1>**	**B2>**	**B3>**
Implanted Pelvis/Metal Insert	864±2 3171±10 4150±10	3167±10 4150±10	866±5 3171±10 6300±10 6795±10	2155±10 2430±10 3171±10 6300±10	1815±10 2850±10 2987±10 6380±10	3172±10 2950±10
Implanted Pelvis/Poly Insert	881±5 1200±5 1607±10 1950±10 2460±10	885±5 1202±5 1607±10 1830±10 2130±10	884±5 1208±5 1600±10	890±10 1207±10 1606±10 1830±10 1950±10 2466±10	840±10 1204±10 1946±10 2466±10 3050±10	1202±10 1605±10 1825±10 1945±10
Implanted Pelvis/Ceramic Insert	1330±10 1690±10 1915±10 3067±10 3580±10 5400±10 6300±10	1690±10 1910±10 2050±10 3580±10 5405±10 6320±20	911±10 3000±10 3550±20 5490±10 9708±10	1880±5 2610±10 3290±10 3580±20	1920±10 2230±10 2600±10 3285±10 3575±20	3060±20 3560±20 5150±10 6740±20 8803±10
Axis	**C1>**	**C2>**	**C3>**	**D1>**	**D2>**	**D3>**
Implanted Femur/Metal Head	265±5 1400±10 1500±10 2105±10 2415±10	265±5 1490±10 2100±10 3630±20	2120±20 2420±10	270±1 2120±10 2300±10	265±5 609±5 1495±5 2070±20 5877±10	265±5 2320±10 3300±10 6530±20 6900±20
Implanted Femur/Ceramic Head	280±5 1440±5 2190±10 2450±20 3625±5	280±5 1540±10 2190±10 2420±10 3615±20 4470±20	1440±10 1550±10 2183±10 2450±10 4735±20	280±5 865±5 1540±10 2190±10 3400±10 3515±20	270±10 640±10 860±10 1440±10 1540±10 2445±10 3410±10 3500±10 4510±10	285±5 2410±10 3400±20 4730±10 7950±10

Table 7. Dominant Frequencies Found in Impact Test (COC 1150 N).

Example Impact Test						
Measurement	**Freq.**	**Freq.**	**Freq.**	**Freq.**	**Freq.**	**Freq.**
Axis	**A1>**	**A2>**	**A3>**	**B1>**	**B2>**	**B3>**
	26	69	47	47	43	48
	683	683	683	459	416	709
	1354	1035	1703	683	683	2163
	2026	1337	3480	1428	1099	3295
	2614	2026	4817	2008	1311	4817
	3685	2248	5071	2902	1957	5071
	5675	3685	5675	4288	2485	6245
	7590	5499	9932	5388	3685	9260
	8577	7309		5780	4680	9932
	9763	8577		6271	4817	
		9788		7583	5208	
				9260	5293	
				9515	5780	
				9863	6854	
Axis	**C1>**	**C2>**	**C3>**	**D1>**	**D2>**	**D3>**
	25	24	623	163	163	25
	440	163	2357	490	576	163
	3505	434	3822	603	2358	623
	4288	1101	4898	1101	3294	1021
	5020	3480	6668	1566	3940	2485
	6774	4816	8228	2331	5071	3940
	8000	5345	9932	2485	6775	4816
	8228	6980		3040	9932	5346
	8757	8000		3405		6060
	9260	8832		3940		6827
	9515	9540		4400		8086
				4944		9260
				5531		
				6880		
				8239		
				8552		
				9863		

CHAPTER V

DISCUSSION AND CONCLUSION

5.1 Conclusions:

The magnitude of the vibration found in tests where the femoral head separates from the acetabular cup is much larger than those tests where load was applied without separation. This difference is much more noticeable in COC than in the other types of bearing surfaces. These results indicate that there is a strong possibility that femoral head sliding during gait has a significant effect on the amount of vibration the hip is exposed to. They also indicate that COC implants transfer more energy in the form of vibration to the surrounding tissue than MOM and MOP implants.

The vibration data found during the impact tests varies widely in both magnitude and frequency. As figures 44-46 demonstrate, the amount of force applied to the components during a test directly affects the magnitude of the vibration measured. The large number of test frequencies from the impact tests demonstrates the complexity the system being examined here. A resonance peak in the impact test (table 7) can be found in the range of practically every component resonant peak. Therefore, the direct effect of a particular component on the vibration of the system is not known for sure. However, because there are peaks of at least some magnitude that correspond with the resonance of the bones, the preliminary indications indicate that the vibration found during these tests can indeed be potentially detrimental to bone, possibly contributing to implant loosening, and ultimately failure of the implant.

5.2 Future Research and Improvements:

While some resonant peaks of the femur and pelvis have been determined, it is not known for sure if exposing the bone to the frequencies would be harmful. Knowing such information would be helpful in evaluating the severity of the problems caused by vibration, if any at all. An experiment exposing a loaded wet femur or pelvis to these frequencies over a significant period of time may lead to insight on the vibrational effects on bone.

There is a discrepancy in the literature as to whether soft tissue significantly affects the vibration and frequencies of bones in vivo. Determining the effect of soft tissue on the vibration of the bones in the hip would help to make future vibration studies more realistic. Two possible methods of determining this effect on the study would be to: 1.) Enclose the synthetic bones in some sort of biological serum like bovine serum or to wrap the bones in wet rags. 2.) Perform the same experiment with fresh, wet, cadaver hip joints.

The testing machine used in this study is primary meant to be used for material testing and therefore only operates on a single axis. Loads on the hip in vivo occur in multiple directions in three dimensions. Therefore, a more accurate and anatomically accurate study could be carried out with some sort of custom designed hip simulator with separation incorporated that moves in three dimensions or by some other type of machine that can move in three dimensions.

Because of time limitations, a low pass filter was not implemented into the data acquisition system. Because of the lack of this low pass filter, which is used to filter out alias signals in the frequency spectrum, errant alias frequencies my appear in the data. It

is impossible to know for sure which signals are erroneous and which are not. However, all of the data was acquired with the same data acquisition system. Therefore, the differences in the results from the different components and testing conditions are comparable to each other. In future studies, it would be necessary to implement an anti-aliasing filter into the data acquisition setup. Once such a system was developed and data was acquired, a comparison could be made to the data presented here to see the true effect that alias signals had on the data.

LIST OF REFERENCES

LIST OF REFERENCES

American Academy of Orthopaedic Surgeons (AAOS), 2003. Research: Improving Musculoskeletal Care in America (IMCA). Osteoarthritis of the hip: Joint Replacement. Accessed Feb, 2005. Available at URL address: http://www3.aaos.org/research/imca/OAHip_Overview.htm

Bergmann, G., Graichen, F., Rohlmann, A., 1993. Hip joint loading during walking and running, measured in two patients. Journal of Biomechanics 26, 969-990.

Bergmann, G., Graichen, F., Rohlmann, A., et al., 1997. Hip joint forces during load carrying. Clinical Orthopaedics Related Research 335, 190-201.

Bergmann, G., Deuretzbacher, G., Heller, M., et al., 2001. Hip contact forces and gait patterns from routine activities. Journal of Biomechanics 34, 859-871.

Berry, D.J., Halasay, M., Harmsen, W.S., et al., 2002a. Abstract: Charnley total hip arthroplasty: follow-up at a minimum of 30 years. 69th Annual Meeting Proceedings, American Academy of Orthopaedic Surgeons, Rosemone, Ill, pp. 635.

Berry, D.J., Harmsen, W.S., Cabanela, M.E., et al., 2002b. Twenty-five-year survivorship of two thousand consecutive primary Charnley total hip replacements: factors affecting survivorship of acetabular and femoral components. Journal of Bone and Joint Surgery 84-A(2), 171-177.

Brand, R.A., Crowninshield, R.D., Wittock, C.E., et al., 1982. A model of lower extremity muscular anatomy. Journal of Biomechanics 104, 304.

Brand, R.A., Pedersen, D.R., Davy, D.T., et al., 1994. Comparison of hip force calculations and measurements in the same patient. The Journal of Arthroplasty 9(1), 45-51.

Brash, J.I., Skorecki, J., 1970. Determination of the modulus of elasticity of bone by a vibration method. Medical and Biological Engineering 8, 389.

Callaghan, J.J., Dennis, D.A., Paprosky, W.G., et al. (Eds.), 1995. Biomaterials and prosthesis design in total hip arthroplasty. In: Orthopaedic Knowledge Update Hip and Knee Reconstruction. American Academy of Orthopaedic Surgeons, Rosemont, IL, pp. 263-268.

Campbell, J.N., Jurist, J.M., 1971. Mechanical impedance of the femur: A preliminary report. Journal of Biomechanics 4, 319-322.

Christensen, A.B., 1982. Resonance of human tibia, method, reproducibility and effect of transaction. Acta Orthopaedica Scandinavica 53, 867.

Christensen, A. B., Ammitzbøll, F., Dyrbye, C., et al., 1986. Assessment of tibial stiffness by vibration testing in-situ- I. Identification of mode shapes in different supporting conditions. Journal of Biomechanics 19(1), 53-60.

Chung, J.K., Pratt, G.W., Babyn, P.S., et al., 1979. A new diagnostic technique for the evaluation of prosthetic fixation. In: Proceedings of the First Annual Conference of the IEEE/Engineering in Medicine and Biological Society. IEEE Publishing Services, New York, pp. 158-160.

Cornilissen, P., 1986. Assessment of tibial stiffness by vibration testing in situ. II. Influence of soft tissues, joints, and fibula. Journal of Biomechanics 19, 551.

Couteau, B., Hobatho, M.C., Darmana, R., et al., 1998a. Experimental and numerical modal analysis of a normal and implanted human femur. Proceedings of the 11th Conference of the European Society of Biomechanics, Toulouse, France 75.

Couteau, B., Hobatho, M.C., Darmana, R., et al., 1998b. Finite element modeling of the vibrational behavior of the human femur using CT-based individualized geometrical and material properties. Journal of Biomechanics 31, 383-386.

Crowninshield, R.D., 1978. Use of optimization techniques to predict muscle forces. Journal of Biomechanical Engineering 100, 88-92.

Davy, D.T., Kotzar, G.M., Brown, R.H., et al., 1988. Telemetric force measurements across the hip after total arthroplasty. Journal of Bone and Joint Surgery 70-A(1), 45-50.

Dencker, H., Moberg, E., 1968. Diagnosis of soft tissue interposition in shaft fractures of the humerus and femur by measuring the conduction of vibrations across the fracture. Acta Chirugica Scandinavica 134, 540.

Dennis, D.A., Komistek, R.D., Northcut, E.J., 2001. "In vivo" determination of hip joint separation and forces generated due to impact loading conditions. Journal of Biomechanics 34, 623-629.

Fiedler, E., O'Brien, S. (Eds.), 2003. Hip Joint Replacement. In: Improving musculoskeletal care in America, (IMCA) Information Series, Osteoarthritis of the hip, A compendium of evidence-based information and resources. American Academy of Orthopaedic Surgeons, Rosemont, IL, pp. 4.1-4.54.

Gerogiou, A.P., Cunningham, J.L., 2001. Accurate diagnosis of hip prosthesis loosening using a vibrational technique. Clinical Biomechanics 16, 315-323.

Hardt, D.E., 1978. Determining muscle forces in the leg during normal human walking. Journal of Biomechanical Engineering 100, 72-28.

Heiner, A.D., Brown, T.D., 2001. Structural properties of a new design of composite replicate femurs and tibias. Journal of Biomechanics 34, 773-781.

Hodge, W.A., Fuan, R.S., Carlson, K.L., et al., 1986. Contact pressures in the human hip joint measured in vivo. Biophysics 83, 2879-2883.

Hurwitz, D.E., Foucher, K.C., Andriacchi, T.P., 2003. A new parametric approach for modeling hip forces during gait. Journal of Biomechanics 36, 113-119.

Inman, D.J., 1994. Engineering Vibration. Prentice-Hall, Englewood Cliffs, NJ.

Jazrawi, L.M., Kummer, F.J., DiCesare, P.E., 1998. Alternative bearing surfaces for total hip arthroplasty. Journal of the American Academy of Orthopaedic Surgeons 6, 198-203.

Johansson, C.B., Albrektsson, T., 1987. Integration of screw implants in the rabbit: a 1-yr follow-up of removal torque of titanium implants. International Journal of Oral and Maxillofacial Implants 2, 24-29.

Jurist, J.M., Cameron, J.R., 1969. Measurement of bone resonant frequency in-vivo. Second International Conference on Medical Physics, Boston, MA, pp. 187.

Jurist, J.M., 1970a. In-Vivo determination of the elastic response of bone II. Ulnar resonant frequency in osteoporotic, diabetic and normal subjects. Physics in Medicine and Biology 15(3), 427-434.

Jurist, J.M., Dymond, A.M., 1970b. Reproducibility of ulnar resonant frequency measurement. Aerospace Medicine 41(8), 875-878.

Jurist, J.M., Kianian, K., Three models of the vibrating ulna. Journal of Biomechanics 6, 331.

Kane, T.R., Levinson, D.A., 2000. Dynamics Online: Theory and Implementation with Autolev. Online Dynamics, Inc., Sunnyvale, CA.

Khalil, T.B., Viano, D.C., Taber, L.A., 1981. Vibrational characteristics of the embalmed human femur. Journal of Sound and Vibration 75, 417-436.

Klenerman, L., 2002. Arthroplasty of the hip. In: Klenerman, L. (Ed.), The Evolution of Orthopaedic Surgery, The Royal Society of Medicine Press Ltd., London, pp. 13-23.

Komistek, R.D., Stiehl, J.B., Dennis, D.A., et al., 1998. Mathematical model of the lower extremity joint reaction forces using Kane's method of dynamics. Journal of Biomechanics 31, 185-189.

Kotzar, G.M., Davy, D.T., Goldberg, V.M., et al., 1991. Telemeterized in vivo hip joint force data: a report on two patients after total hop surgery. Journal of Orthopaedic Research 9, 621-633.

Krischak, G.D., Nikolaus, J.W., Zabel, T., et al., 2003. Influence of preoperative mechanical bone quality and bone mineral density on aseptic loosening of total hip arthroplasty after seven years. Clinical Biomechanics 18, 916-923.

Li, P.L., Jones, N.B., Gregg, P.J., 1996. Vibration analysis in the detection of total hip prosthetic loosening. Medical Engineering and Physics 18(7), 596-600.

Lippmann, R.K., 1932. The use of ausculiatory percussion for the examination of fractures. Journal of Bone and Joint Surgery 14, 148.

Lowet, G., Van Auderkercke, R., Van Der Perre, G., et al., 1993. The relation between resonant frequencies and torsional stiffness of long bones in-vitro. Validation of a simple beam model. Journal of Biomechanics 26(6), 689-696.

Madsen, M.S., Ritter, M.A., Morris, H.H., et al., 2004. The effect of total hip arthroplasty surgical approach on gait. Journal of Orthopedic Research 22, 44-50.

Markey, E.L., Jurist, J.M., 1974. Tibial resonant frequency measurements as an index of the strength of fracture union. Wisconsin Medical Journal 73(5), S62-S65.

Meredith, N., Alleyne, D., Cawley, P., 1996. Quantitative determination of the stability of the implant-tissue interface using resonance frequency analysis. Clinical Oral Implants Research 7(3), 261-267.

Meredith, N., Shagaldi, F., Alleyne, D., et al., 1997. The application of resonance frequency measurements to study the stability of titanium implants during healing in the rabbit tibia. Clinical Oral Implant Research 8, 234-243.

Morrison, J.B., 1968. Bioengineering analysis of force actions transmitted by the knee joint. Biomedical Engineering 3, 164-170.

Morrison, J.B., 1970. The mechanics of the knee joint in relation to normal walking. Journal of Biomechanics 3, 51-61.

Nakaktsuchi, Y., Tsuchikane, A., Nomura, A., 1996. The vibrational mode of the tibia and assessment of bone union in experimental fracture healing using the impulse response method. Medical Engineering and Physics 18(7), 575-583.

Nokes, L., Mintow-Czyz, W.J., Mackie, I., et al., 1984. Direct and indirect determination of tibial natural frequency- A comparison of frequency domain analysis and fast fourier transform. Journal of Biomedical Engineering 6(1), 45-48.

Nokes, L.D., Thorne, G.C., 1988. Vibrations in orthopedics. Critical Reviews in Biomedical Engineering 15(4), 309-349.

Orne, D., Young, D.R., The effects of variable mass and geometry, pretwist, shear deformation, and rotatory inertia on the resonant frequencies of intact long bones: A finite element model analysis. Journal of Biomechanics 9, 763-770.

Oppenheim, A.V., Schafer, R.W., 1999. Discrete-Time Signal Processing. Prentice Hall, Saddle River, NJ.

Paavolainen, P., Pukkala, E., Pulkkinen, T., et al., 2002. Causes of death after total hip arthroplasty: a nationwide cohort study with 24, 638 patients. Journal of Arthroplasty 17(3), 274-281.

Paul, J.P., 1965. Bioengineering studies of the forces transmitted by joints engineering analysis. In: Kenedi, R.M., (Ed.), Biomechanics and Related Bioengineering Topics, Pergamon Press, Oxford, pp. 369-380.

Paul, J.P., 1976. Approaches to Design: Force actions transmitted by joints in the human body. Proceedings of the Royal Society of London 192, 163-172.

Pelker, R.R., Saha, S., 1983. Stress wave propagation in bone. Journal of Biomechanics 16, 481.

Rasmusson, L., Stegersjö, G., Kahnberg, K.E., et al., 1999. Implant stability measurements using resoanance frequency analysis in the grafted maxilla: A cross-sectional pilot study. Clinical Implant Dentistry and Related Research 1(2), 70-74.

Roberts, M.J., 2004. Signals and Systems. McGraw Hill, Boston, MA.

Rosenstein, A.D., McCoy, G.F., Bulstrode, C.J., 1989. The differentiation of loose and secure femoral implants in total hip replacement using a vibrational technique: an anatomical and pilot study. Proceedings of the Institution of Mechanical Engineers 203, 77-81.

Rydell, N.W., 1966. Intravital measurements of forces acting on the hip joint. In: Evans, F.G. (Ed.), Studies on the anatomy and function of bone and joints. Springer, Berlin, pp. 52-68.

Saha, S., Lakes, R.S., 1977. A non-invasive technique for detecting stress waves in bone using the piezoelectric effect. IEEE Transactions on Biomedical Engineering 24, 508.

Seirig, A., Arvikar, R.J., 1973. The prediction of muscular load sharing and joint forces in the lower extremities during walking. Journal of Biomechanics 8, 89-102.

Sharp, D.J., Porter, K.M., 1985. The Charnley total hip replacement in patients under 40. Clinical Orthopedics 201, 51-56.

Sonstegard, D.A., Matthews, L.S., 1976. Sonic diagnosis of bone fracture healing- A preliminary study. Journal of Biomechanics 9, 689.

Taylor, J.G., Perry, J., Meswania, J.M., et al., 1994. Telemetry of strain in vivo from a proximal femoral replacement: early results. Journal of Orthopaedic Research.

Taylor, S.J., Walker, P.S., 2001. Forces and moments telemetered from two distal femoral replacements during various activities. Journal of Biomechanics 34, 839-848.

Taylor, W.R., Roland, E., Ploeg, H., et al., 2002. Determination of orthotropic bone elastic constants using FEA and modal analysis. Journal of Biomechanics 35, 767-773.

Thomas, A.M., Luo, D.Z., Dunn, J.W., 1991. Response of human femur to mechanical vibration. Journal of Biomedical Engineering 13(1), 58-60.

Thomson, W.T., 1988. Theory of Vibration with Applications. Prentice-Hall, Englewood Cliffs, NJ.

Towheed, T.E., Hochberg, M.C., 1996. Health-related quality of life after total hip replacement. Seminars in Arthritis and Rheumatism 26(1), 483-491.

Tsuchikane, A., Naktsuchi, Y., Nomura, A., 1995. The influence of joints and soft tissue on the natural frequency fo the human tibia using the impulse response method. Proceedings of the Institution of Mechanical Engineers Part H 209(3), 149-155.

Van der Perre, G., Cornelissen, P., 1983. On the mechanical resonance of human tibia in-vitro. Journal of Biomechanics 16, 549-552.

Van Der Perre, G., Lowet, G., 1996. In-Vivo assessment of bone mechanical properties by vibration and ultrasonic wave propagation analysis. Bone 18(Supp. 1), 29S-35S.

Willman, G., 2000. Ceramic femoral head retrieval data. Clinical Orthopaedics and Related Research 379, 22-28.

Wright T.M., Goodman, S.B. (Eds.), 2000. What is the clinical scope of implant wear in the hip and how has it changed since 1995? In: Implant Wear in Total Joint Replacement: Clinical and Biological Issues, Material and Design Considerations. American Academy of Orthopaedic Surgeons, Rosemont, IL, pp. 3-7.

APPENDIX

Matlab Code for Data Processing:

```
clear
load mom250d_1.txt
a=mom250d_1;
[col,row]=size(a)
samp=20000;
ta=[0:1:length(a)-1];
tb=ta/samp;

% Setting accelerometer channel of interest
ch=9;
% Giving channel of interest a variable name
acc=a(:,ch)*9.81;

% Defines the channel where the force data is
force=a(:,14)*100*4.448*.0001;

%%%%%%%%%%% Determine n's of band-pass filter and n's of stop band
%%%%%%%%%%% filter

%%%%%% BAND PASS
%Wp represents the pass-band portion of this filter 10Hz to 7kHz
Wp(1)=10/10000;
Wp(2)=7000/10000;
%max dB loss that we want through our pass band
Rp=3;

%Ws represents the starting points for the band stop filter one at 5Hz
and
%the other one at 8khz
Ws(1)=5/10000;
Ws(2)=8000/10000;
%min dB loss that we want through our stop band
Rs=10;

%band pass params
[n_bp,Wn_bp]=buttord(Wp,Ws,Rp,Rs)
[b_bp,a_bp]=butter(n_bp,Wn_bp);
figure(1)
freqz(b_bp,a_bp,length(a),samp);
fprintf(1,'\nn_bp: %g',n_bp);


%%%%%% BAND STOP
%Wp represents the pass-band portion of this filter 655 Hz and 685 Hz
Wp(1)=655/10000;
Wp(2)=685/10000;
%max dB loss that we want through our pass band
Rp=3;

%Ws represents the starting points for the band stop filter one at 665
Hz and
```

```
%the other one at 675 Hz
Ws(1)=665/10000;
Ws(2)=675/10000;
%min dB loss that we want through our stop band
Rs=10;

%band STOP params
[n_bs,Wn_bs]=buttord(Wp,Ws,Rp,Rs)
[b_bs,a_bs]=butter(n_bs,Wn_bs,'stop');
figure(2)
freqz(b_bs,a_bs,length(a),samp);
fprintf(1,'\nn_bs: %g',n_bs);

%here we want to create a hanning window that is
1/numOverlappedSections of the original sample
%length N. This is due to the fact that the hanning window in PSD is
%overlapped multiple times to create the PSD approximation using
welches
%method

numOverlappedSections=8;
sizeHanning=round(length(a)/numOverlappedSections);
hanning_win=hanning(sizeHanning);

[Pxx,f]=pwelch(butter2_results,hanning_win,[],[],samp);

[Pxx2,f2]=pwelch(acc,hanning_win,[],[],samp);

plotconversion=20*log10(Pxx)/2;
plotconversion3=20*log10(Pxx2)/2;

figure(10)
plot(f,plotconversion)

figure(11)
plot(f_old,plotconversion2)

figure(12)
plot(tb,acc)

figure(13)
plot(tb, butter2_results)

figure(14)
plot(f2,plotconversion3)

output1=[f plotconversion];
output2=[tb' acc];
output3=[tb' butter2_results];
output4=[f2 plotconversion3];

save mom_1.txt output1 -ASCII -TABS
```

```
save coc_Acc.txt output2 -ASCII -TABS
save Filter_coc_Acc.txt output3 -ASCII -TABS
save Unfiltered_coc_FFT.txt output4 -ASCII -TABS
```

Component Resonant Test PSD's:

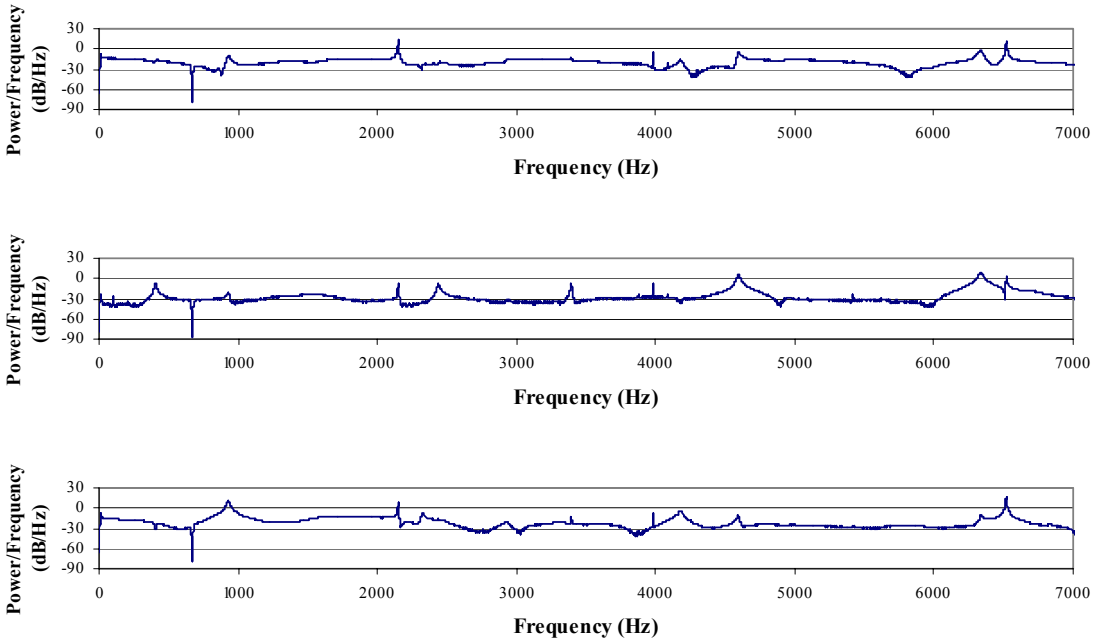

Figure A-1. PSD of a Resonance Test for a Hip Stem without Femoral Head Attached. The Signals are for the A1-axis (upper), A2-axis (middle) and A3-axis (lower).

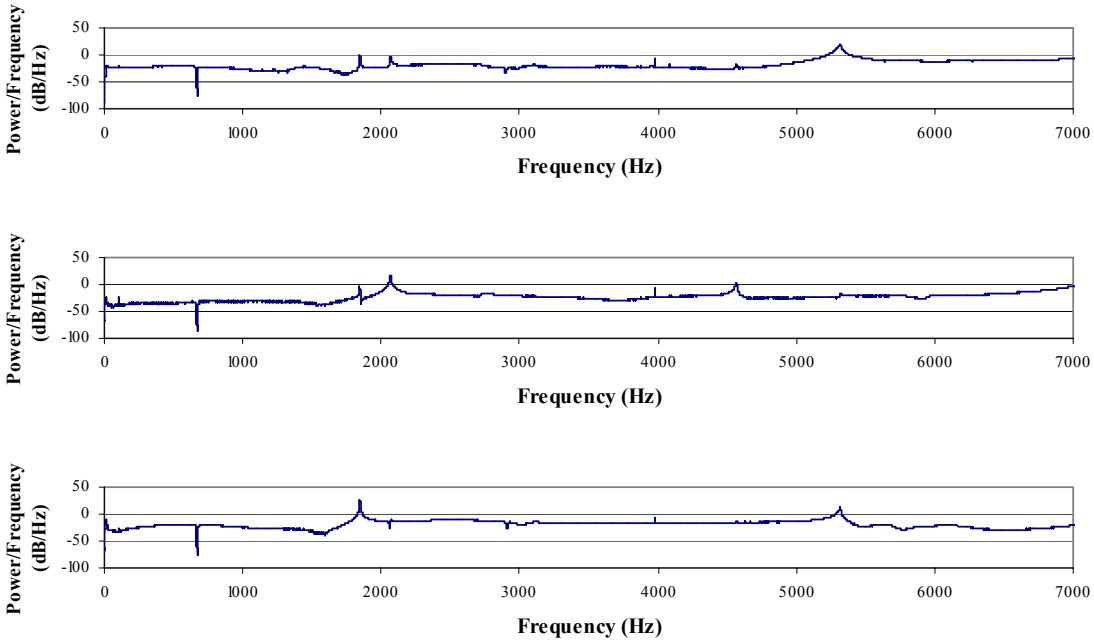

Figure A-2. PSD of a Resonance Test for a Hip Stem with Metal Femoral Head Attached. The Signals are for the A1-axis (upper), A2-axis (middle) and A3-axis (lower).

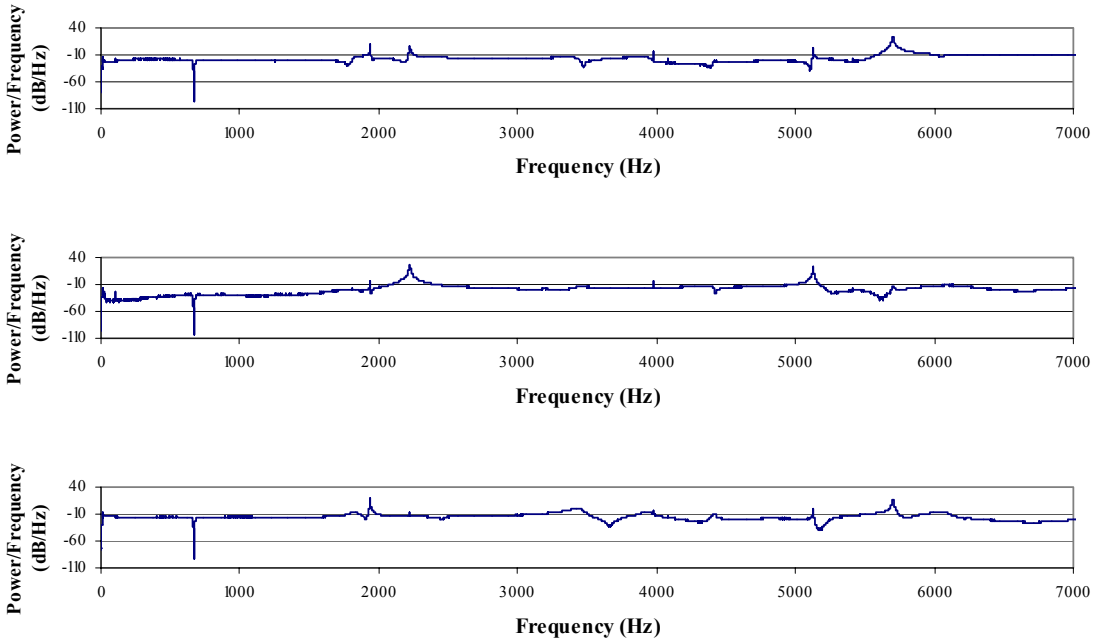

Figure A-3. PSD of a Resonance Test for a Hip Stem with Ceramic Femoral Head Attached. The Signals are for the A1-axis (upper), A2-axis (middle) and A3-axis (lower).

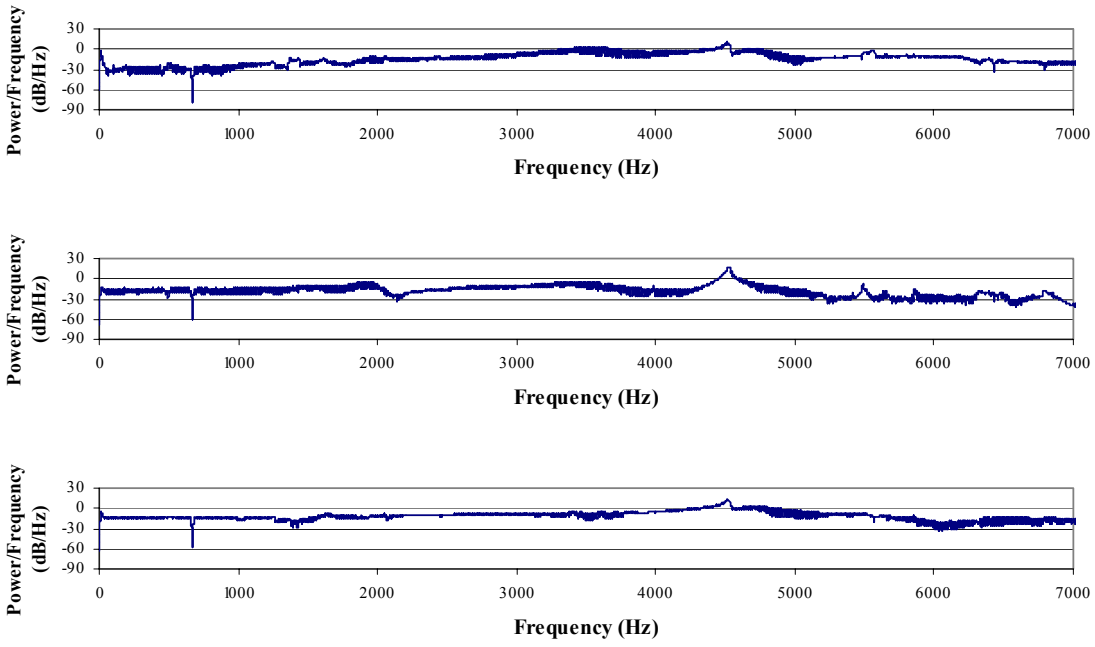

Figure A-4. PSD of a Resonance Test for an Acetabular Cup without Liner Inserted. The Signals are for the A1-axis (upper), A2-axis (middle) and A3-axis (lower).

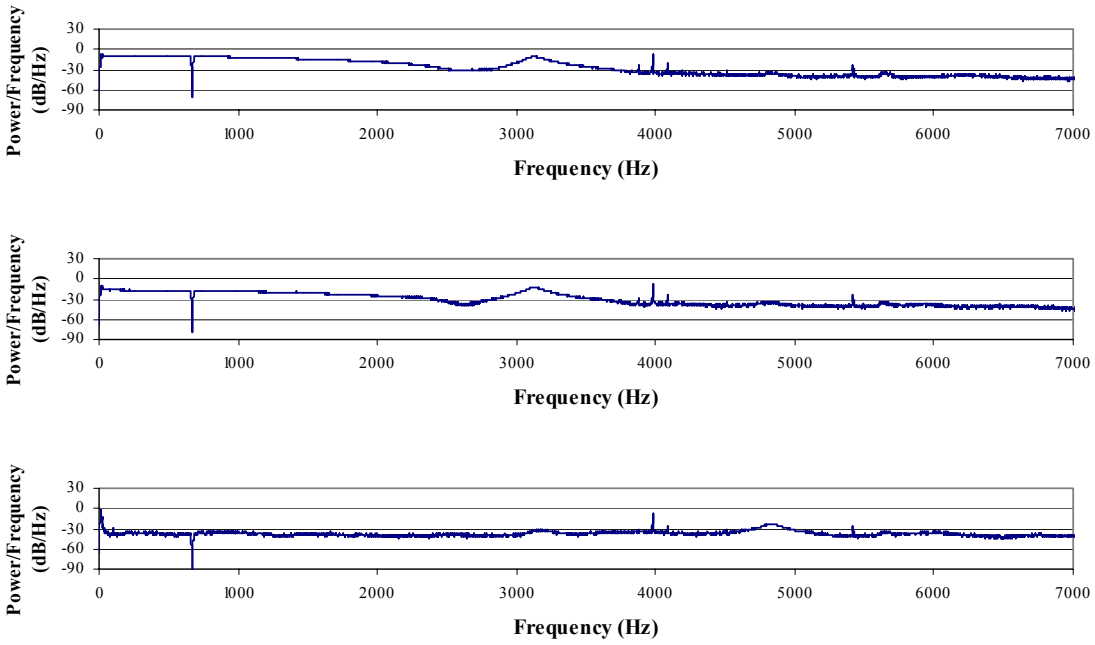

Figure A-5. PSD of a Resonance Test for an Acetabular Cup with Polyethylene Liner Inserted. The Signals are for the A1-axis (upper), A2-axis (middle) and A3-axis (lower).

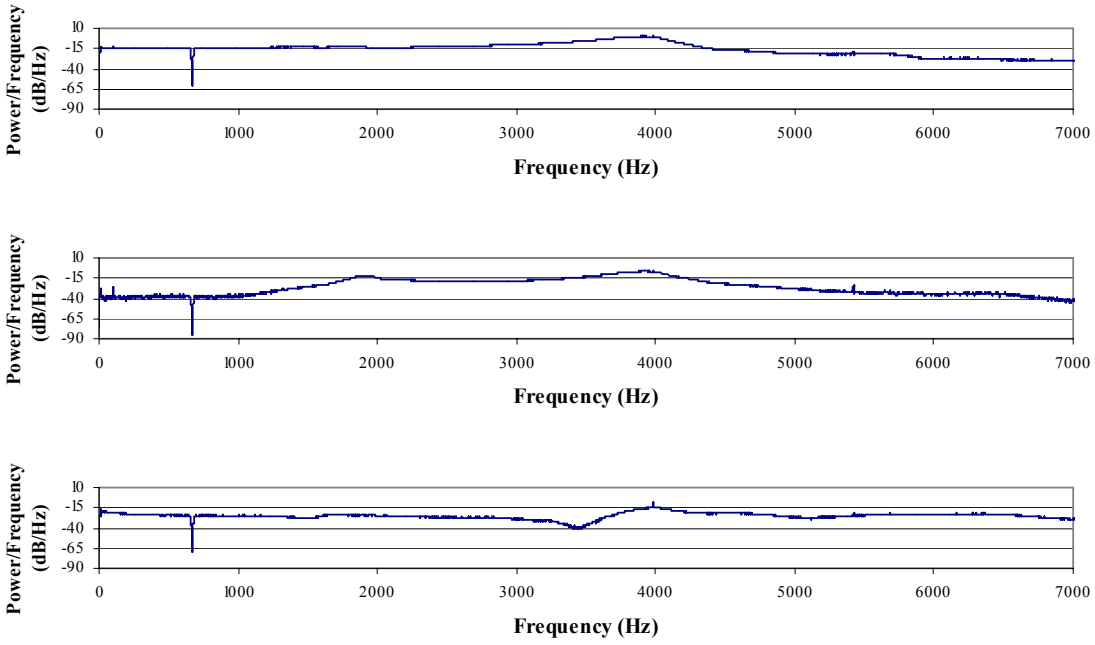

Figure A-6. PSD of a Resonance Test for an Acetabular Cup with Metal Liner Inserted. The Signals are for the A1-axis (upper), A2-axis (middle) and A3-axis (lower).

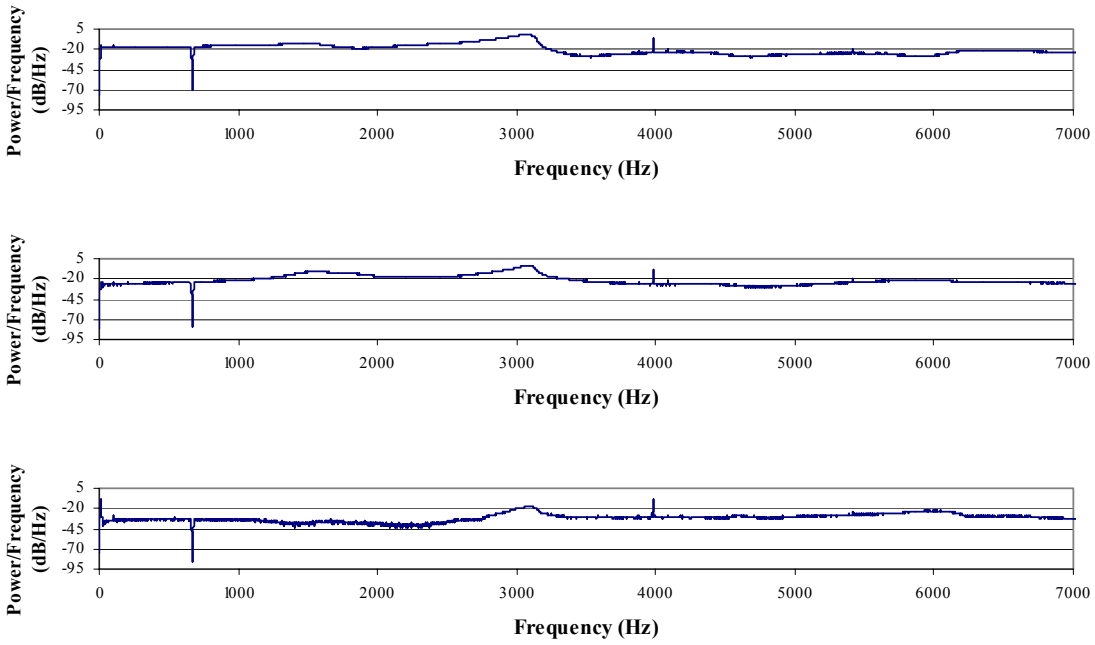

Figure A-7. PSD of a Resonance Test for an Acetabular Cup with Ceramic Liner Inserted. The Signals are for the A1-axis (upper), A2-axis (middle) and A3-axis (lower).

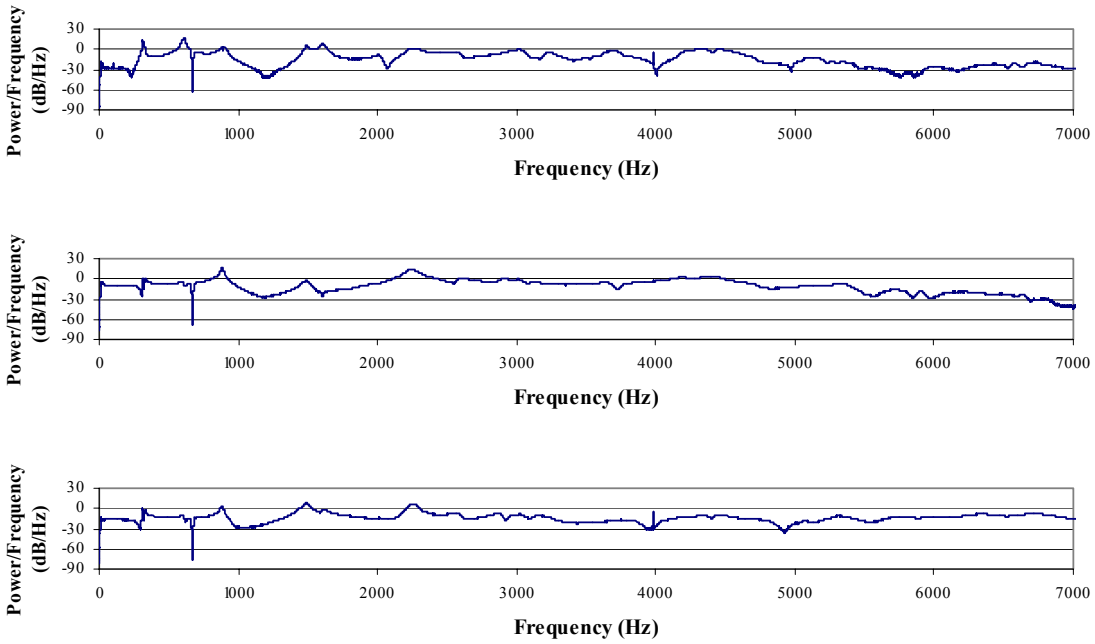

Figure A-8. PSD of a Resonance Test for Normal Synthetic Femur. The Signals are for the A1-axis (upper), A2-axis (middle) and A3-axis (lower).

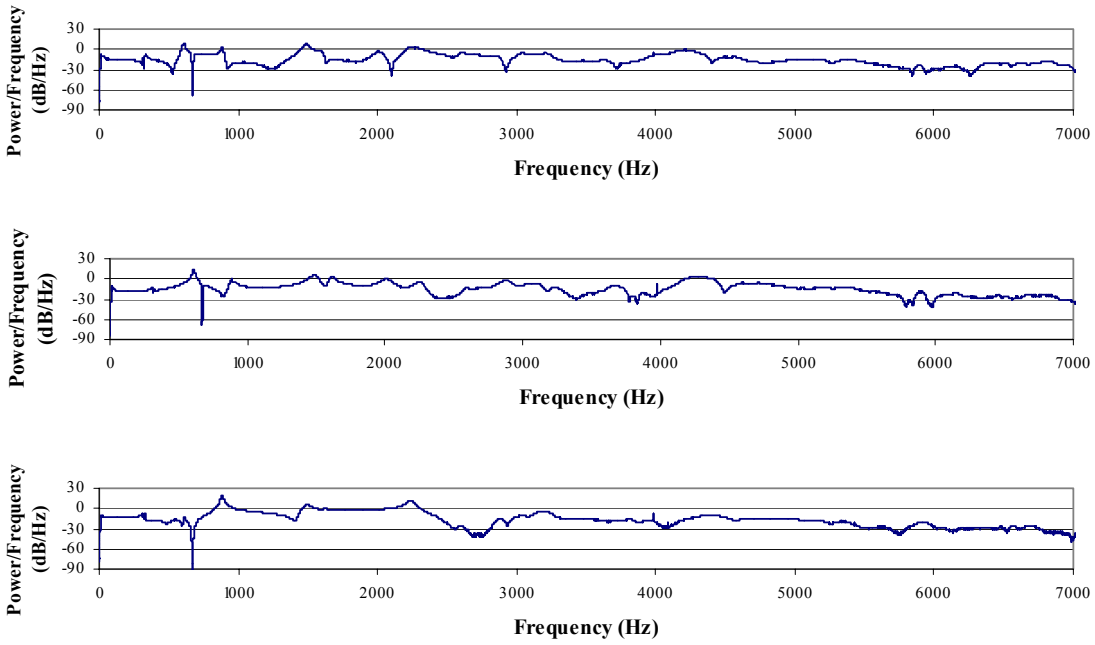

Figure A-9. PSD of a Resonance Test for Normal Synthetic Femur. The Signals are for the B1-axis (upper), B2-axis (middle) and B3-axis (lower).

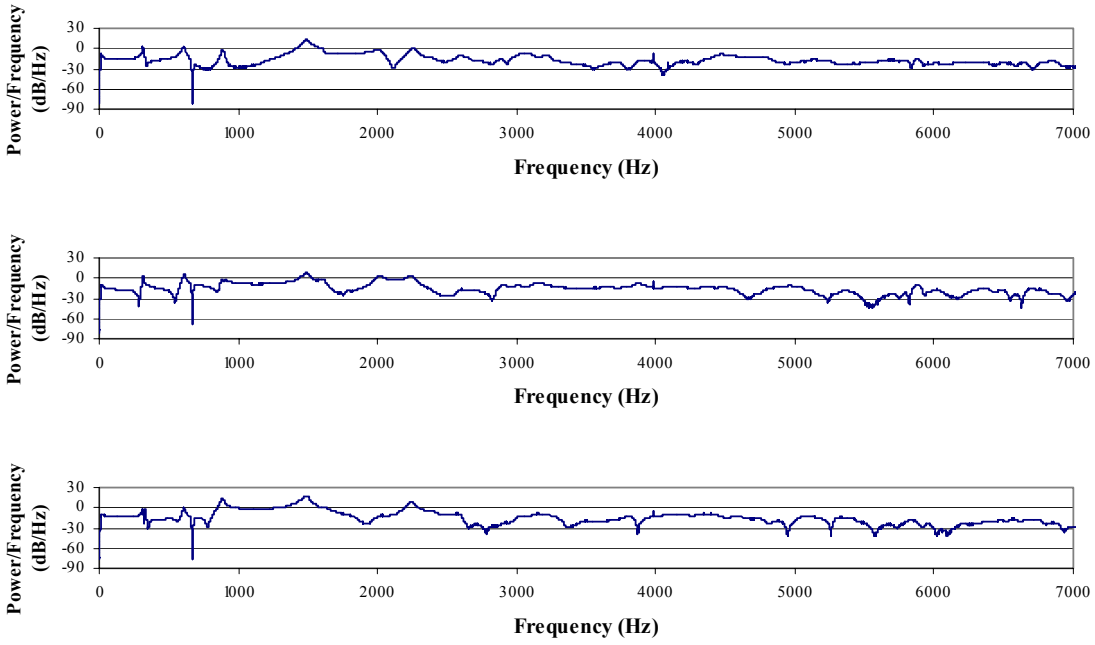

Figure A-10. PSD of a Resonance Test for Normal Synthetic Femur. The Signals are for the C1-axis (upper), C2-axis (middle) and C3-axis (lower).

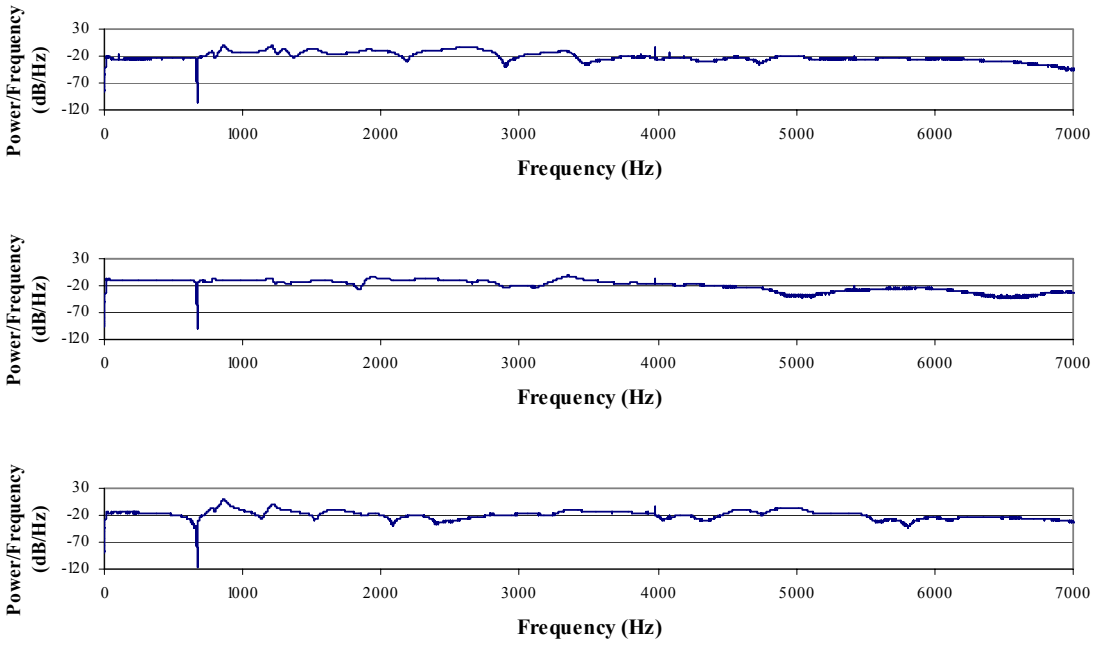

Figure A-11. PSD of a Resonance Test for Normal Synthetic Pelvis. The Signals are for the A1-axis (upper), A2-axis (middle) and A3-axis (lower).

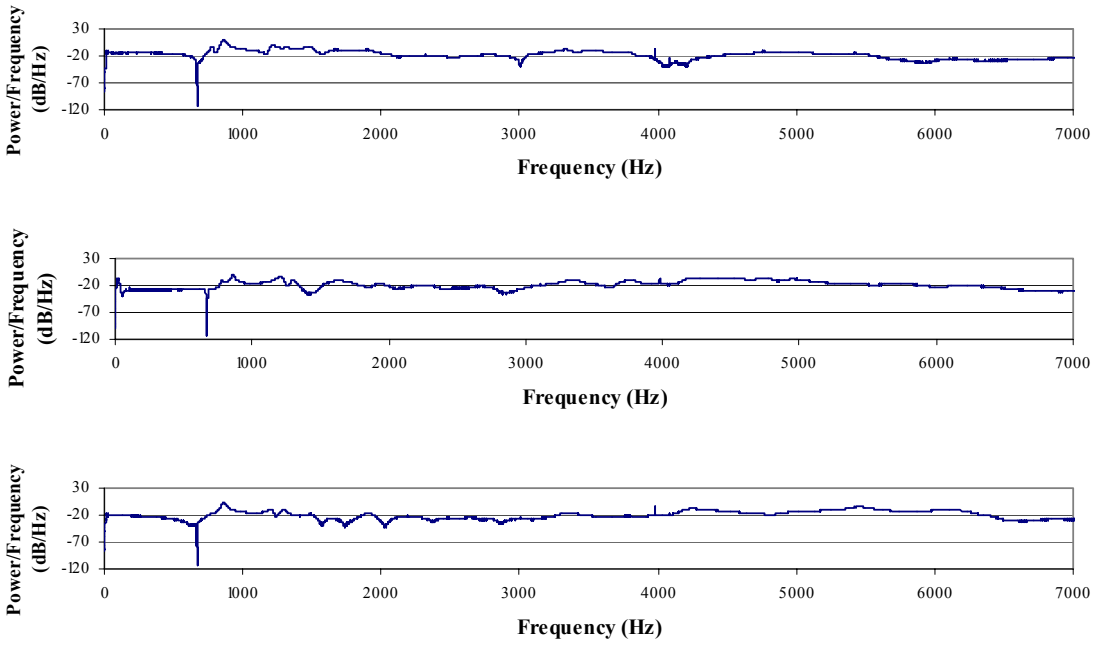

Figure A-12. PSD of a Resonance Test for Normal Synthetic Pelvis. The Signals are for the B1-axis (upper), B2-axis (middle) and B3-axis (lower).

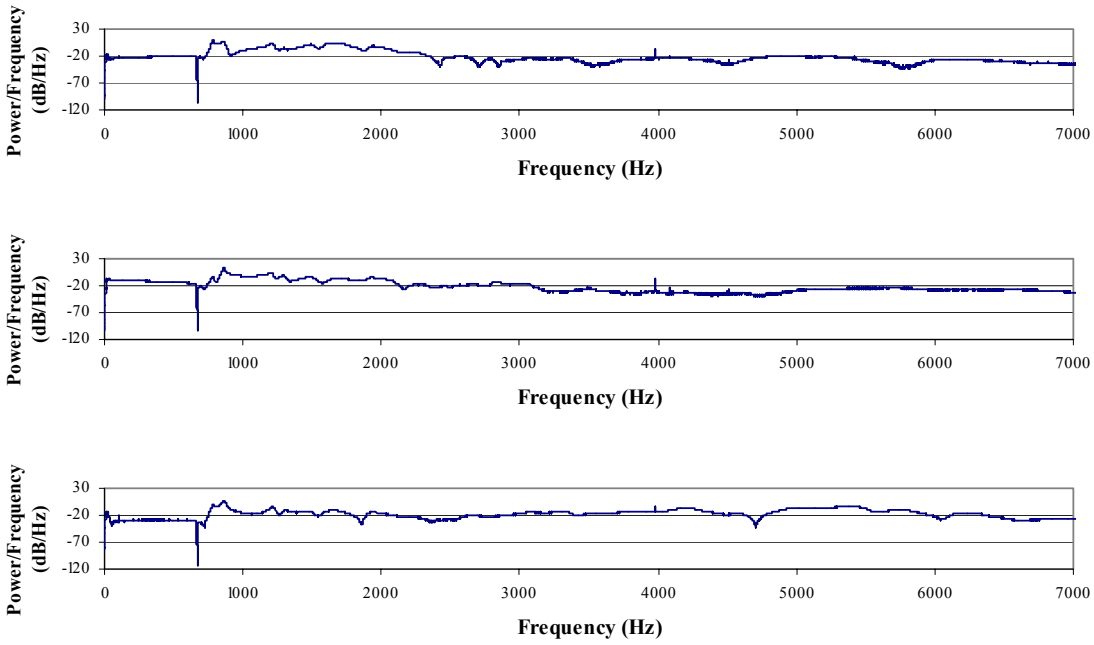

Figure A-13. PSD of a Resonance Test for Normal Synthetic Pelvis. The Signals are for the C1-axis (upper), C2-axis (middle) and C3-axis (lower).

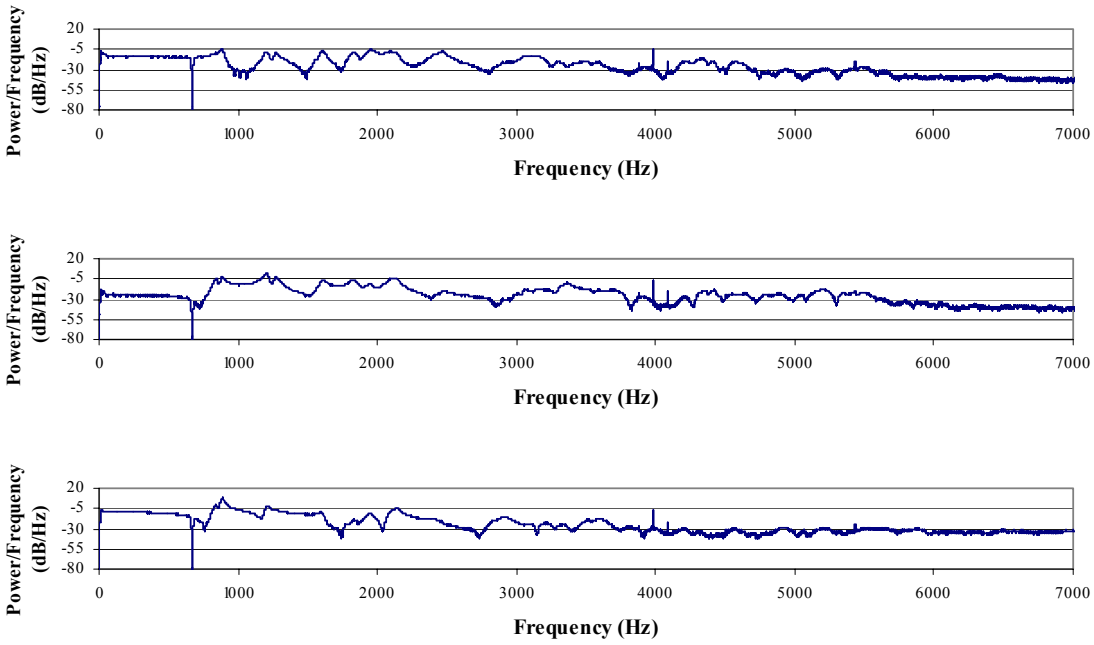

Figure A-14. PSD of a Resonance Test for a Synthetic Pelvis Implanted with Acetabular Cup with Polyethylene Liner. The Signals are for the A1-axis (upper), A2-axis (middle) and A3-axis (lower).

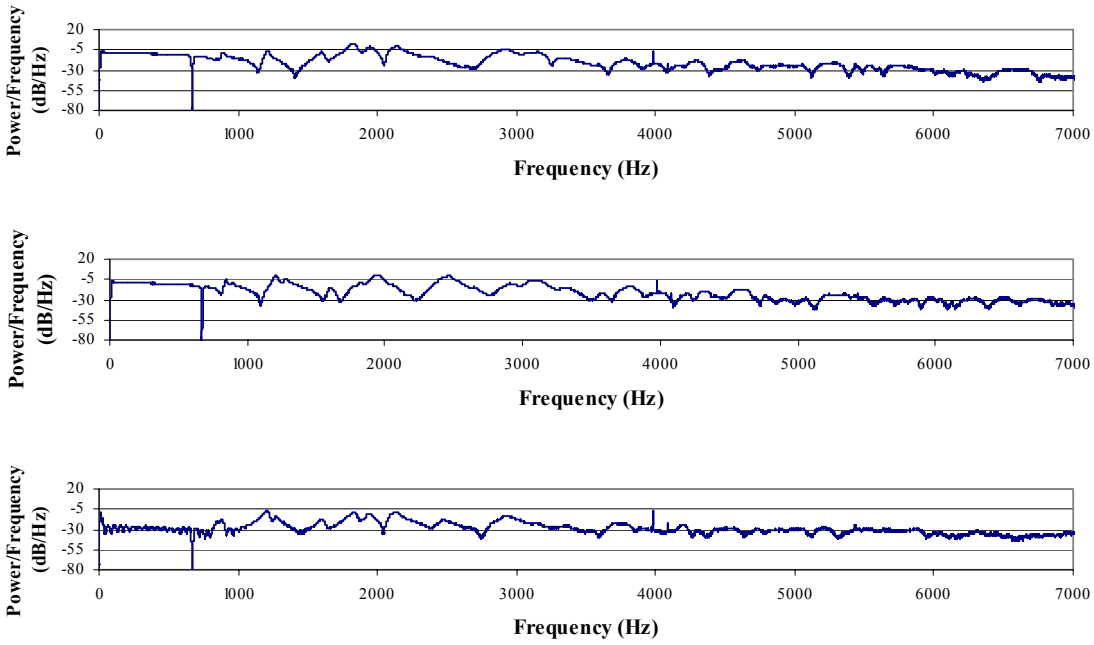

Figure A-15. PSD of a Resonance Test for a Synthetic Pelvis Implanted with Acetabular Cup with Polyethylene Liner. The Signals are for the B1-axis (upper), B2-axis (middle) and B3-axis (lower).

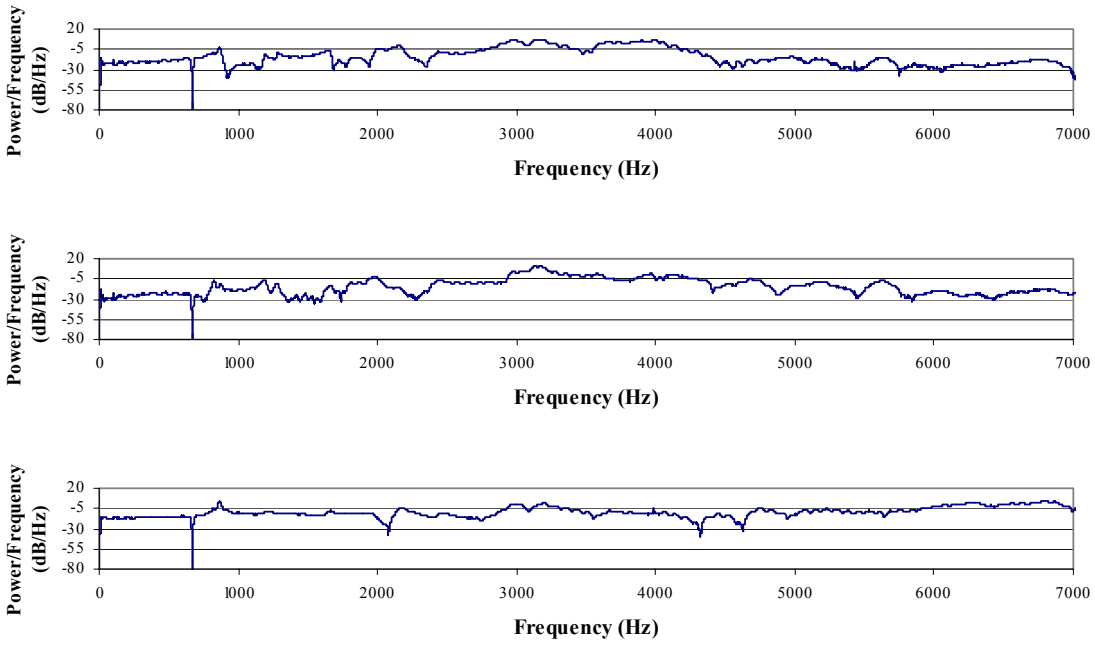

Figure A-16. PSD of a Resonance Test for a Synthetic Pelvis Implanted with Acetabular Cup with Metal Liner. The Signals are for the A1-axis (upper), A2-axis (middle) and A3-axis (lower).

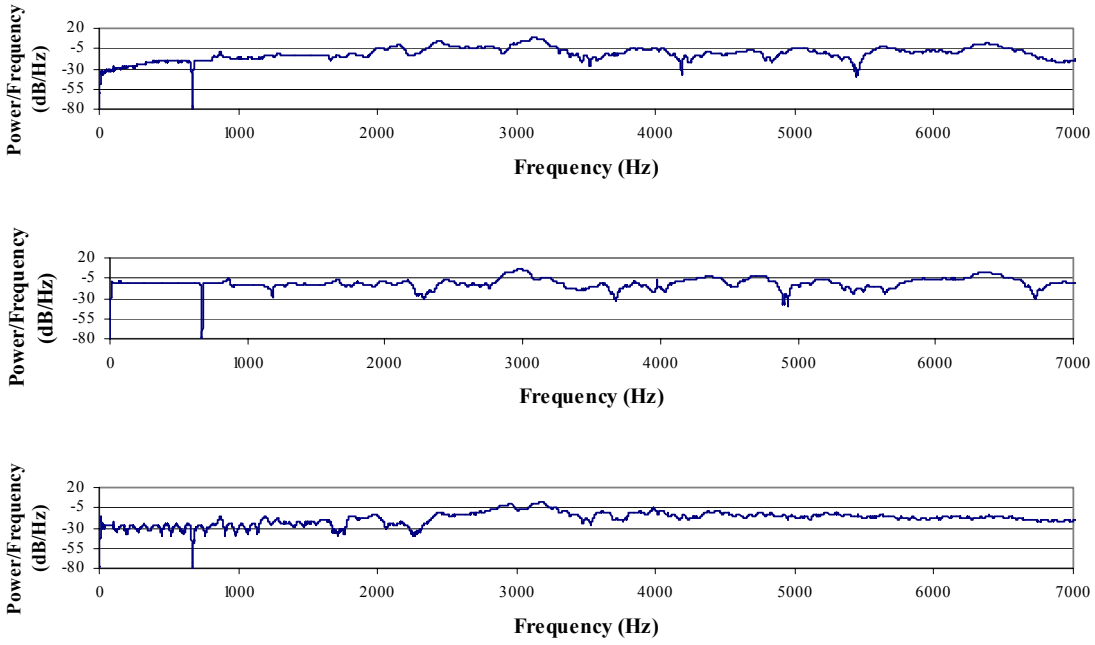

Figure A-17. PSD of a Resonance Test for a Synthetic Pelvis Implanted with Acetabular Cup with Metal Liner. The Signals are for the B1-axis (upper), B2-axis (middle) and B3-axis (lower).

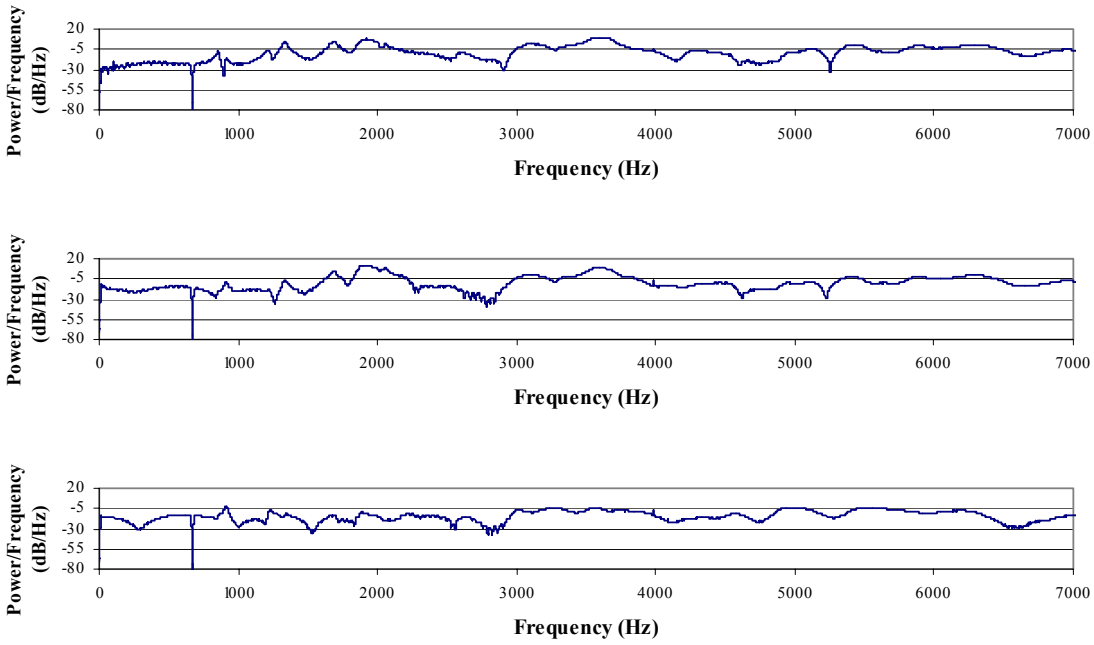

Figure A-18. PSD of a Resonance Test for a Synthetic Pelvis Implanted with Acetabular Cup with Ceramic Liner. The Signals are for the A1-axis (upper), A2-axis (middle) and A3-axis (lower).

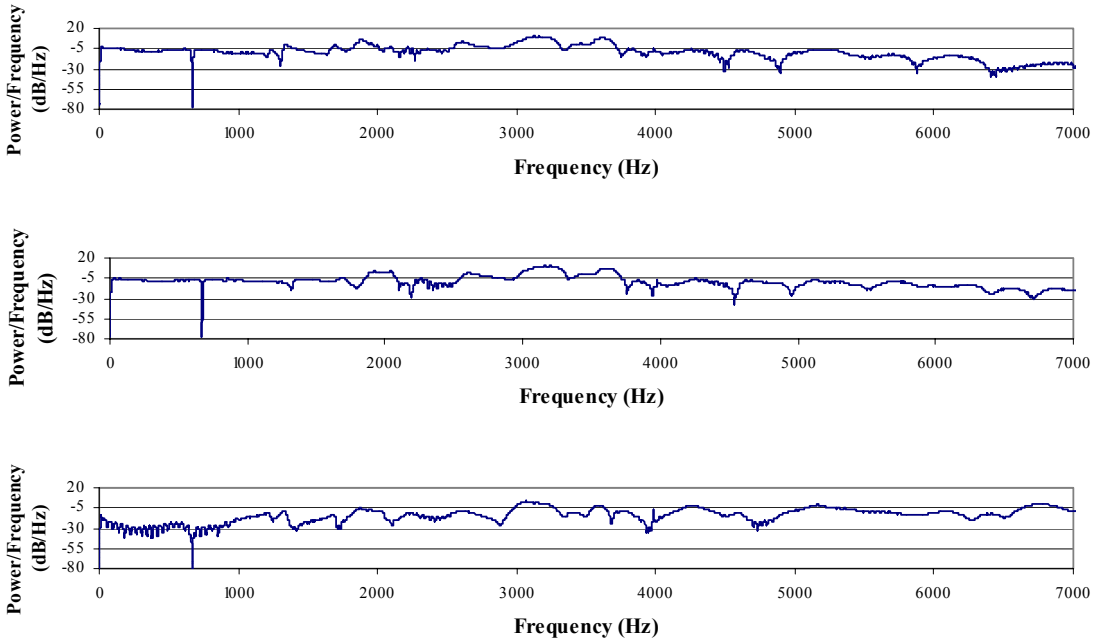

Figure A-19. PSD of a Resonance Test for a Synthetic Pelvis Implanted with Acetabular Cup with Ceramic Liner. The Signals are for the B1-axis (upper), B2-axis (middle) and B3-axis (lower).

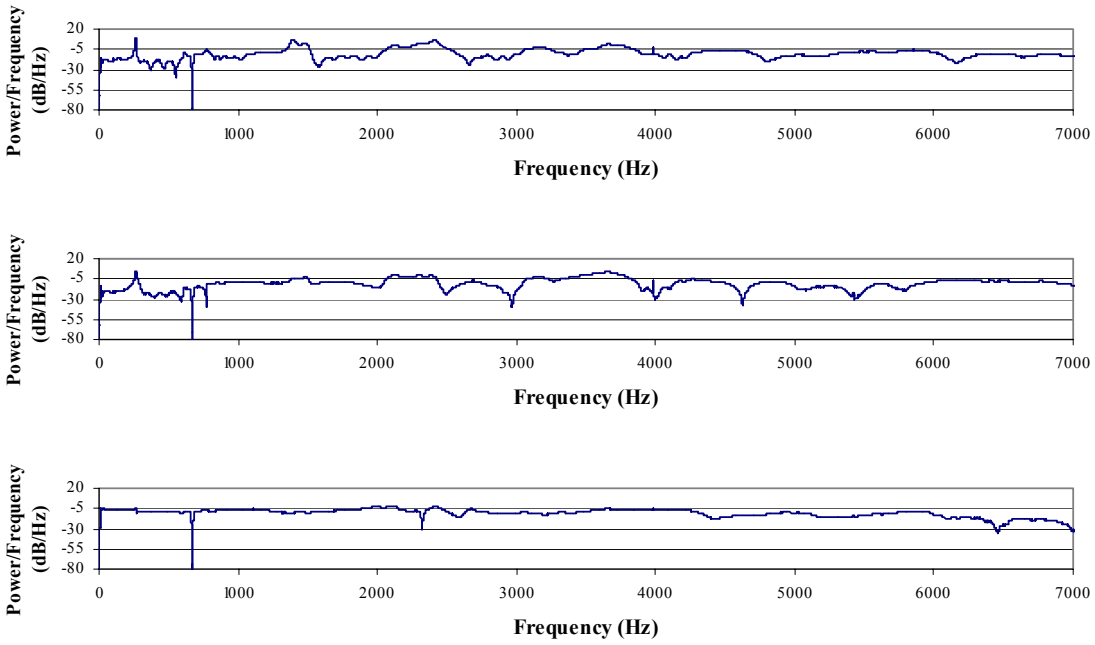

Figure A-20. PSD of a Resonance Test for a Synthetic Femur Implanted with Hip Stem with Metal Head. The Signals are for the C1-axis (upper), C2-axis (middle) and C3-axis (lower).

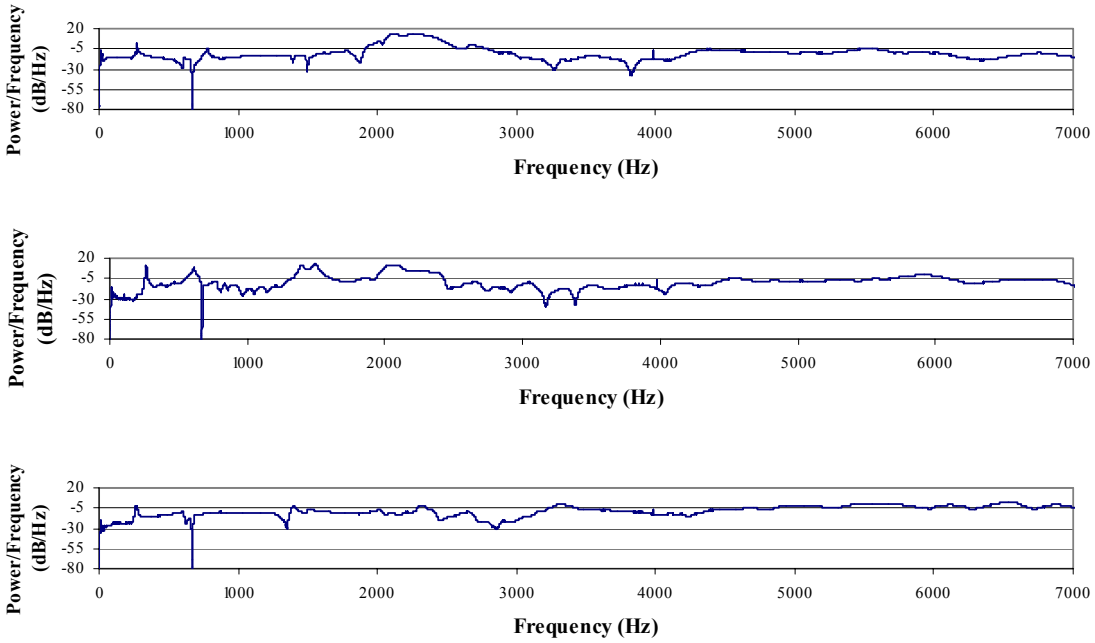

Figure A-21. PSD of a Resonance Test for a Synthetic Femur Implanted with Hip Stem with Metal Head. The Signals are for the D1-axis (upper), D2-axis (middle) and D3-axis (lower).

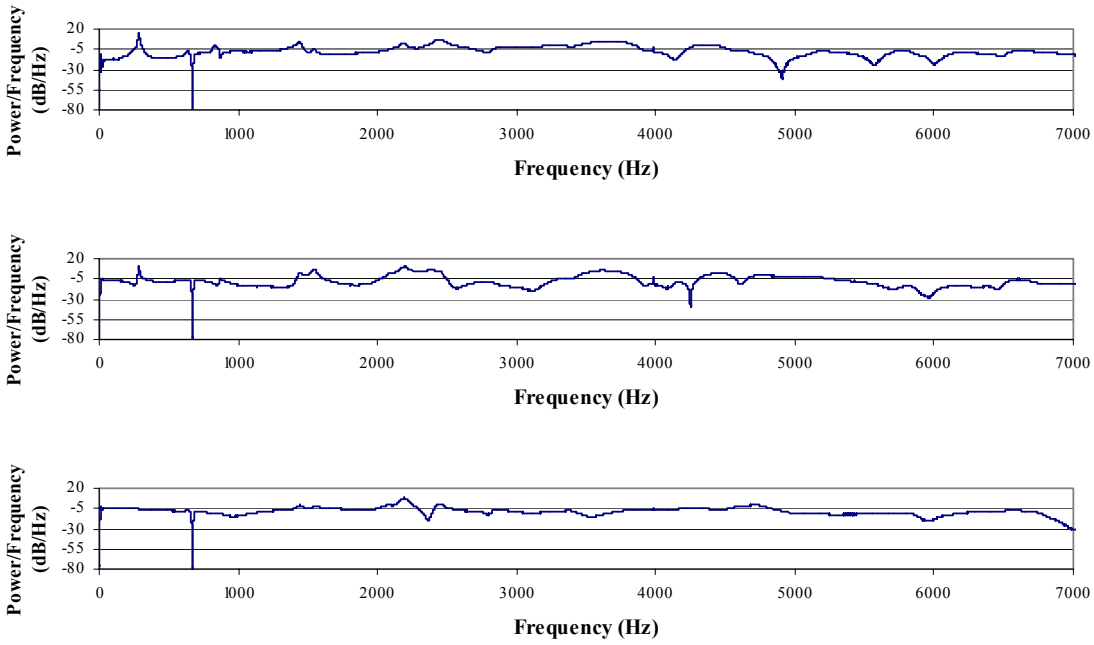

Figure A-22. PSD of a Resonance Test for a Synthetic Femur Implanted with Hip Stem with Ceramic Head. The Signals are for the C1-axis (upper), C2-axis (middle) and C3-axis (lower).

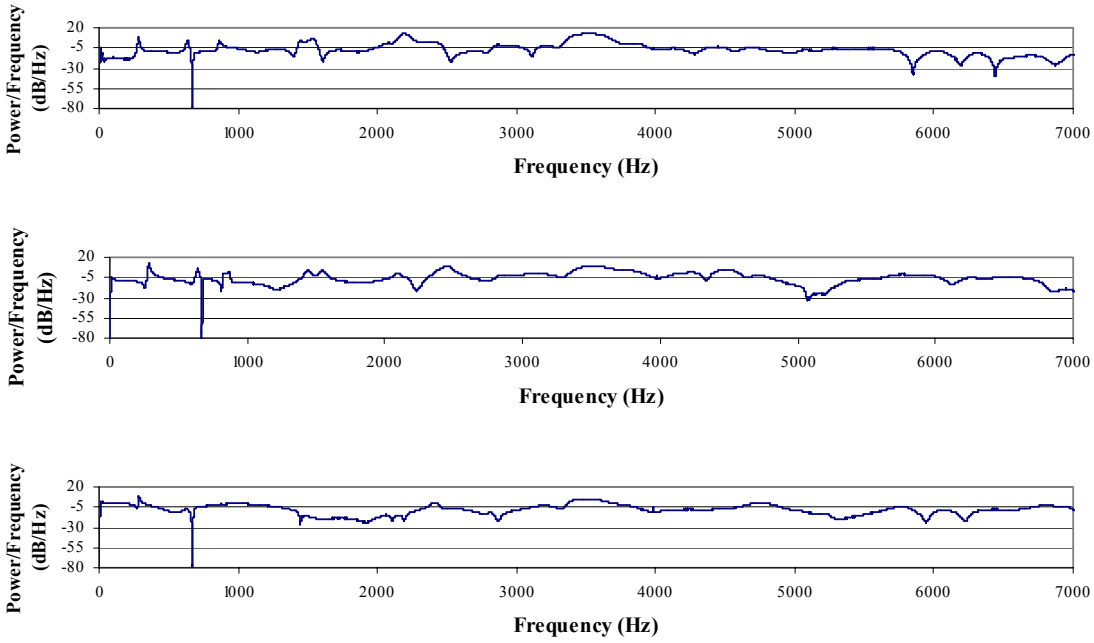

Figure A-23. PSD of a Resonance Test for a Synthetic Femur Implanted with Hip Stem with Ceramic Head. The Signals are for the D1-axis (upper), D2-axis (middle) and D3-axis (lower).

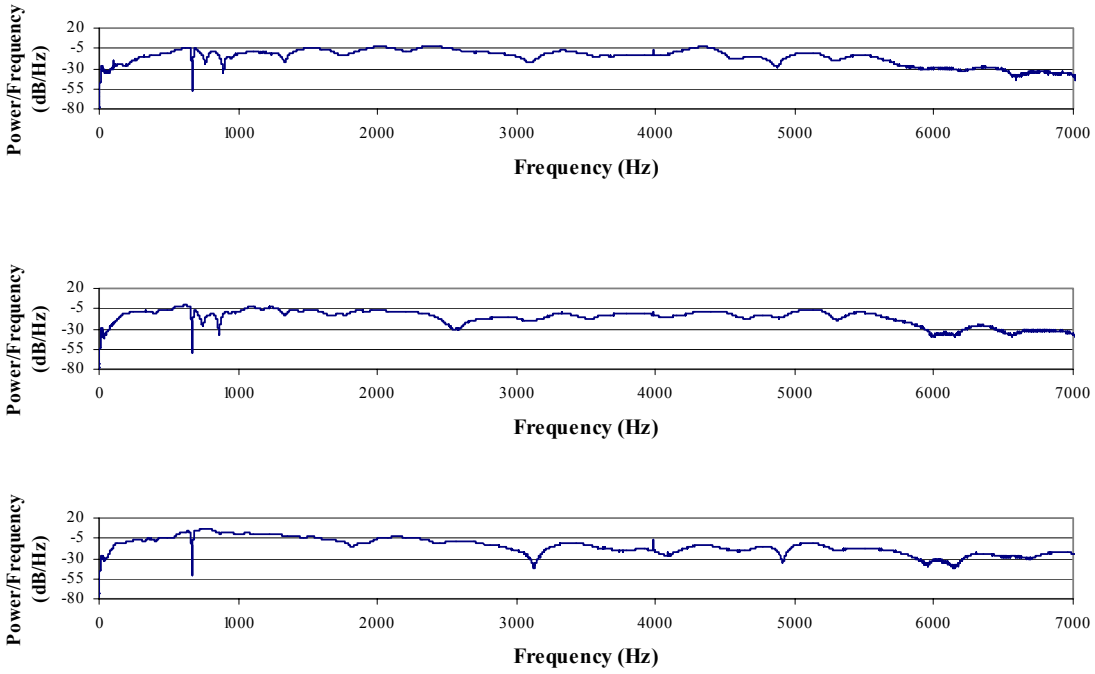

Figure A-24. PSD of a Resonance Test for a Synthetic Pelvis Implanted with Acetabular Cup with Polyethylene Insert Resting within its Fixture. The Signals are for the A1-axis (upper), A2-axis (middle) and A3-axis (lower).

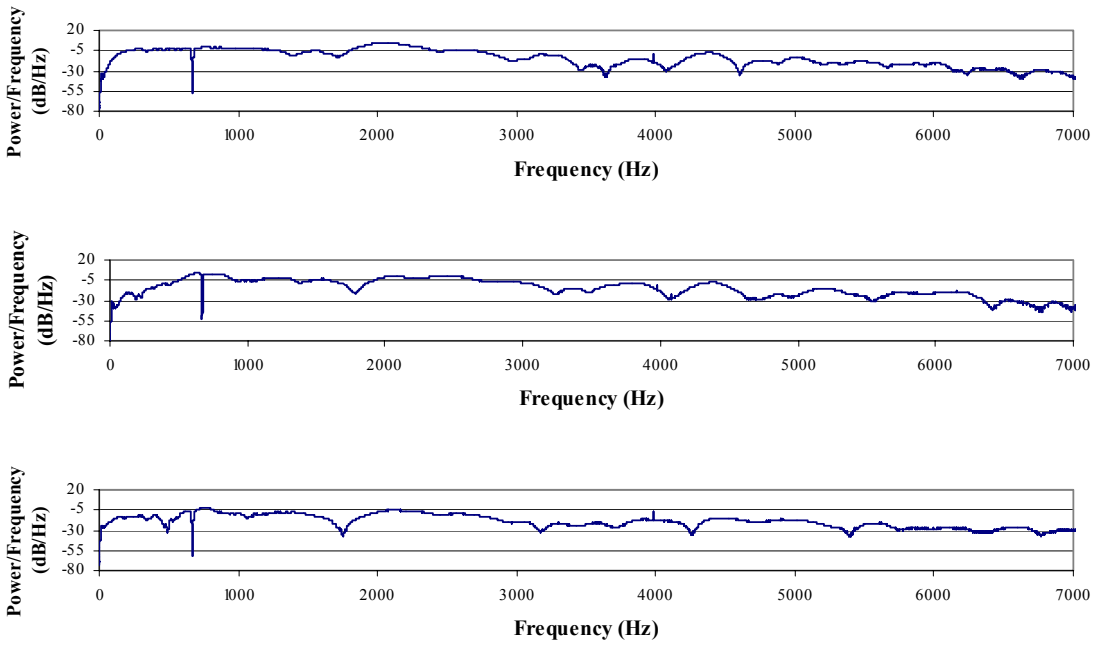

Figure A-25. PSD of a Resonance Test for a Synthetic Pelvis Implanted with Acetabular Cup with Polyethylene Insert Resting within its Fixture. The Signals are for the B1-axis (upper), B2-axis (middle) and B3-axis (lower).

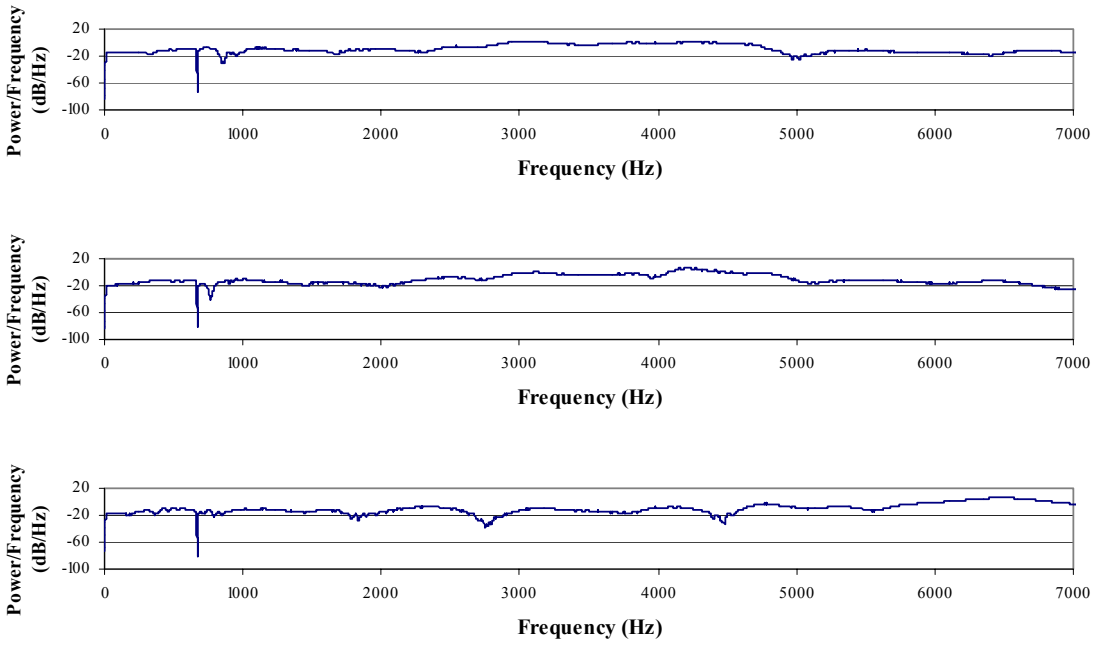

Figure A-26. PSD of a Resonance Test for a Synthetic Pelvis Implanted with Acetabular Cup with Metal Insert Resting within its Fixture. The Signals are for the A1-axis (upper), A2-axis (middle) and A3-axis (lower).

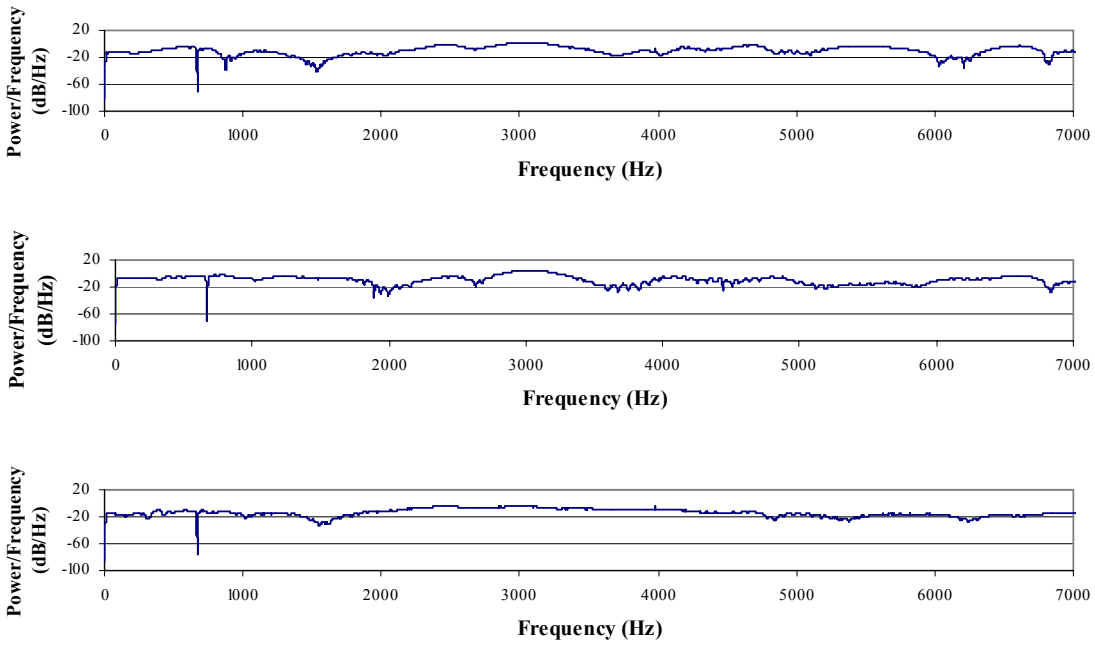

Figure A-27. PSD of a Resonance Test for a Synthetic Pelvis Implanted with Acetabular Cup with Metal Insert Resting within its Fixture. The Signals are for the B1-axis (upper), B2-axis (middle) and B3-axis (lower).

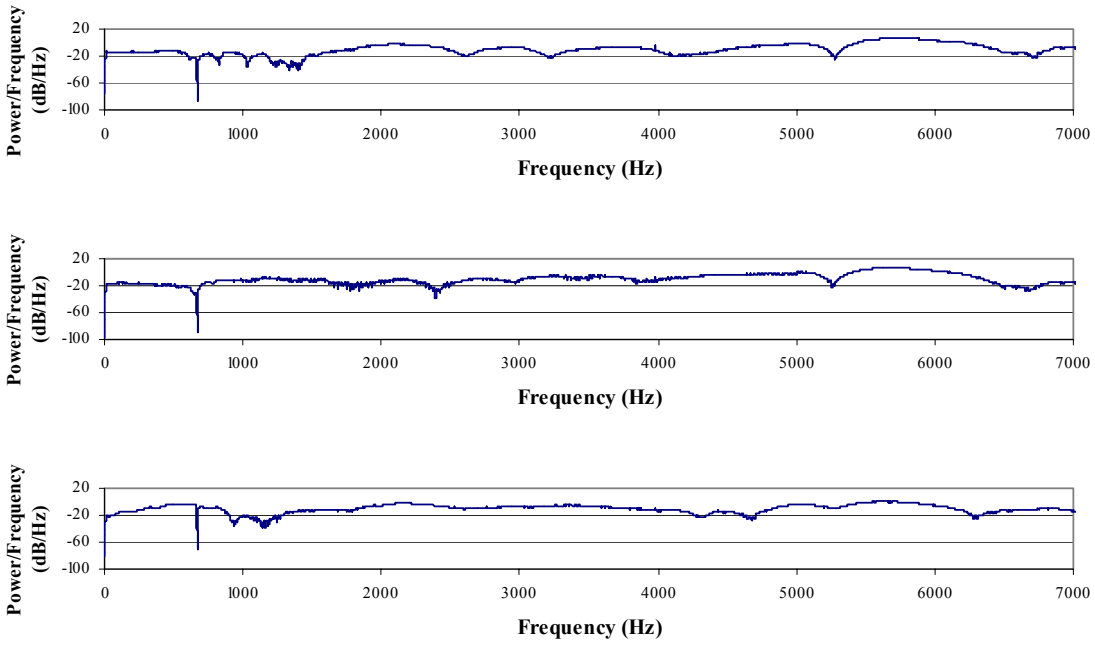

Figure A-28. PSD of a Resonance Test for a Synthetic Pelvis Implanted with Acetabular Cup with Ceramic Insert Resting within its Fixture. The Signals are for the A1-axis (upper), A2-axis (middle) and A3-axis (lower).

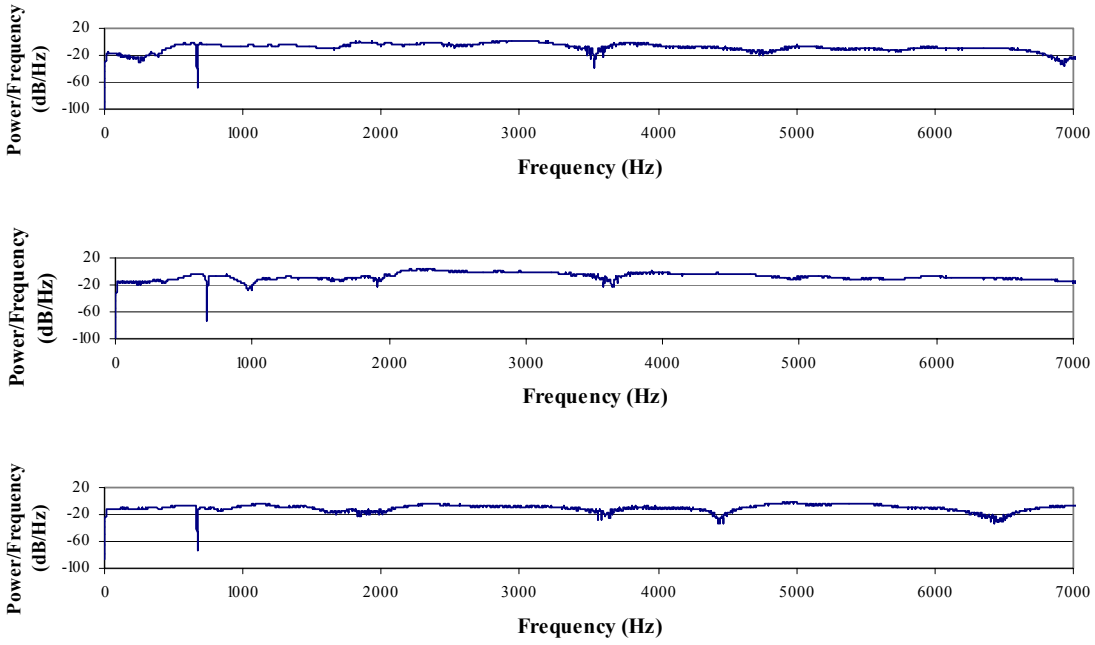

Figure A-29. PSD of a Resonance Test for a Synthetic Pelvis Implanted with Acetabular Cup with Ceramic Insert Resting within its Fixture. The Signals are for the B1-axis (upper), B2-axis (middle) and B3-axis (lower).

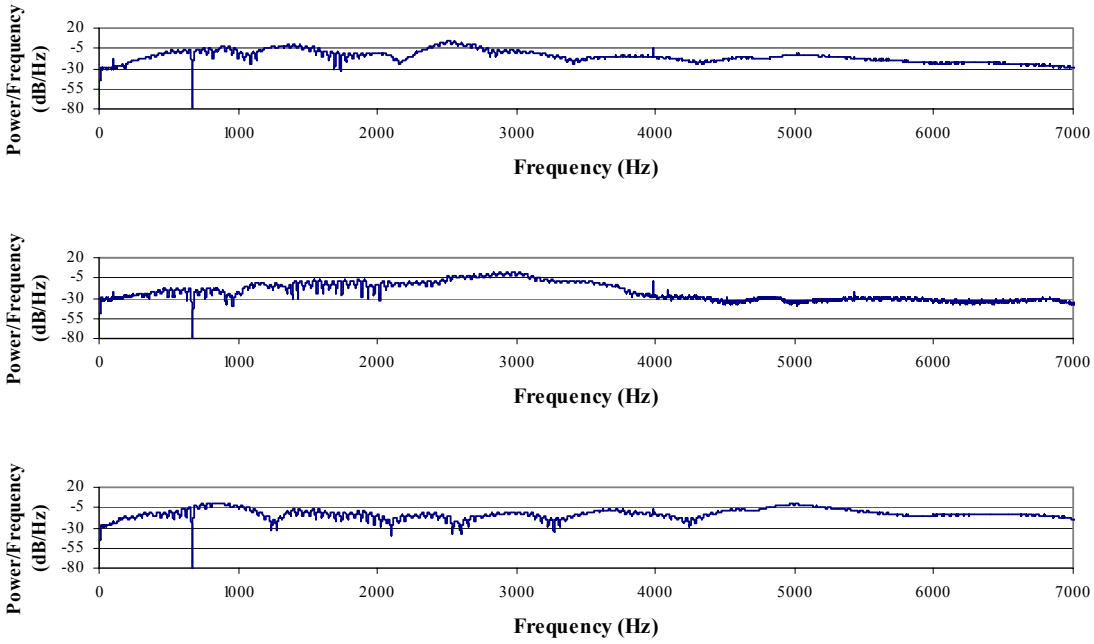

Figure A-30. PSD of a Resonance Test for a Normal Synthetic Pelvis Resting within its Fixture. The Signals are for the A1-axis (upper), A2-axis (middle) and A3-axis (lower).

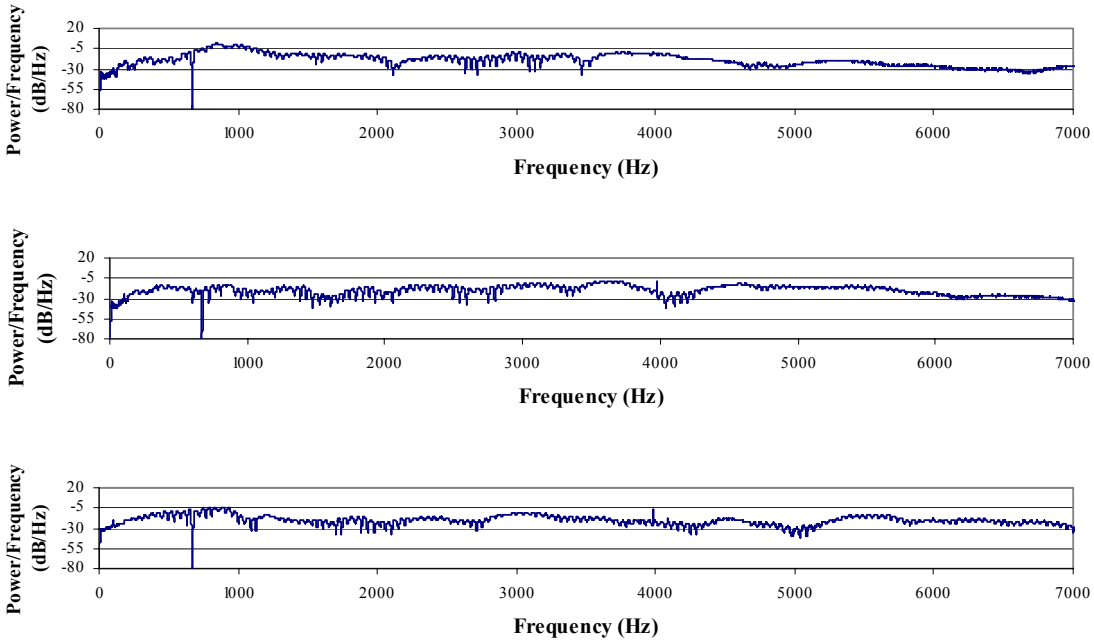

Figure A-31. PSD of a Resonance Test for a Normal Synthetic Pelvis Resting within its Fixture. The Signals are for the B1-axis (upper), B2-axis (middle) and B3-axis (lower).

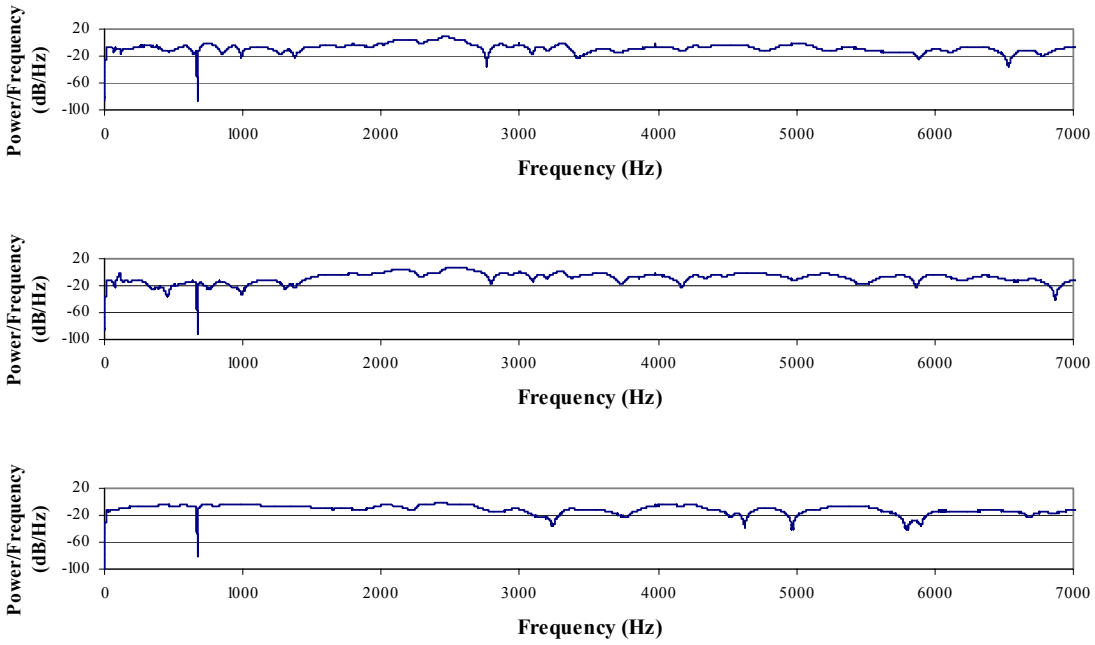

Figure A-32. PSD of a Resonance Test for a Synthetic Femur Implanted with Hip Stem with Metal Head Resting within its Fixture. The Signals are for the C1-axis (upper), C2-axis (middle) and C3-axis (lower).

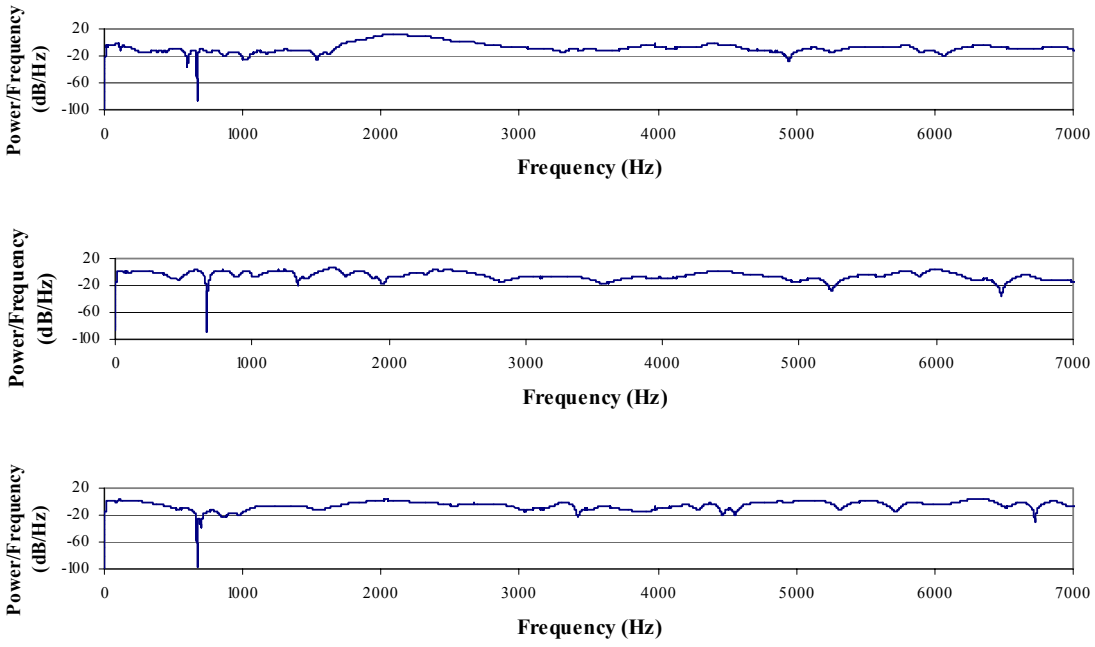

Figure A-33. PSD of a Resonance Test for a Synthetic Femur Implanted with Hip Stem with Metal Head Resting within its Fixture. The Signals are for the D1-axis (upper), D2-axis (middle) and D3-axis (lower).

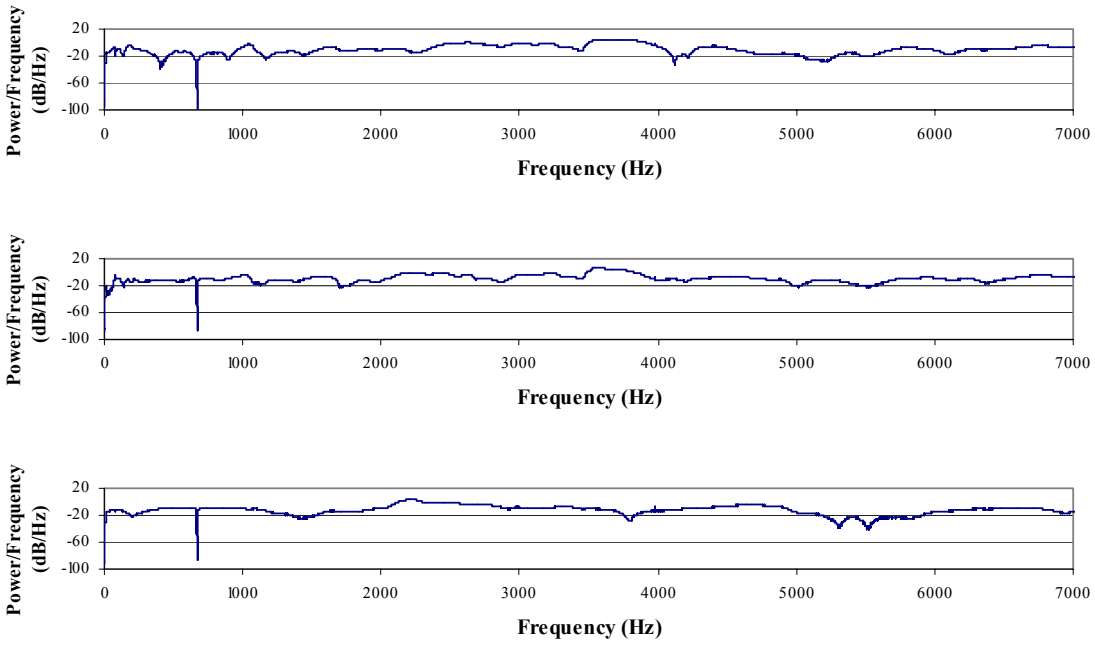

Figure A-34. PSD of a Resonance Test for a Synthetic Femur Implanted with Hip Stem with Ceramic Head Resting within its Fixture. The Signals are for the C1-axis (upper), C2-axis (middle) and C3-axis (lower).

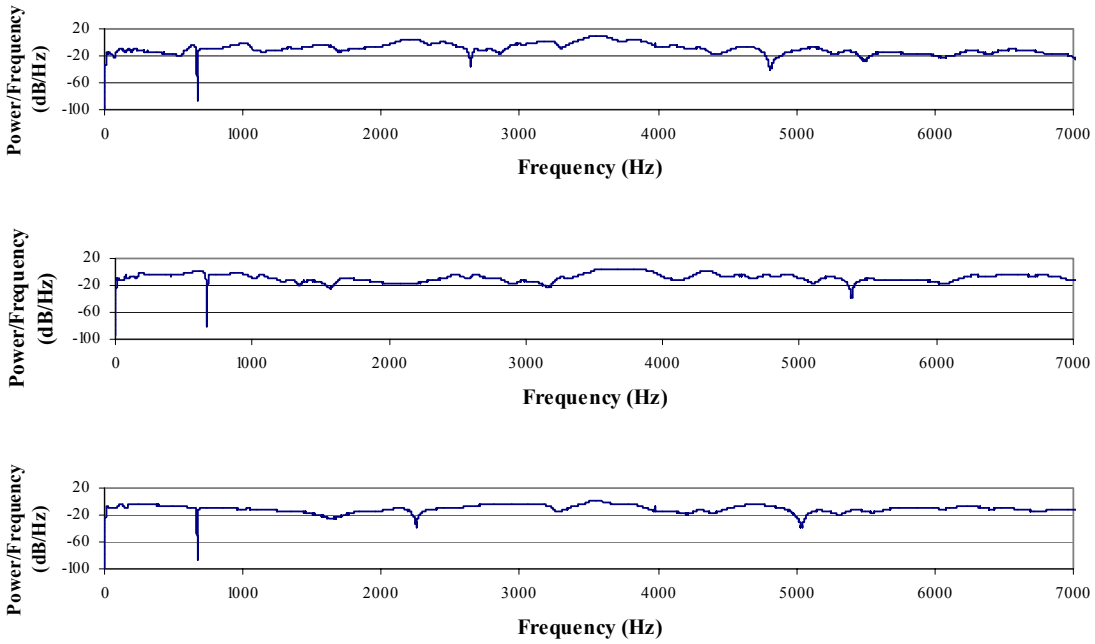

Figure A-35. PSD of a Resonance Test for a Synthetic Femur Implanted with Hip Stem with Ceramic Head Resting within its Fixture. The Signals are for the D1-axis (upper), D2-axis (middle) and D3-axis (lower).

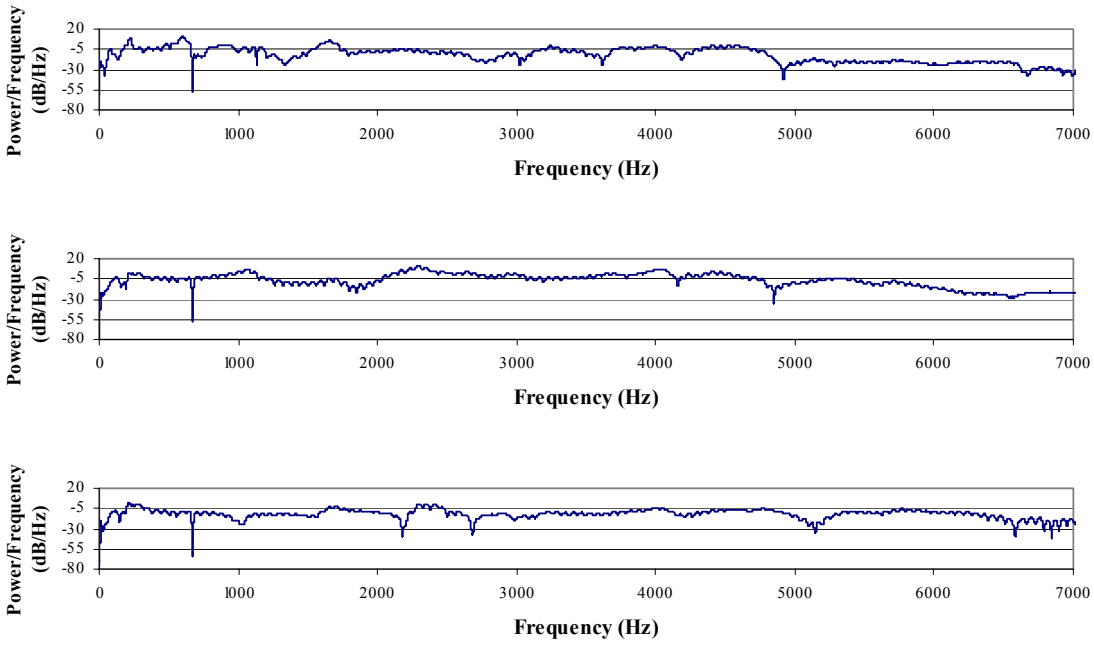

Figure A-36. PSD of a Resonance Test for a Normal Synthetic Femur Resting within its Fixture. The Signals are for the C1-axis (upper), C2-axis (middle) and C3-axis (lower).

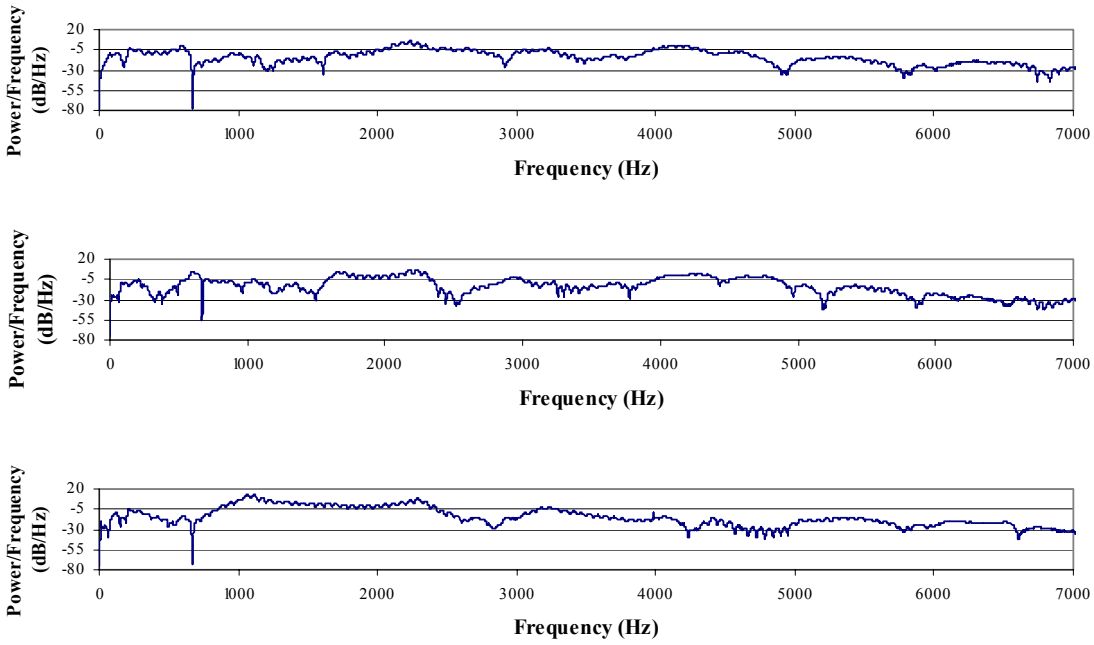

Figure A-37. PSD of a Resonance Test for a Normal Synthetic Femur Resting within its Fixture. The Signals are for the D1-axis (upper), D2-axis (middle) and D3-axis (lower).

Impact Test Acceleration Signals:

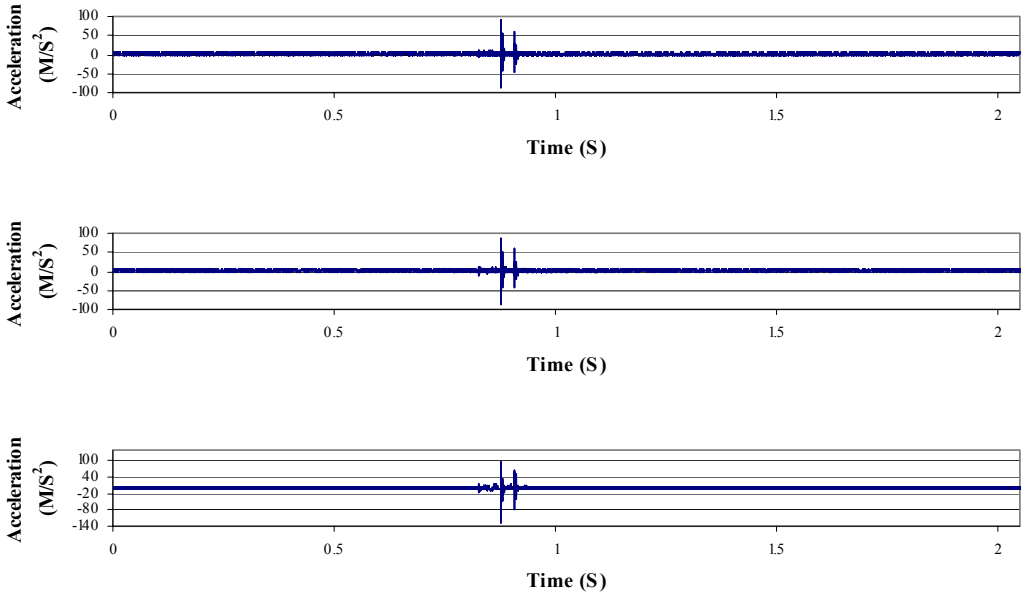

Figure A-38. Acceleration data from the pelvis accelerometer for a metal-on-polyethylene THA, subjected to a 680 Newton impact load. The signals are for the A1-axis (upper), A2-axis (middle) and A3-axis (lower).

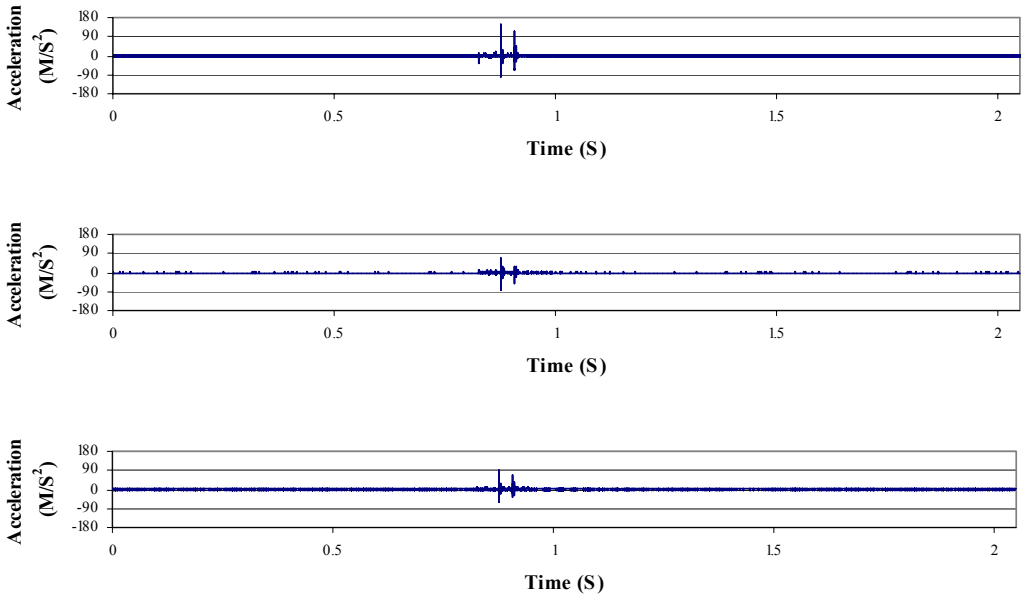

Figure A-39. Acceleration data from the acetabular cup accelerometer for a metal-on-polyethylene THA, subjected to a 680 Newton impact load. The signals are for the B1-axis (upper), B2-axis (middle) and B3-axis (lower).

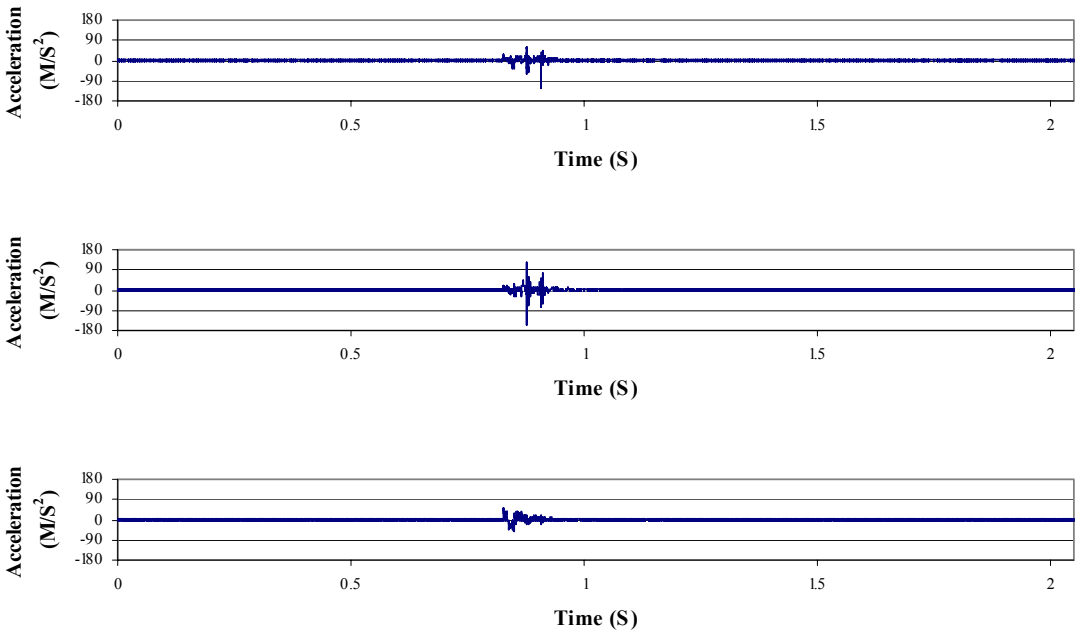

Figure A-40. Acceleration data from the femoral stem accelerometer for a metal-on-polyethylene THA, subjected to a 680 Newton impact load. The signals are for the C1-axis (upper), C2-axis (middle) and C3-axis (lower).

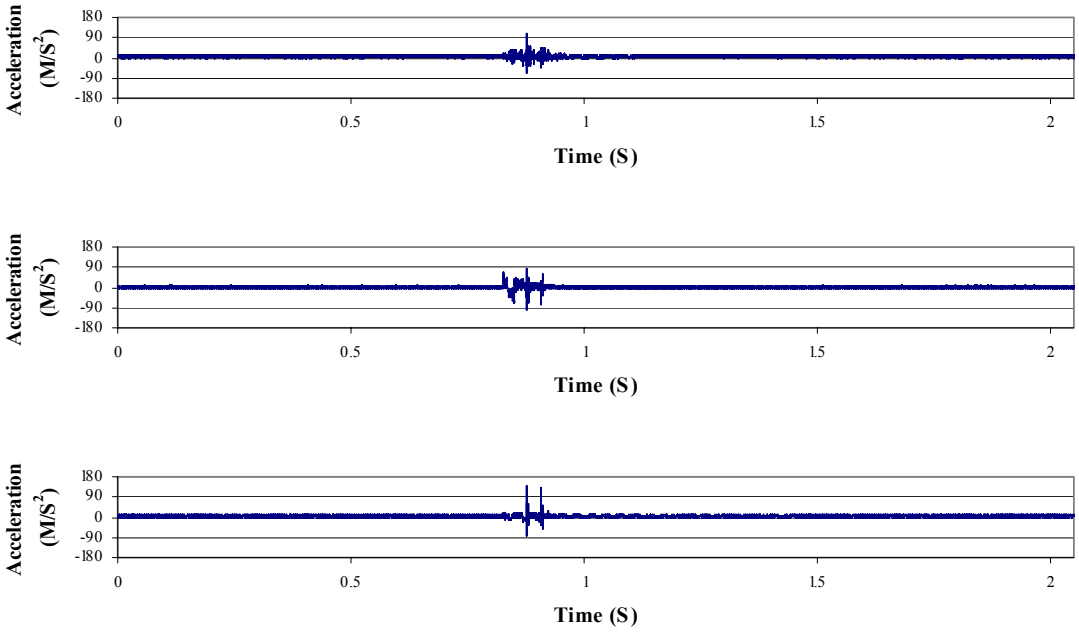

Figure A-41. Acceleration data from the greater trochanter accelerometer for a metal-on-polyethylene THA, subjected to a 680 Newton impact load. The signals are for the D1-axis (upper), D2-axis (middle) and D3-axis (lower).

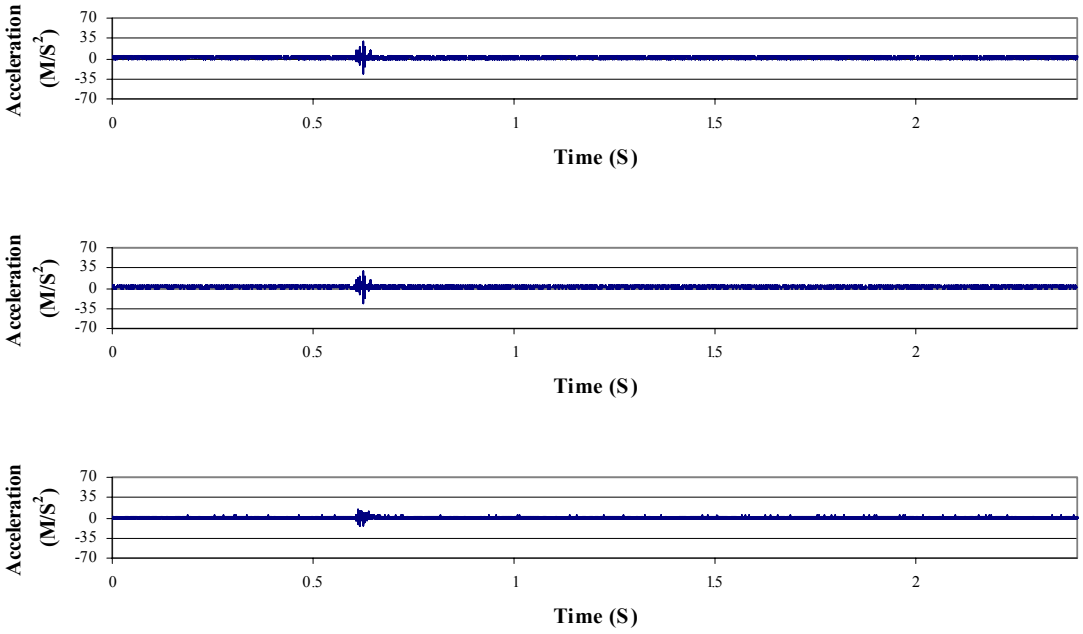

Figure A-42. Acceleration data from the pelvis accelerometer for a metal-on-metal THA, subjected to a 680 Newton impact load. The signals are for the A1-axis (upper), A2-axis (middle) and A3-axis (lower).

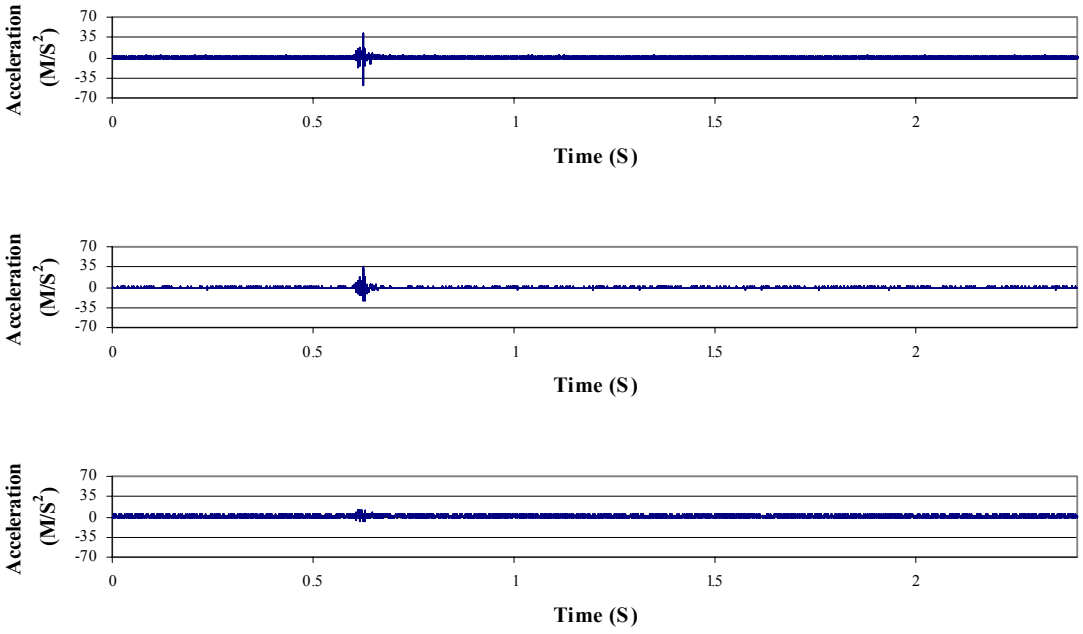

Figure A-43. Acceleration data from the acetabular cup accelerometer for a metal-on-metal THA, subjected to a 680 Newton impact load. The signals are for the B1-axis (upper), B2-axis (middle) and B3-axis (lower).

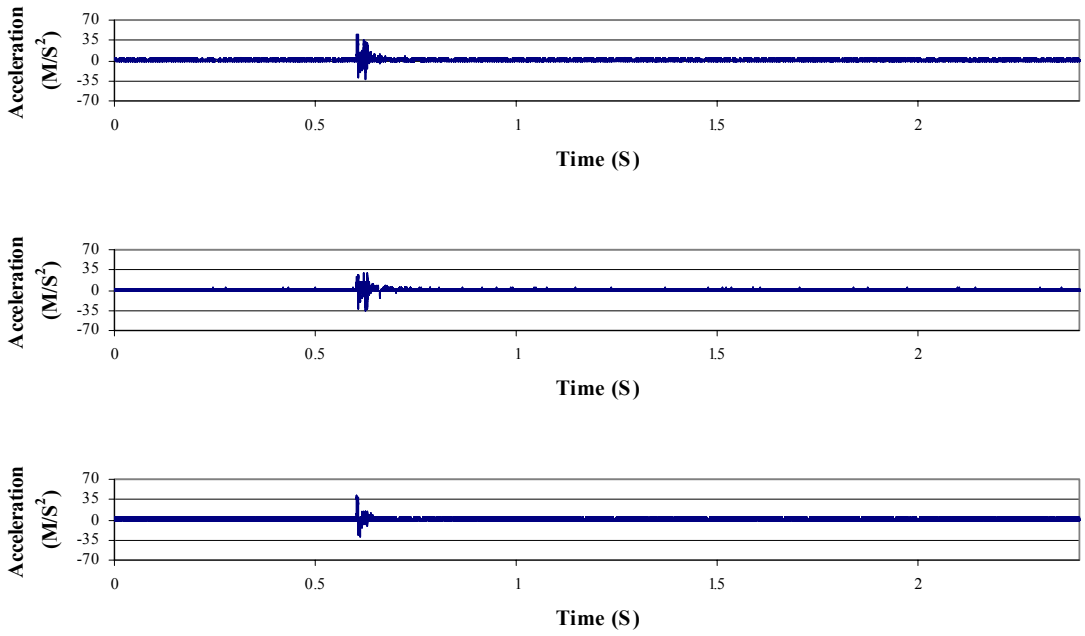

A-44. Acceleration data from the femoral stem accelerometer for a metal-on-metal THA, subjected to a 680 Newton impact load. The signals are for the C1-axis (upper), C2-axis (middle) and C3-axis (lower).

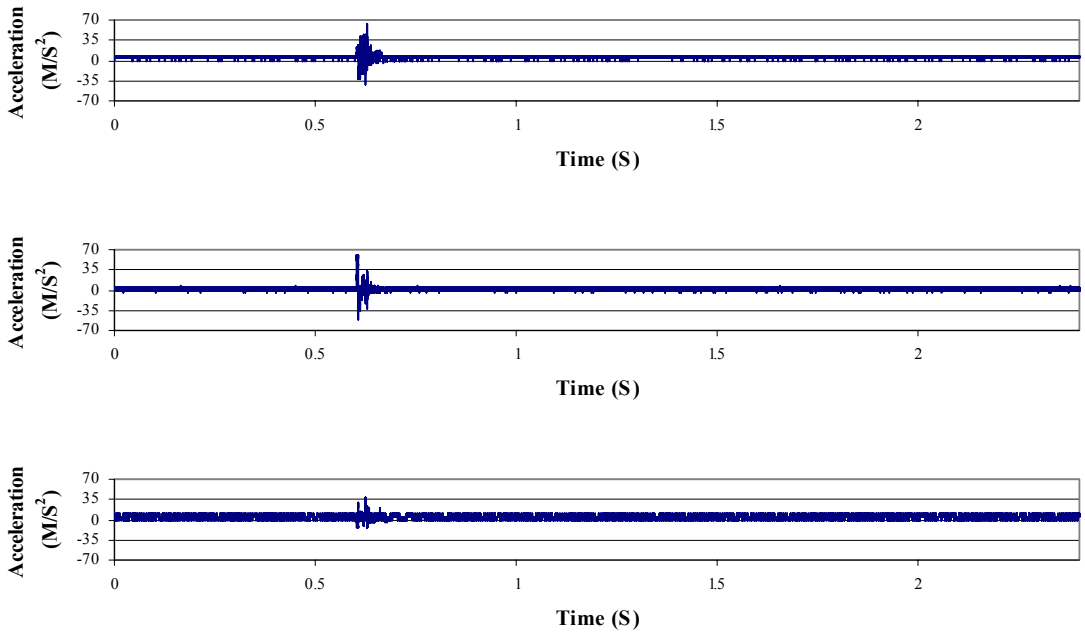

Figure A-45. Acceleration data from the greater trochanter accelerometer for a metal-on-metal THA, subjected to a 680 Newton impact load. The signals are for the D1-axis (upper), D2-axis (middle) and D3-axis (lower).

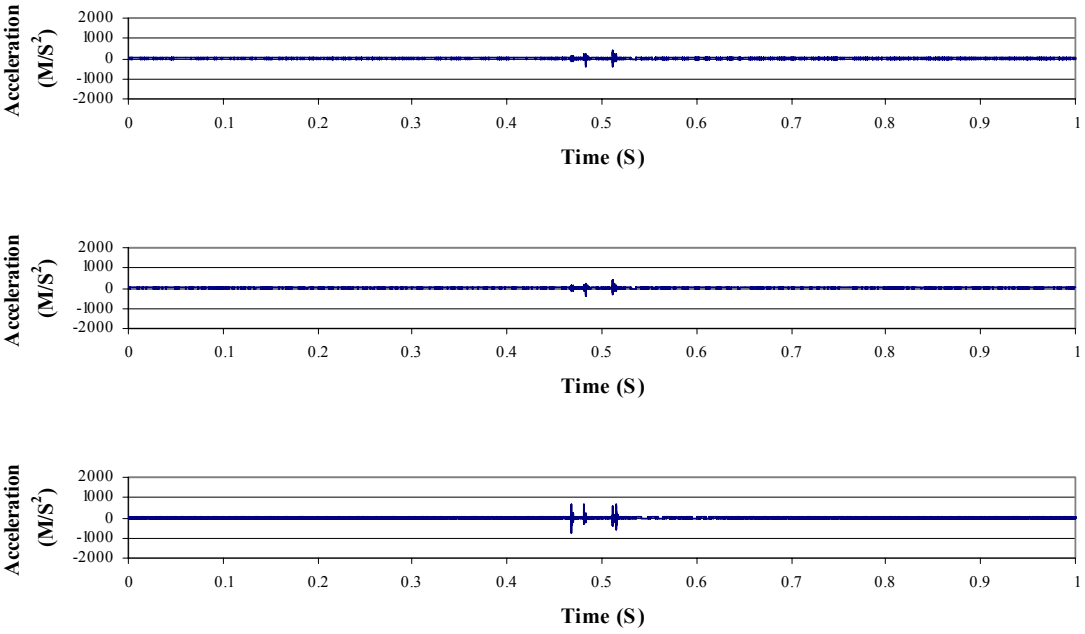

Figure A-46. Acceleration data from the pelvis accelerometer for a ceramic-on-ceramic THA, subjected to a 680 Newton impact load. The signals are for the A1-axis (upper), A2-axis (middle) and A3-axis (lower).

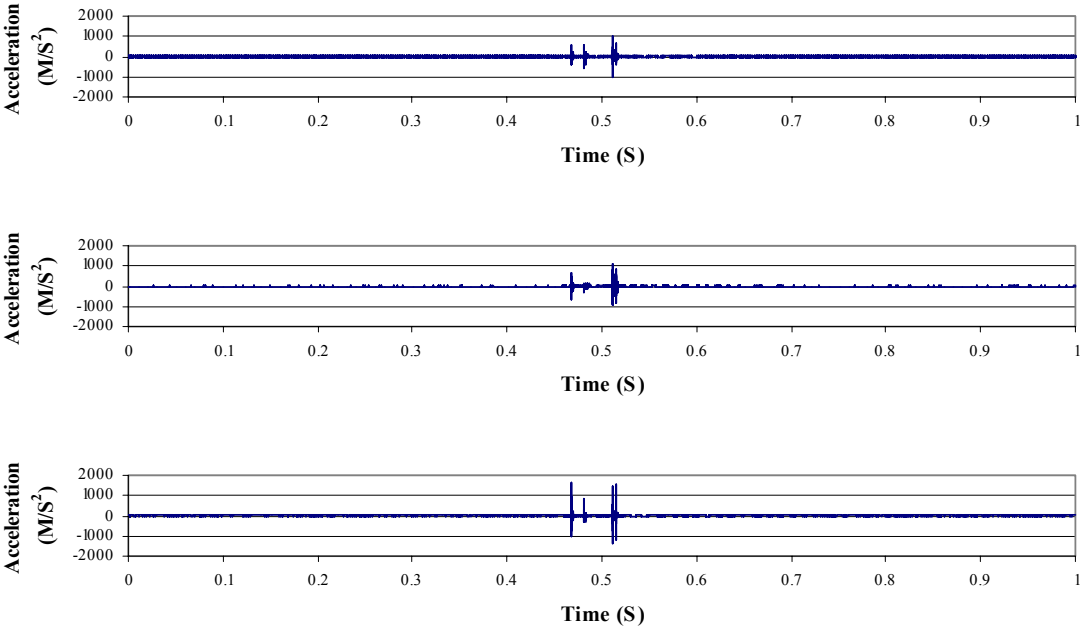

Figure A-47. Acceleration data from the acetabular cup accelerometer for a ceramic-on-ceramic THA, subjected to a 680 Newton impact load. The signals are for the B1-axis (upper), B2-axis (middle) and B3-axis (lower).

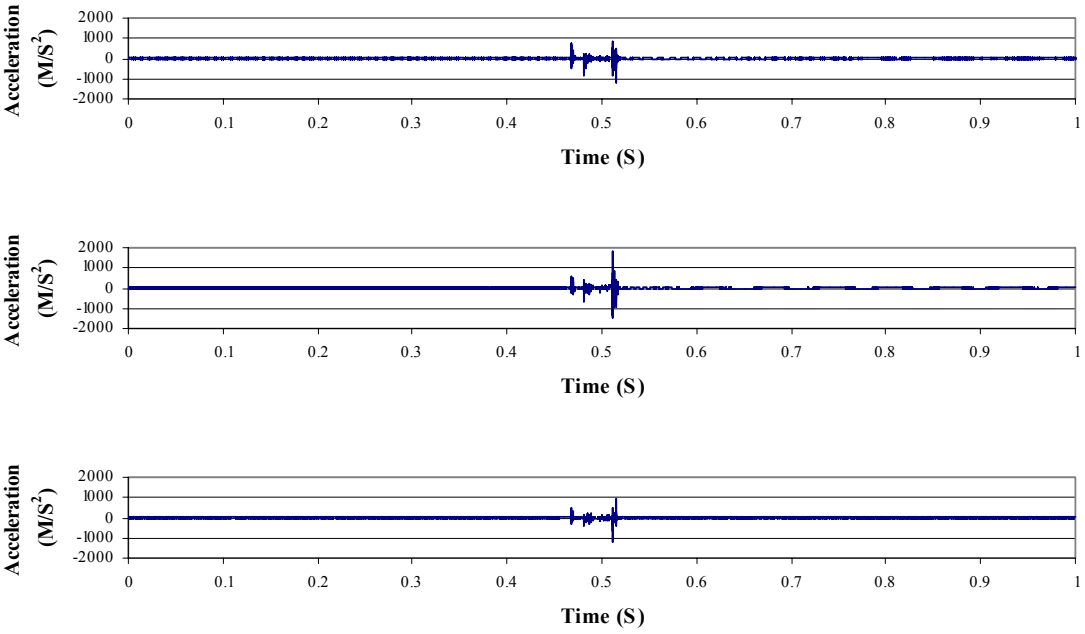

Figure A-48. Acceleration data from the femoral stem accelerometer for a ceramic-on-ceramic THA, subjected to a 680 Newton impact load. The signals are for the C1-axis (upper), C2-axis (middle) and C3-axis (lower).

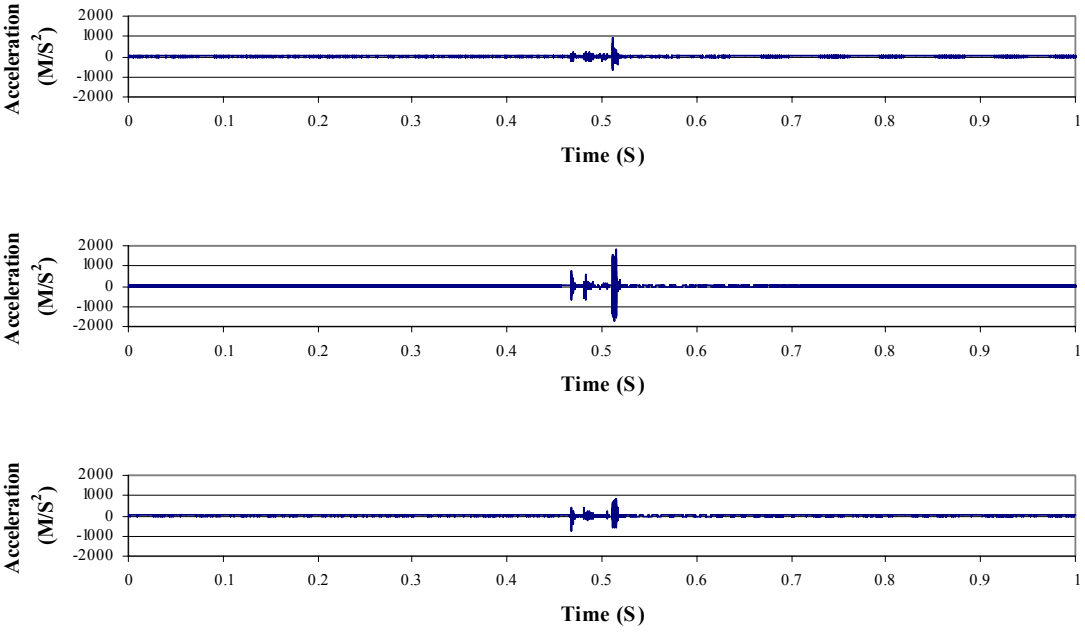

Figure A-49. Acceleration data from the greater trochanter accelerometer for a ceramic-on-ceramic THA, subjected to a 680 Newton impact load. The signals are for the D1-axis (upper), D2-axis (middle) and D3-axis (lower).

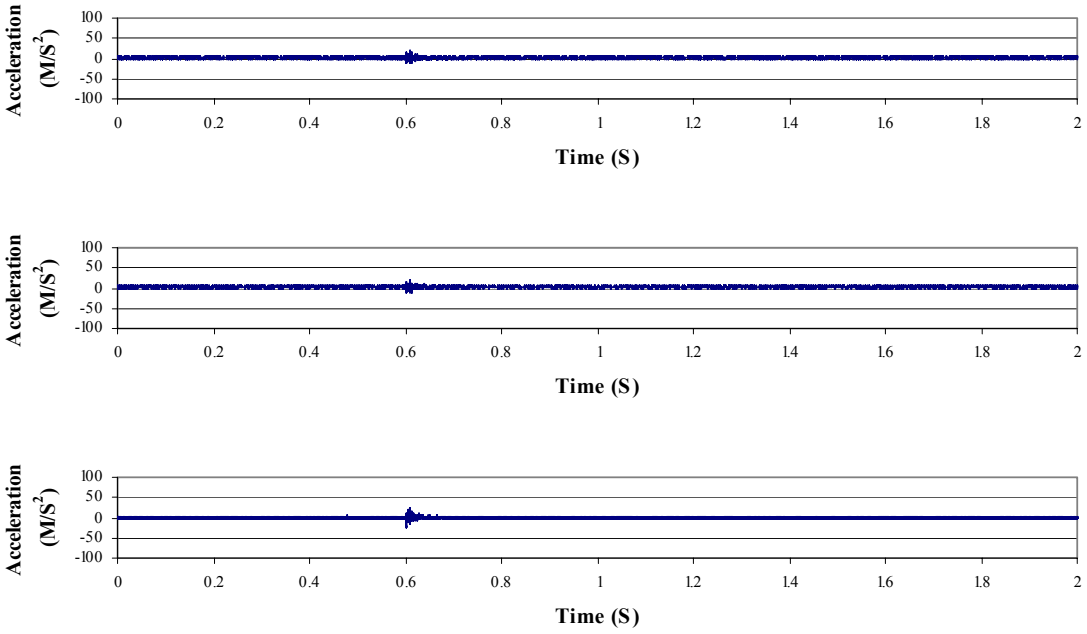

Figure A-50. Acceleration data from the pelvis accelerometer for a metal-on-polyethylene THA, subjected to an 1150 Newton impact load. The signals are for the A1-axis (upper), A2-axis (middle) and A3-axis (lower).

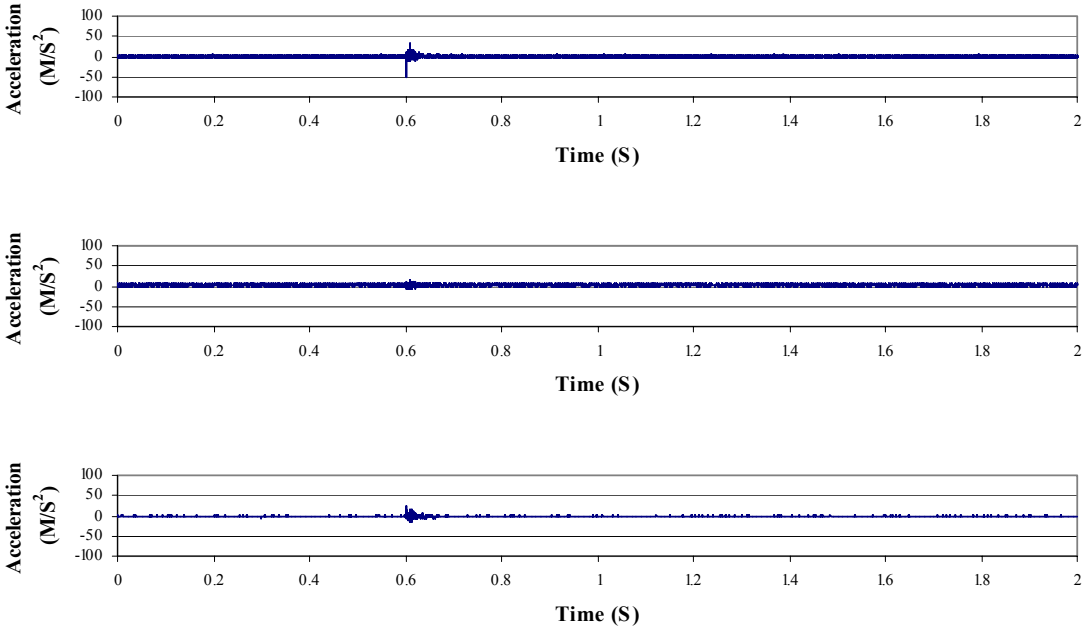

Figure A-51. Acceleration data from the acetabular cup accelerometer for a metal-on-polyethylene THA, subjected to an 1150 Newton impact load. The signals are for the B1-axis (upper), B2-axis (middle) and B3-axis (lower).

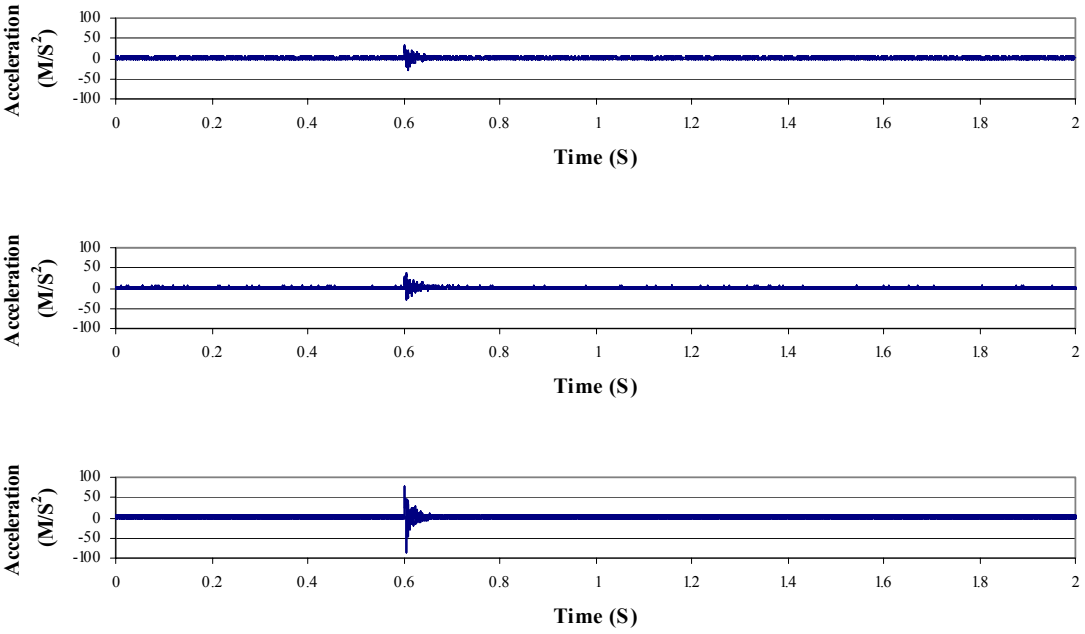

Figure A-52. Acceleration data from the femoral stem accelerometer for a metal-on-polyethylene THA, subjected to an 1150 Newton impact load. The signals are for the C1-axis (upper), C2-axis (middle) and C3-axis (lower).

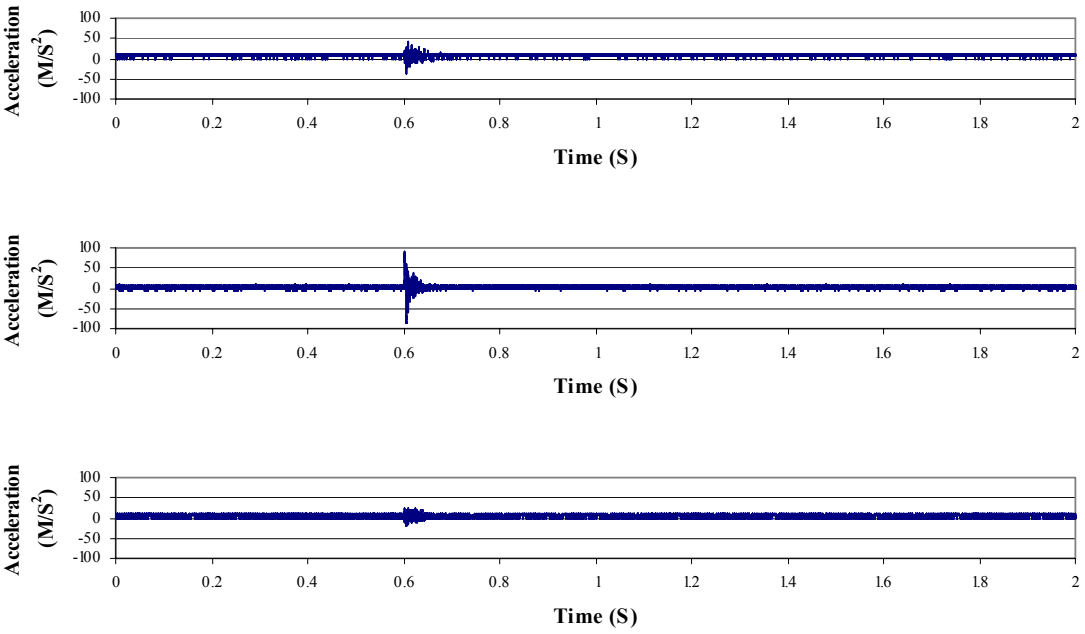

Figure A-53. Acceleration data from the greater trochanter accelerometer for a metal-on-polyethylene THA, subjected to an 1150 Newton impact load. The signals are for the D1-axis (upper), D2-axis (middle) and D3-axis (lower).

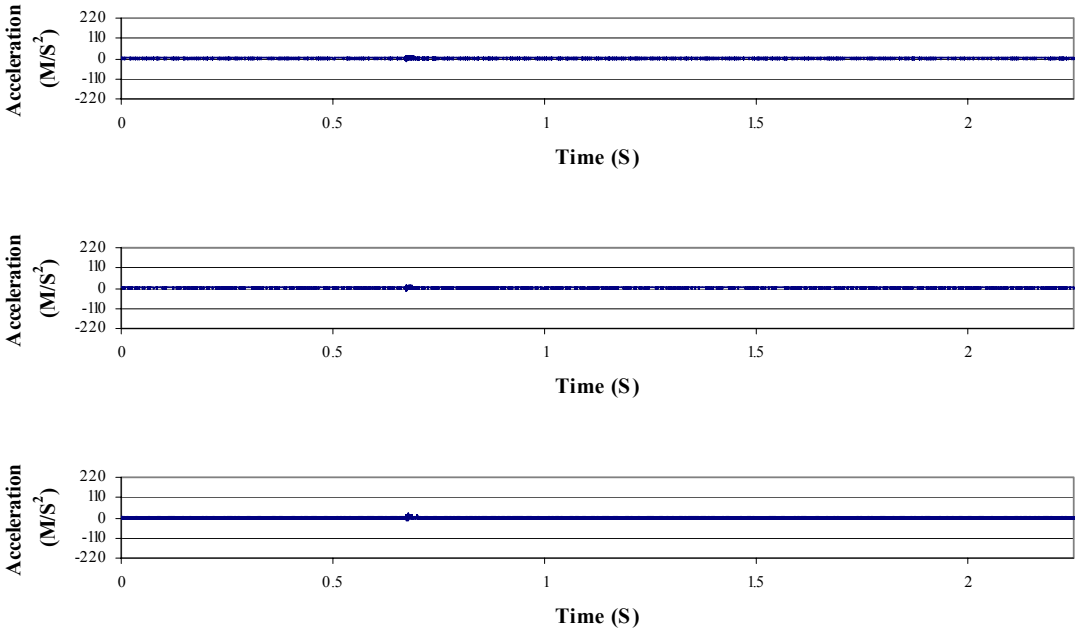

Figure A-54. Acceleration data from the pelvis accelerometer for a metal-on-metal THA, subjected to an 1150 Newton impact load. The signals are for the A1-axis (upper), A2-axis (middle) and A3-axis (lower).

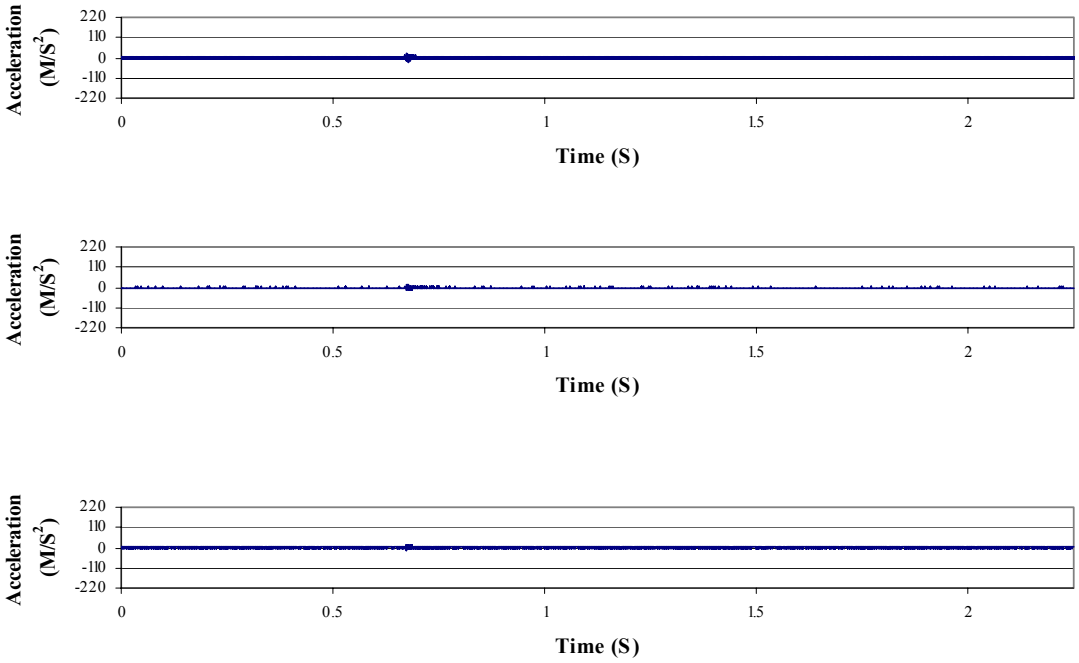

Figure A-55. Acceleration data from the acetabular cup accelerometer for a metal-on-metal THA, subjected to an 1150 Newton impact load. The signals are for the B1-axis (upper), B2-axis (middle) and B3-axis (lower).

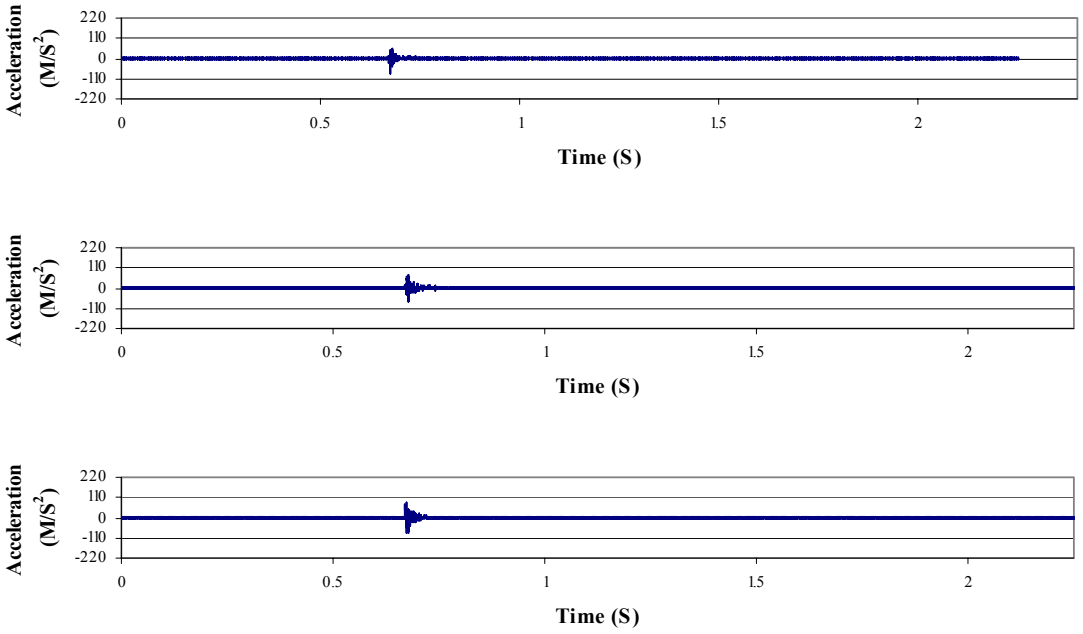

Figure A-56. Acceleration data from the femoral stem accelerometer for a metal-on-metal THA, subjected to an 1150 Newton impact load. The signals are for the C1-axis (upper), C2-axis (middle) and C3-axis (lower).

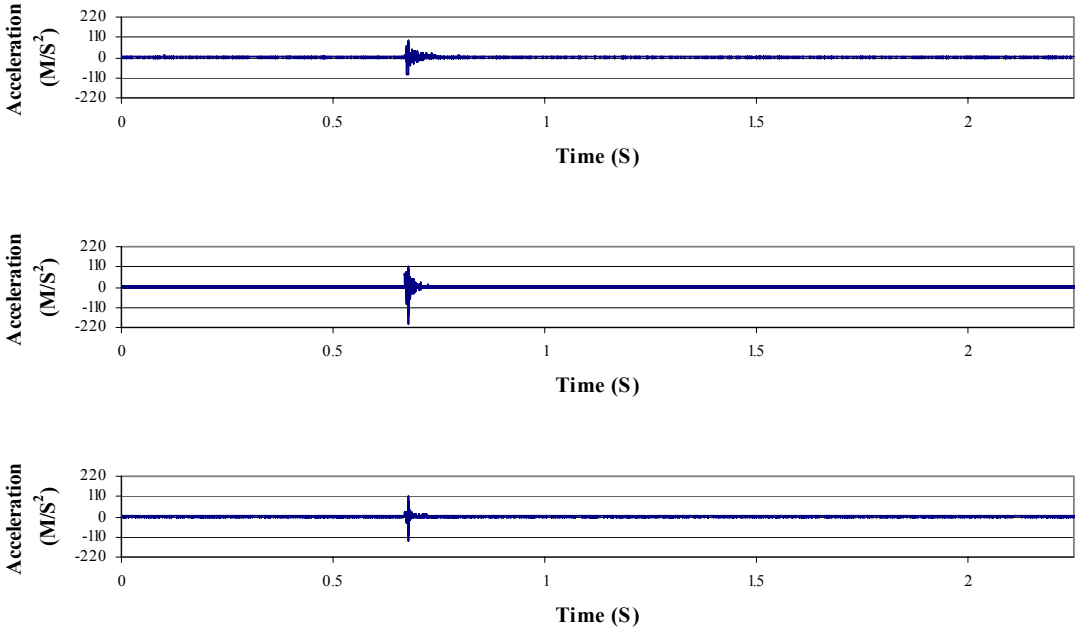

Figure A-57. Acceleration data from the greater trochanter accelerometer for a metal-on-metal THA, subjected to an 1150 Newton impact load. The signals are for the D1-axis (upper), D2-axis (middle) and D3-axis (lower).

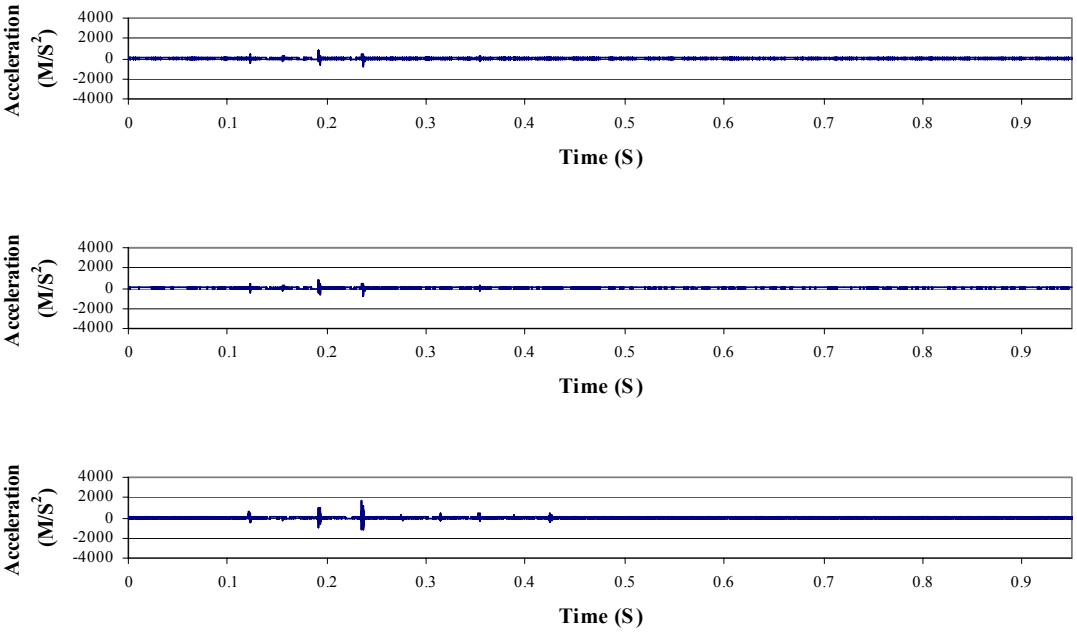

Figure A-58. Acceleration data from the pelvis accelerometer for a ceramic-on-ceramic THA, subjected to an 1150 Newton impact load. The signals are for the A1-axis (upper), A2-axis (middle) and A3-axis (lower).

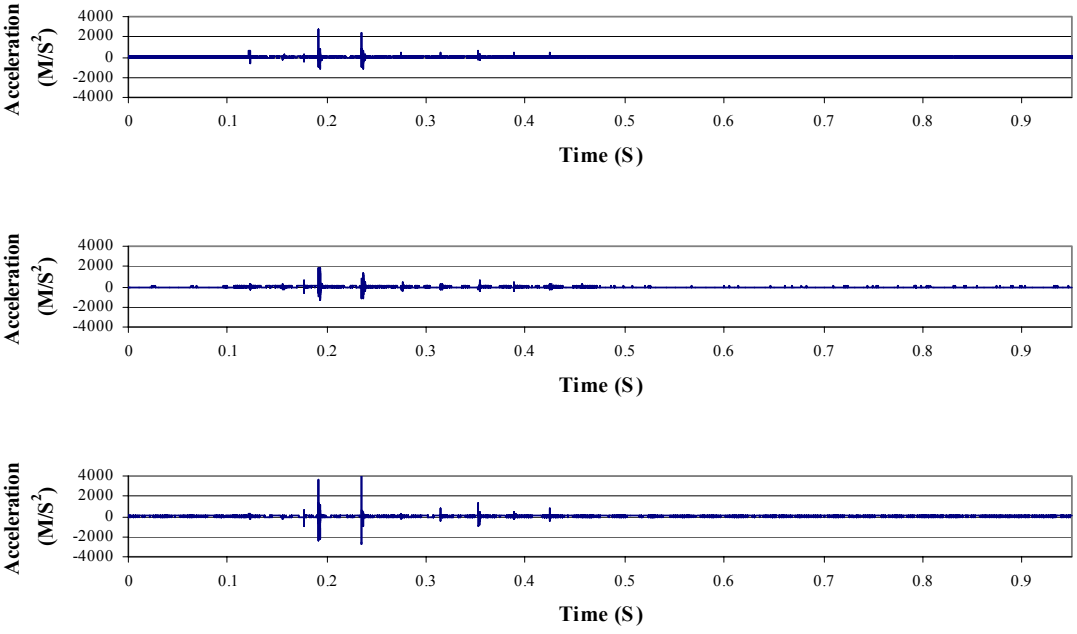

Figure A-59. Acceleration data from the acetabular cup accelerometer for a ceramic-on-ceramic THA, subjected to an 1150 Newton impact load. The signals are for the B1-axis (upper), B2-axis (middle) and B3-axis (lower).

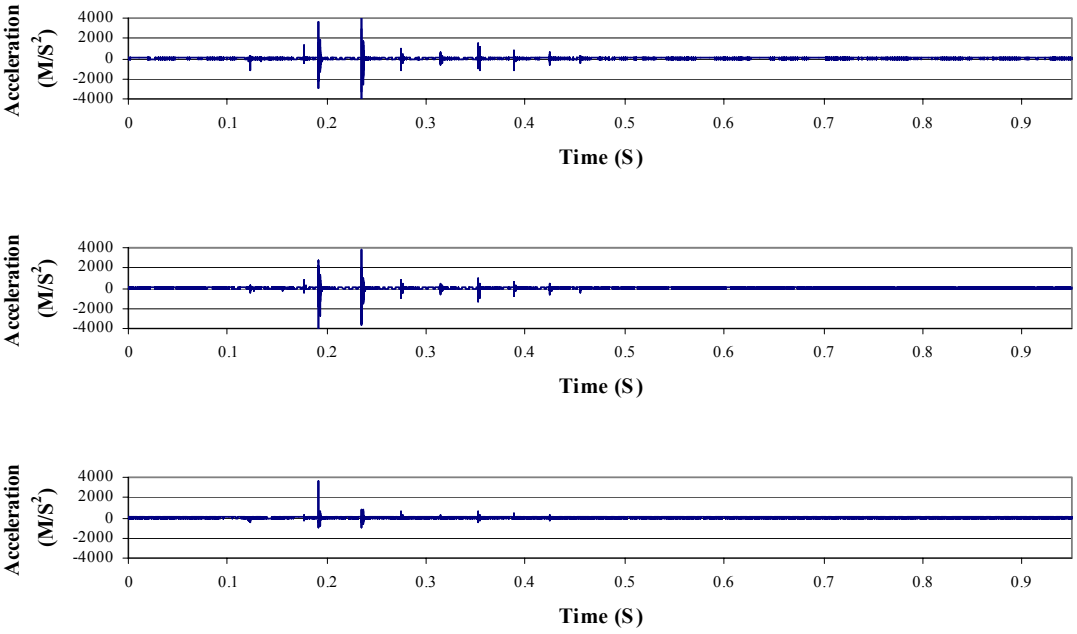

Figure A-60. Acceleration data from the femoral stem accelerometer for a ceramic-on-ceramic THA, subjected to an 1150 Newton impact load. The signals are for the C1-axis (upper), C2-axis (middle) and C3-axis (lower).

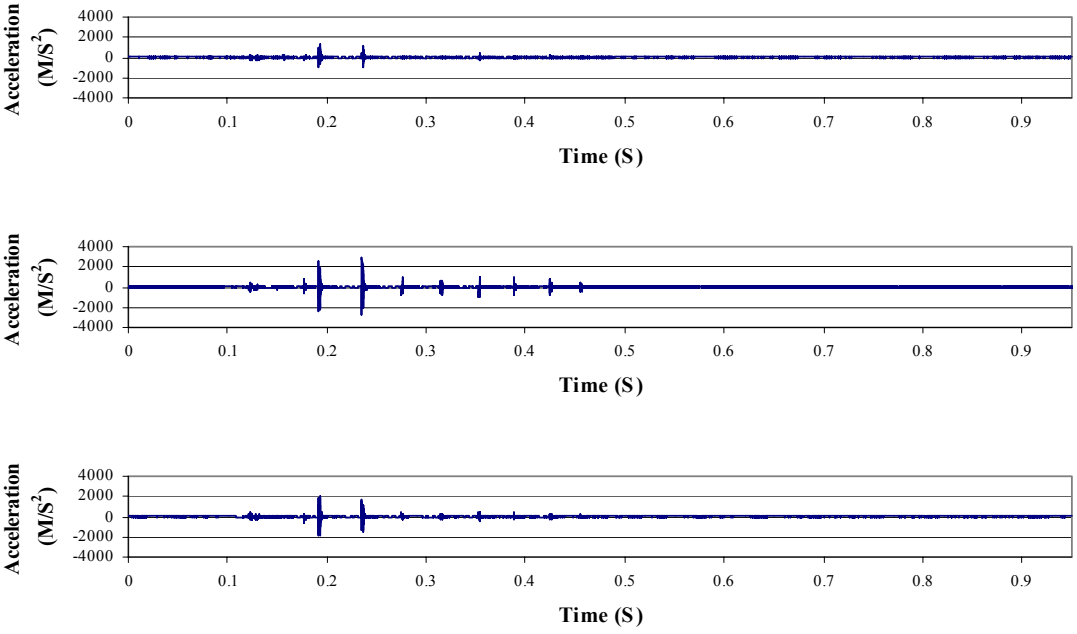

Figure A-61. Acceleration data from the greater trochanter accelerometer for a ceramic-on-ceramic THA, subjected to an 1150 Newton impact load. The signals are for the D1-axis (upper), D2-axis (middle) and D3-axis (lower).

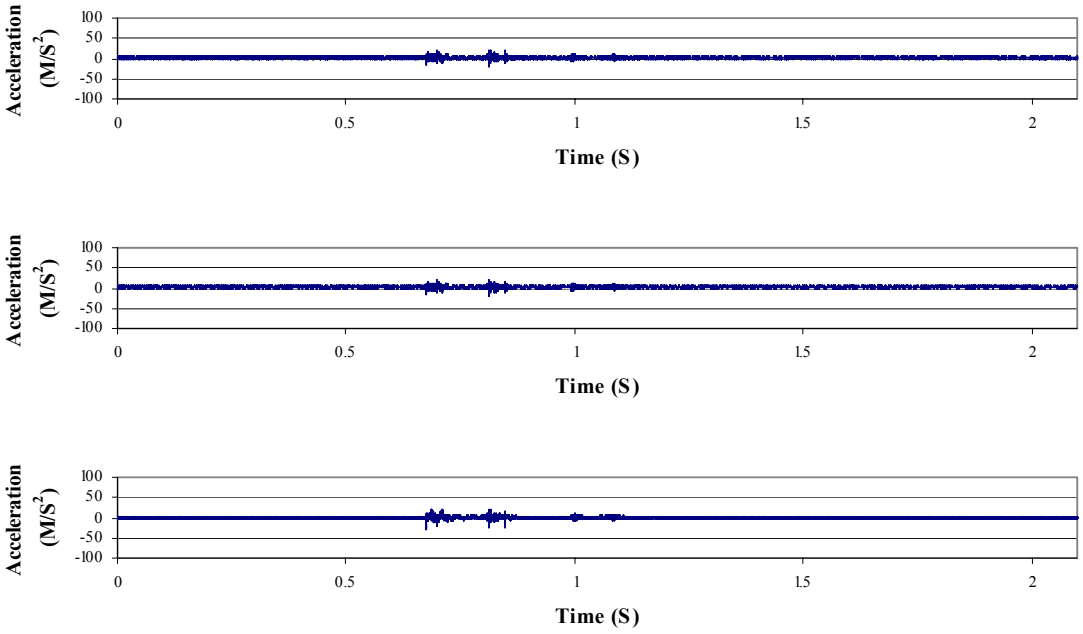

Figure A-62. Acceleration data from the pelvis accelerometer for a metal-on-polyethylene THA, subjected to a 1280 Newton impact load. The signals are for the A1-axis (upper), A2-axis (middle) and A3-axis (lower).

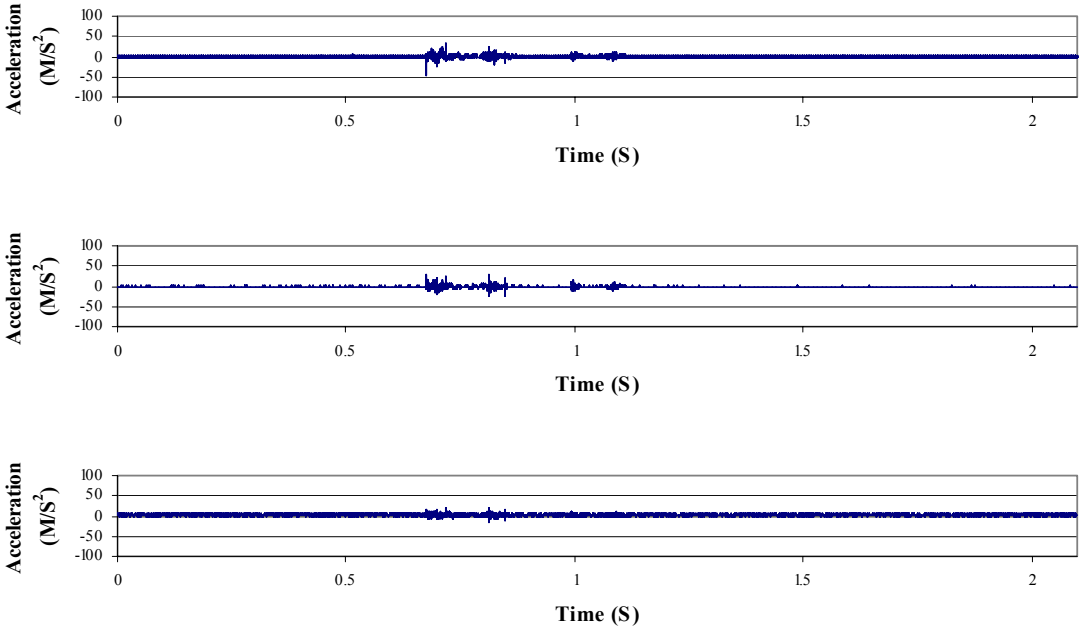

Figure A-63. Acceleration data from the acetabular cup accelerometer for a metal-on-polyethylene THA, subjected to a 1280 Newton impact load. The signals are for the B1-axis (upper), B2-axis (middle) and B3-axis (lower).

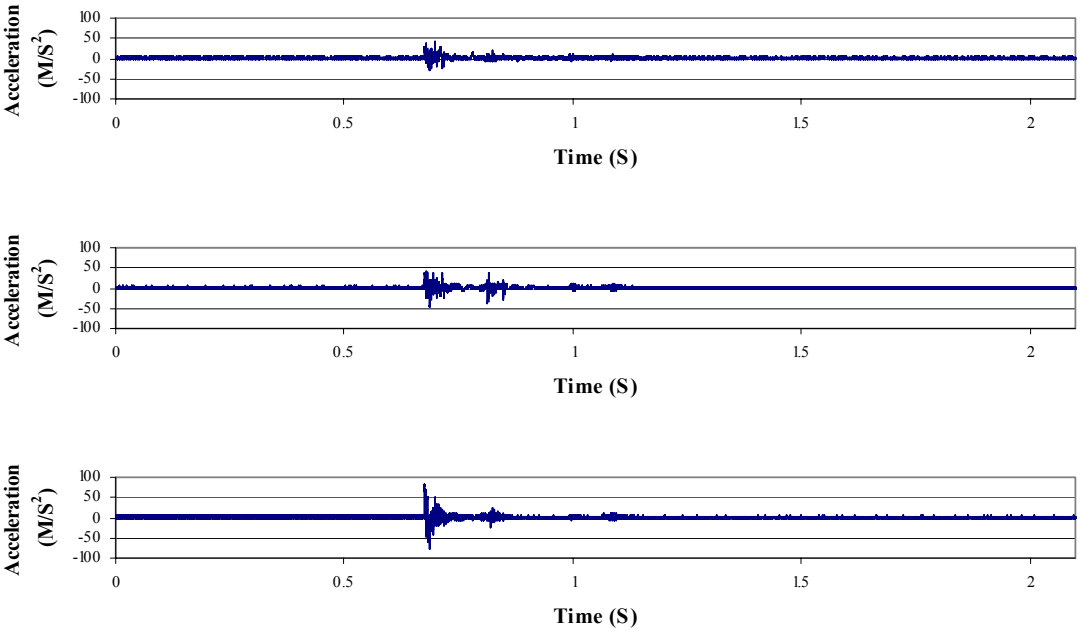

Figure A-64. Acceleration data from the femoral stem accelerometer for a metal-on-polyethylene THA, subjected to a 1280 Newton impact load. The signals are for the C1-axis (upper), C2-axis (middle) and C3-axis (lower).

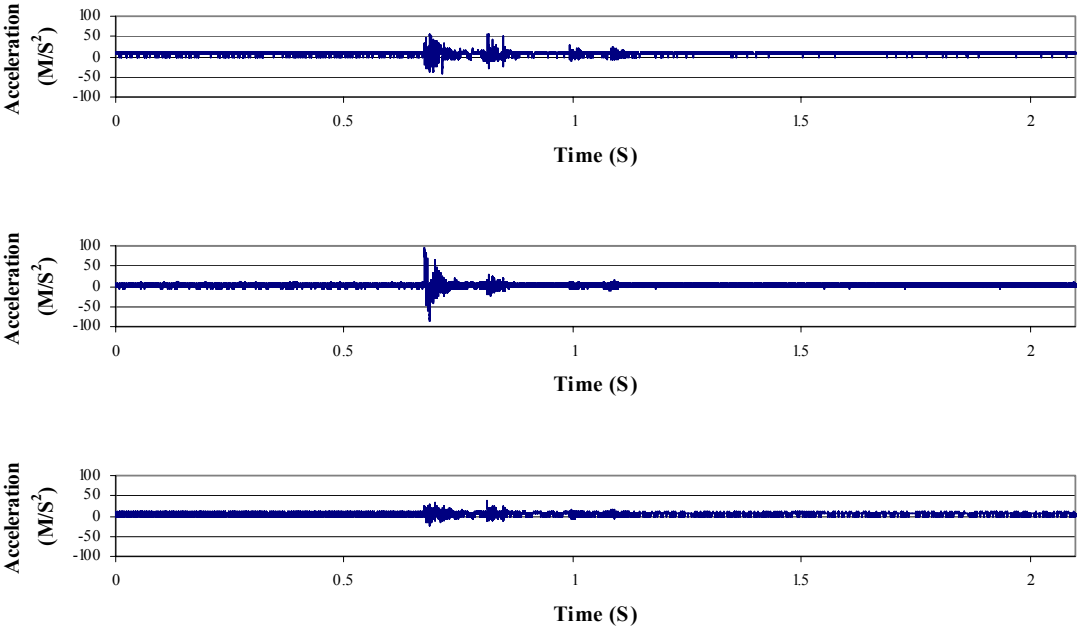

Figure A-65. Acceleration data from the greater trochanter accelerometer for a metal-on-polyethylene THA, subjected to a 1280 Newton impact load. The signals are for the D1-axis (upper), D2-axis (middle) and D3-axis (lower).

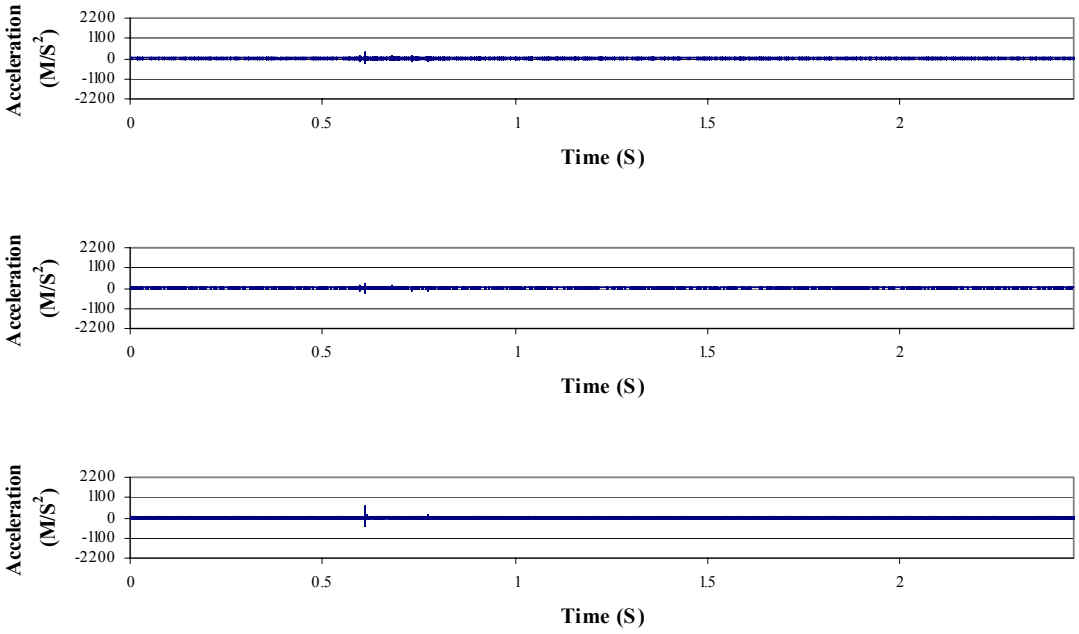

Figure A-66. Acceleration data from the pelvis accelerometer for a metal-on-metal THA, subjected to a 1280 Newton impact load. The signals are for the A1-axis (upper), A2-axis (middle) and A3-axis (lower).

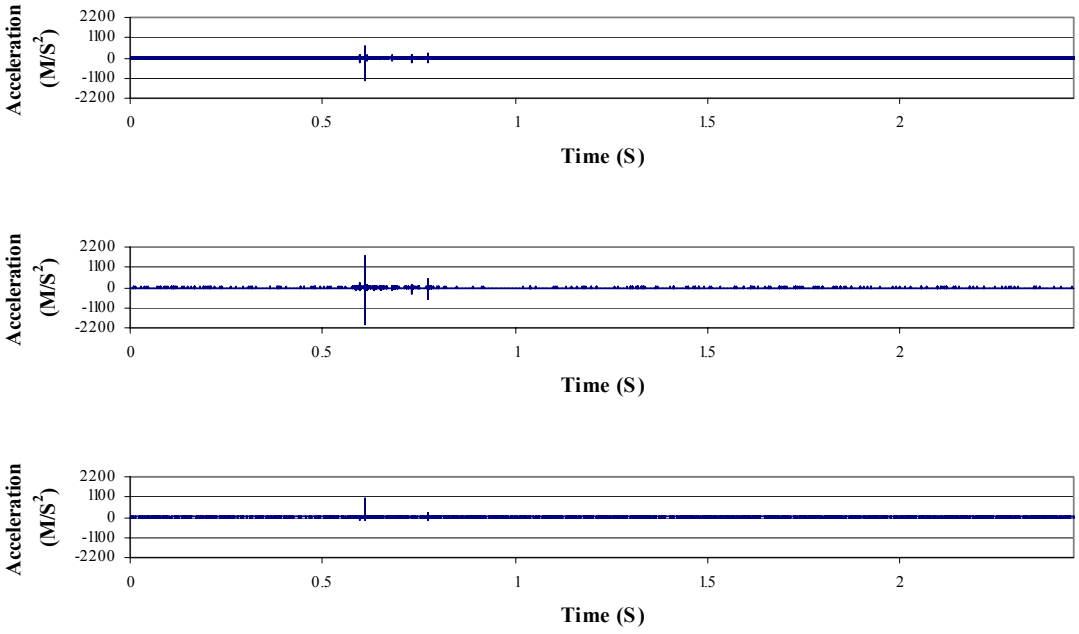

Figure A-67. Acceleration data from the acetabular cup accelerometer for a metal-on-metal THA, subjected to a 1280 Newton impact load. The signals are for the B1-axis (upper), B2-axis (middle) and B3-axis (lower).

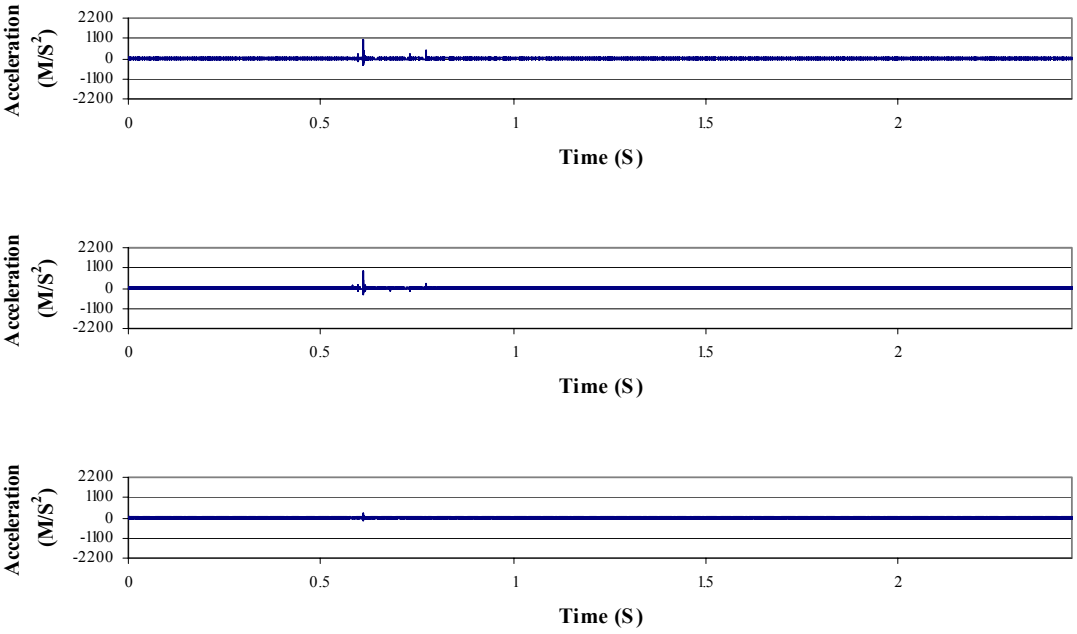

Figure A-68. Acceleration data from the femoral stem accelerometer for a metal-on-metal THA, subjected to a 1280 Newton impact load. The signals are for the C1-axis (upper), C2-axis (middle) and C3-axis (lower).

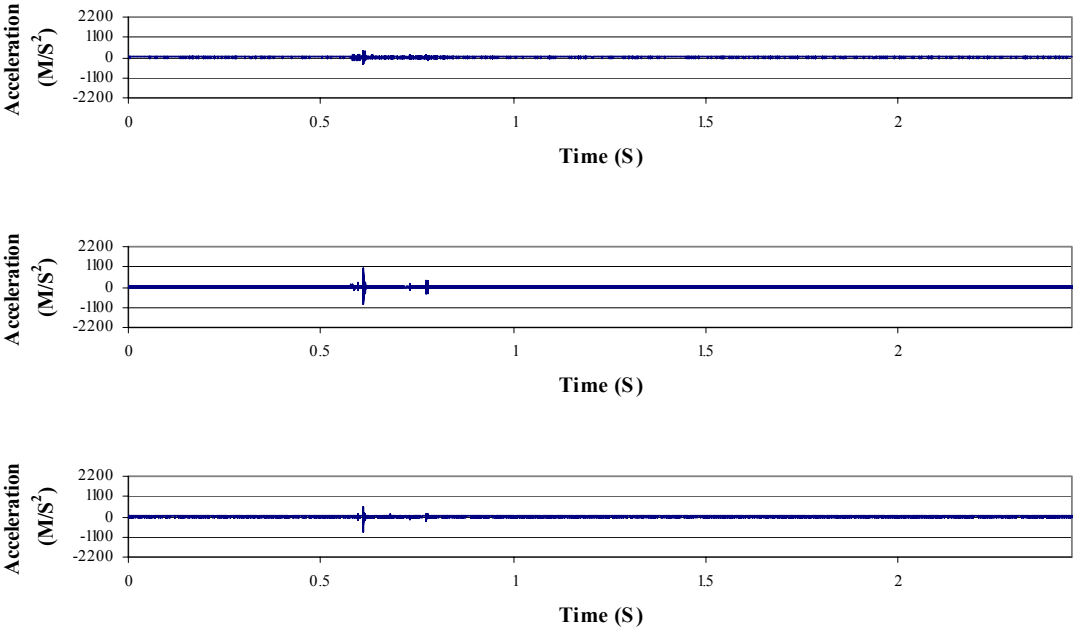

Figure A-69. Acceleration data from the greater trochanter accelerometer for a metal-on-metal THA, subjected to a 1280 Newton impact load. The signals are for the D1-axis (upper), D2-axis (middle) and D3-axis (lower).

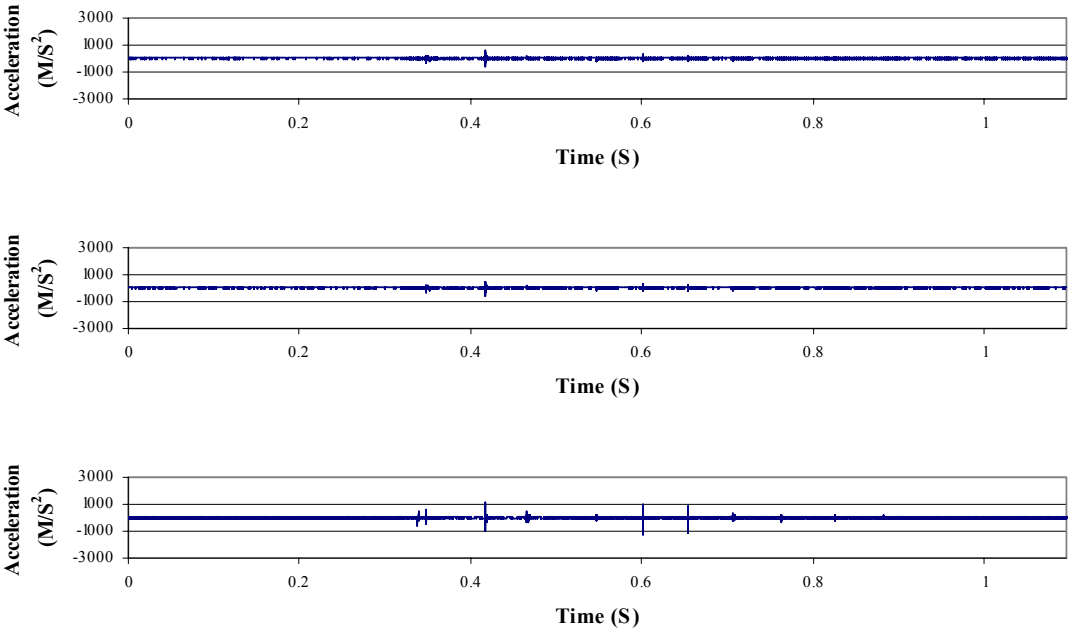

Figure A-70. Acceleration data from the pelvis accelerometer for a ceramic-on-ceramic THA, subjected to a 1280 Newton impact load. The signals are for the A1-axis (upper), A2-axis (middle) and A3-axis (lower).

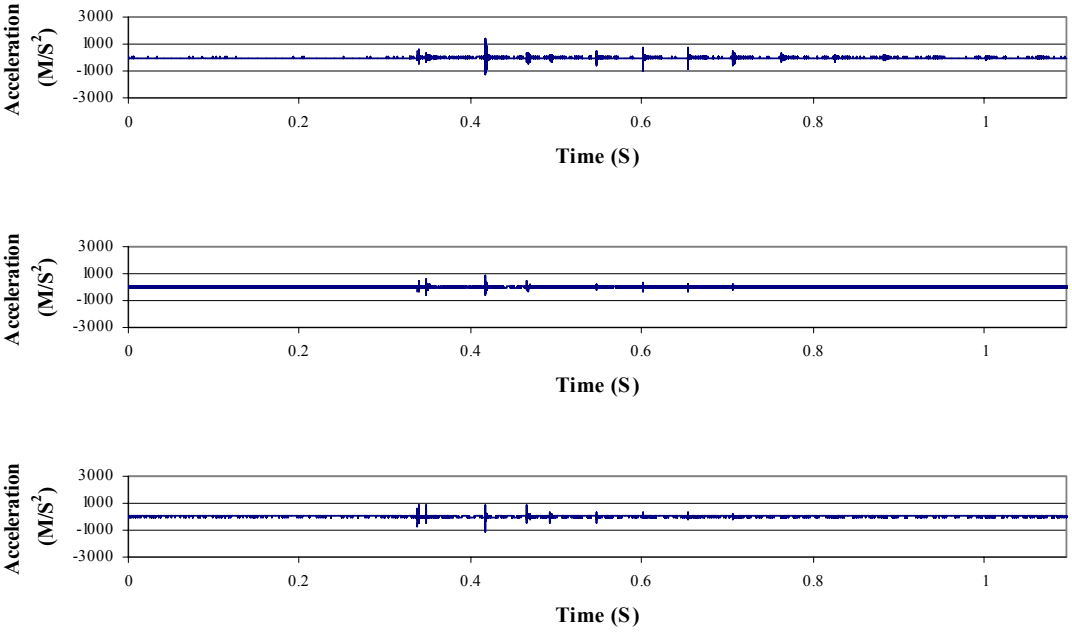

Figure A-71. Acceleration data from the acetabular cup accelerometer for a ceramic-on-ceramic THA, subjected to a 1280 Newton impact load. The signals are for the B1-axis (upper), B2-axis (middle) and B3-axis (lower).

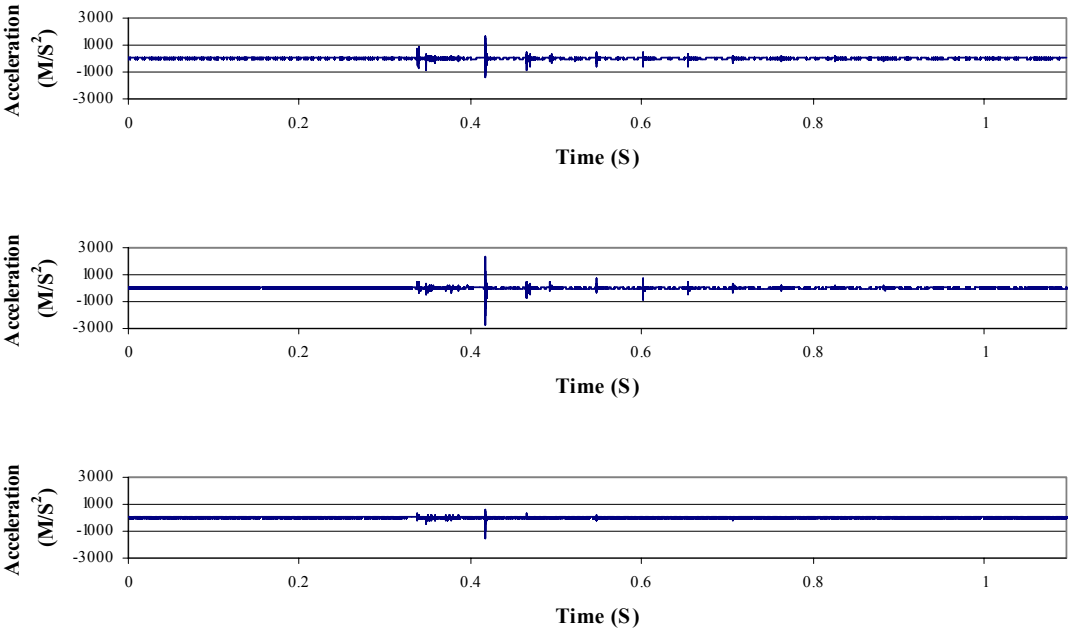

Figure A-72. Acceleration data from the femoral stem accelerometer for a ceramic-on-ceramic THA, subjected to a 1280 Newton impact load. The signals are for the C1-axis (upper), C2-axis (middle) and C3-axis (lower).

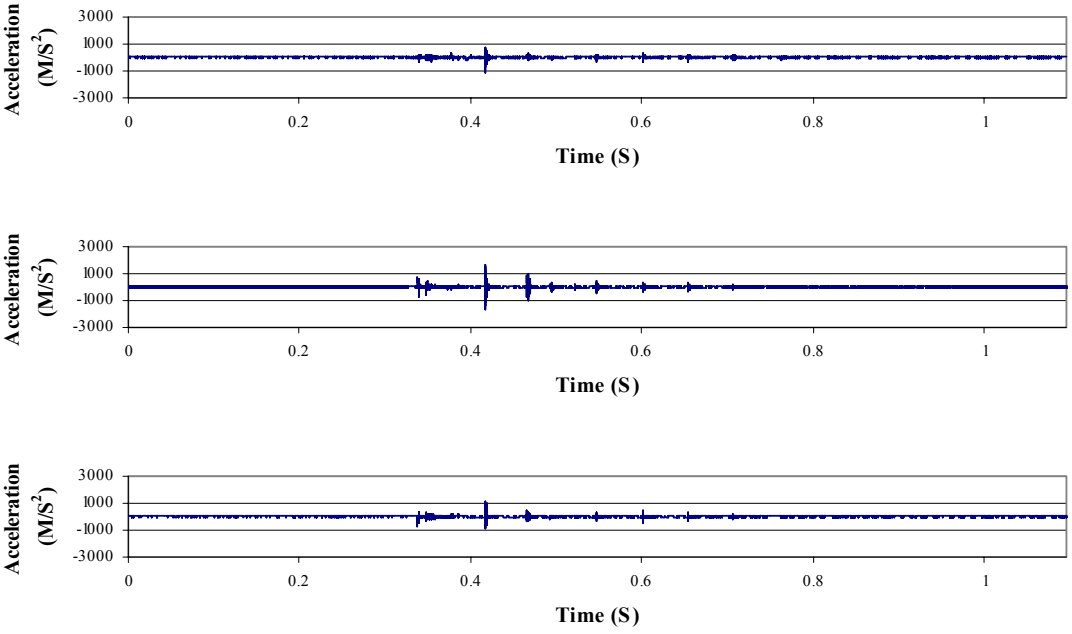

Figure A-73. Acceleration data from the greater trochanter accelerometer for a ceramic-on-ceramic THA, subjected to a 1280 Newton impact load. The signals are for the D1-axis (upper), D2-axis (middle) and D3-axis (lower).

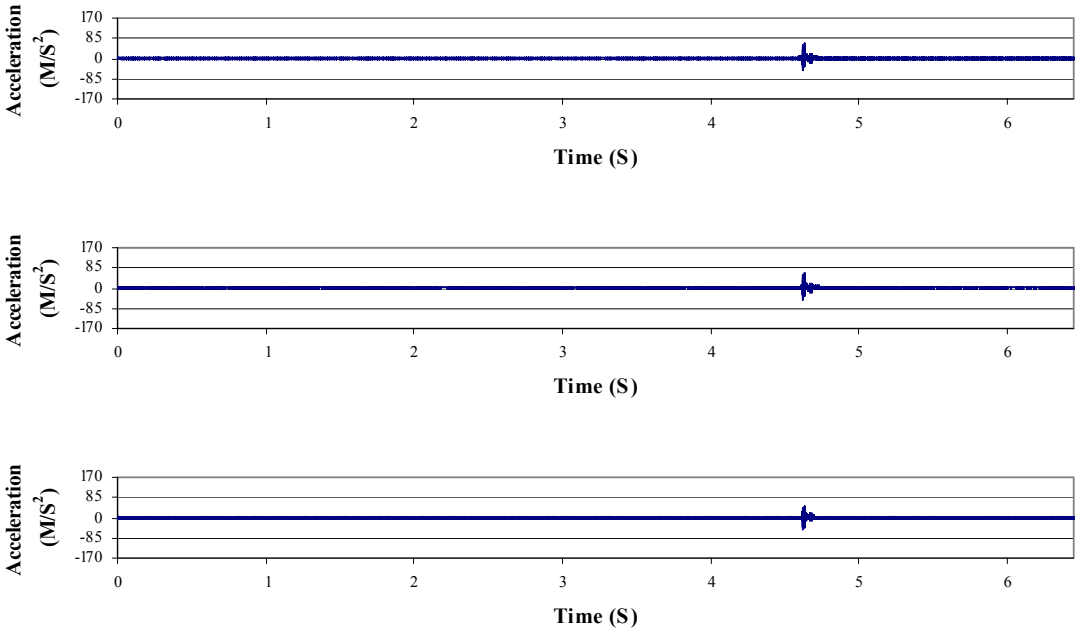

Figure A-74. Acceleration data from the pelvis accelerometer for a metal-on-polyethylene THA, subjected to a 1500 Newton impact load. The signals are for the A1-axis (upper), A2-axis (middle) and A3-axis (lower).

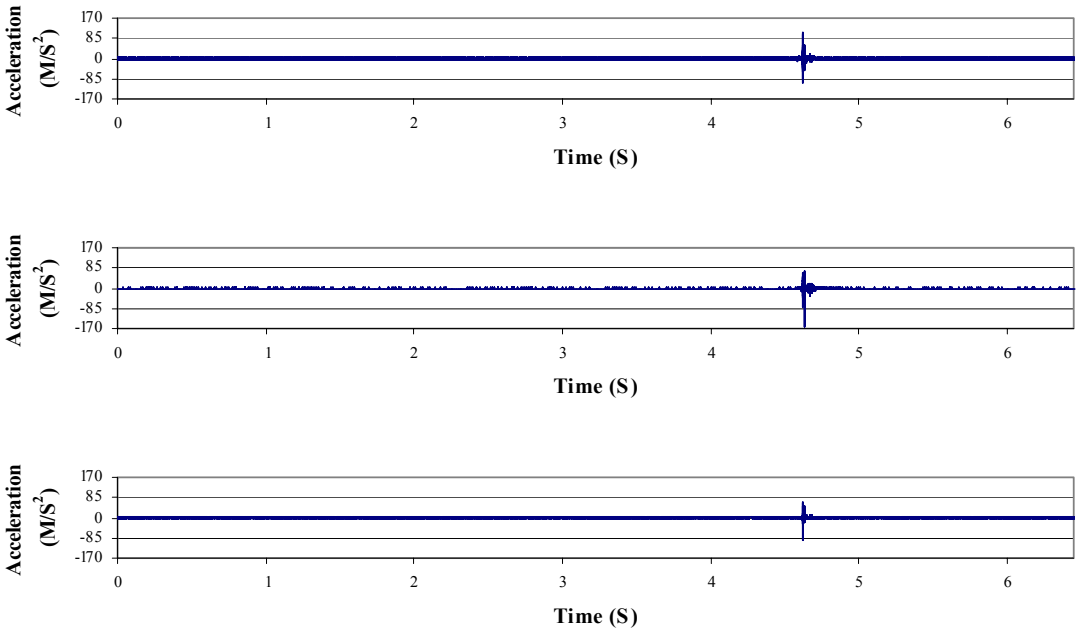

Figure A-75. Acceleration data from the acetabular cup accelerometer for a metal-on-polyethylene THA, subjected to a 1500 Newton impact load. The signals are for the B1-axis (upper), B2-axis (middle) and B3-axis (lower).

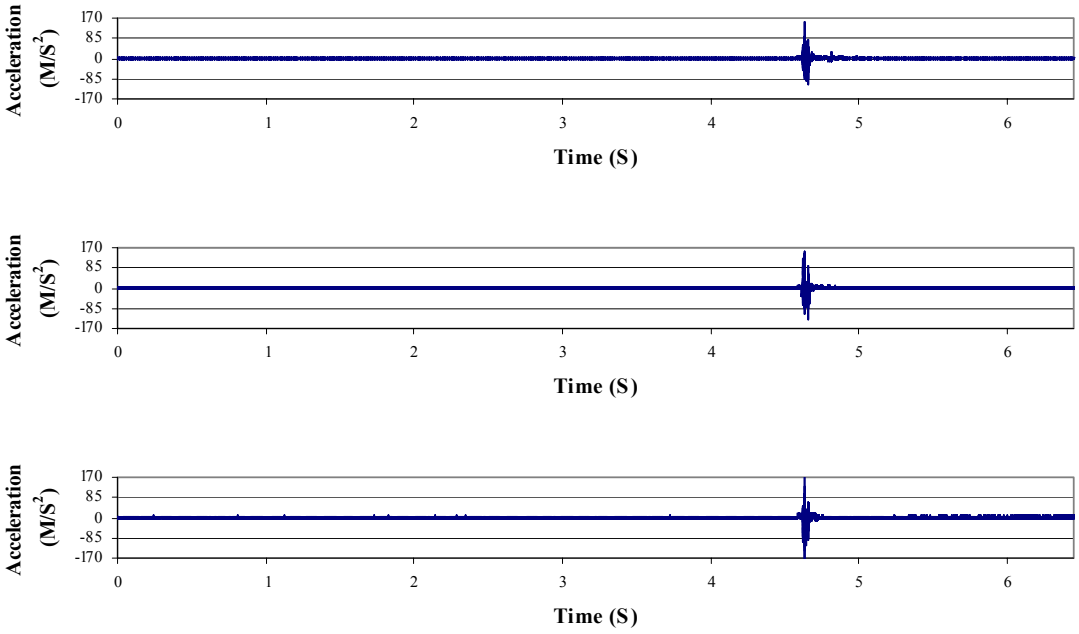

Figure A-76. Acceleration data from the femoral stem accelerometer for a metal-on-polyethylene THA, subjected to a 1500 Newton impact load. The signals are for the C1-axis (upper), C2-axis (middle) and C3-axis (lower).

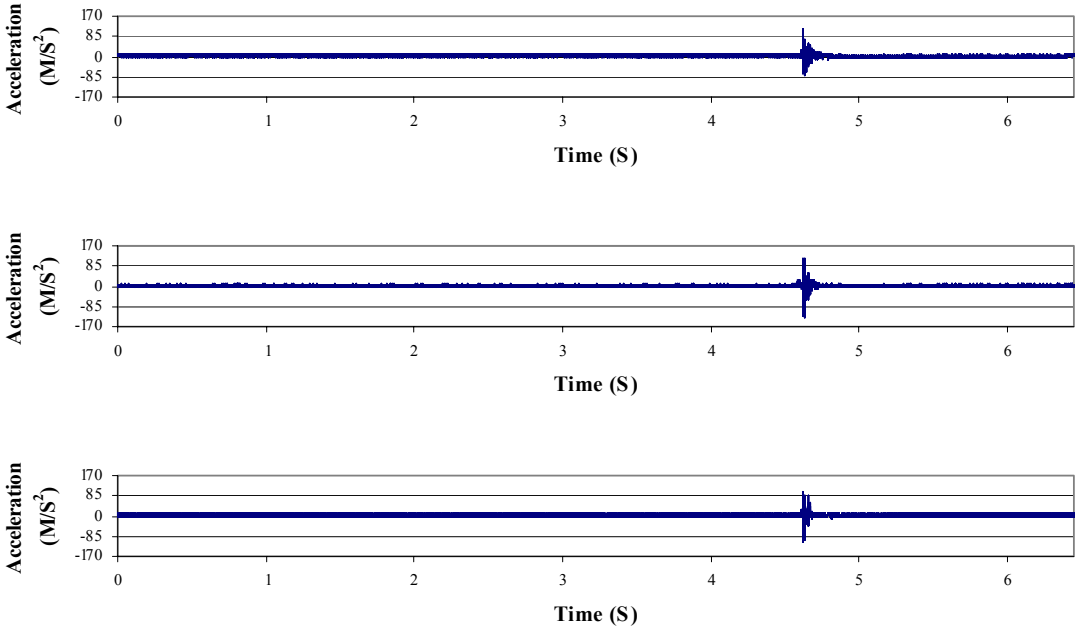

Figure A-77. Acceleration data from the greater trochanter accelerometer for a metal-on-polyethylene THA, subjected to a 1500 Newton impact load. The signals are for the D1-axis (upper), D2-axis (middle) and D3-axis (lower).

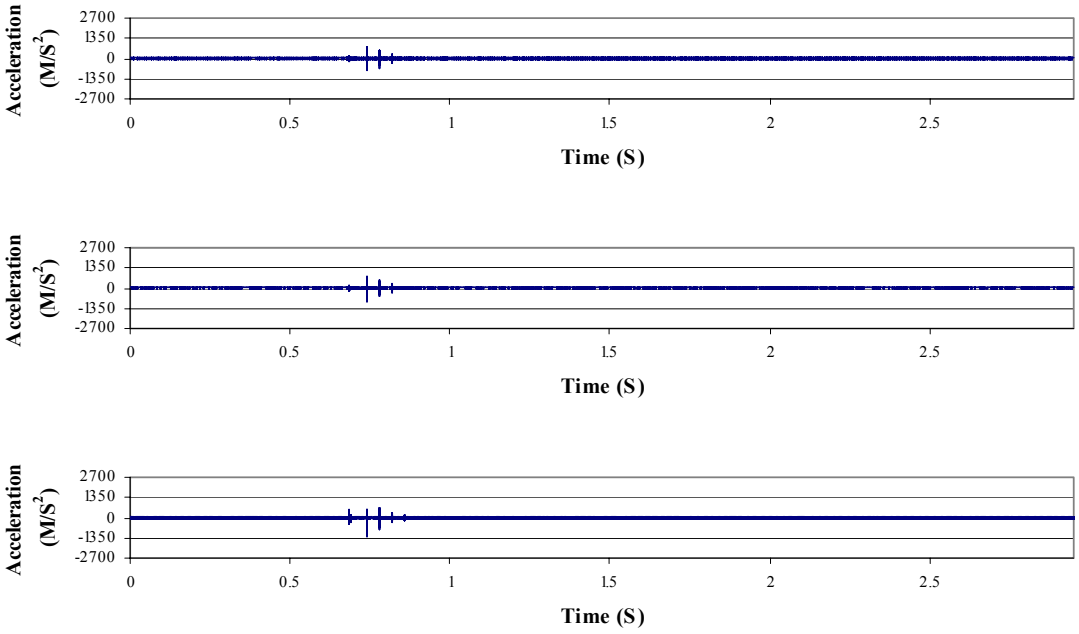

Figure A-78. Acceleration data from the pelvis accelerometer for a metal-on-metal THA, subjected to a 1500 Newton impact load. The signals are for the A1-axis (upper), A2-axis (middle) and A3-axis (lower).

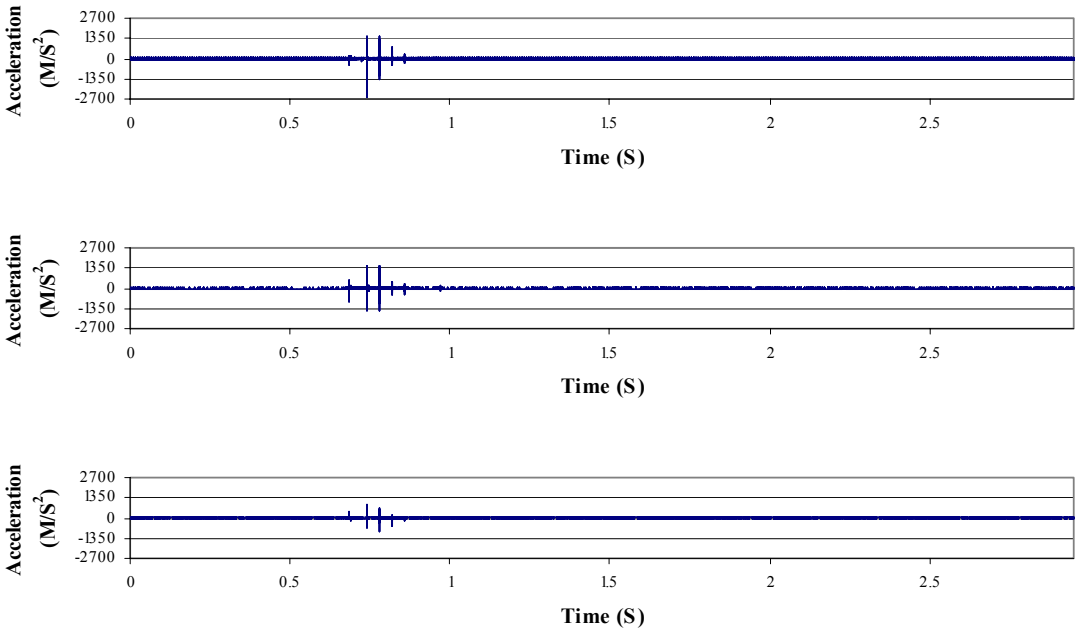

Figure A-79. Acceleration data from the acetabular cup accelerometer for a metal-on-metal THA, subjected to a 1500 Newton impact load. The signals are for the B1-axis (upper), B2-axis (middle) and B3-axis (lower).

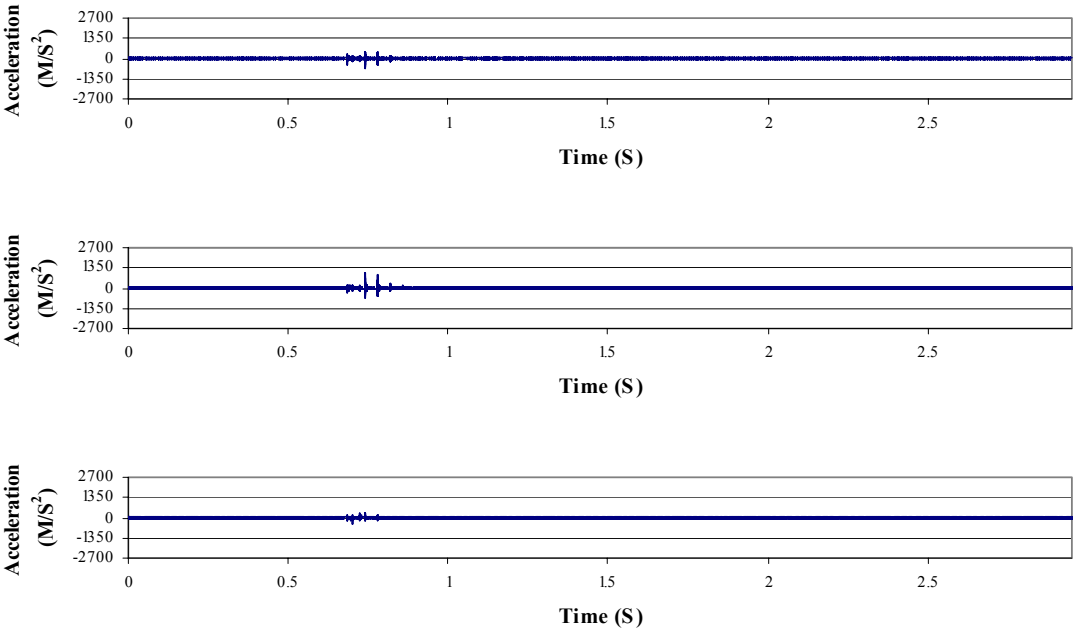

Figure A-80. Acceleration data from the femoral stem accelerometer for a metal-on-metal THA, subjected to a 1500 Newton impact load. The signals are for the C1-axis (upper), C2-axis (middle) and C3-axis (lower).

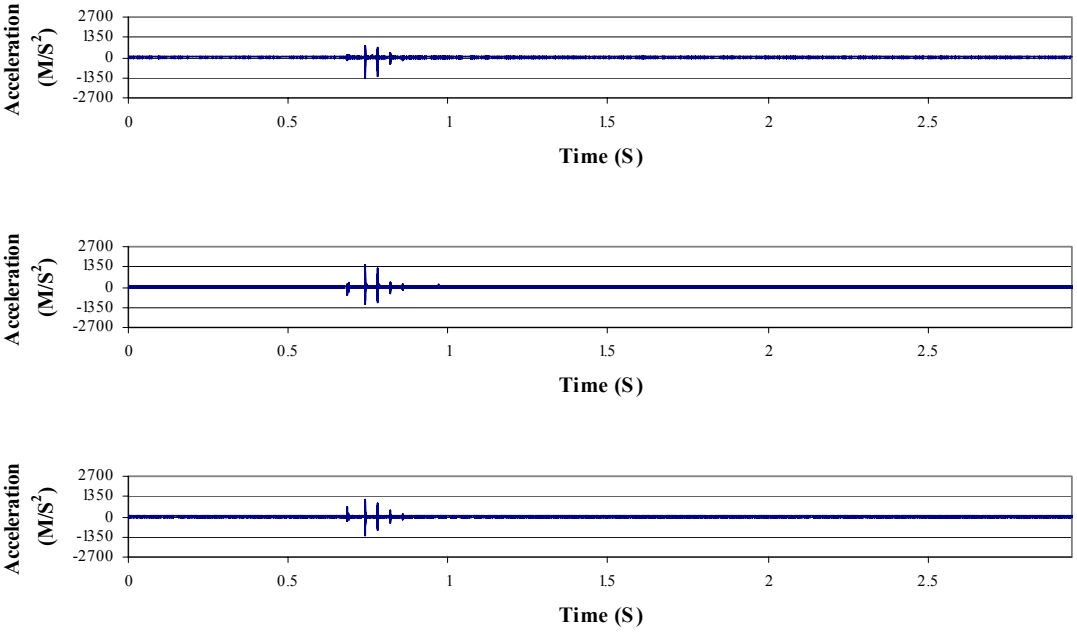

Figure A-81. Acceleration data from the greater trochanter accelerometer for a metal-on-metal THA, subjected to a 1500 Newton impact load. The signals are for the D1-axis (upper), D2-axis (middle) and D3-axis (lower).

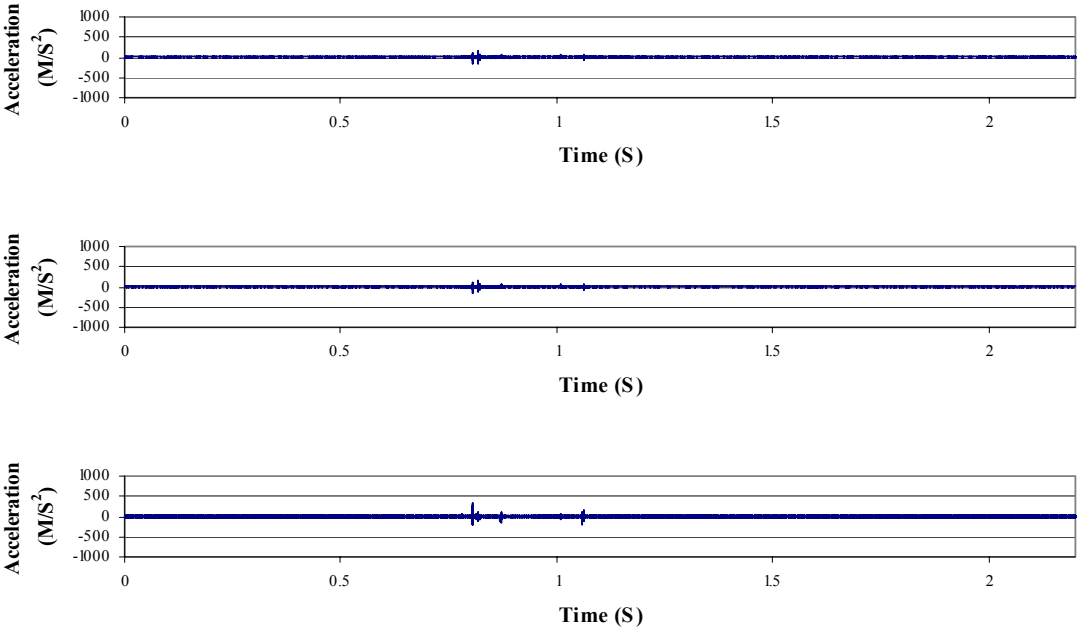

Figure A-82. Acceleration data from the pelvis accelerometer for a ceramic-on-ceramic THA, subjected to a 1500 Newton impact load. The signals are for the A1-axis (upper), A2-axis (middle) and A3-axis (lower).

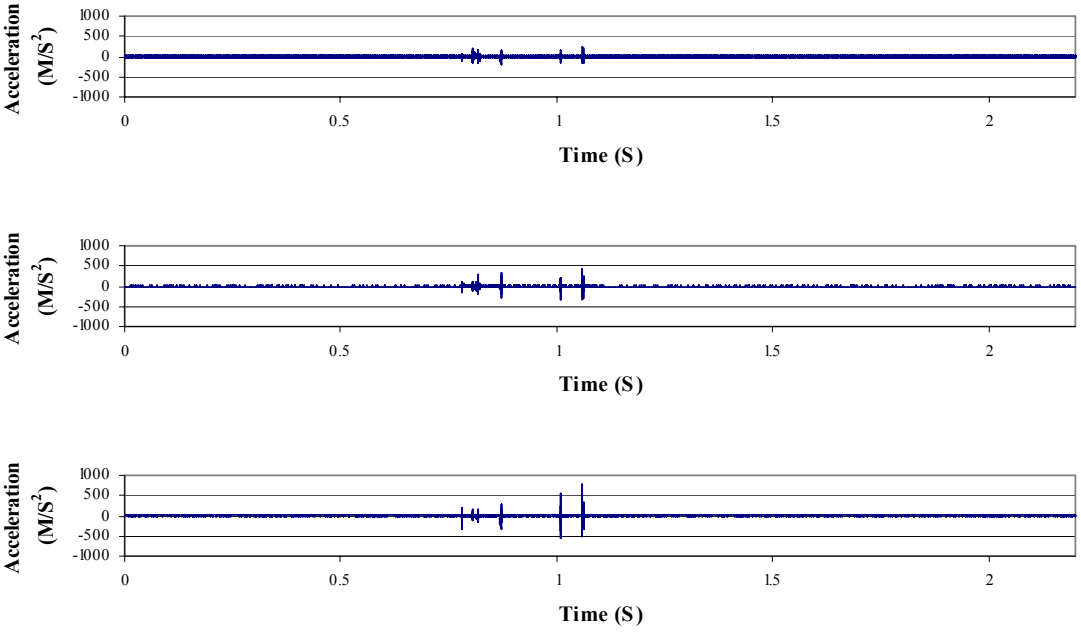

Figure A-83. Acceleration data from the acetabular cup accelerometer for a ceramic-on-ceramic THA, subjected to a 1500 Newton impact load. The signals are for the B1-axis (upper), B2-axis (middle) and B3-axis (lower).

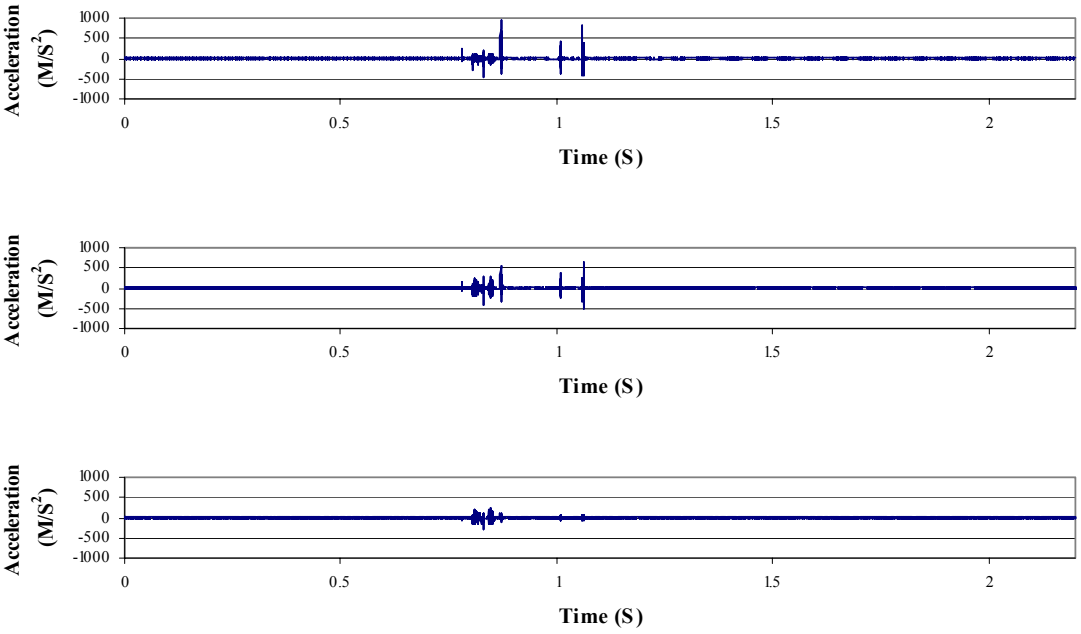

Figure A-84. Acceleration data from the femoral stem accelerometer for a ceramic-on-ceramic THA, subjected to a 1500 Newton impact load. The signals are for the C1-axis (upper), C2-axis (middle) and C3-axis (lower).

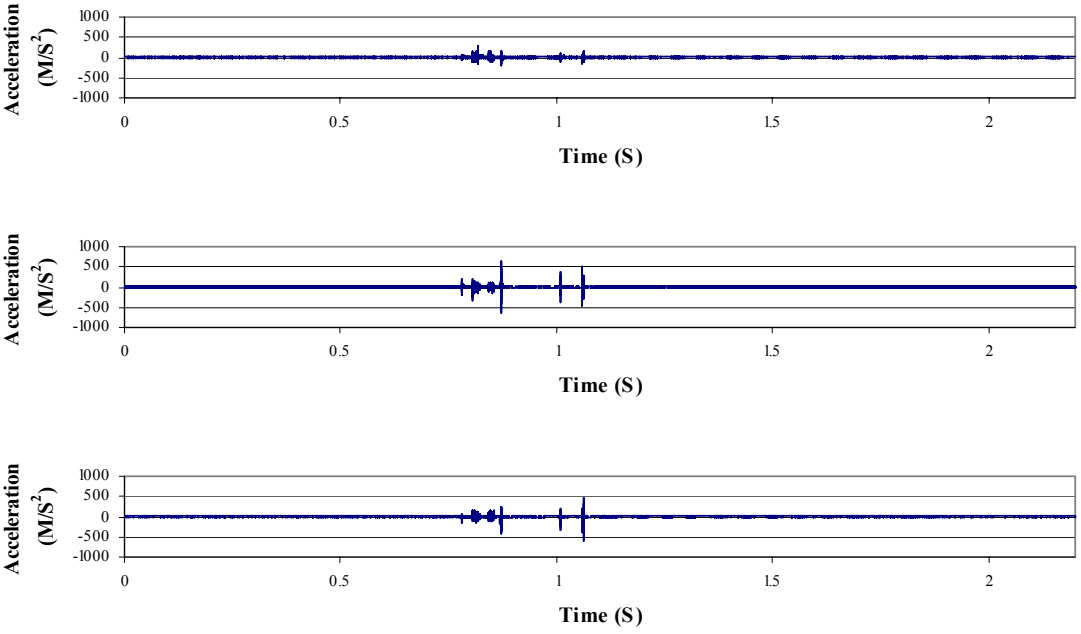

Figure A-85. Acceleration data from the greater trochanter accelerometer for a ceramic-on-ceramic THA, subjected to a 1500 Newton impact load. The signals are for the D1-axis (upper), D2-axis (middle) and D3-axis (lower).

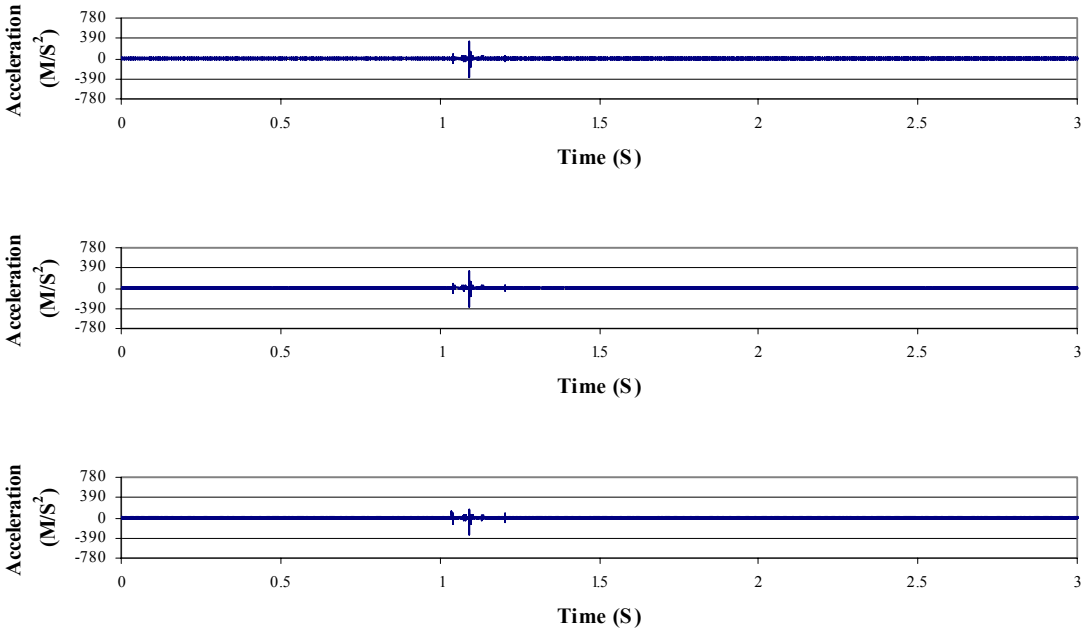

Figure A-86. Acceleration data from the pelvis accelerometer for a metal-on-polyethylene THA, subjected to a 1730 Newton impact load. The signals are for the A1-axis (upper), A2-axis (middle) and A3-axis (lower).

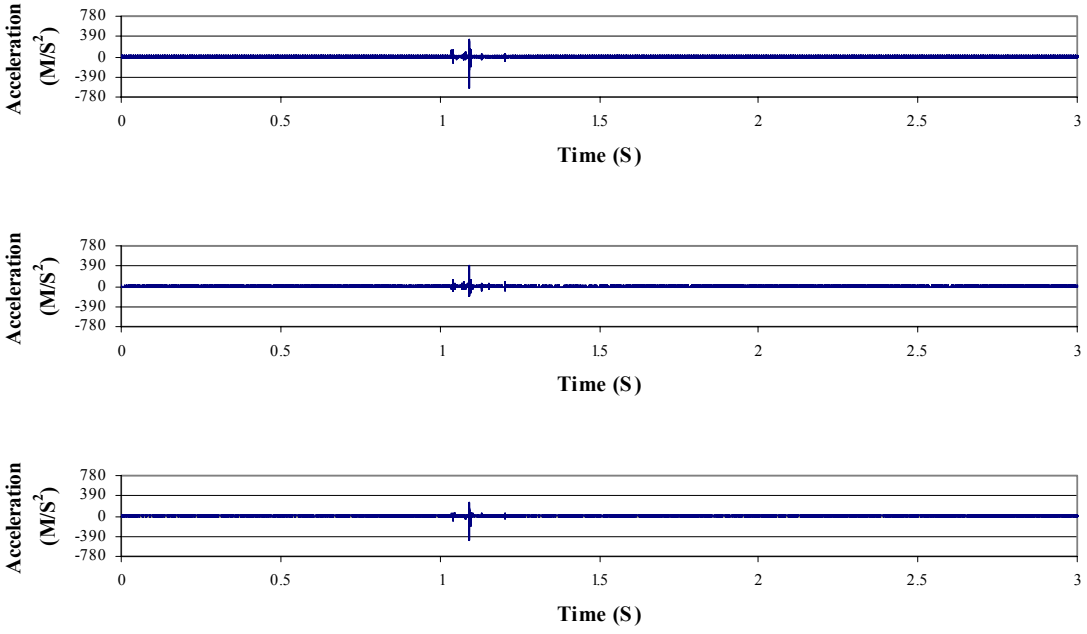

Figure A-87. Acceleration data from the acetabular cup accelerometer for a metal-on-polyethylene THA, subjected to a 1730 Newton impact load. The signals are for the B1-axis (upper), B2-axis (middle) and B3-axis (lower).

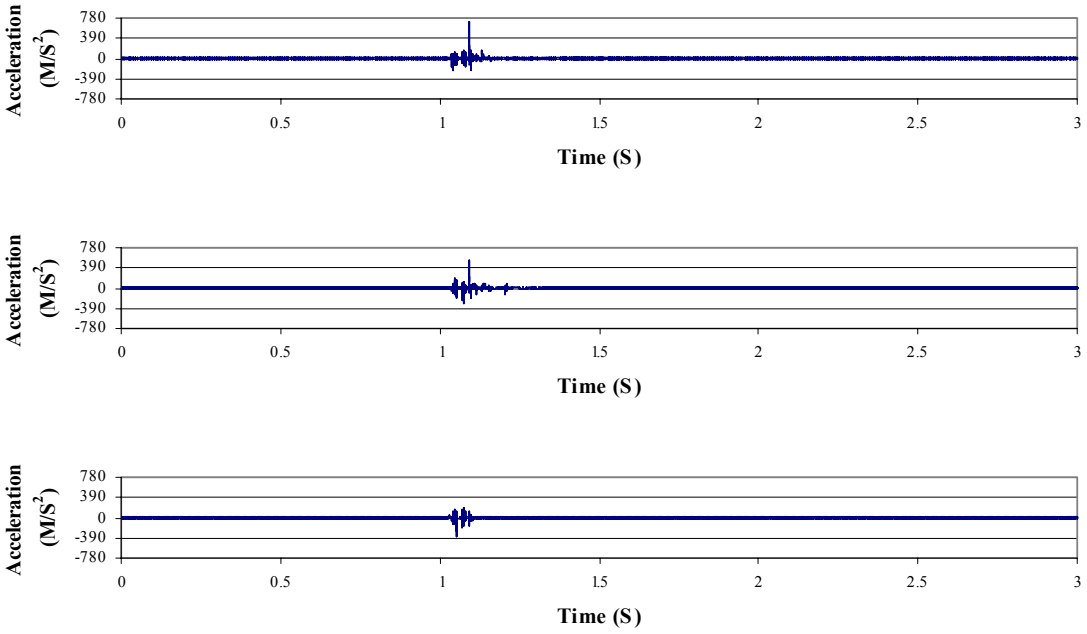

Figure A-88. Acceleration data from the femoral stem accelerometer for a metal-on-polyethylene THA, subjected to a 1730 Newton impact load. The signals are for the C1-axis (upper), C2-axis (middle) and C3-axis (lower).

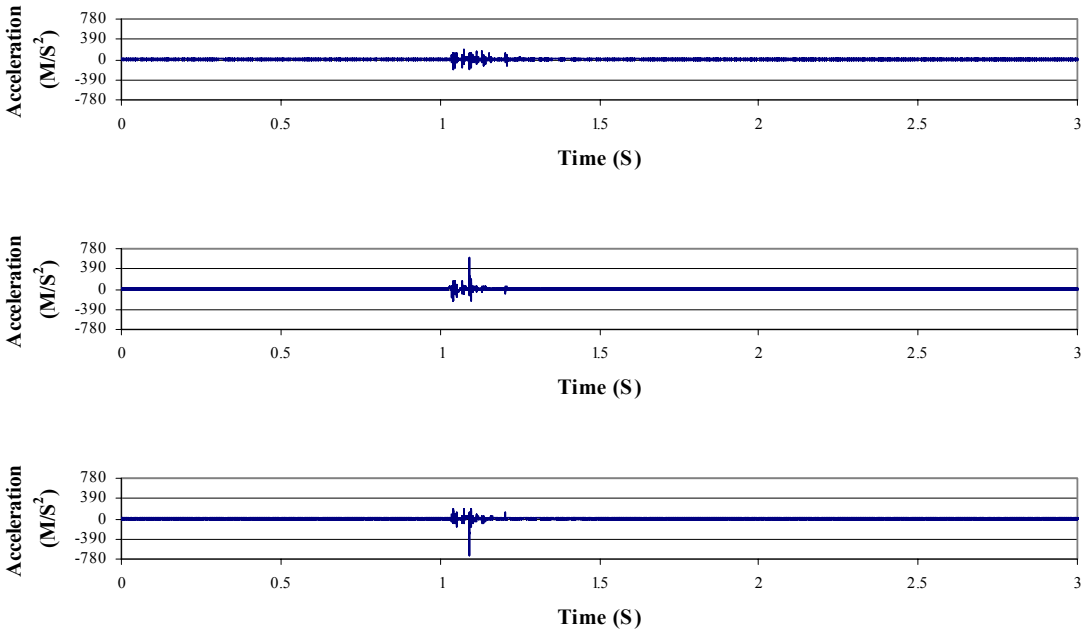

Figure A-89. Acceleration data from the greater trochanter accelerometer for a metal-on-polyethylene THA, subjected to a 1730 Newton impact load. The signals are for the D1-axis (upper), D2-axis (middle) and D3-axis (lower).

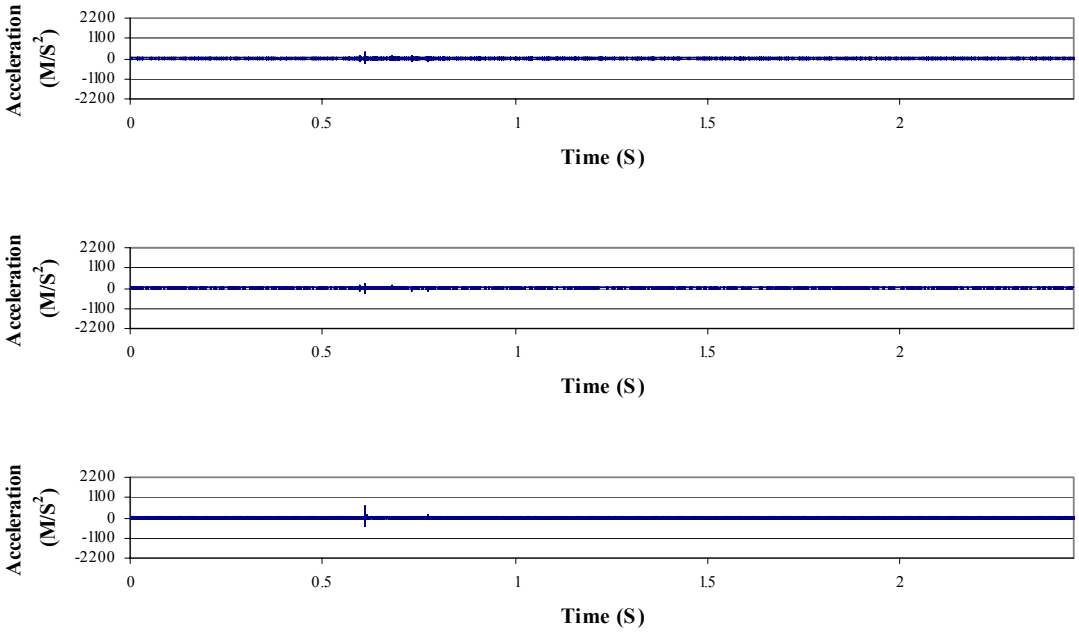

Figure A-90. Acceleration data from the pelvis accelerometer for a metal-on-metal THA, subjected to a 1730 Newton impact load. The signals are for the A1-axis (upper), A2-axis (middle) and A3-axis (lower).

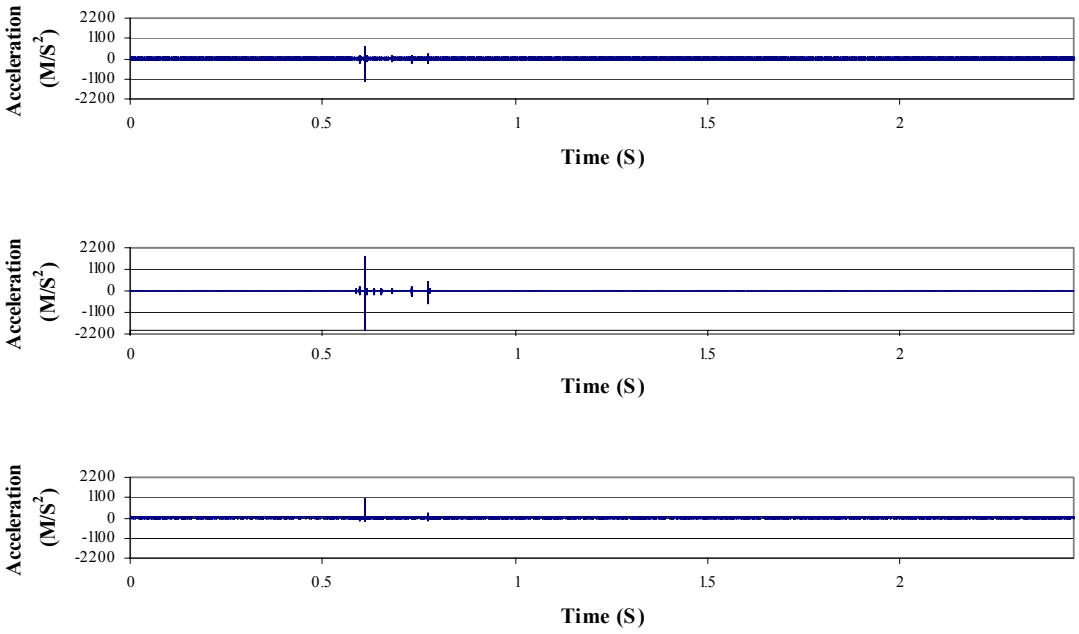

Figure A-91. Acceleration data from the acetabular cup accelerometer for a metal-on-metal THA, subjected to a 1730 Newton impact load. The signals are for the B1-axis (upper), B2-axis (middle) and B3-axis (lower).

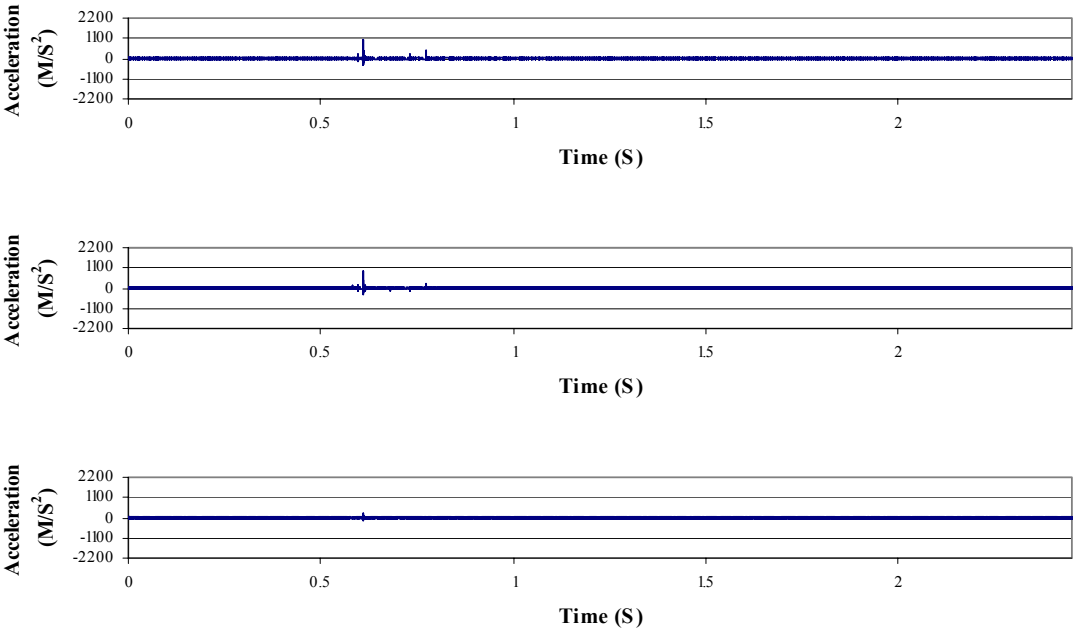

Figure A-92. Acceleration data from the femoral stem accelerometer for a metal-on-metal THA, subjected to a 1730 Newton impact load. The signals are for the C1-axis (upper), C2-axis (middle) and C3-axis (lower).

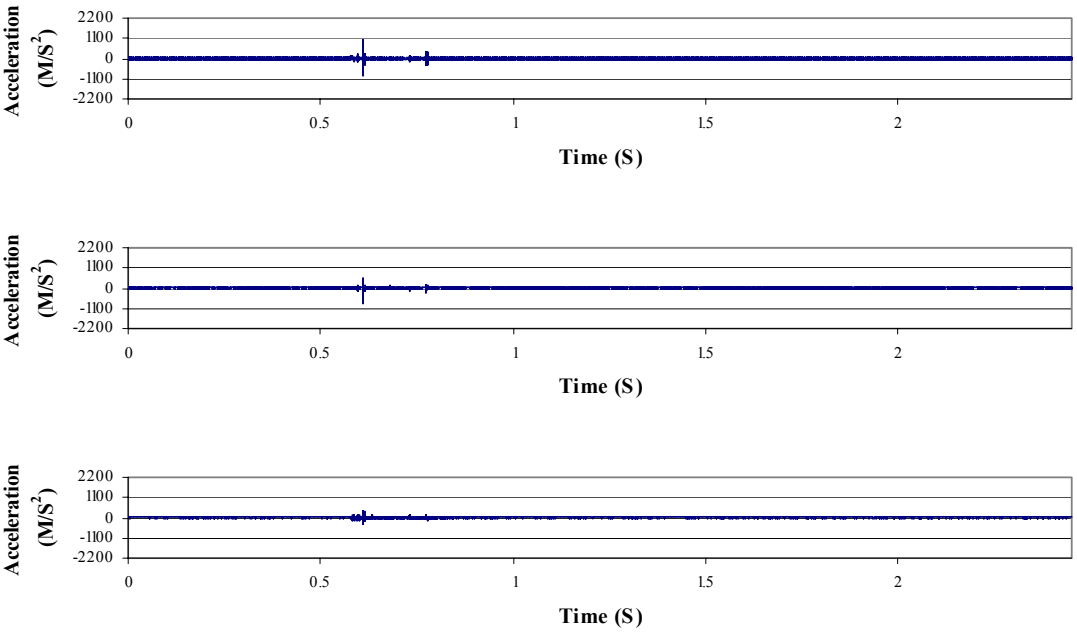

Figure A-93. Acceleration data from the greater trochanter accelerometer for a metal-on-metal THA, subjected to a 1730 Newton impact load. The signals are for the D1-axis (upper), D2-axis (middle) and D3-axis (lower).

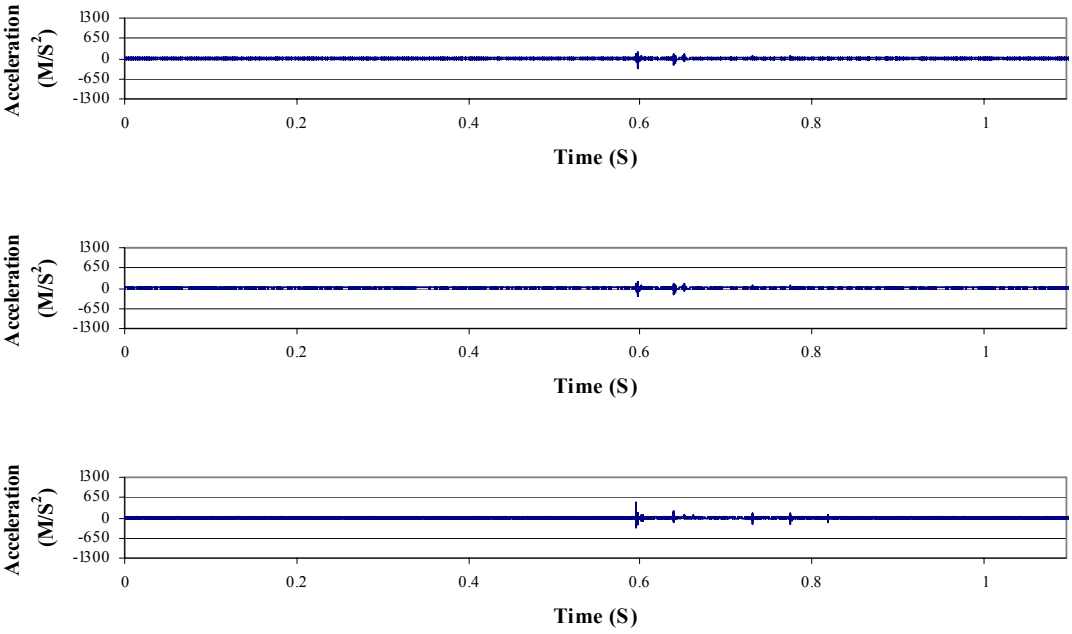

Figure A-94. Acceleration data from the pelvis accelerometer for a ceramic-on-ceramic THA, subjected to a 1730 Newton impact load. The signals are for the A1-axis (upper), A2-axis (middle) and A3-axis (lower).

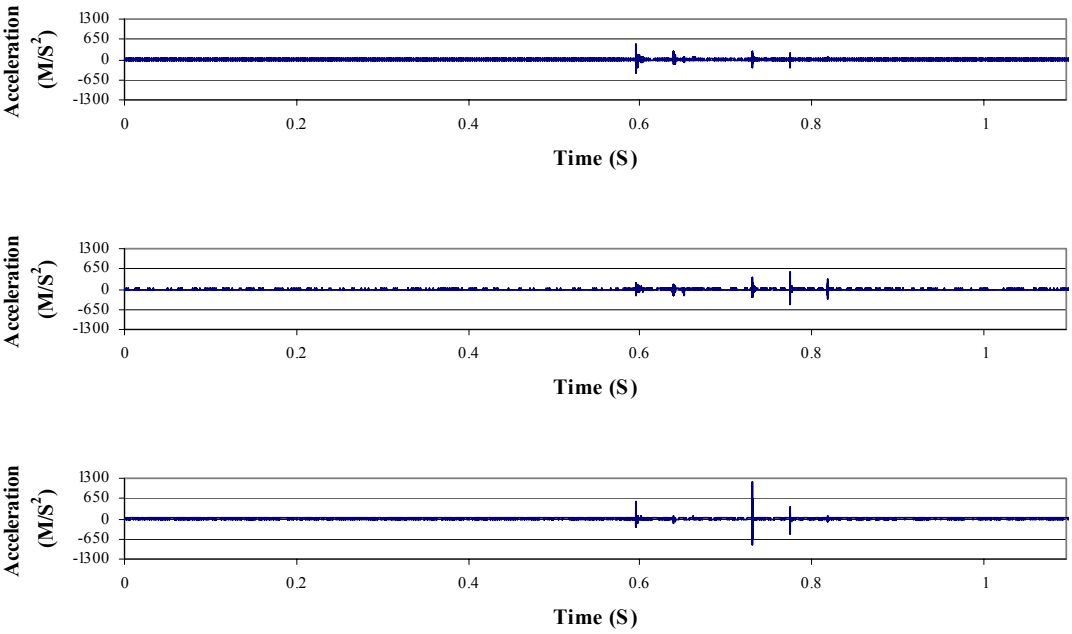

Figure A-95. Acceleration data from the acetabular cup accelerometer for a ceramic-on-ceramic THA, subjected to a 1730 Newton impact load. The signals are for the B1-axis (upper), B2-axis (middle) and B3-axis (lower).

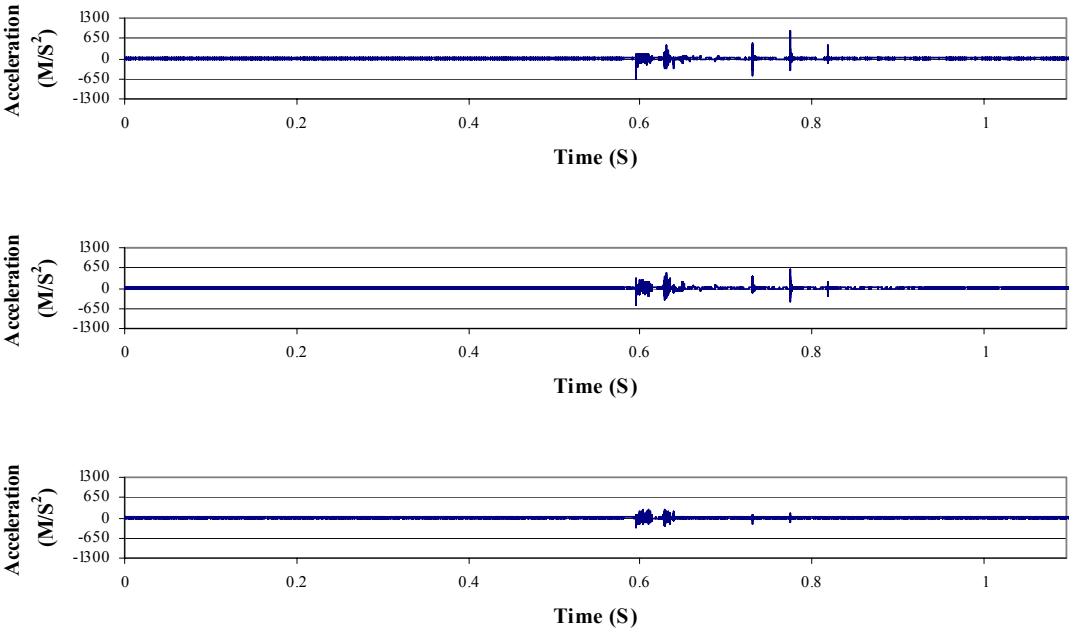

Figure A-96. Acceleration data from the femoral stem accelerometer for a ceramic-on-ceramic THA, subjected to a 1730 Newton impact load. The signals are for the C1-axis (upper), C2-axis (middle) and C3-axis (lower).

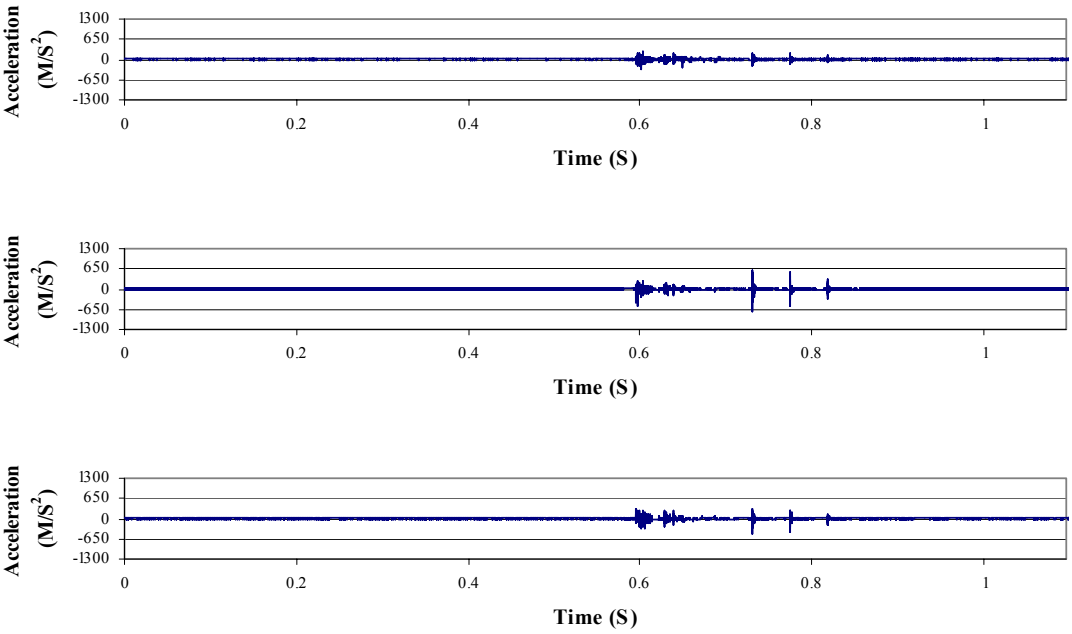

Figure A-97. Acceleration data from the greater trochanter accelerometer for a ceramic-on-ceramic THA, subjected to a 1730 Newton impact load. The signals are for the D1-axis (upper), D2-axis (middle) and D3-axis (lower).

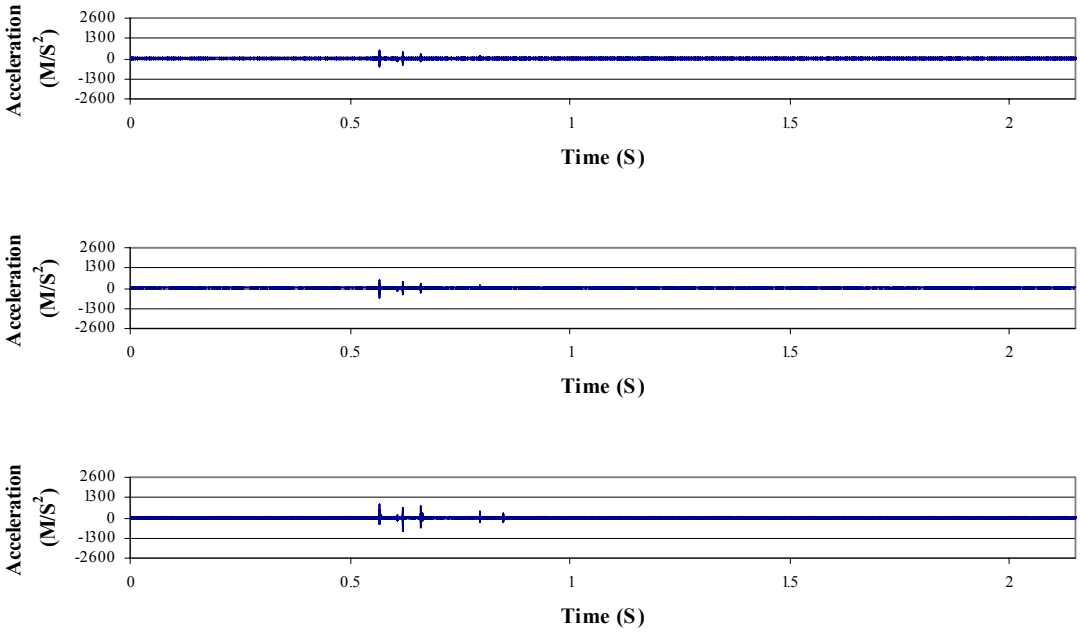

Figure A-98. Acceleration data from the pelvis accelerometer for a metal-on-polyethylene THA, subjected to a 1900 Newton impact load. The signals are for the A1-axis (upper), A2-axis (middle) and A3-axis (lower).

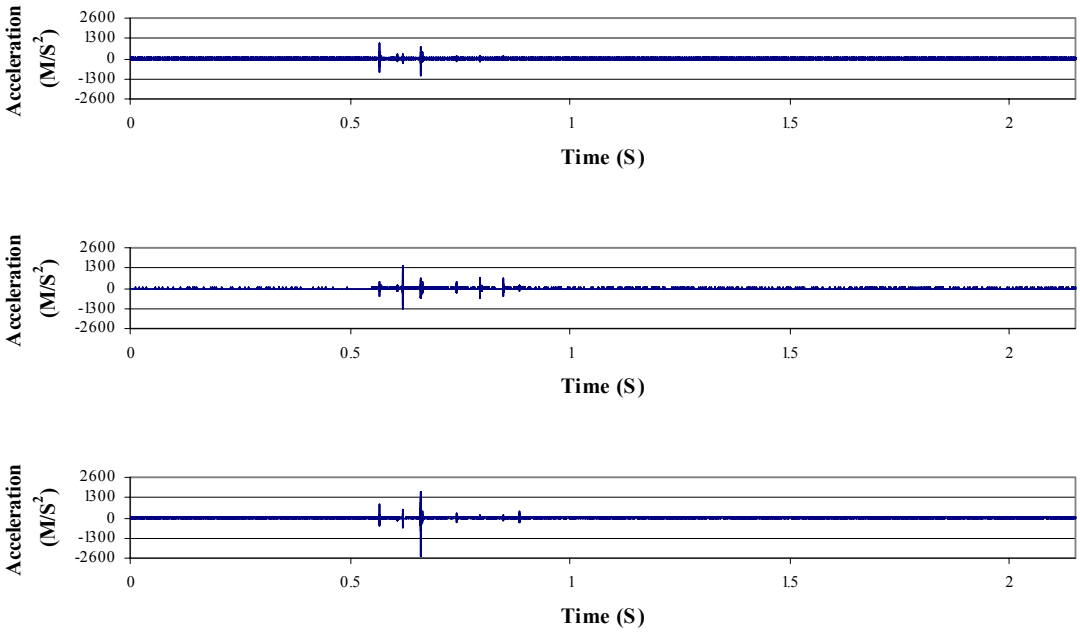

Figure A-99. Acceleration data from the acetabular cup accelerometer for a metal-on-polyethylene THA, subjected to a 1900 Newton impact load. The signals are for the B1-axis (upper), B2-axis (middle) and B3-axis (lower).

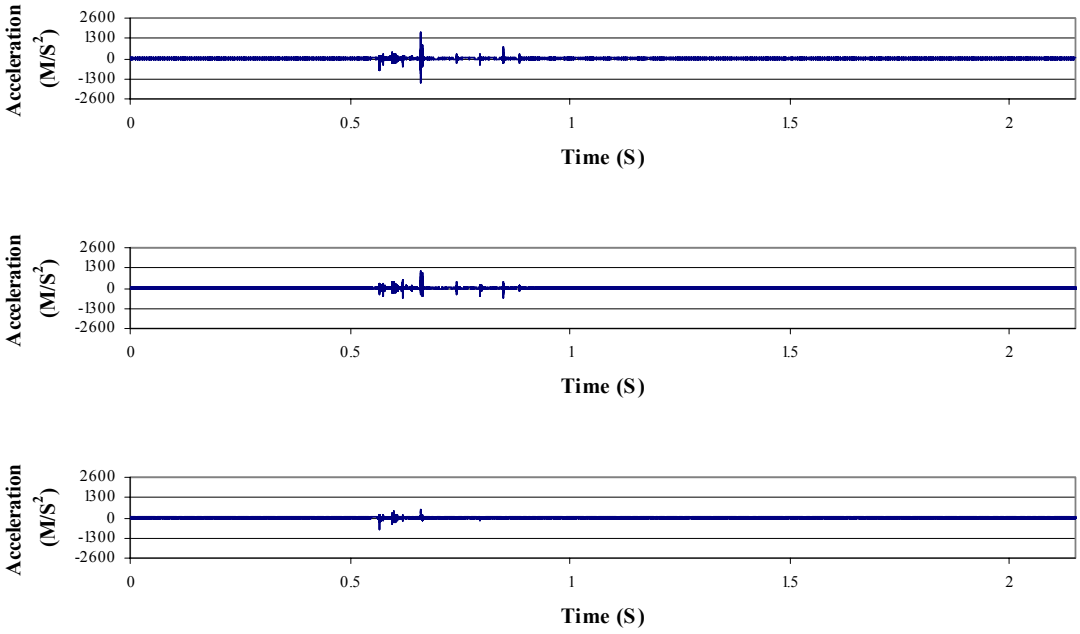

Figure A-100. Acceleration data from the femoral stem accelerometer for a metal-on-polyethylene THA, subjected to a 1900 Newton impact load. The signals are for the C1-axis (upper), C2-axis (middle) and C3-axis (lower).

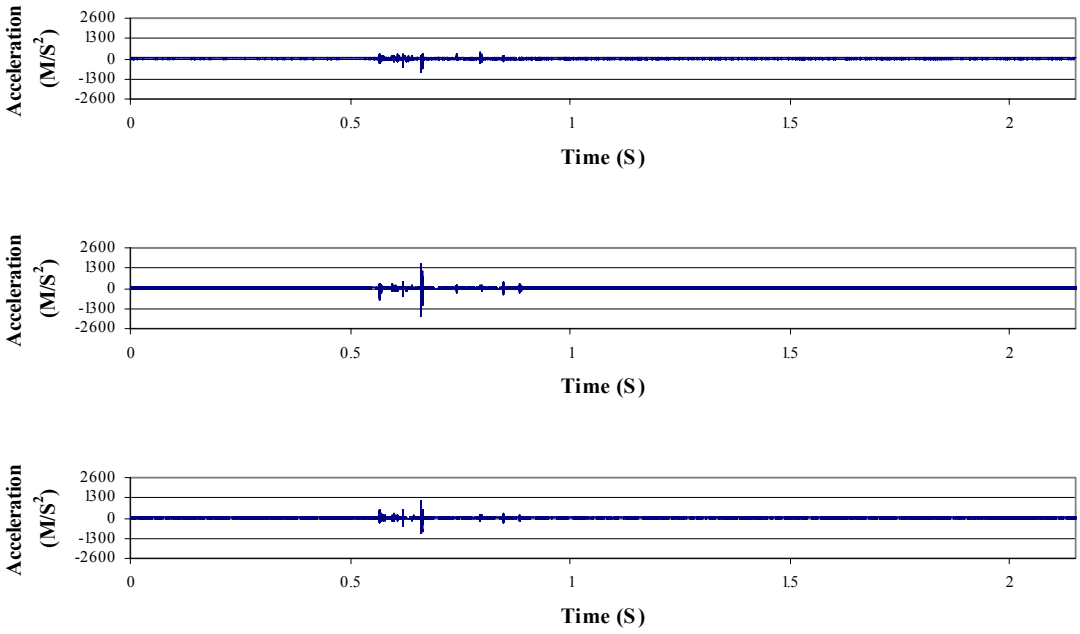

Figure A-101. Acceleration data from the greater trochanter accelerometer for a metal-on-polyethylene THA, subjected to a 1900 Newton impact load. The signals are for the D1-axis (upper), D2-axis (middle) and D3-axis (lower).

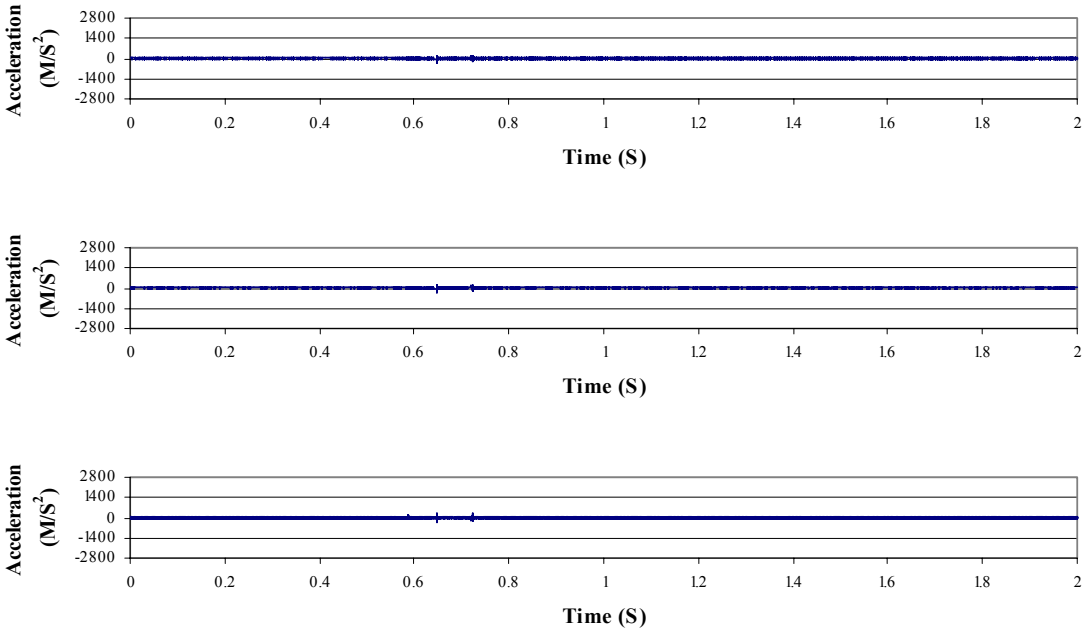

Figure A-102. Acceleration data from the pelvis accelerometer for a metal-on-metal THA, subjected to a 1900 Newton impact load. The signals are for the A1-axis (upper), A2-axis (middle) and A3-axis (lower).

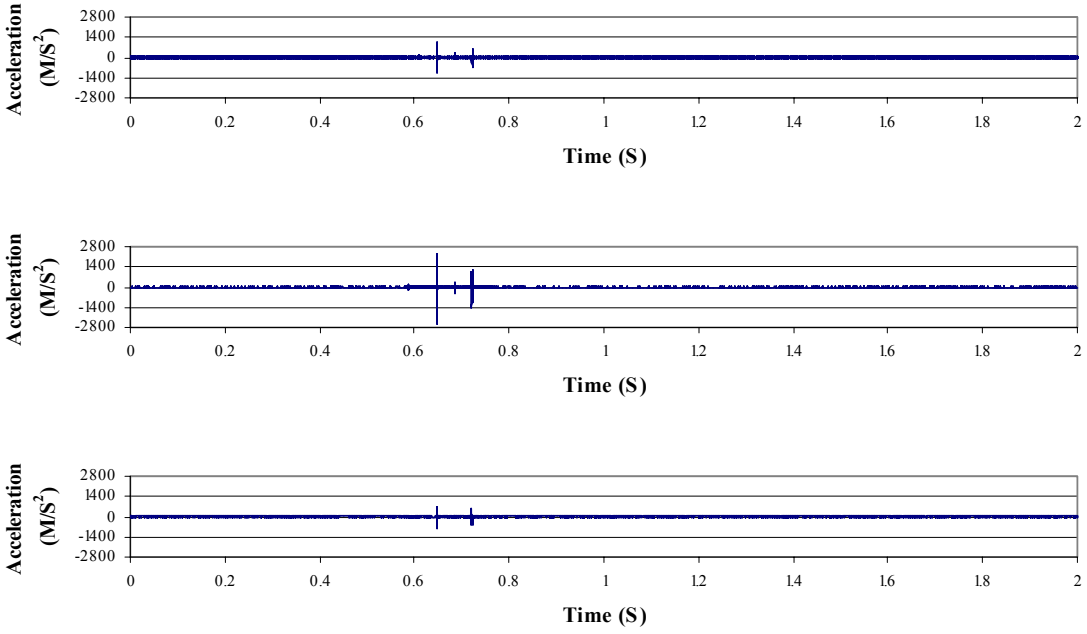

Figure A-103. Acceleration data from the acetabular cup accelerometer for a metal-on-metal THA, subjected to a 1900 Newton impact load. The signals are for the B1-axis (upper), B2-axis (middle) and B3-axis (lower).

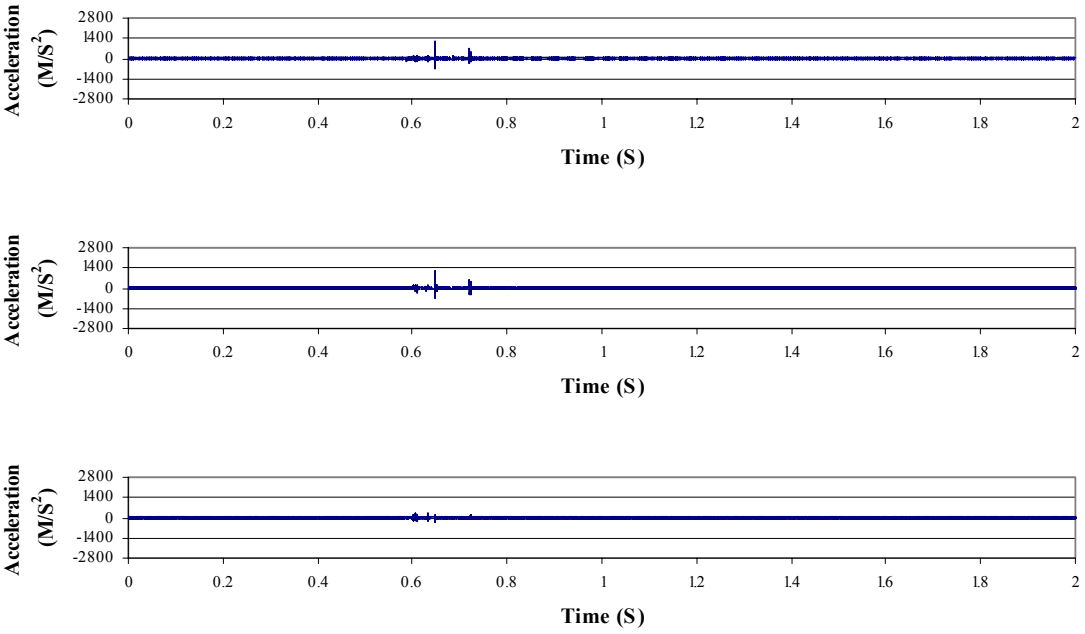

Figure A-104. Acceleration data from the femoral stem accelerometer for a metal-on-metal THA, subjected to a 1900 Newton impact load. The signals are for the C1-axis (upper), C2-axis (middle) and C3-axis (lower).

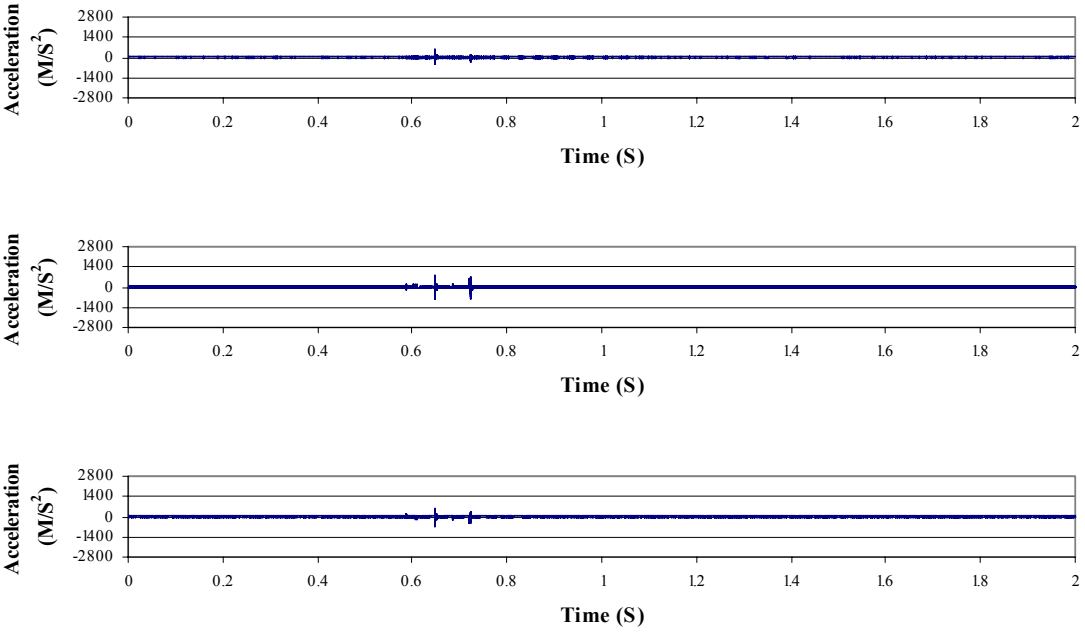

Figure A-105. Acceleration data from the greater trochanter accelerometer for a metal-on-metal THA, subjected to a 1900 Newton impact load. The signals are for the D1-axis (upper), D2-axis (middle) and D3-axis (lower).

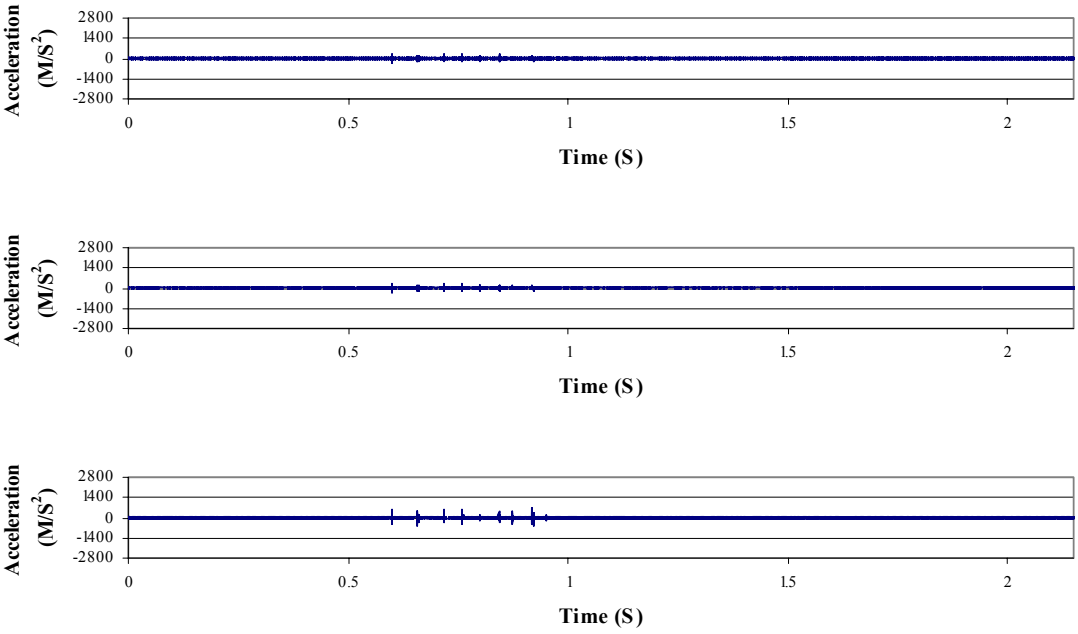

Figure A-106. Acceleration data from the pelvis accelerometer for a ceramic-on-ceramic THA, subjected to a 1900 Newton impact load. The signals are for the A1-axis (upper), A2-axis (middle) and A3-axis (lower).

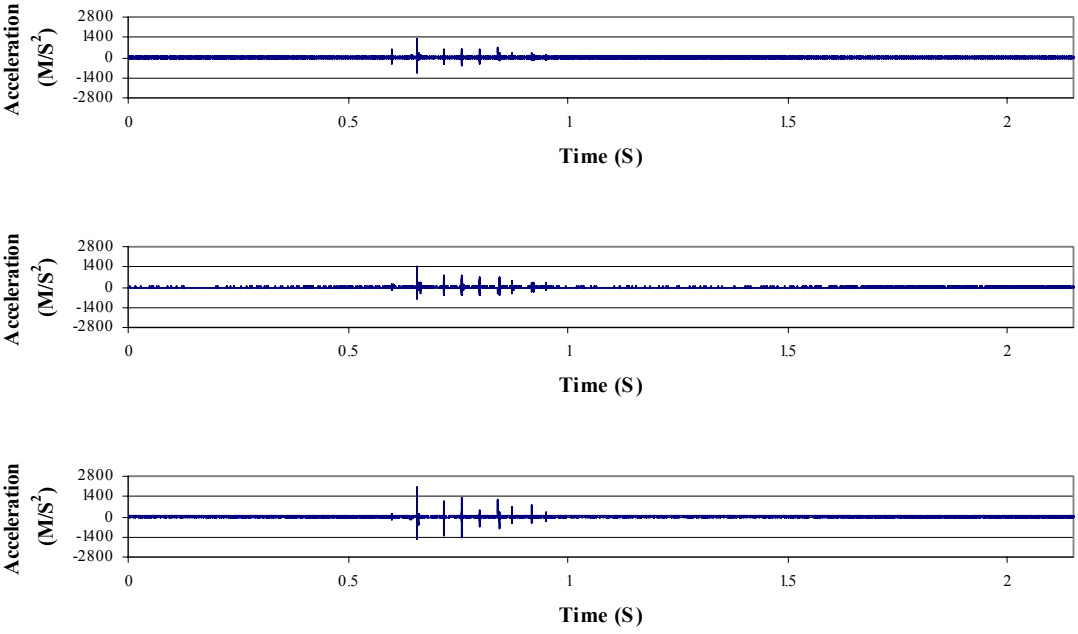

Figure A-107. Acceleration data from the acetabular cup accelerometer for a ceramic-on-ceramic THA, subjected to a 1900 Newton impact load. The signals are for the B1-axis (upper), B2-axis (middle) and B3-axis (lower).

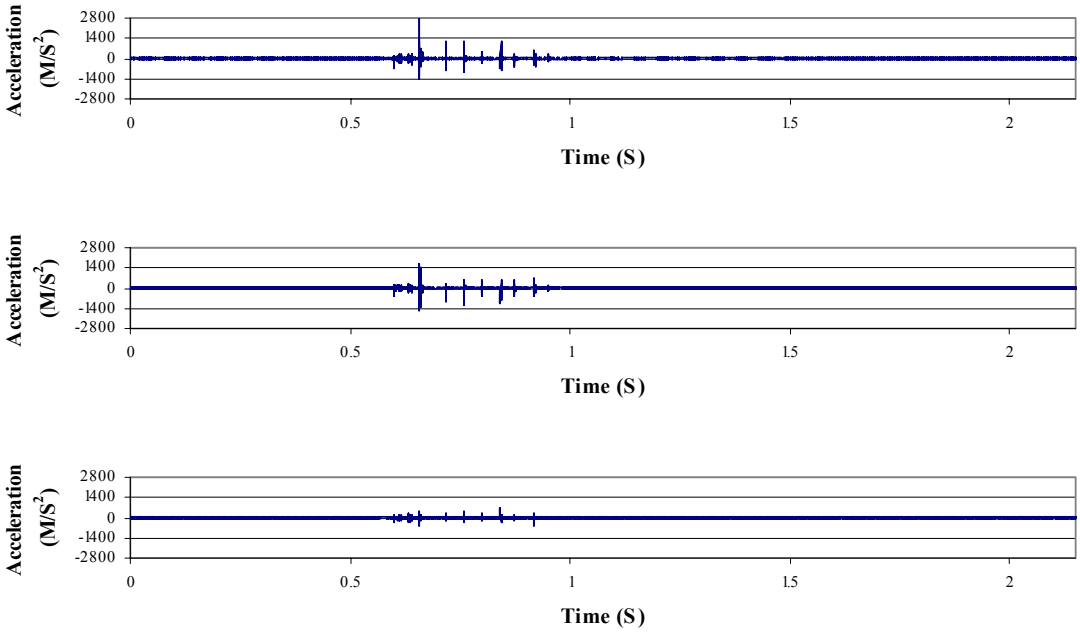

Figure A-108. Acceleration data from the femoral stem accelerometer for a ceramic-on-ceramic THA, subjected to a 1900 Newton impact load. The signals are for the C1-axis (upper), C2-axis (middle) and C3-axis (lower).

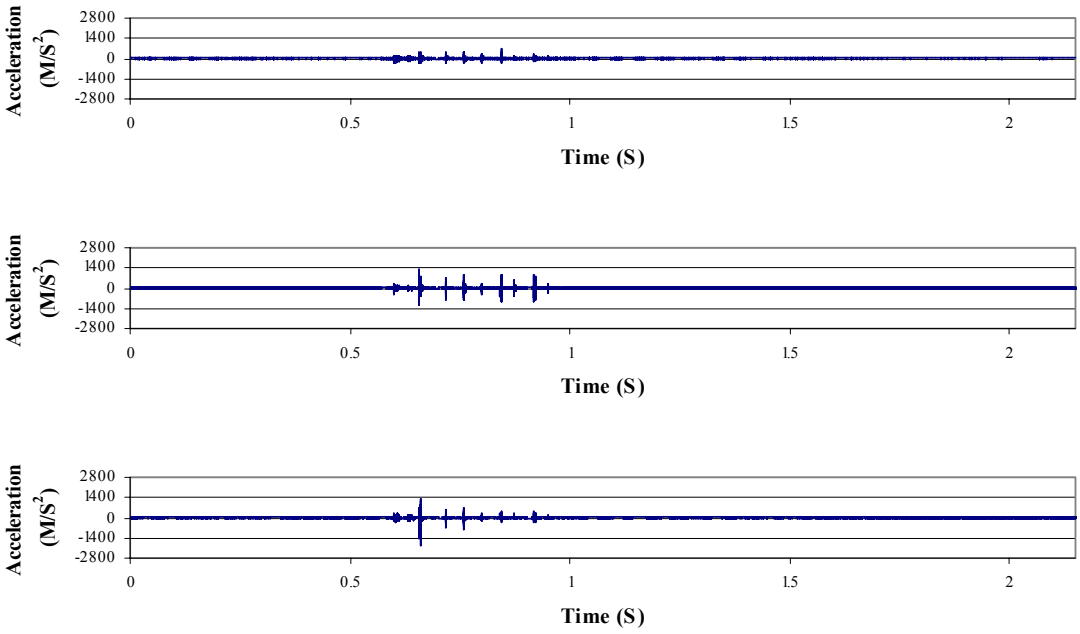

Figure A-109. Acceleration data from the greater trochanter accelerometer for a ceramic-on-ceramic THA, subjected to a 1900 Newton impact load. The signals are for the D1-axis (upper), D2-axis (middle) and D3-axis (lower).

Impact Test FFT's:

Note: These FFT's represent raw data and are intended for the purposes of giving a general overview only.

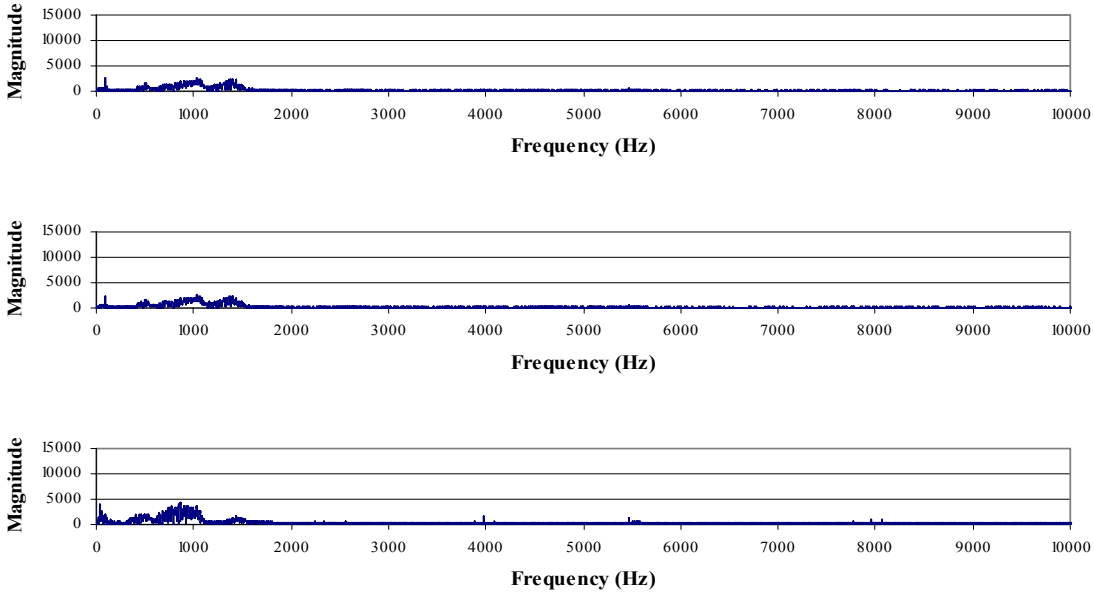

Figure A-110. FFT data from the pelvis accelerometer for a metal-on-polyethylene THA, subjected to a 680 Newton impact load. The signals are for the A1-axis (upper), A2-axis (middle) and A3-axis (lower).

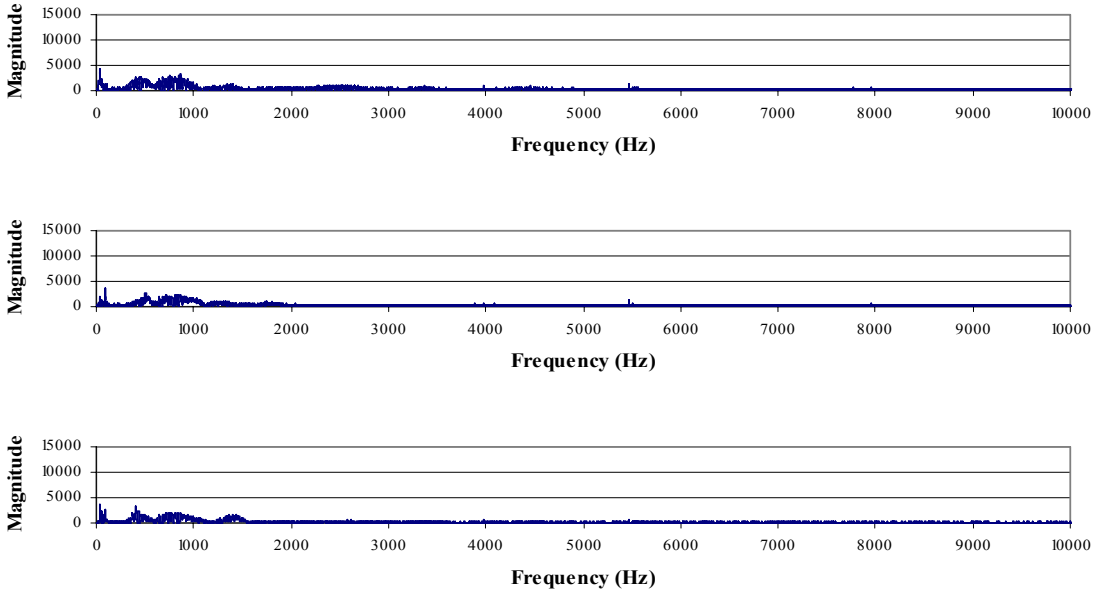

Figure A-111. FFT data from the acetabular cup accelerometer for a metal-on-polyethylene THA, subjected to a 680 Newton impact load. The signals are for the B1-axis (upper), B2-axis (middle) and B3-axis (lower).

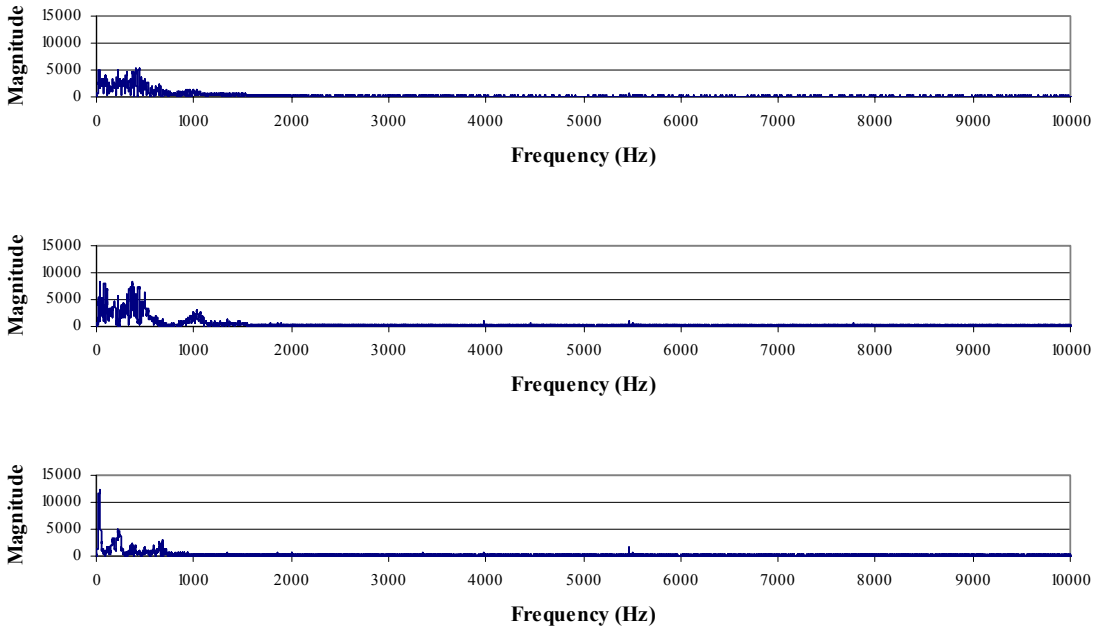

Figure A-112. FFT data from the femoral stem accelerometer for a metal-on-polyethylene THA, subjected to a 680 Newton impact load. The signals are for the C1-axis (upper), C2-axis (middle) and C3-axis (lower).

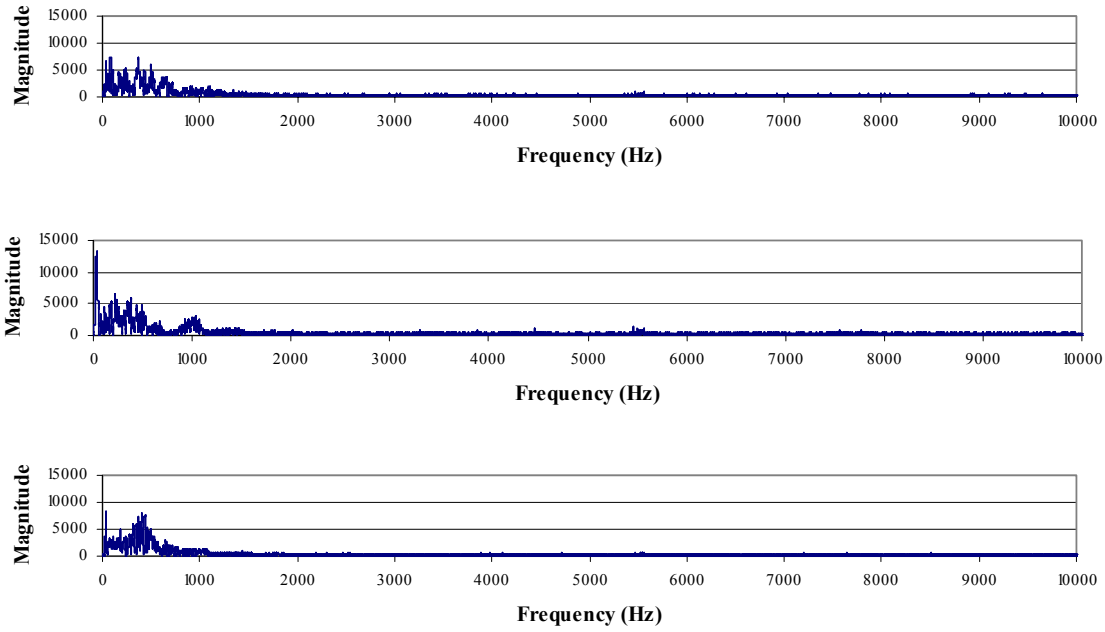

Figure A-113. FFT data from the greater trochanter accelerometer for a metal-on-polyethylene THA, subjected to a 680 Newton impact load. The signals are for the D1-axis (upper), D2-axis (middle) and D3-axis (lower).

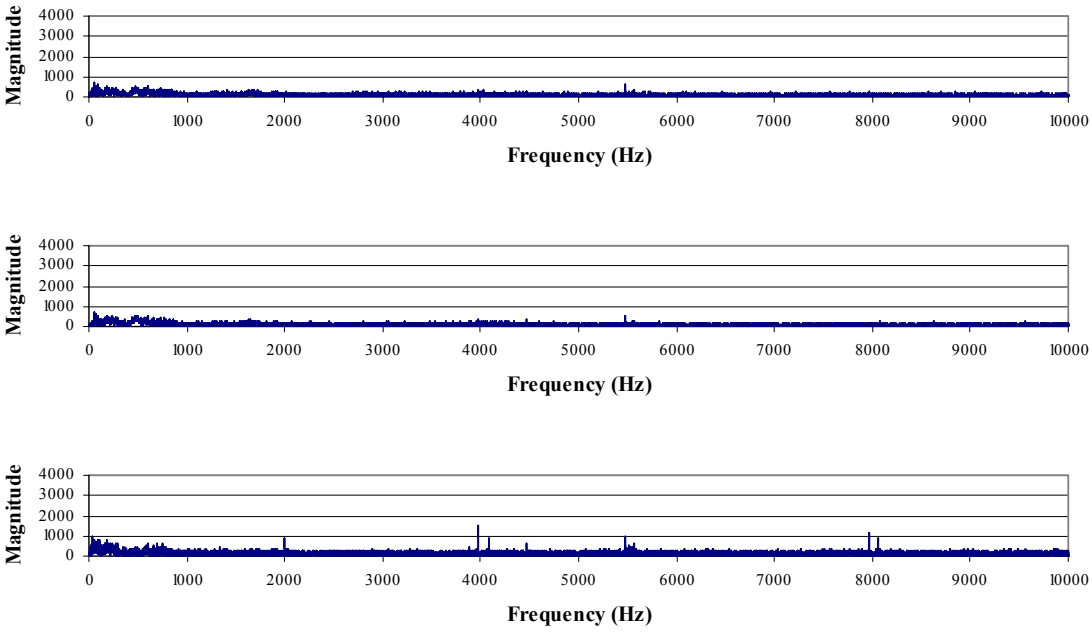

Figure A-114. FFT data from the pelvis accelerometer for a metal-on-metal THA, subjected to a 680 Newton impact load. The signals are for the A1-axis (upper), A2-axis (middle) and A3-axis (lower).

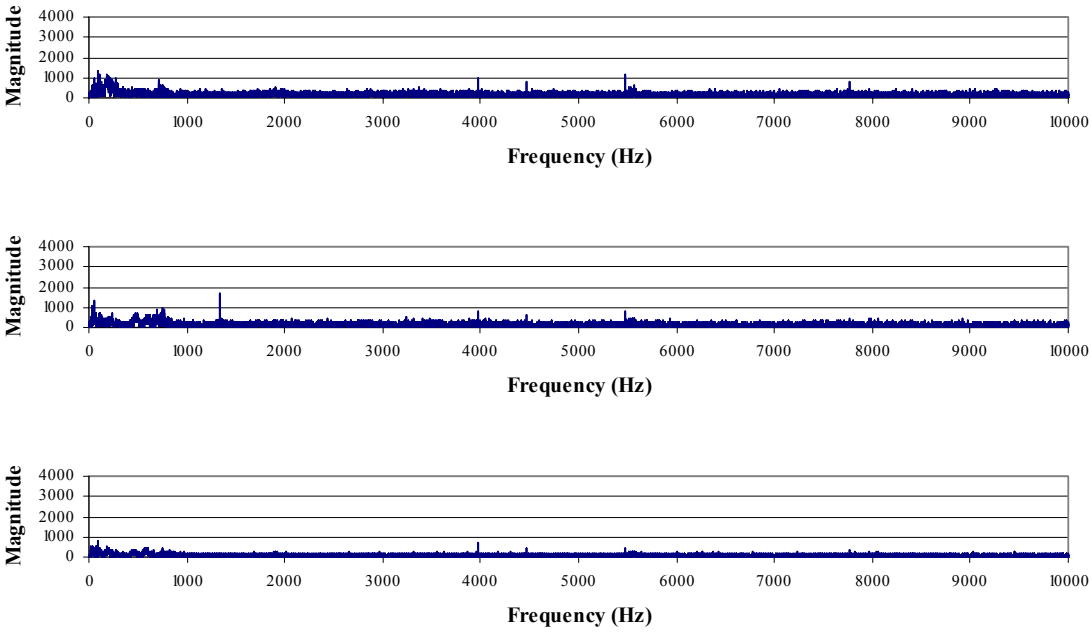

Figure A-115. FFT data from the acetabular cup accelerometer for a metal-on-metal THA, subjected to a 680 Newton impact load. The signals are for the B1-axis (upper), B2-axis (middle) and B3-axis (lower).

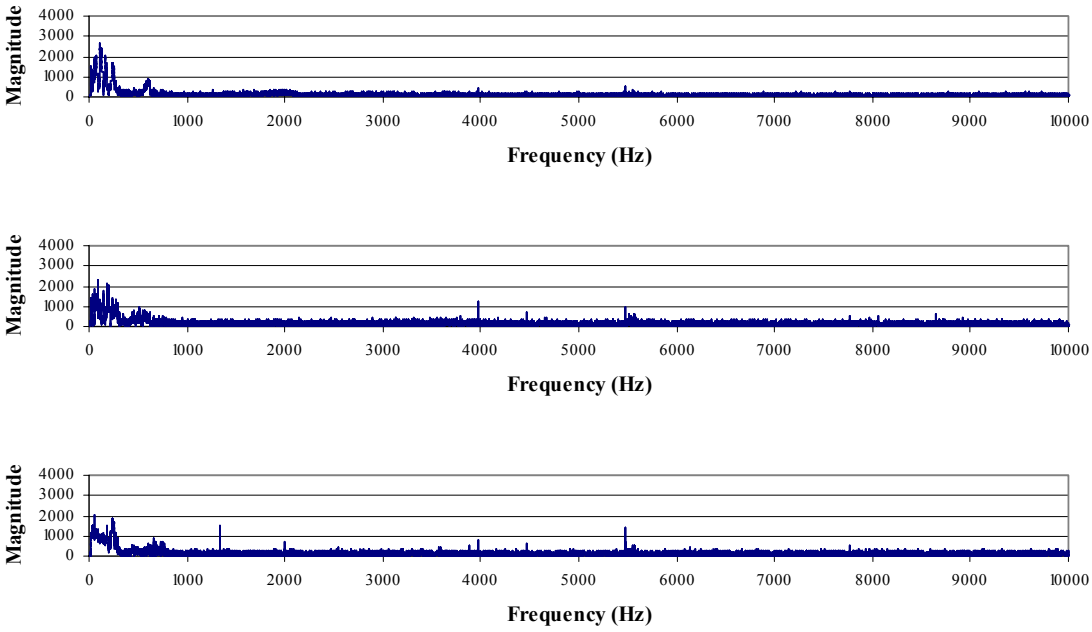

Figure A-116. FFT data from the femoral stem accelerometer for a metal-on-metal THA, subjected to a 680 Newton impact load. The signals are for the C1-axis (upper), C2-axis (middle) and C3-axis (lower).

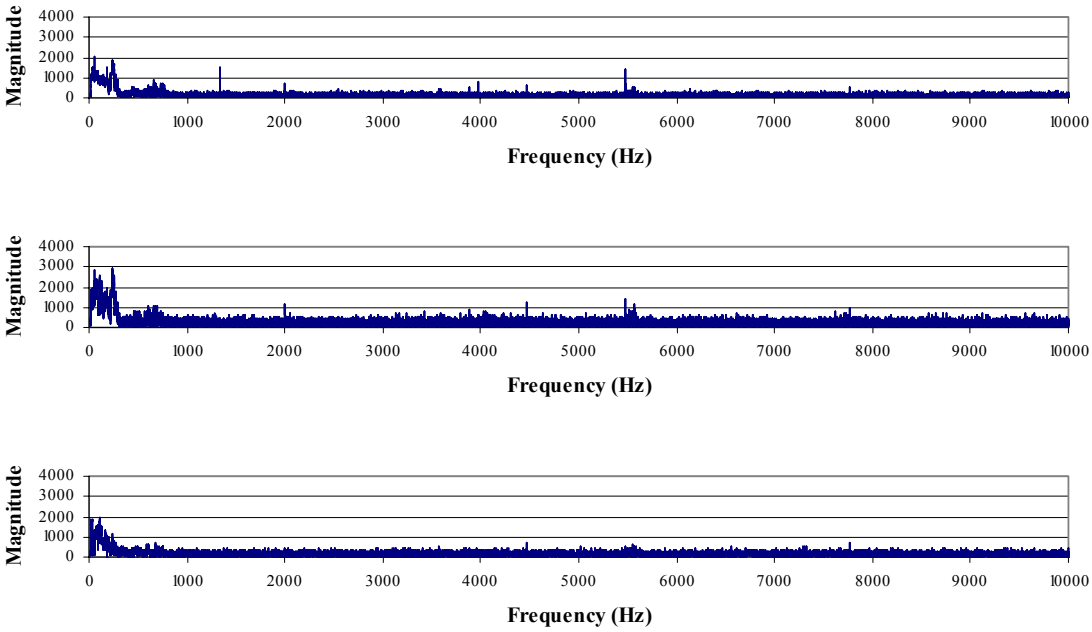

Figure A-117. FFT data from the greater trochanter accelerometer for a metal-on-metal THA, subjected to a 680 Newton impact load. The signals are for the D1-axis (upper), D2-axis (middle) and D3-axis (lower).

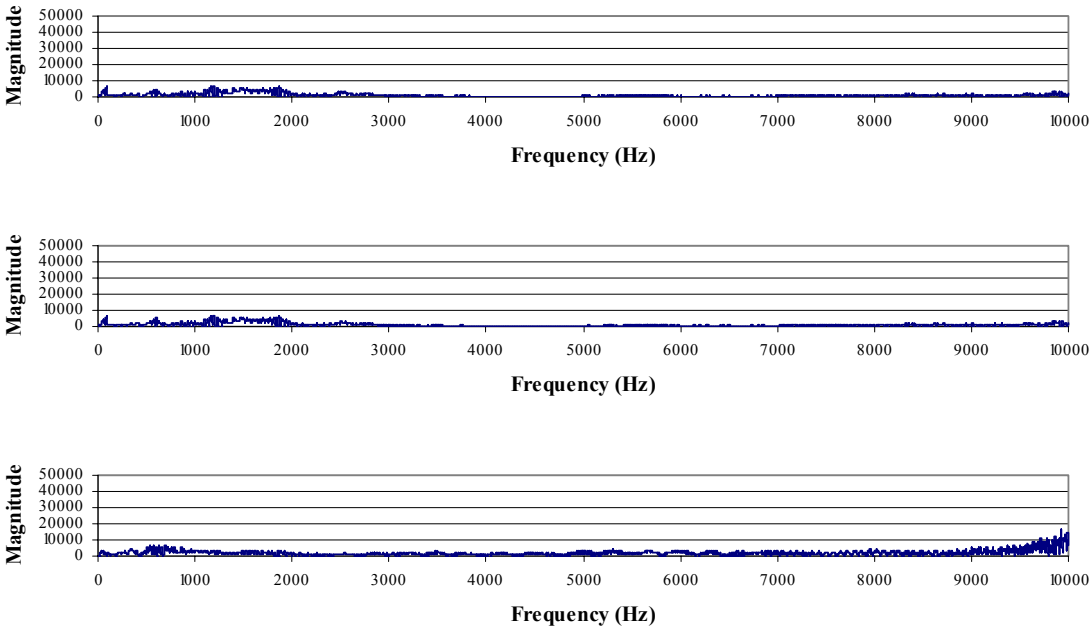

Figure A-118. FFT data from the pelvis accelerometer for a ceramic-on-ceramic THA, subjected to a 680 Newton impact load. The signals are for the A1-axis (upper), A2-axis (middle) and A3-axis (lower).

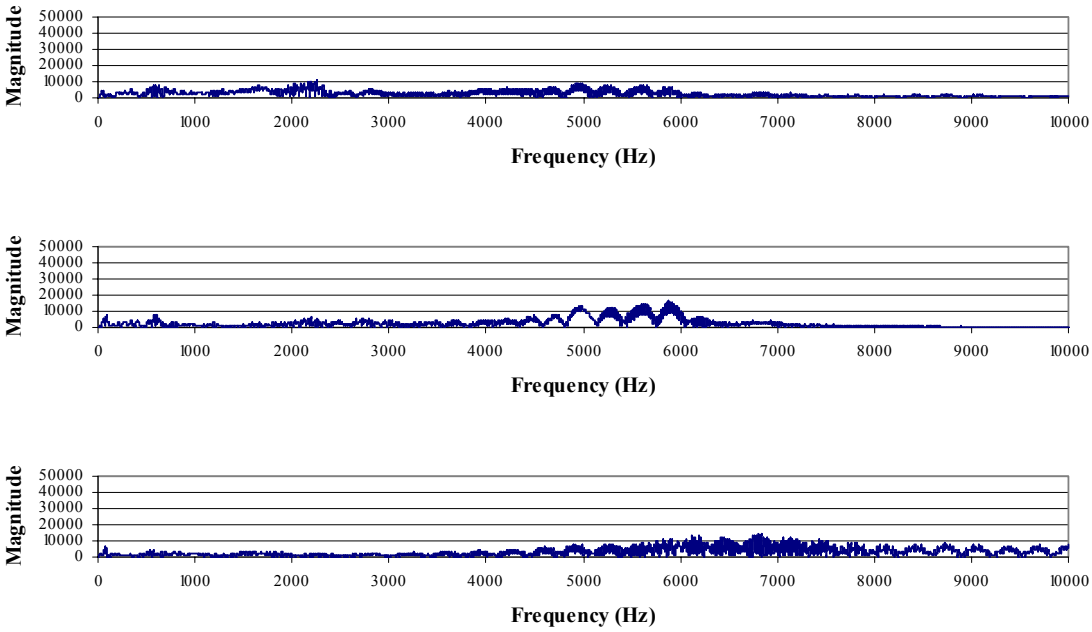

Figure A-119. FFT data from the acetabular cup accelerometer for a ceramic-on-ceramic THA, subjected to a 680 Newton impact load. The signals are for the B1-axis (upper), B2-axis (middle) and B3-axis (lower).

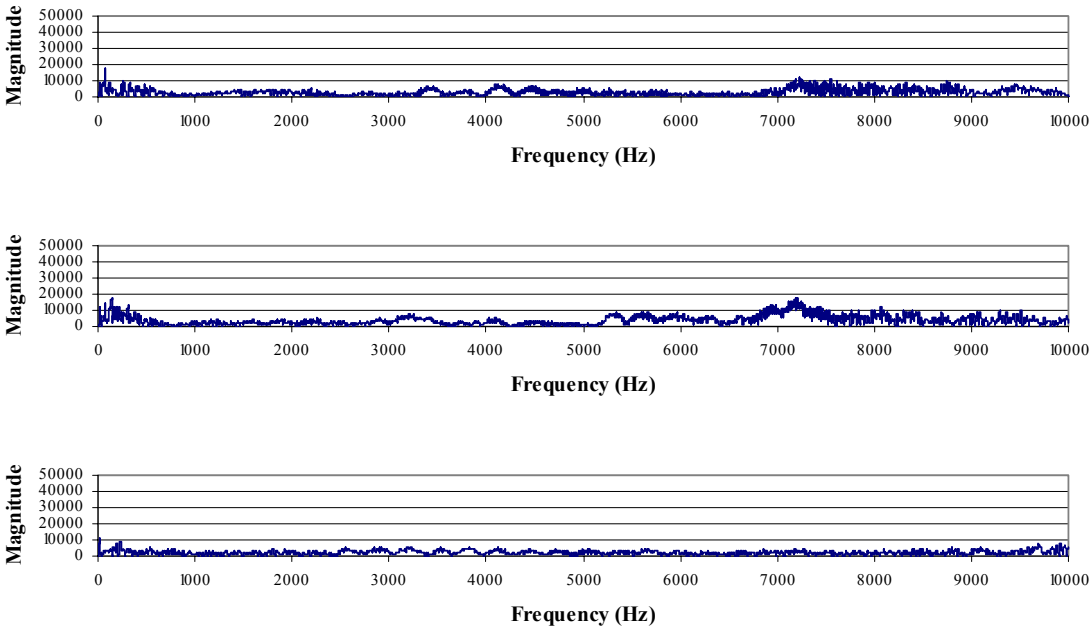

Figure A-120. FFT data from the femoral stem accelerometer for a ceramic-on-ceramic THA, subjected to a 680 Newton impact load. The signals are for the C1-axis (upper), C2-axis (middle) and C3-axis (lower).

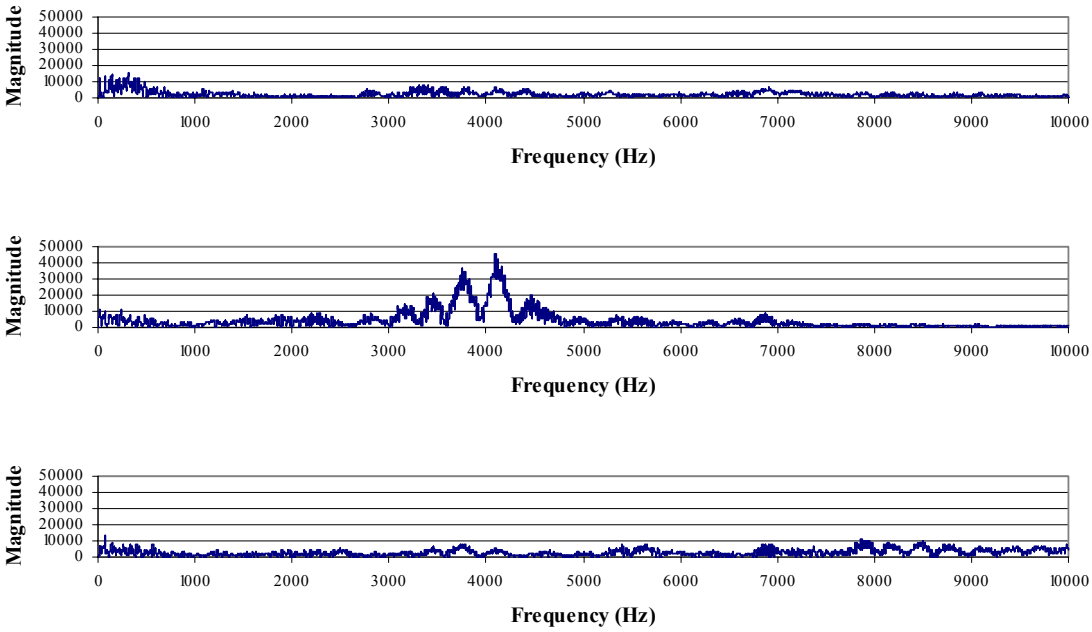

Figure A-121. FFT data from the greater trochanter accelerometer for a ceramic-on-ceramic THA, subjected to a 680 Newton impact load. The signals are for the D1-axis (upper), D2-axis (middle) and D3-axis (lower).

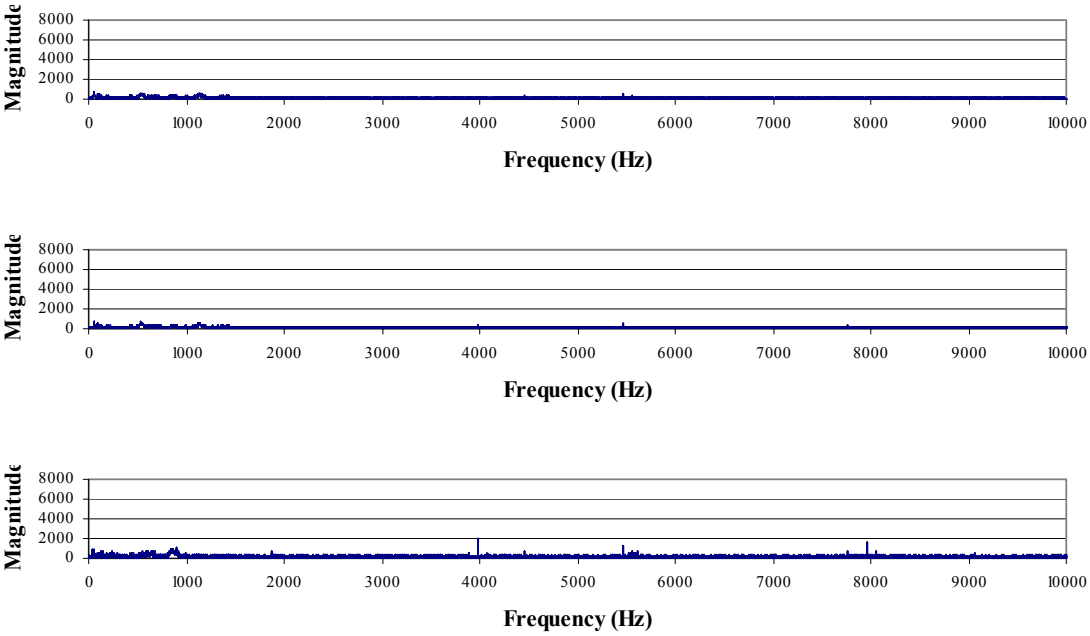

Figure A-122. FFT data from the pelvis accelerometer for a metal-on-polyethylene THA, subjected to an 1150 Newton impact load. The signals are for the A1-axis (upper), A2-axis (middle) and A3-axis (lower).

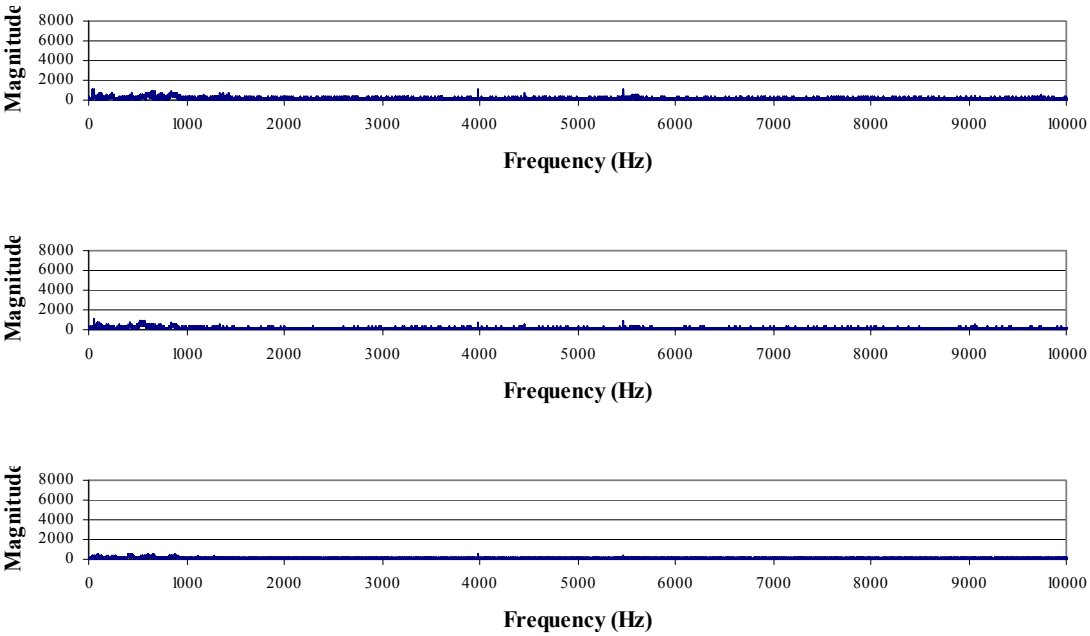

Figure A-123. FFT data from the acetabular cup accelerometer for a metal-on-polyethylene THA, subjected to an 1150 Newton impact load. The signals are for the B1-axis (upper), B2-axis (middle) and B3-axis (lower).

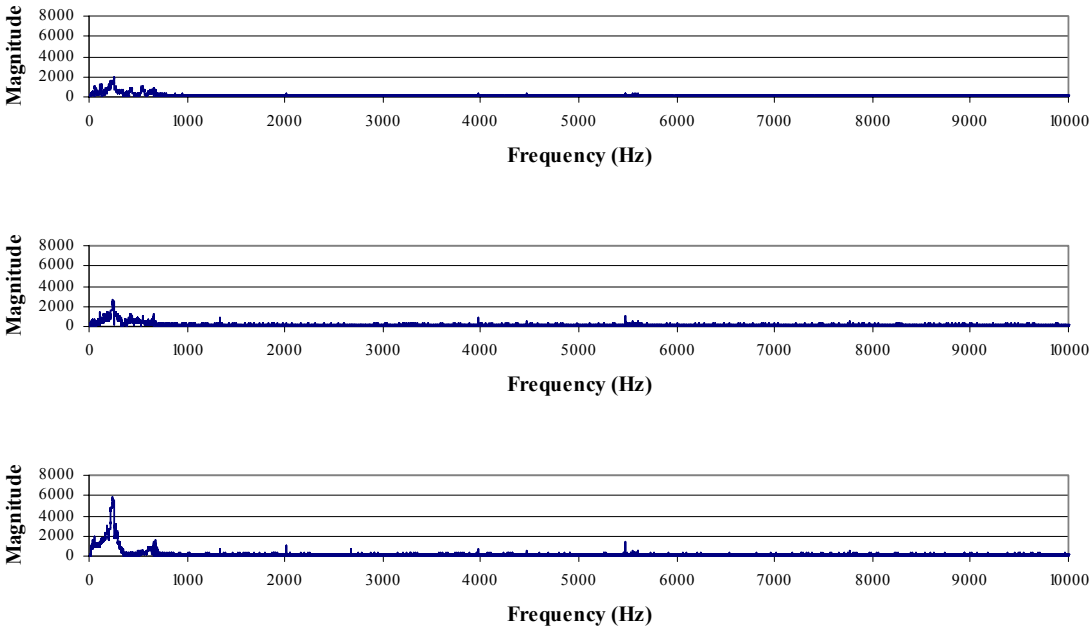

Figure A-124. FFT data from the femoral stem accelerometer for a metal-on-polyethylene THA, subjected to an 1150 Newton impact load. The signals are for the C1-axis (upper), C2-axis (middle) and C3-axis (lower).

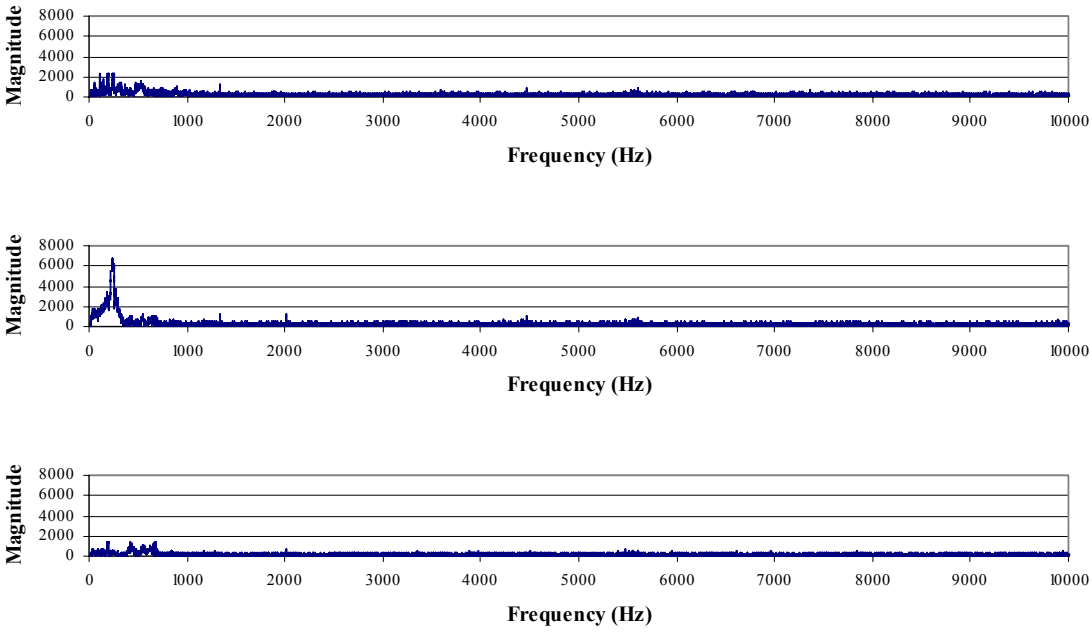

Figure A-125. FFT data from the greater trochanter accelerometer for a metal-on-polyethylene THA, subjected to an 1150 Newton impact load. The signals are for the D1-axis (upper), D2-axis (middle) and D3-axis (lower).

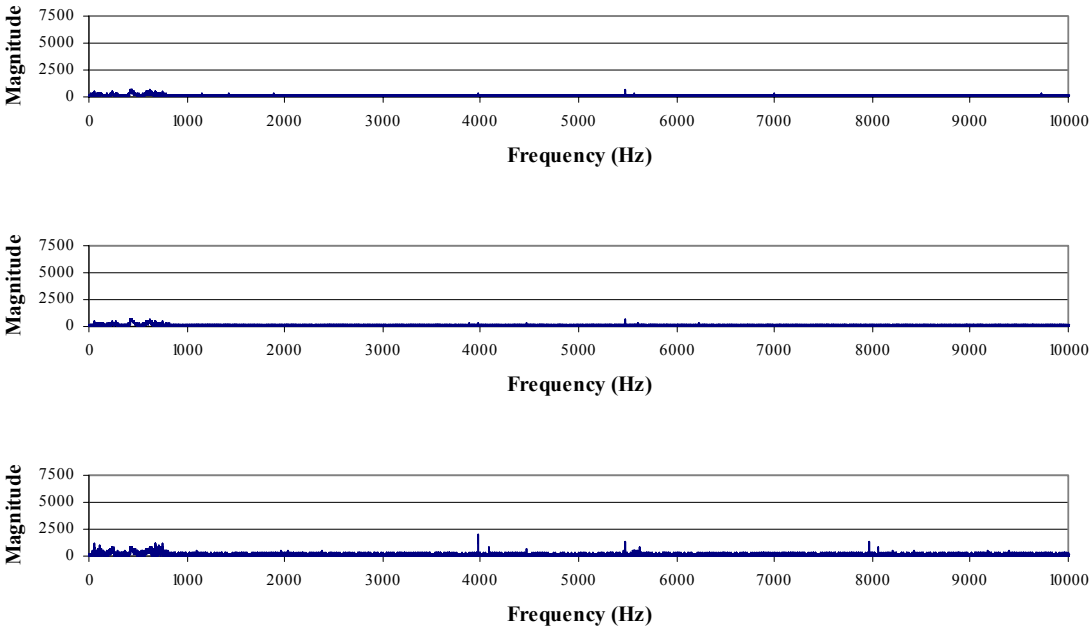

Figure A-126. FFT data from the pelvis accelerometer for a metal-on-metal THA, subjected to an 1150 Newton impact load. The signals are for the A1-axis (upper), A2-axis (middle) and A3-axis (lower).

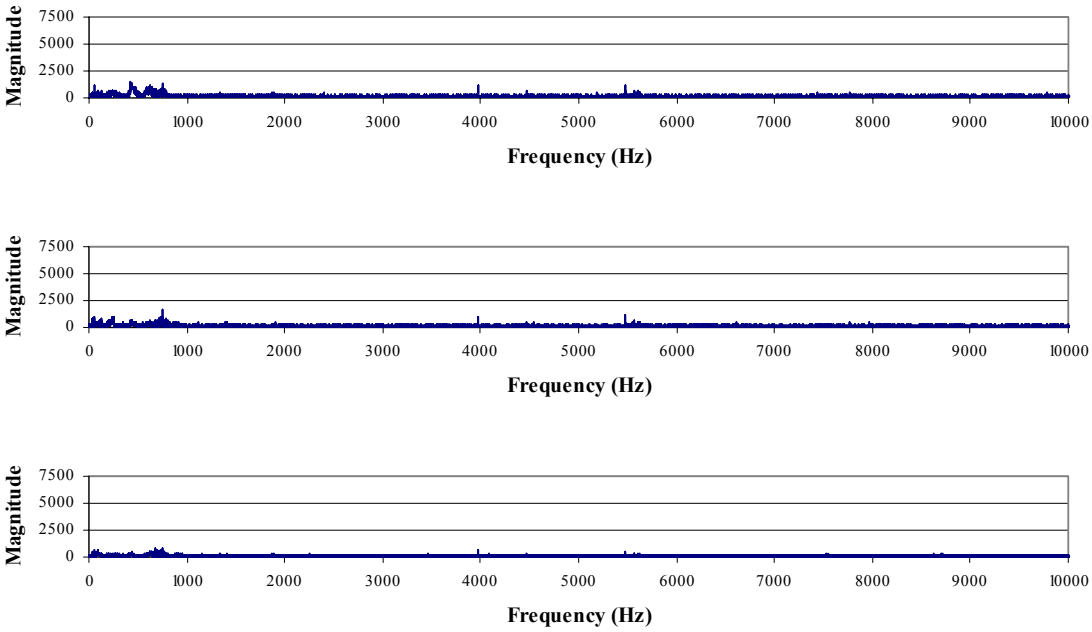

Figure A-127 FFT data from the acetabular cup accelerometer for a metal-on-metal THA, subjected to an 1150 Newton impact load. The signals are for the B1-axis (upper), B2-axis (middle) and B3-axis (lower).

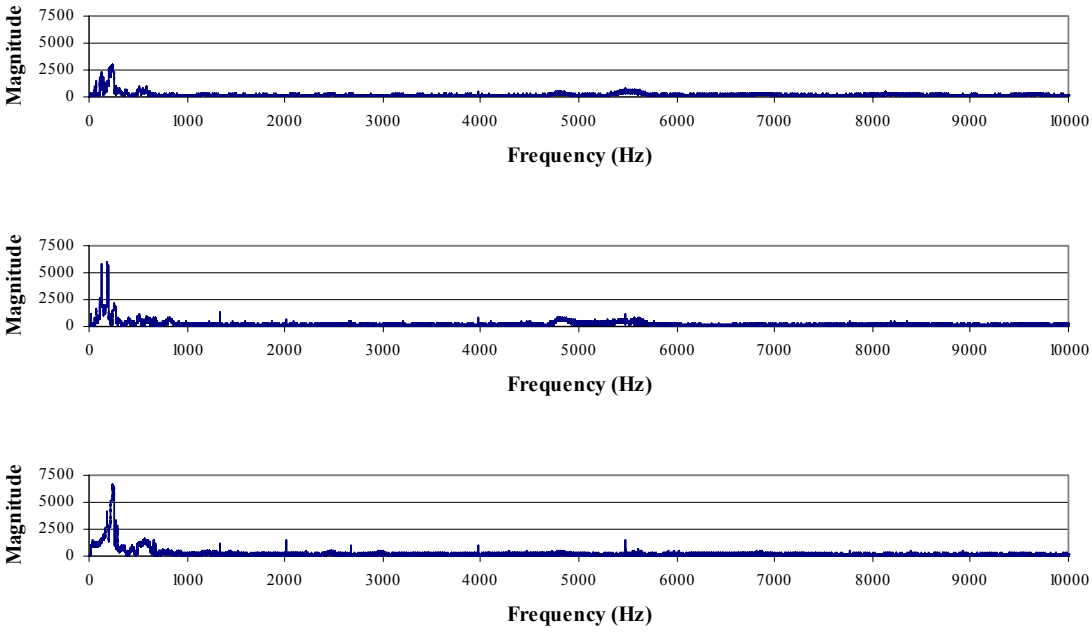

Figure A-128. FFT data from the femoral stem accelerometer for a metal-on-metal THA, subjected to an 1150 Newton impact load. The signals are for the C1-axis (upper), C2-axis (middle) and C3-axis (lower).

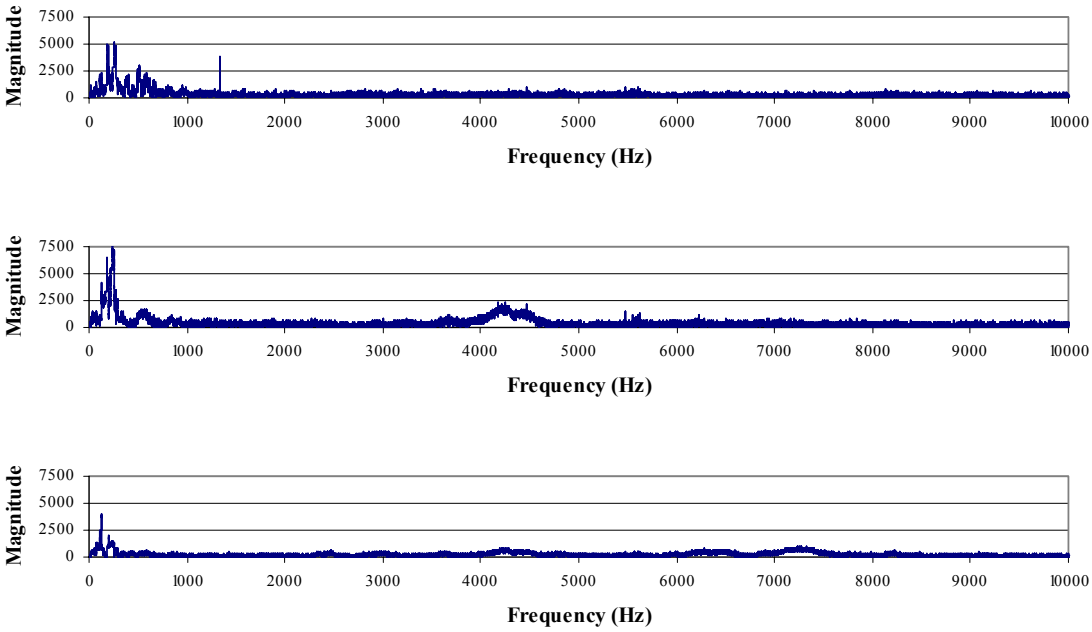

Figure A-129. FFT data from the greater trochanter accelerometer for a metal-on-metal THA, subjected to an 1150 Newton impact load. The signals are for the D1-axis (upper), D2-axis (middle) and D3-axis (lower).

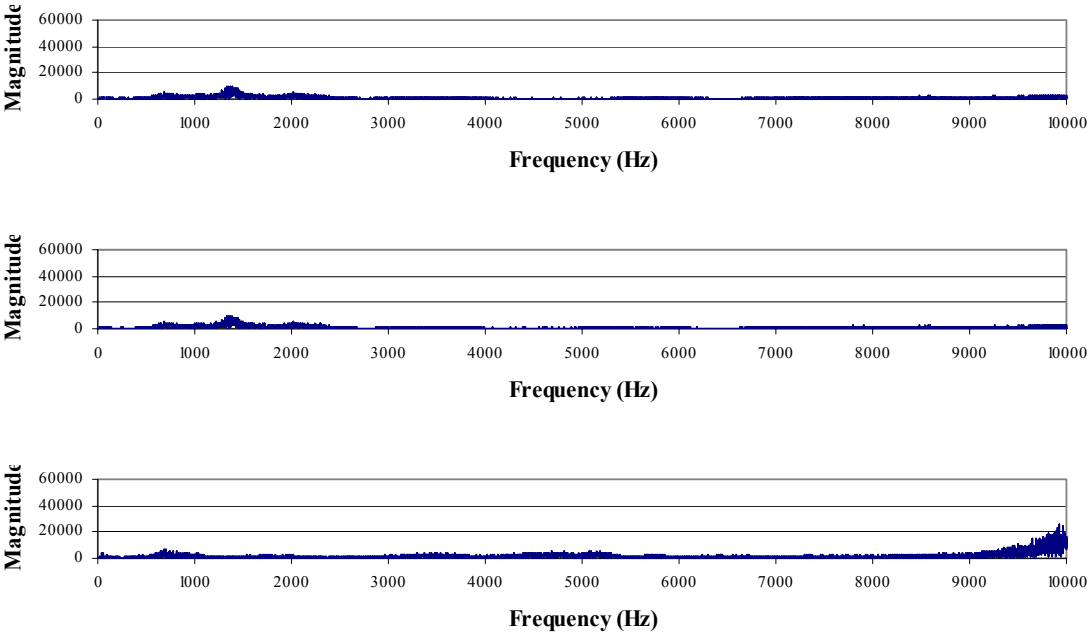

Figure A-130. FFT data from the pelvis accelerometer for a ceramic-on-ceramic THA, subjected to an 1150 Newton impact load. The signals are for the A1-axis (upper), A2-axis (middle) and A3-axis (lower).

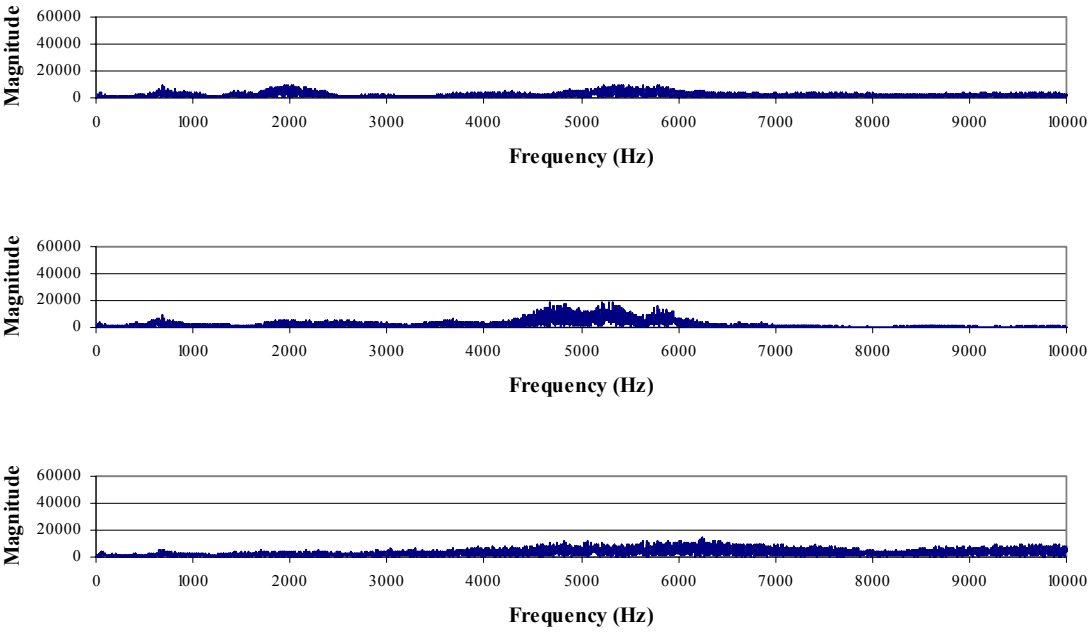

Figure A-131. FFT data from the acetabular cup accelerometer for a ceramic-on-ceramic THA, subjected to an 1150 Newton impact load. The signals are for the B1-axis (upper), B2-axis (middle) and B3-axis (lower).

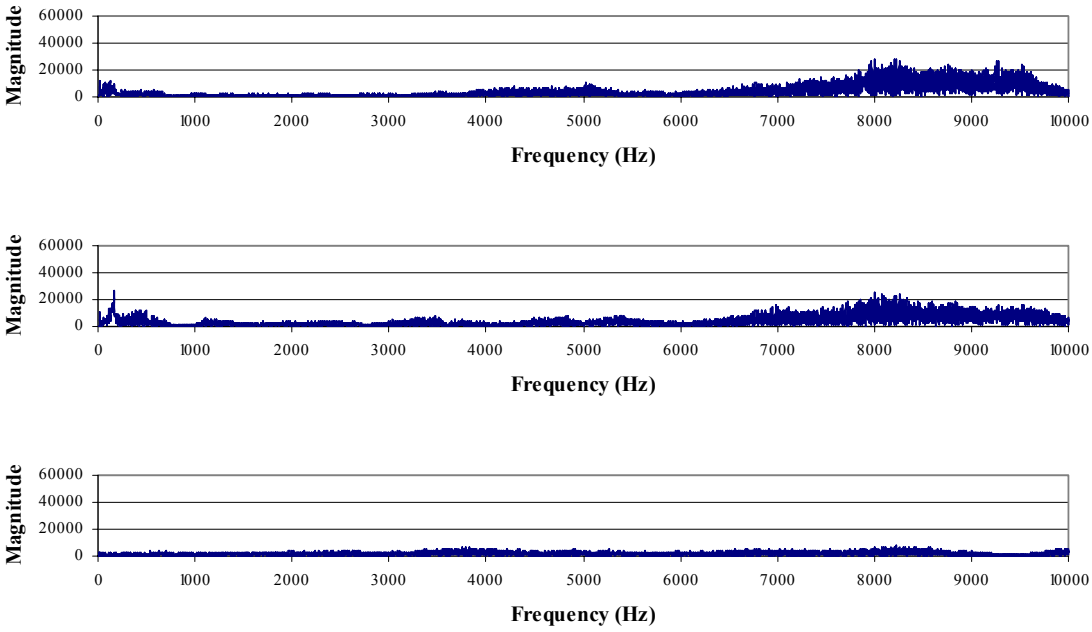

Figure A-132. FFT data from the femoral stem accelerometer for a ceramic-on-ceramic THA, subjected to an 1150 Newton impact load. The signals are for the C1-axis (upper), C2-axis (middle) and C3-axis (lower).

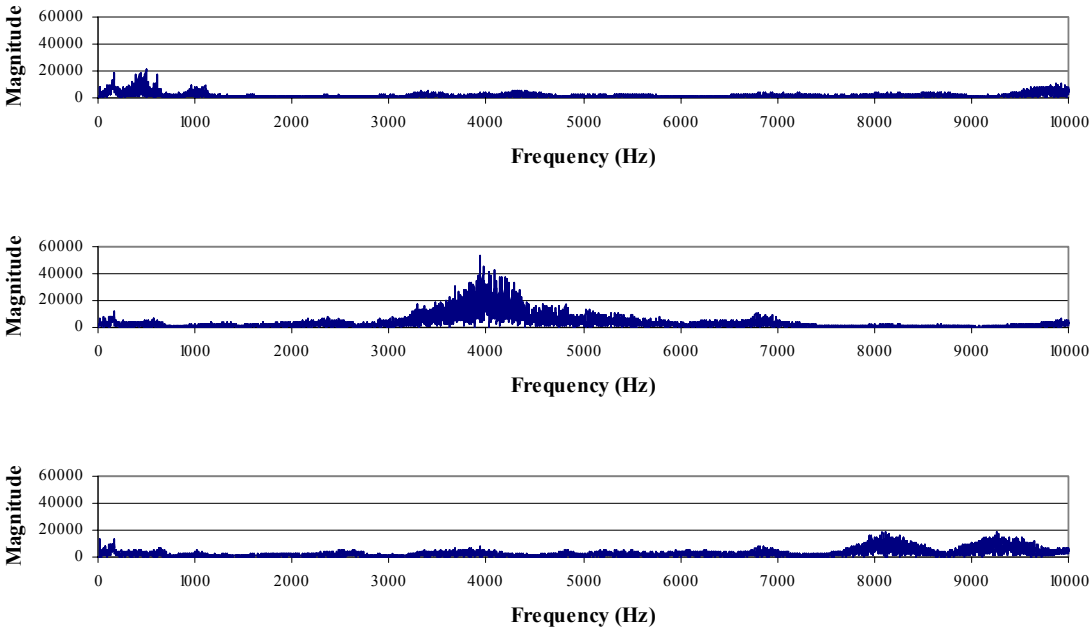

Figure A-133. FFT data from the greater trochanter accelerometer for a ceramic-on-ceramic THA, subjected to an 1150 Newton impact load. The signals are for the D1-axis (upper), D2-axis (middle) and D3-axis (lower).

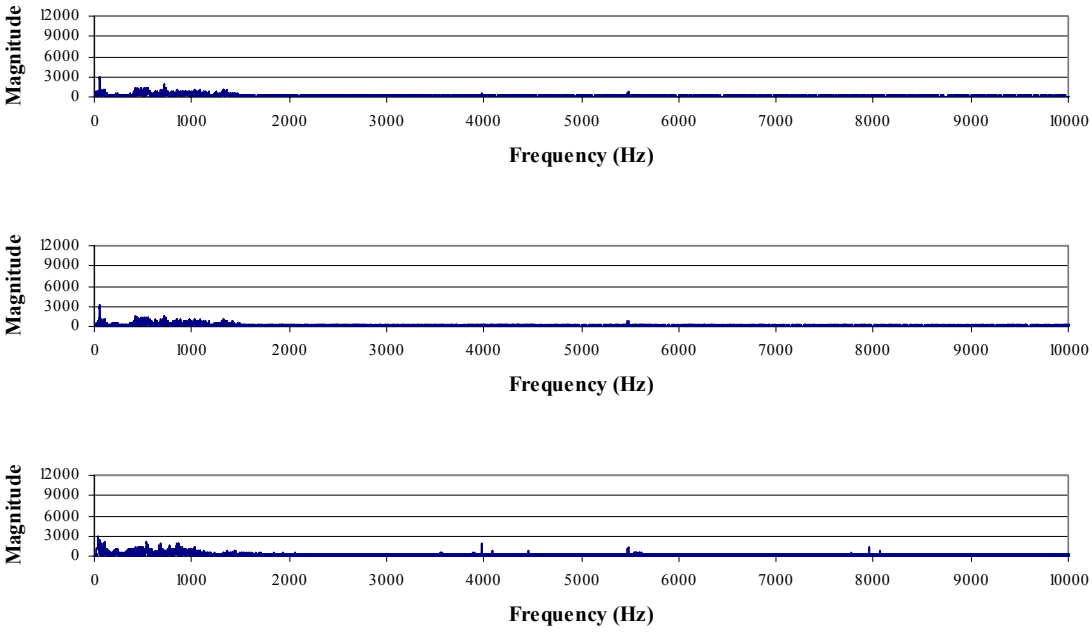

Figure A-134. FFT data from the pelvis accelerometer for a metal-on-polyethylene THA, subjected to a 1280 Newton impact load. The signals are for the A1-axis (upper), A2-axis (middle) and A3-axis (lower).

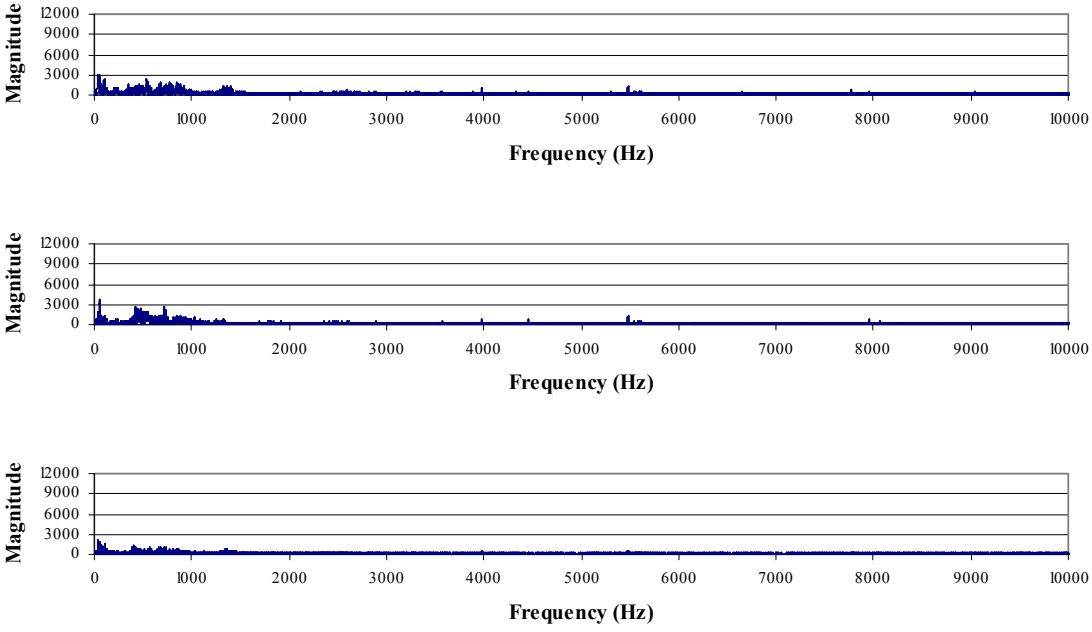

Figure A-135. FFT data from the acetabular cup accelerometer for a metal-on-polyethylene THA, subjected to a 1280 Newton impact load. The signals are for the B1-axis (upper), B2-axis (middle) and B3-axis (lower).

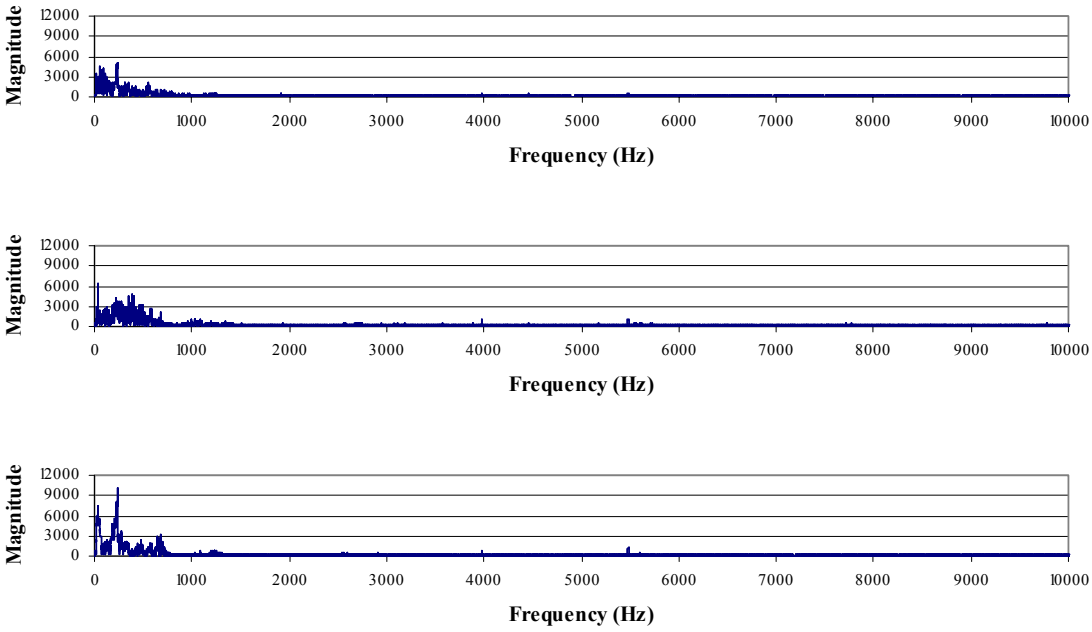

Figure A-136. FFT data from the femoral stem accelerometer for a metal-on-polyethylene THA, subjected to a 1280 Newton impact load. The signals are for the C1-axis (upper), C2-axis (middle) and C3-axis (lower).

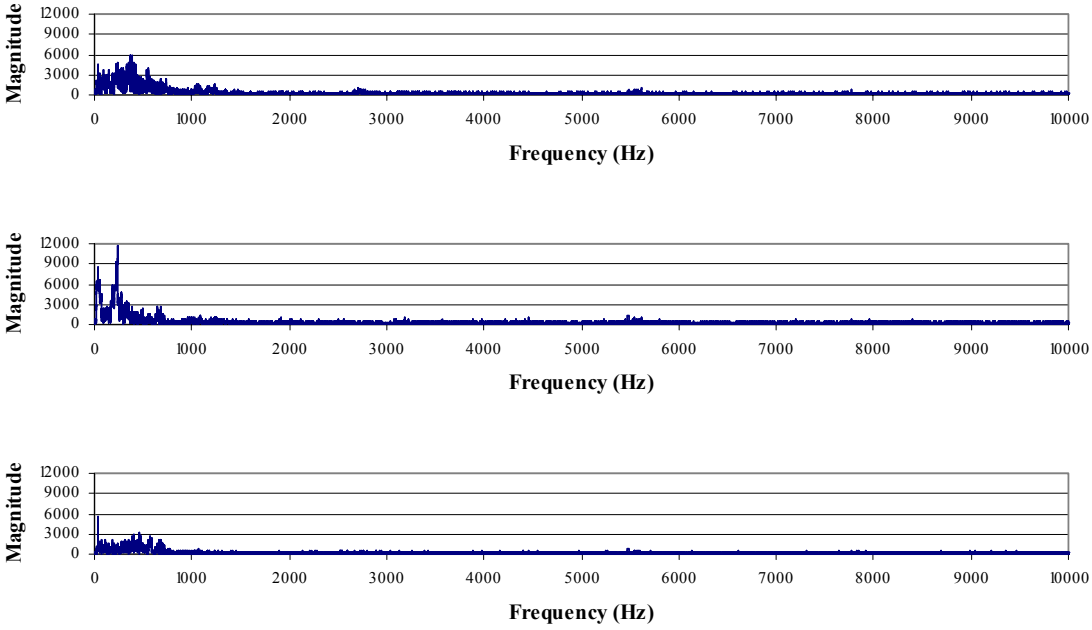

Figure A-137. FFT data from the greater trochanter accelerometer for a metal-on-polyethylene THA, subjected to a 1280 Newton impact load. The signals are for the D1-axis (upper), D2-axis (middle) and D3-axis (lower).

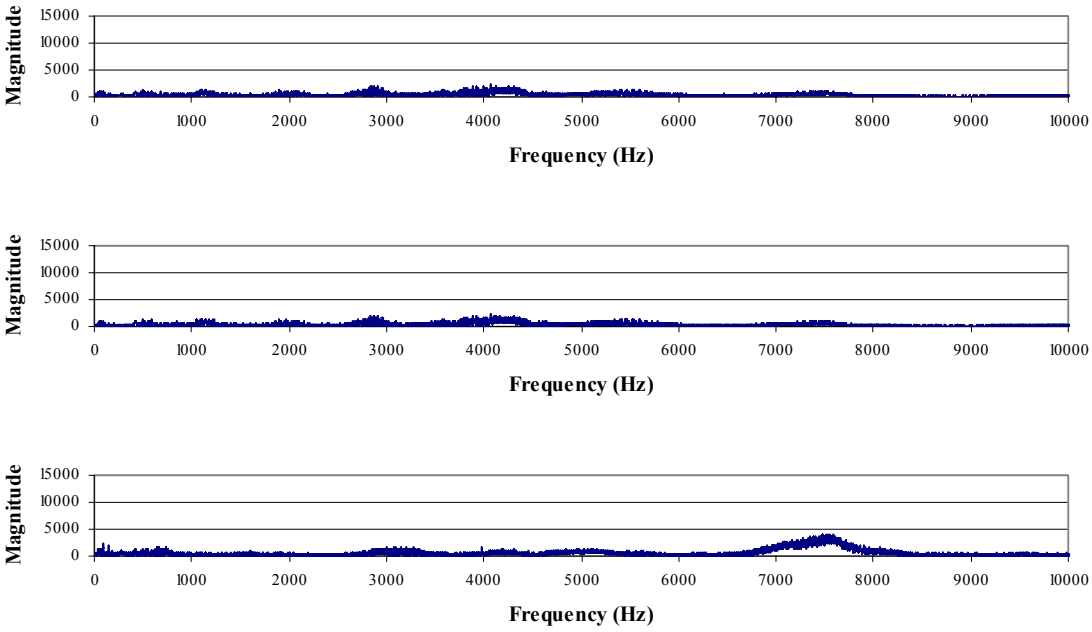

Figure A-138. FFT data from the pelvis accelerometer for a metal-on-metal THA, subjected to a 1280 Newton impact load. The signals are for the A1-axis (upper), A2-axis (middle) and A3-axis (lower).

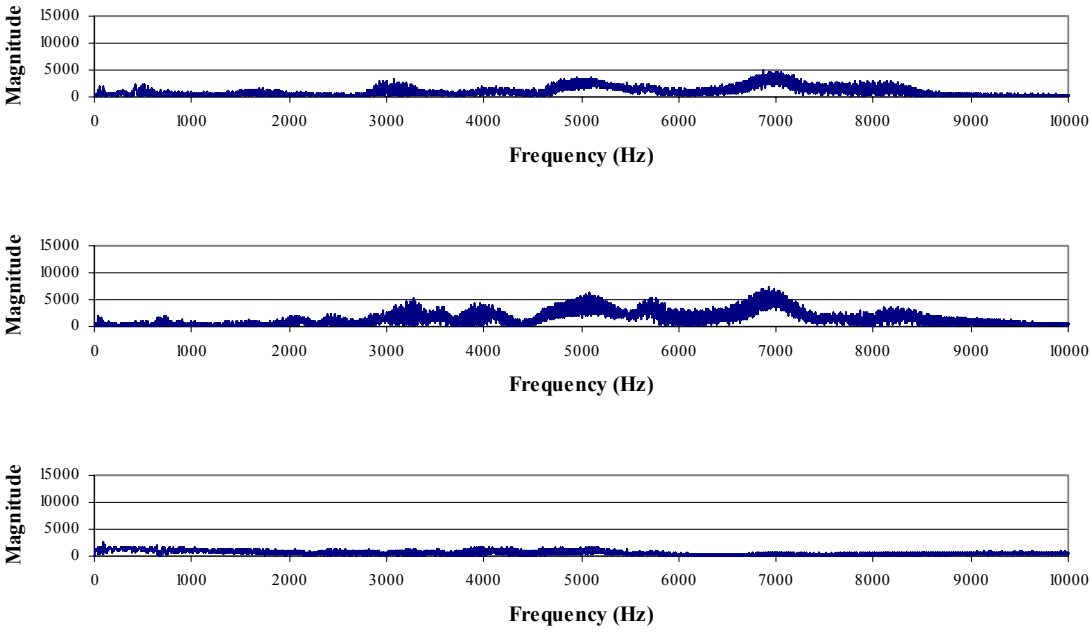

Figure A-139. FFT data from the acetabular cup accelerometer for a metal-on-metal THA, subjected to a 1280 Newton impact load. The signals are for the B1-axis (upper), B2-axis (middle) and B3-axis (lower).

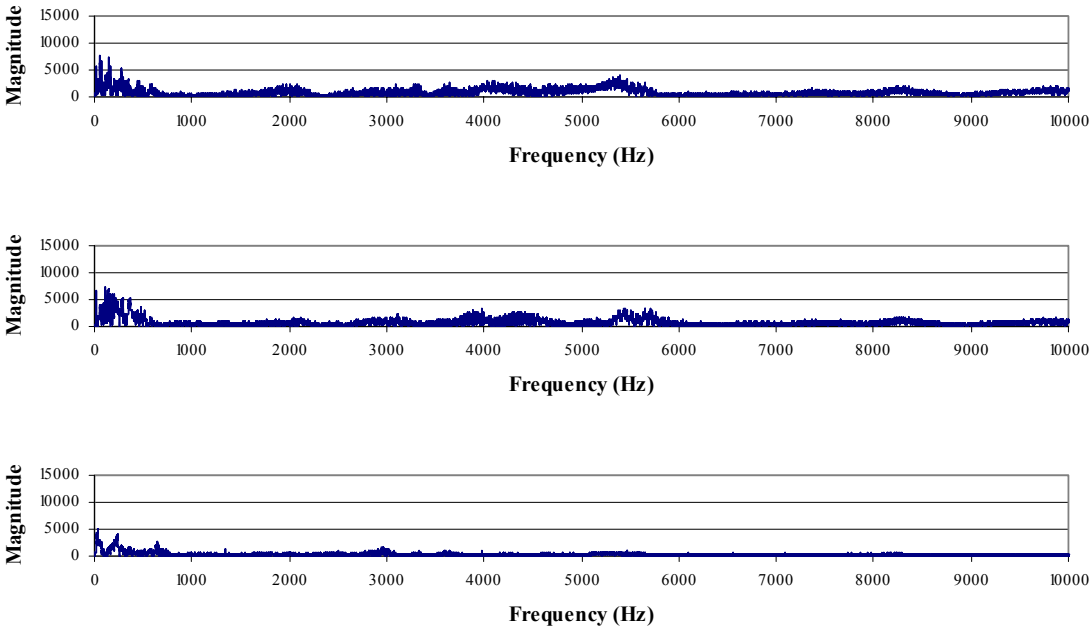

Figure A-140. FFT data from the femoral stem accelerometer for a metal-on-metal THA, subjected to a 1280 Newton impact load. The signals are for the C1-axis (upper), C2-axis (middle) and C3-axis (lower).

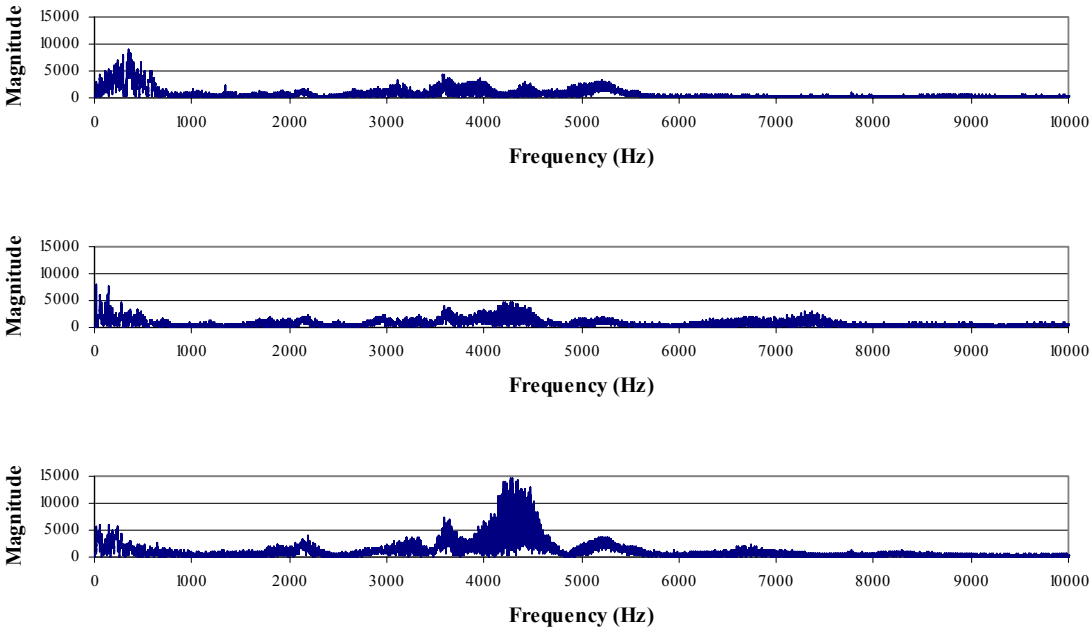

Figure A-141. FFT data from the greater trochanter accelerometer for a metal-on-metal THA, subjected to a 1280 Newton impact load. The signals are for the D1-axis (upper), D2-axis (middle) and D3-axis (lower).

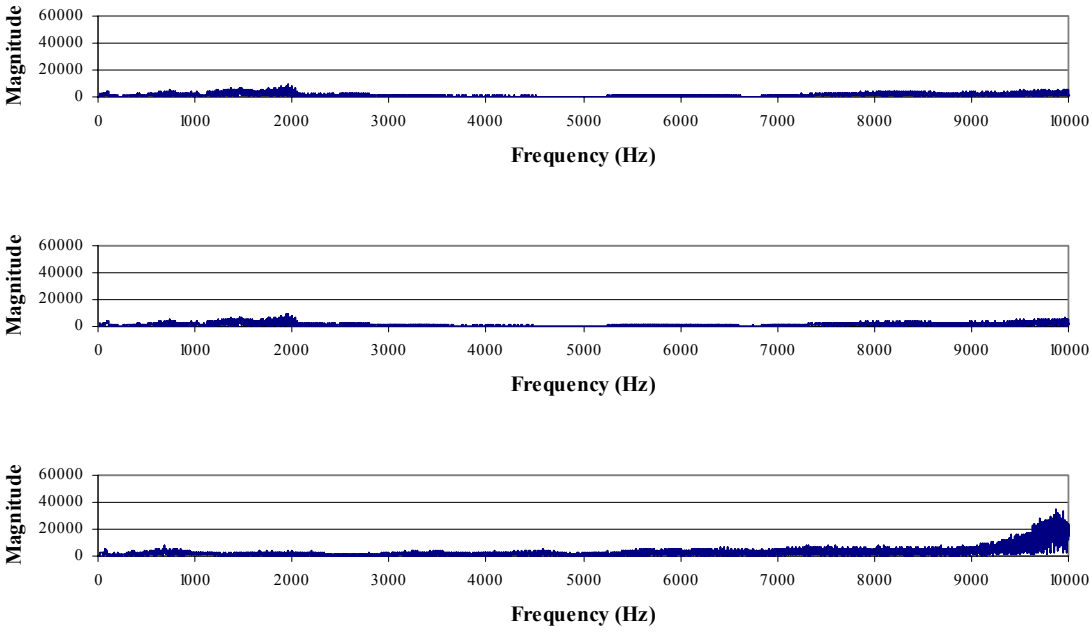

Figure A-142. FFT data from the pelvis accelerometer for a ceramic-on-ceramic THA, subjected to a 1280 Newton impact load. The signals are for the A1-axis (upper), A2-axis (middle) and A3-axis (lower).

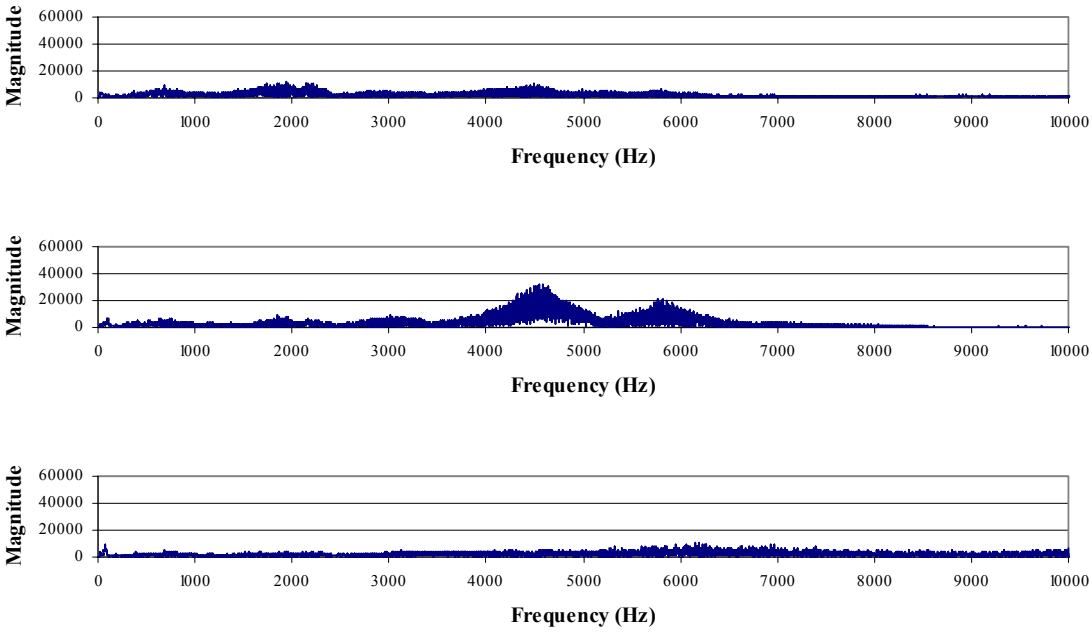

Figure A-143. FFT data from the acetabular cup accelerometer for a ceramic-on-ceramic THA, subjected to a 1280 Newton impact load. The signals are for the B1-axis (upper), B2-axis (middle) and B3-axis (lower).

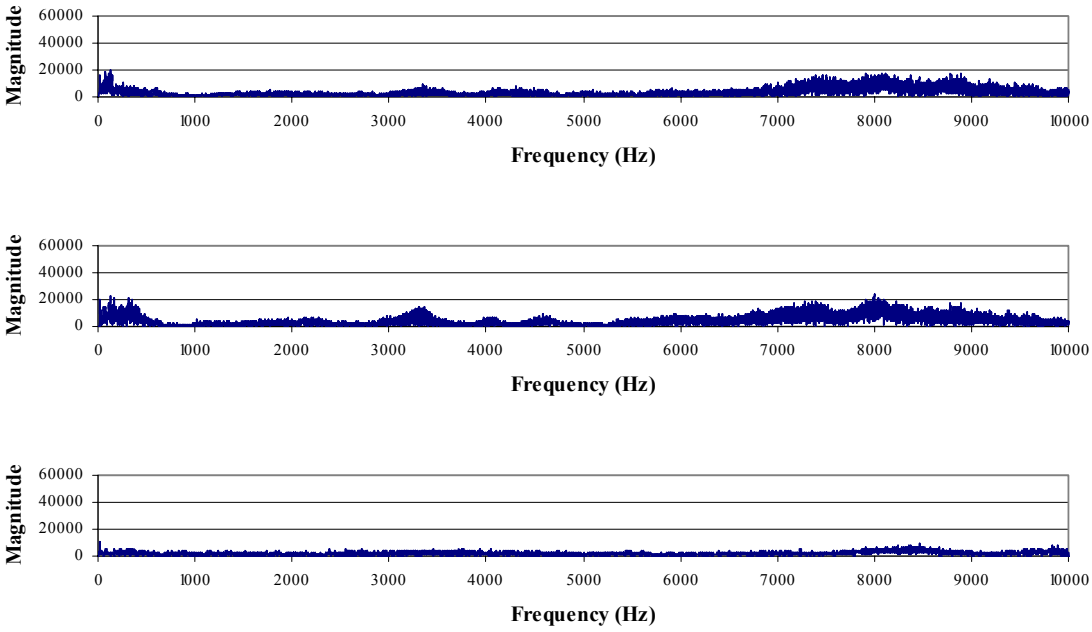

Figure A-144. FFT data from the femoral stem accelerometer for a ceramic-on-ceramic THA, subjected to a 1280 Newton impact load. The signals are for the C1-axis (upper), C2-axis (middle) and C3-axis (lower).

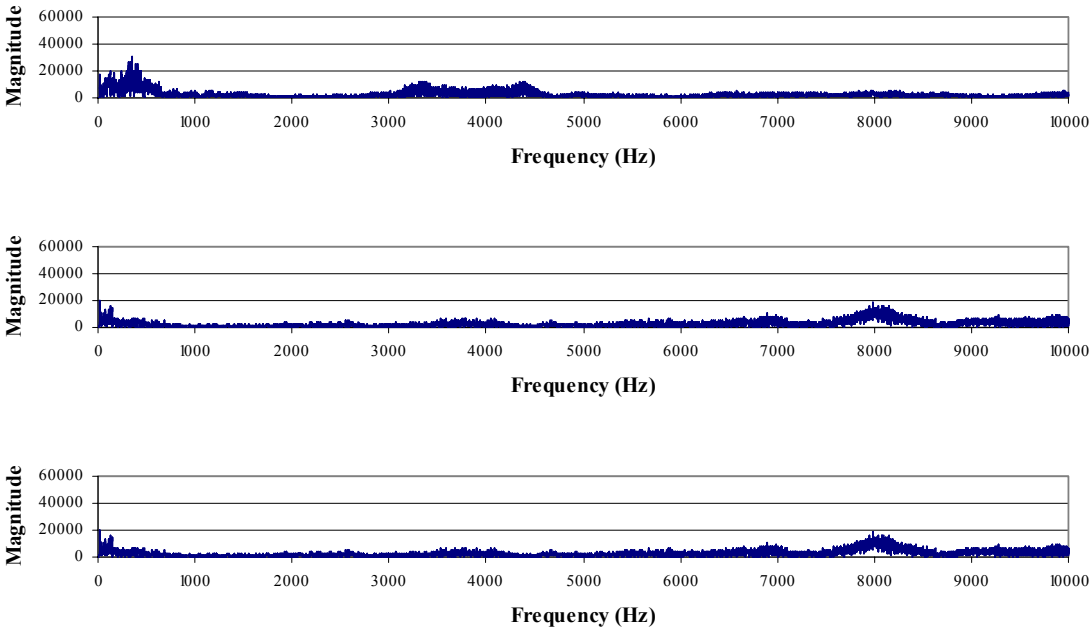

Figure A-145. FFT data from the greater trochanter accelerometer for a ceramic-on-ceramic THA, subjected to a 1280 Newton impact load. The signals are for the D1-axis (upper), D2-axis (middle) and D3-axis (lower).

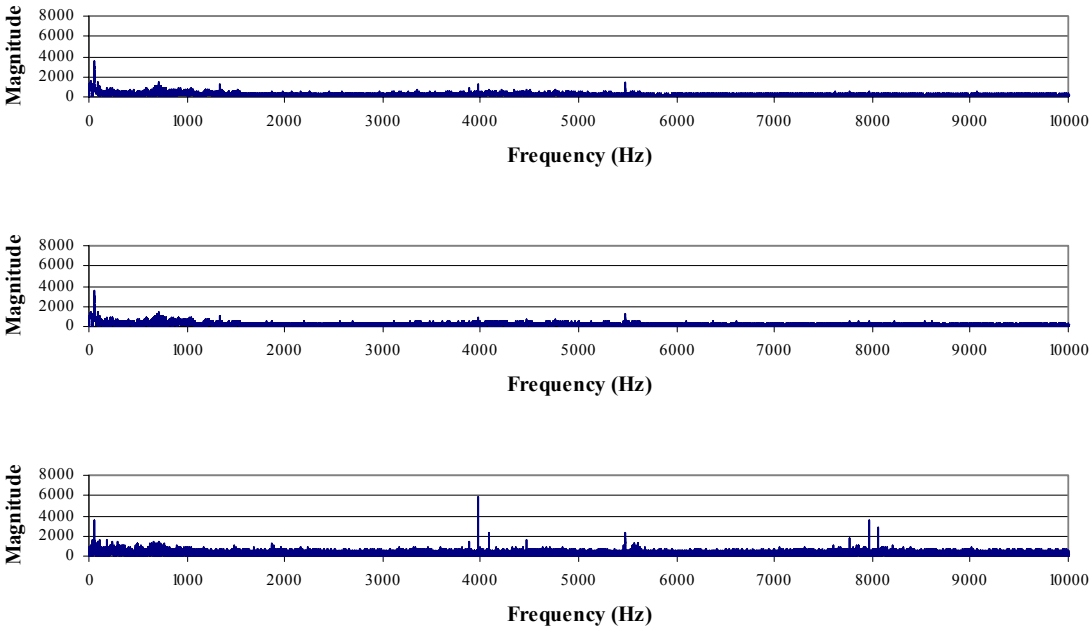

Figure A-146. FFT data from the pelvis accelerometer for a metal-on-polyethylene THA, subjected to a 1500 Newton impact load. The signals are for the A1-axis (upper), A2-axis (middle) and A3-axis (lower).

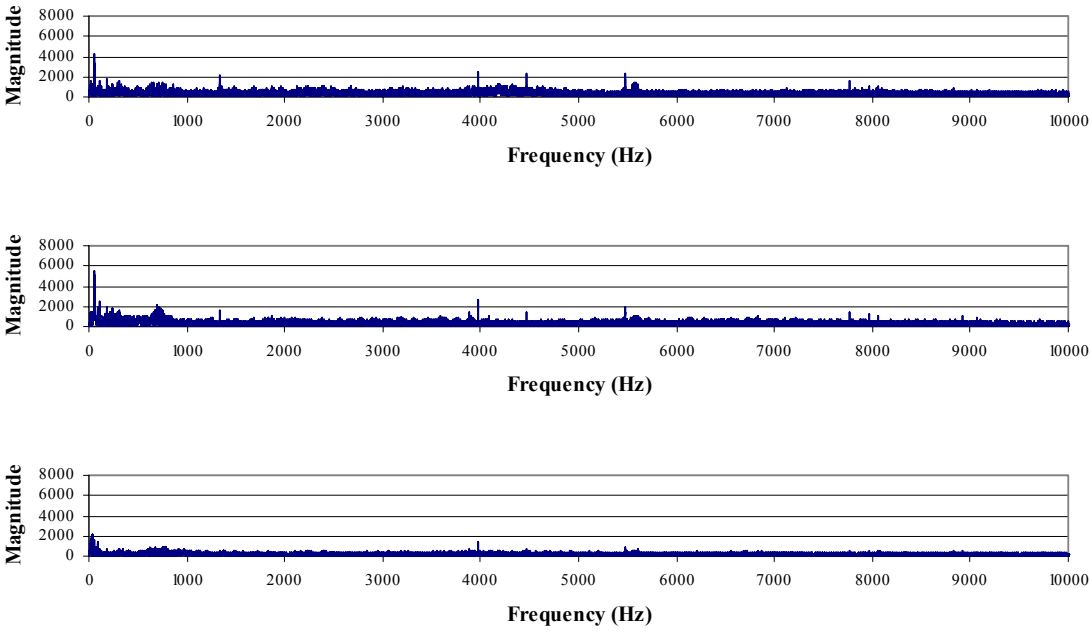

Figure A-147. FFT data from the acetabular cup accelerometer for a metal-on-polyethylene THA, subjected to a 1500 Newton impact load. The signals are for the B1-axis (upper), B2-axis (middle) and B3-axis (lower).

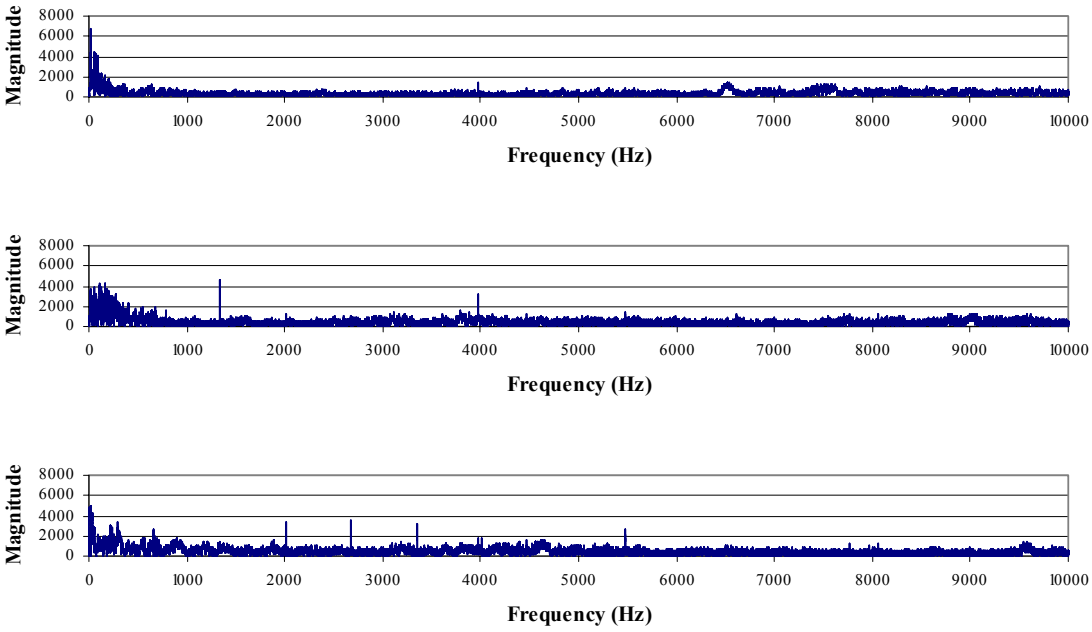

Figure A-148. FFT data from the femoral stem accelerometer for a metal-on-polyethylene THA, subjected to a 1500 Newton impact load. The signals are for the C1-axis (upper), C2-axis (middle) and C3-axis (lower).

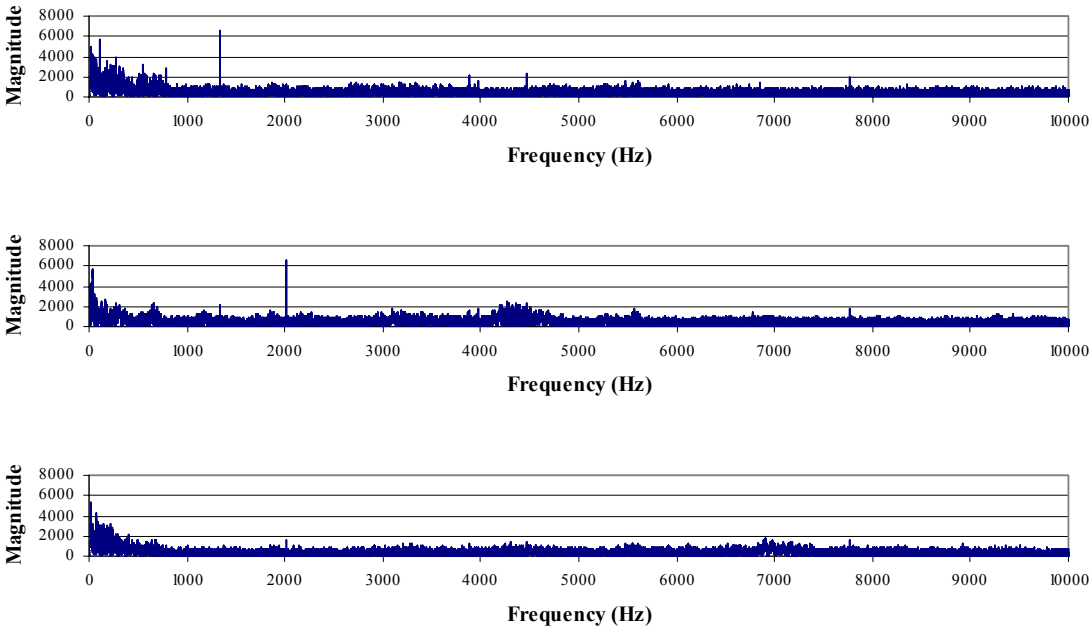

Figure A-149. FFT data from the greater trochanter accelerometer for a metal-on-polyethylene THA, subjected to a 1500 Newton impact load. The signals are for the D1-axis (upper), D2-axis (middle) and D3-axis (lower).

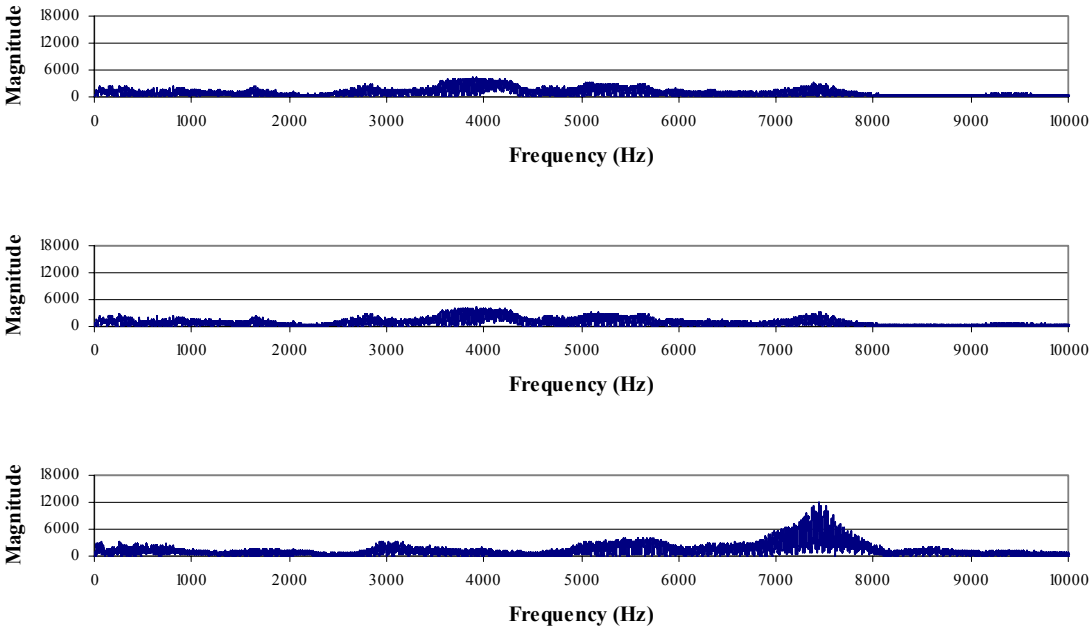

Figure A-150. FFT data from the pelvis accelerometer for a metal-on-metal THA, subjected to a 1500 Newton impact load. The signals are for the A1-axis (upper), A2-axis (middle) and A3-axis (lower).

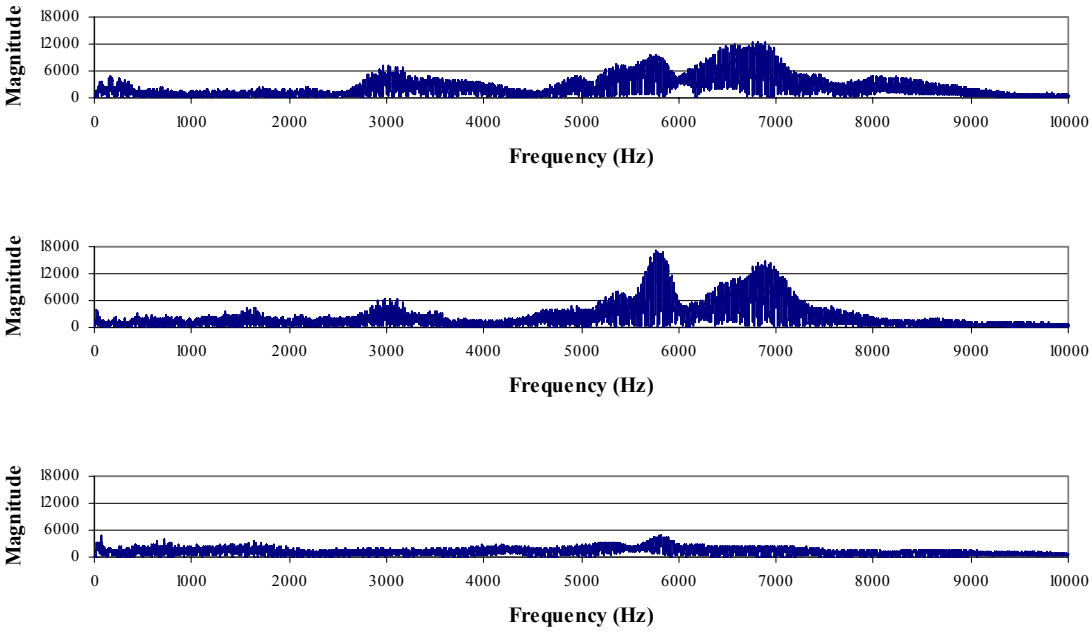

Figure A-151. FFT data from the acetabular cup accelerometer for a metal-on-metal THA, subjected to a 1500 Newton impact load. The signals are for the B1-axis (upper), B2-axis (middle) and B3-axis (lower).

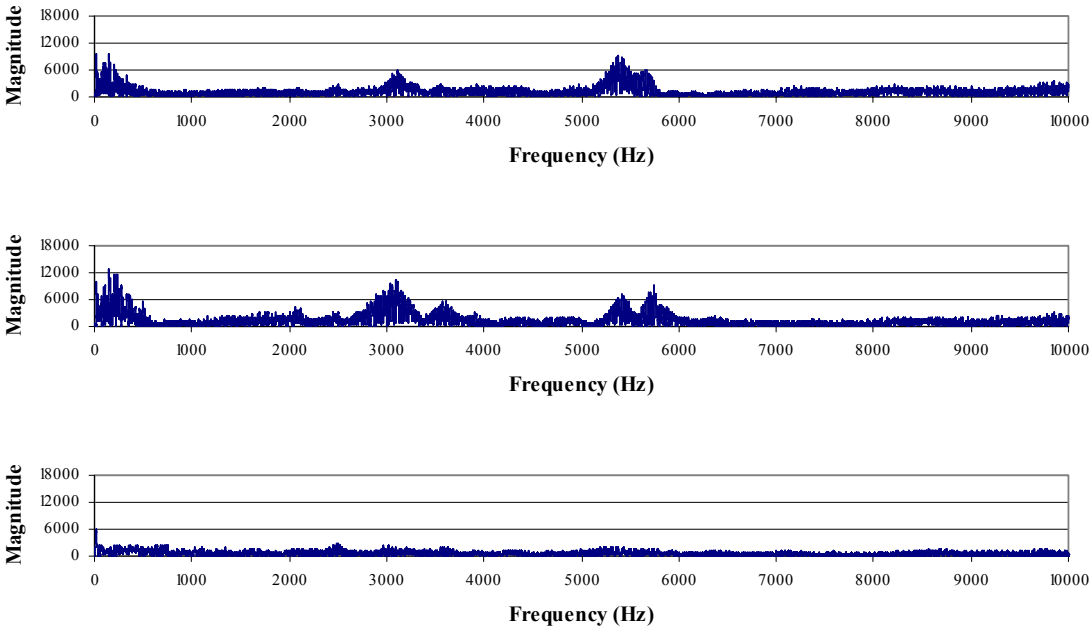

Figure A-152. FFT data from the femoral stem accelerometer for a metal-on-metal THA, subjected to a 1500 Newton impact load. The signals are for the C1-axis (upper), C2-axis (middle) and C3-axis (lower).

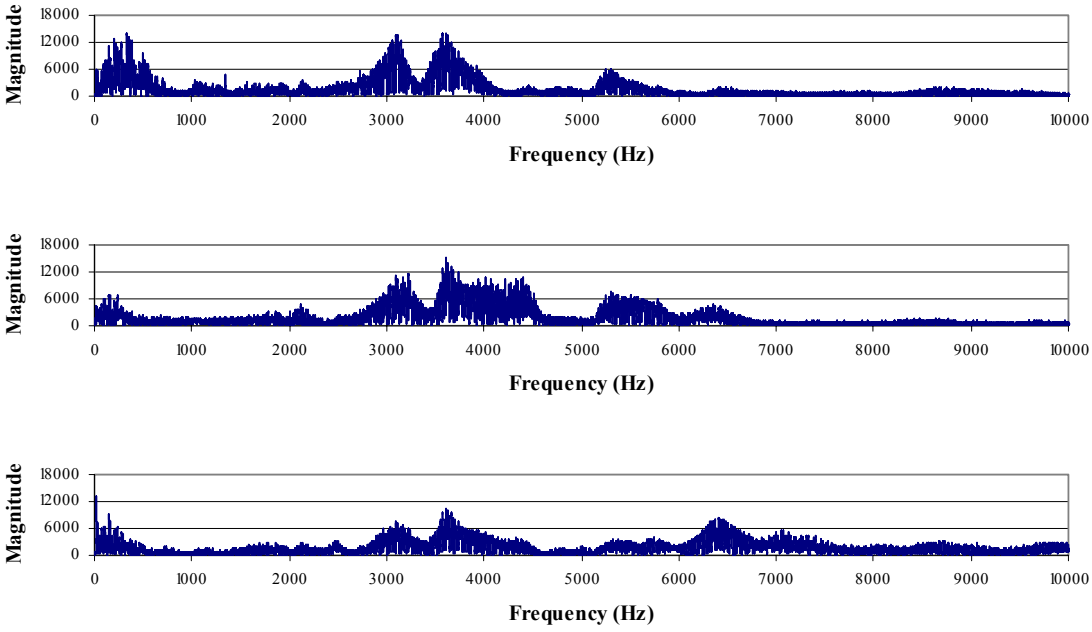

Figure A-153. FFT data from the greater trochanter accelerometer for a metal-on-metal THA, subjected to a 1500 Newton impact load. The signals are for the D1-axis (upper), D2-axis (middle) and D3-axis (lower).

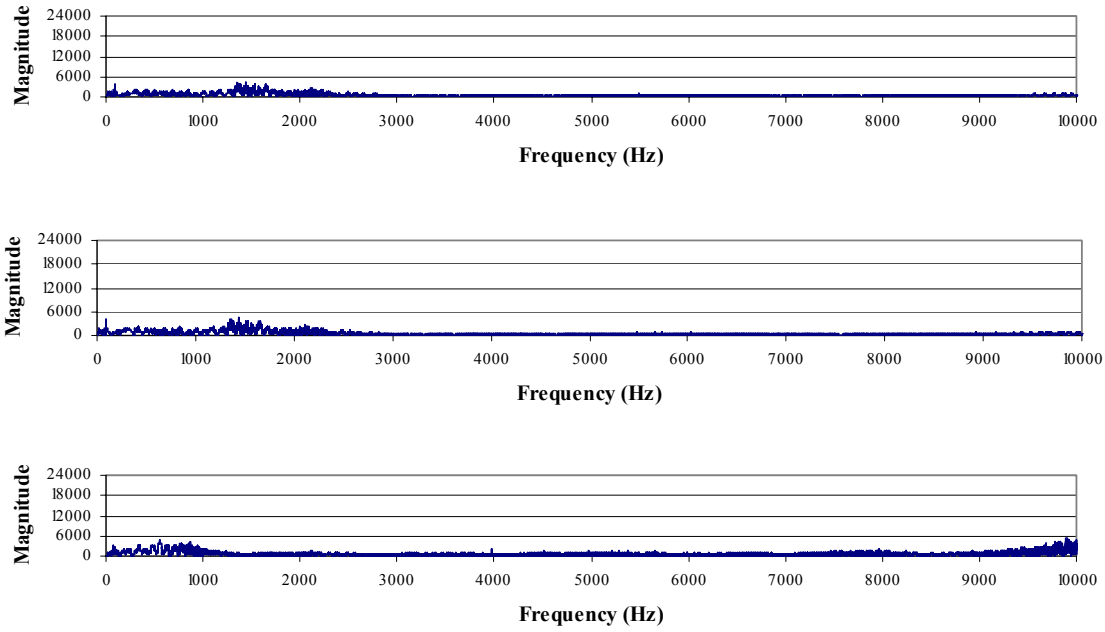

Figure A-154. FFT data from the pelvis accelerometer for a ceramic-on-ceramic THA, subjected to a 1500 Newton impact load. The signals are for the A1-axis (upper), A2-axis (middle) and A3-axis (lower).

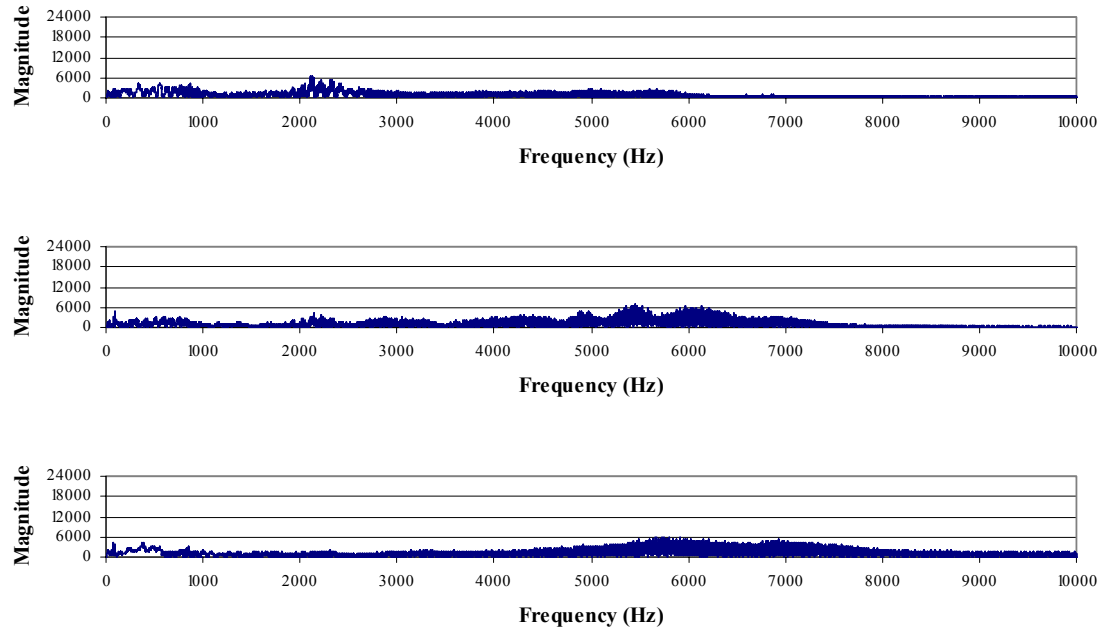

Figure A-155. FFT data from the acetabular cup accelerometer for a ceramic-on-ceramic THA, subjected to a 1500 Newton impact load. The signals are for the B1-axis (upper), B2-axis (middle) and B3-axis (lower).

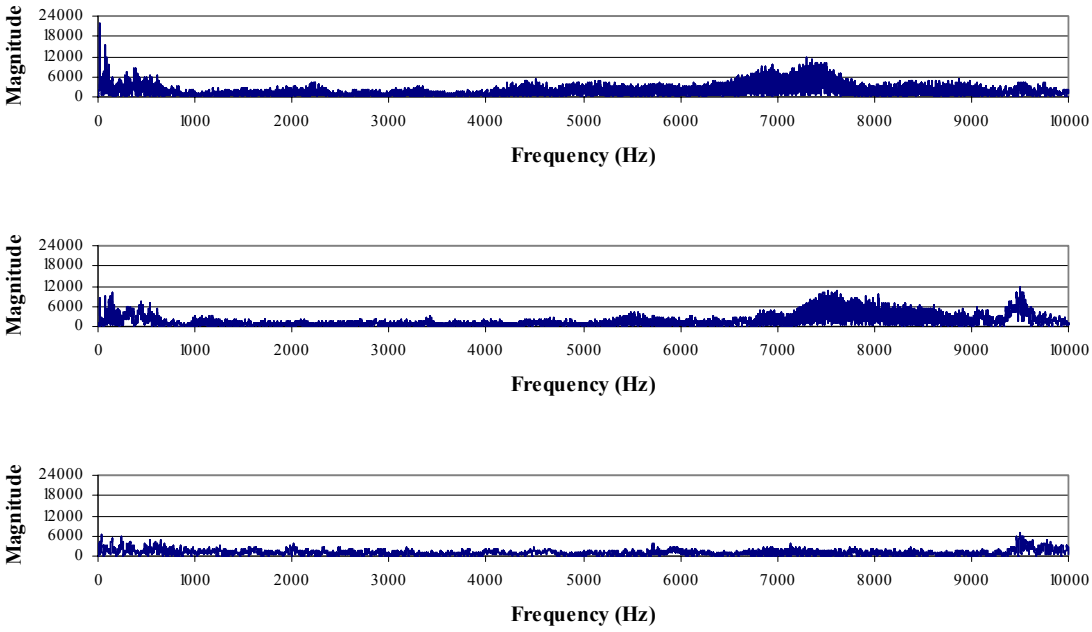

Figure A-156. FFT data from the femoral stem accelerometer for a ceramic-on-ceramic THA, subjected to a 1500 Newton impact load. The signals are for the C1-axis (upper), C2-axis (middle) and C3-axis (lower).

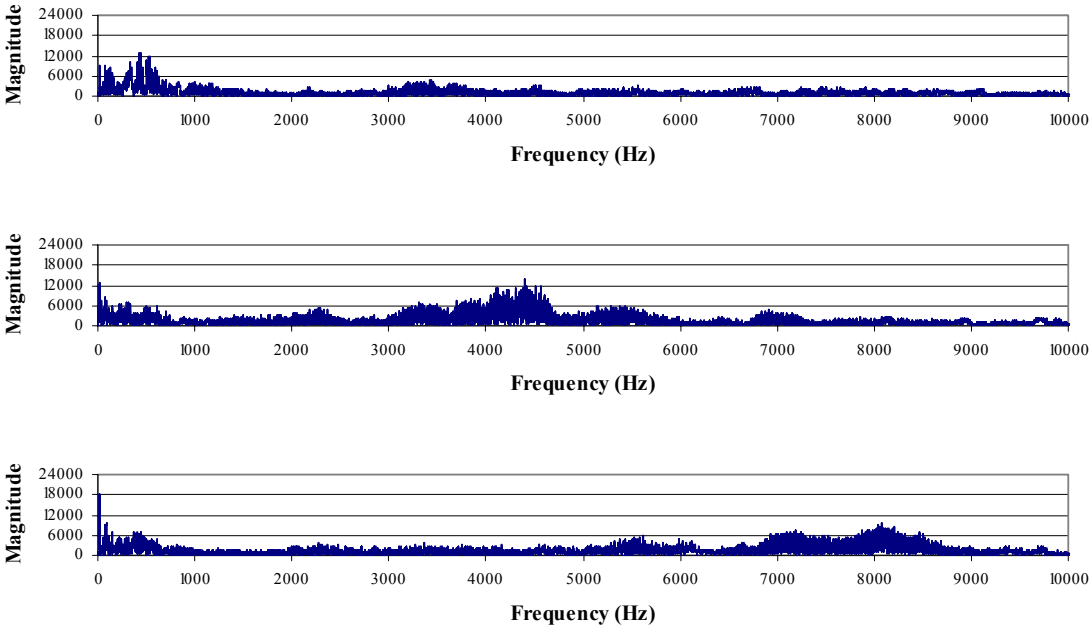

Figure A-157. FFT data from the greater trochanter accelerometer for a ceramic-on-ceramic THA, subjected to a 1500 Newton impact load. The signals are for the D1-axis (upper), D2-axis (middle) and D3-axis (lower).

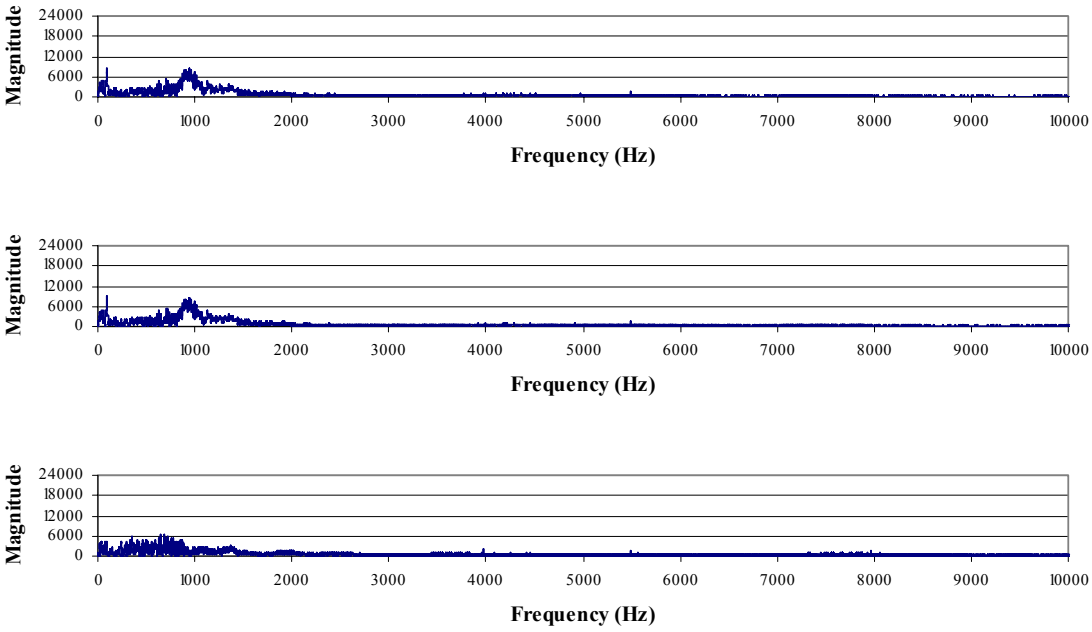

Figure A-158. FFT data from the pelvis accelerometer for a metal-on-polyethylene THA, subjected to a 1730 Newton impact load. The signals are for the A1-axis (upper), A2-axis (middle) and A3-axis (lower).

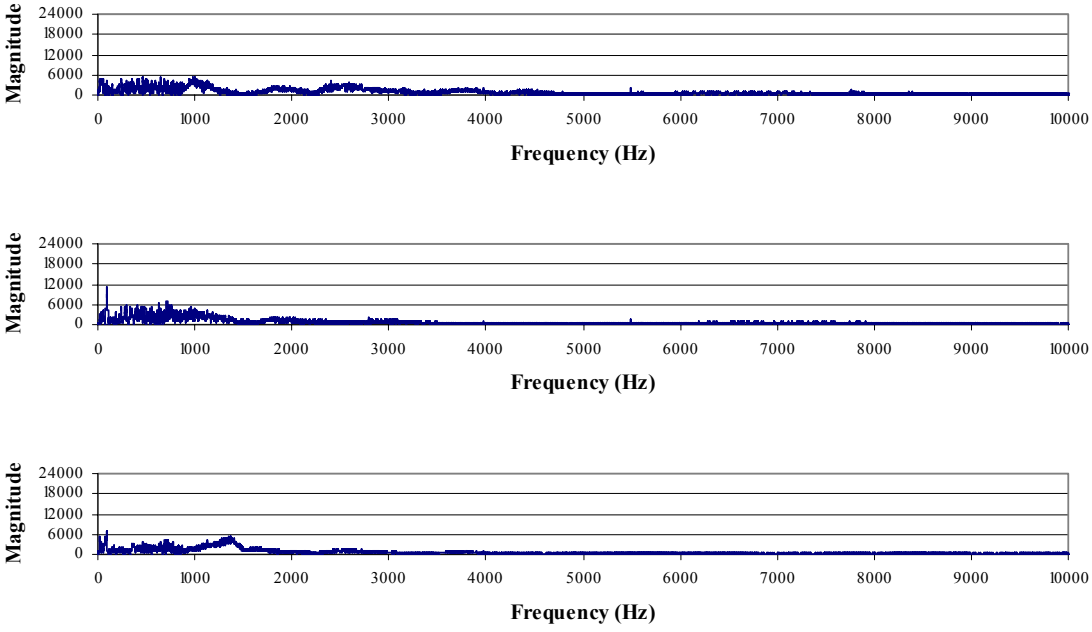

Figure A-159. FFT data from the acetabular cup accelerometer for a metal-on-polyethylene THA, subjected to a 1730 Newton impact load. The signals are for the B1-axis (upper), B2-axis (middle) and B3-axis (lower).

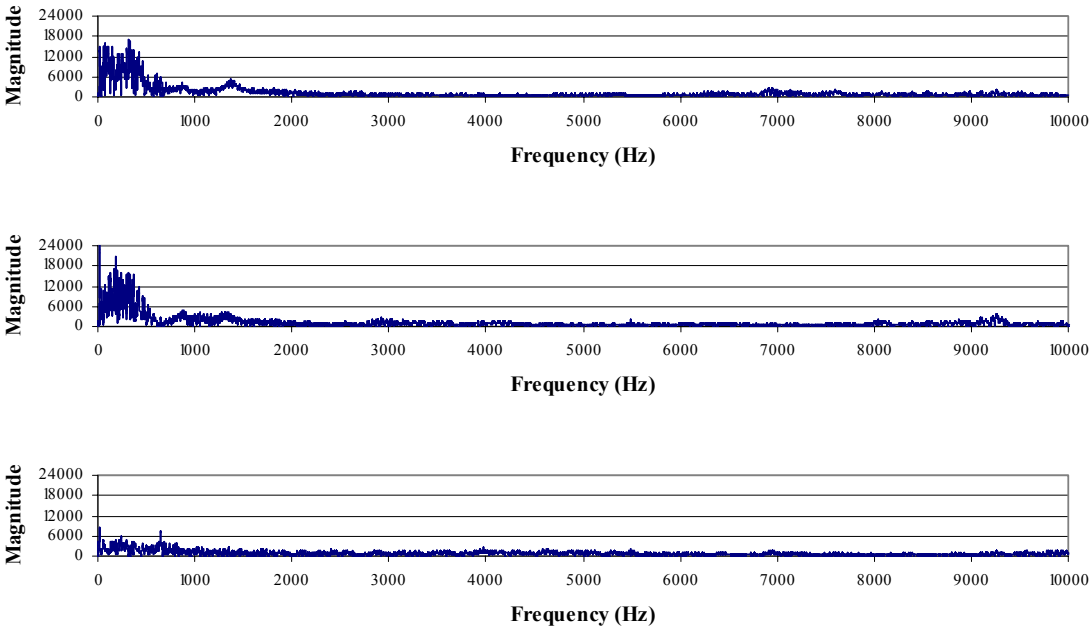

Figure A-160. FFT data from the femoral stem accelerometer for a metal-on-polyethylene THA, subjected to a 1730 Newton impact load. The signals are for the C1-axis (upper), C2-axis (middle) and C3-axis (lower).

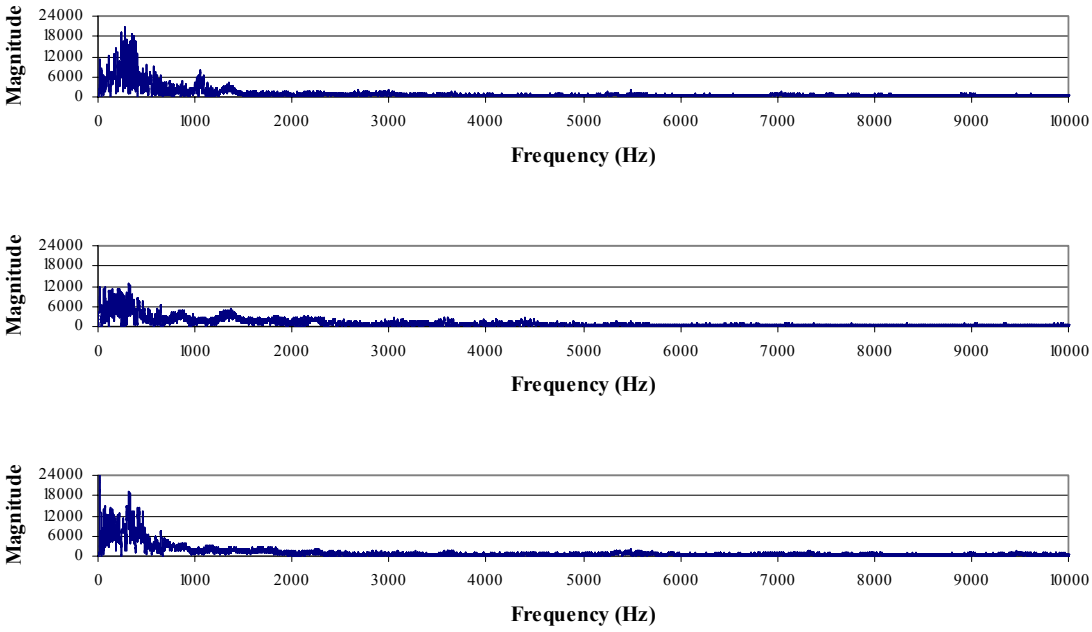

Figure A-161. FFT data from the greater trochanter accelerometer for a metal-on-polyethylene THA, subjected to a 1730 Newton impact load. The signals are for the D1-axis (upper), D2-axis (middle) and D3-axis (lower).

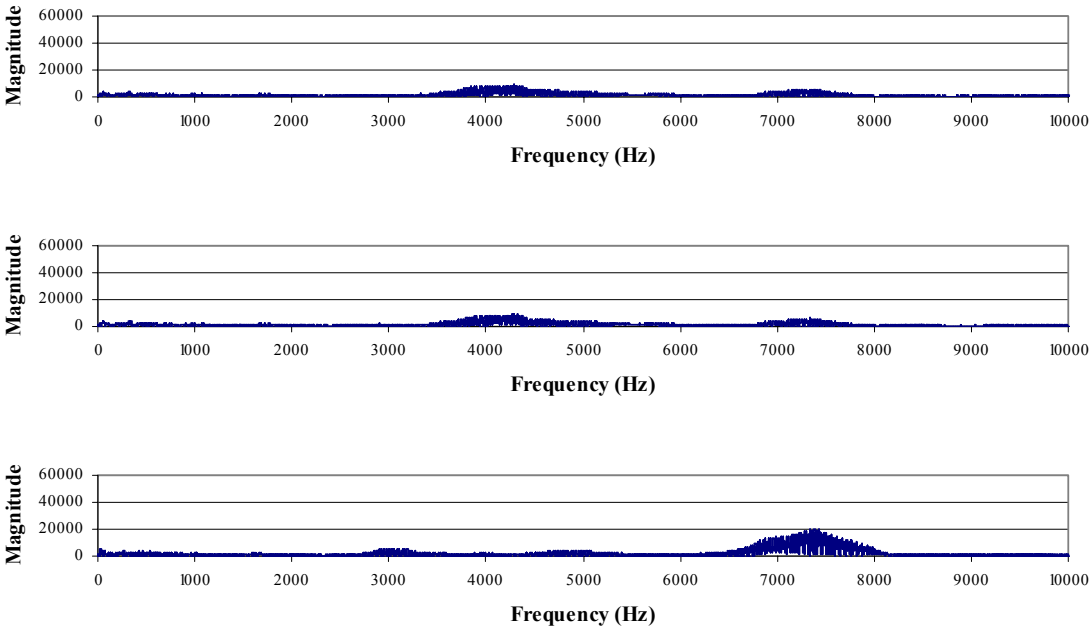

Figure A-162. FFT data from the pelvis accelerometer for a metal-on-metal THA, subjected to a 1730 Newton impact load. The signals are for the A1-axis (upper), A2-axis (middle) and A3-axis (lower).

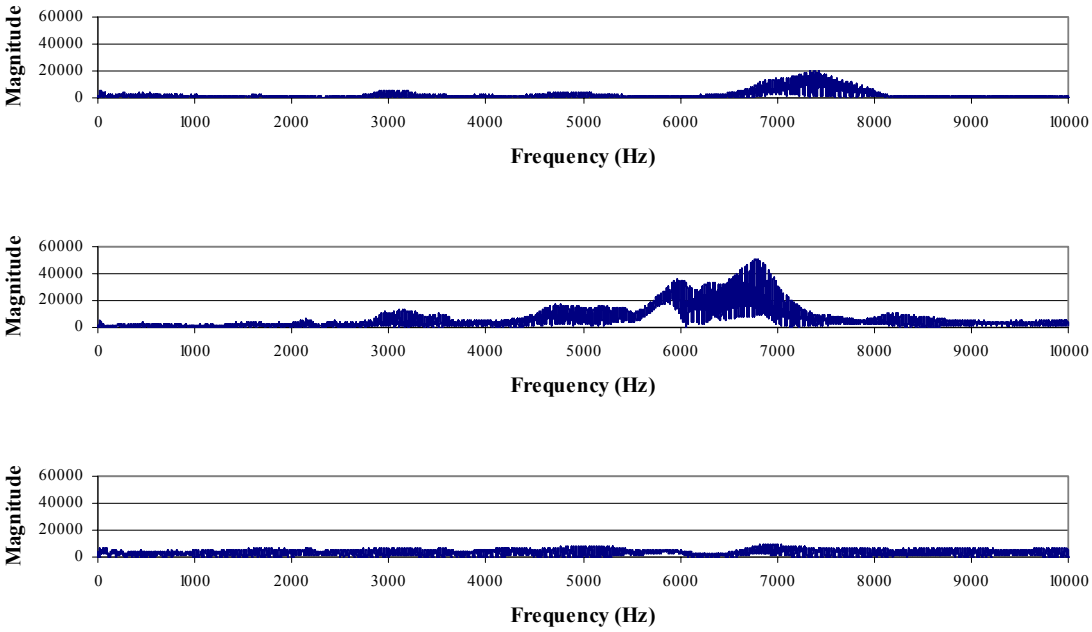

Figure A-163. FFT data from the acetabular cup accelerometer for a metal-on-metal THA, subjected to a 1730 Newton impact load. The signals are for the B1-axis (upper), B2-axis (middle) and B3-axis (lower).

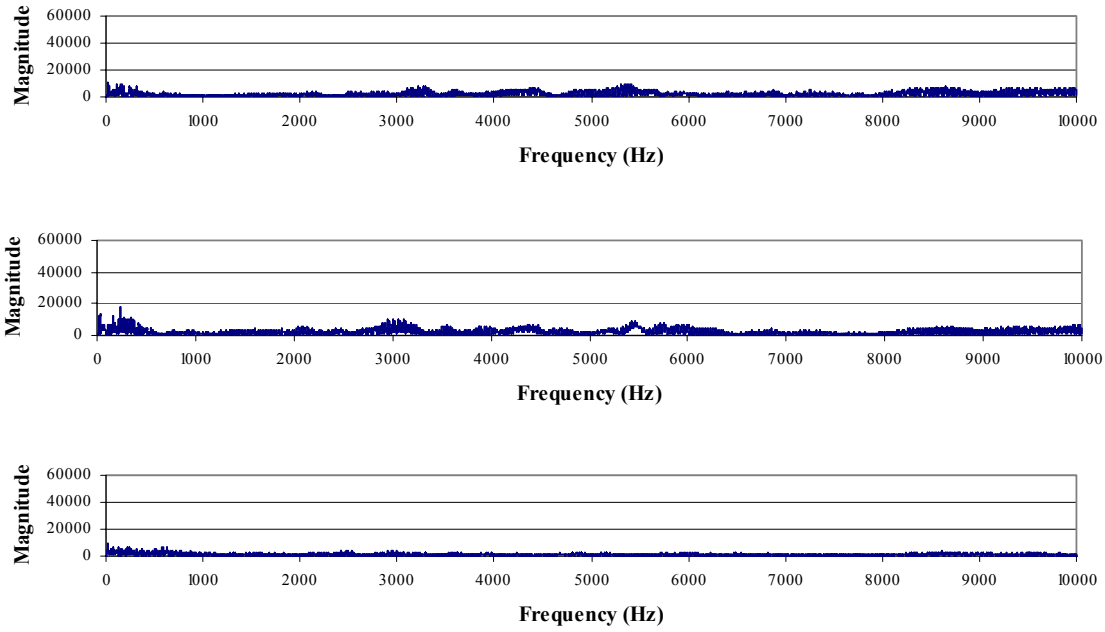

Figure A-164. FFT data from the femoral stem accelerometer for a metal-on-metal THA, subjected to a 1730 Newton impact load. The signals are for the C1-axis (upper), C2-axis (middle) and C3-axis (lower).

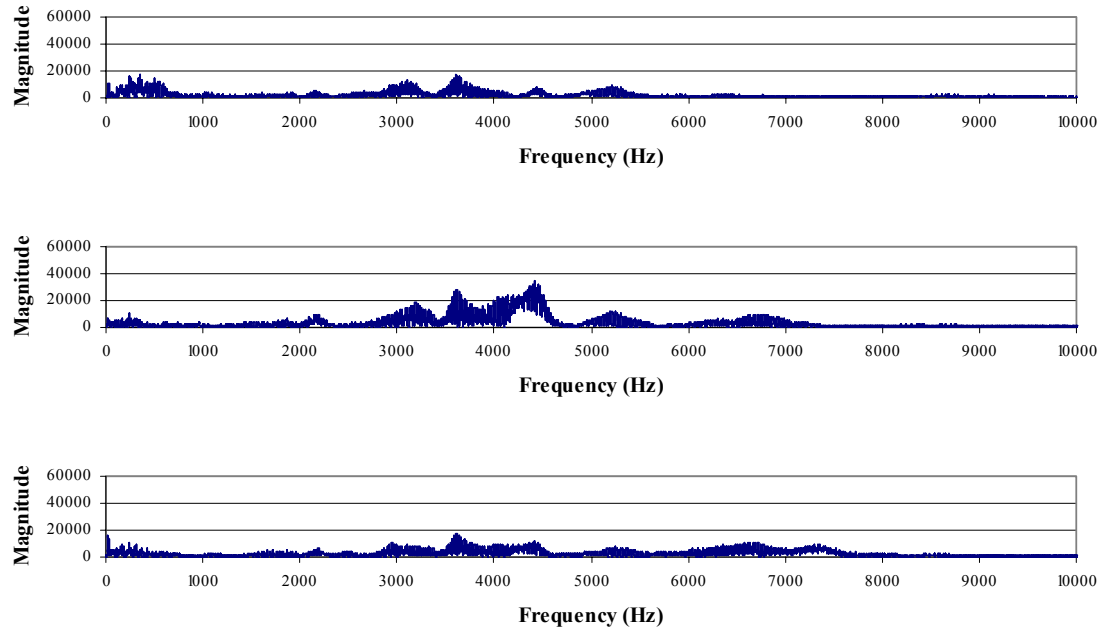

Figure A-165. FFT data from the greater trochanter accelerometer for a metal-on-metal THA, subjected to a 1730 Newton impact load. The signals are for the D1-axis (upper), D2-axis (middle) and D3-axis (lower).

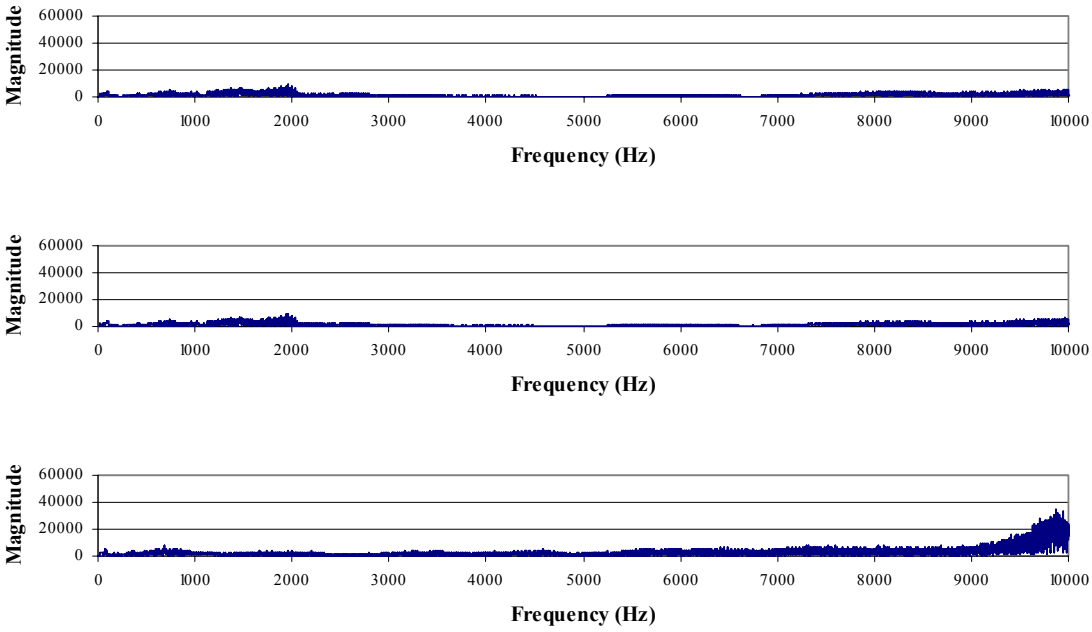

Figure A-166. FFT data from the pelvis accelerometer for a ceramic-on-ceramic THA, subjected to a 1730 Newton impact load. The signals are for the A1-axis (upper), A2-axis (middle) and A3-axis (lower).

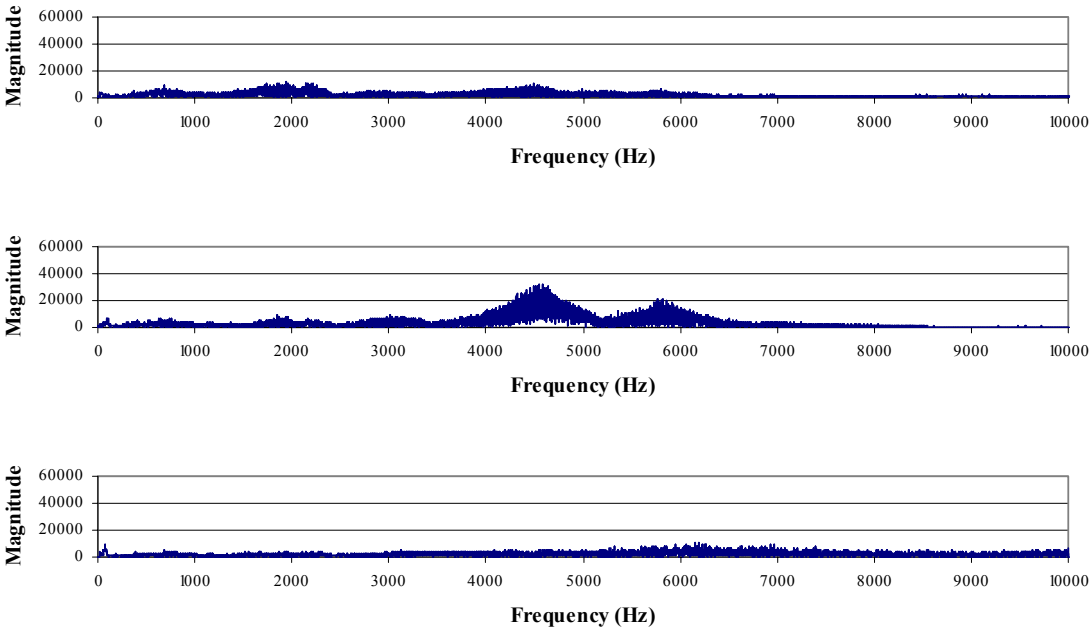

Figure A-167. FFT data from the acetabular cup accelerometer for a ceramic-on-ceramic THA, subjected to a 1730 Newton impact load. The signals are for the B1-axis (upper), B2-axis (middle) and B3-axis (lower).

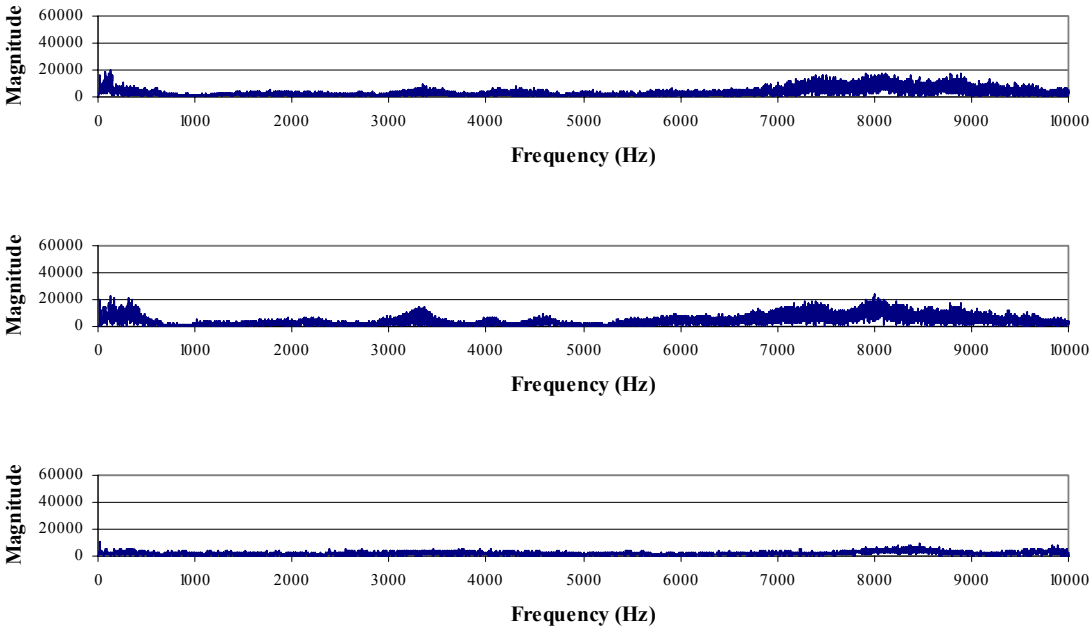

Figure A-168. FFT data from the femoral stem accelerometer for a ceramic-on-ceramic THA, subjected to a 1730 Newton impact load. The signals are for the C1-axis (upper), C2-axis (middle) and C3-axis (lower).

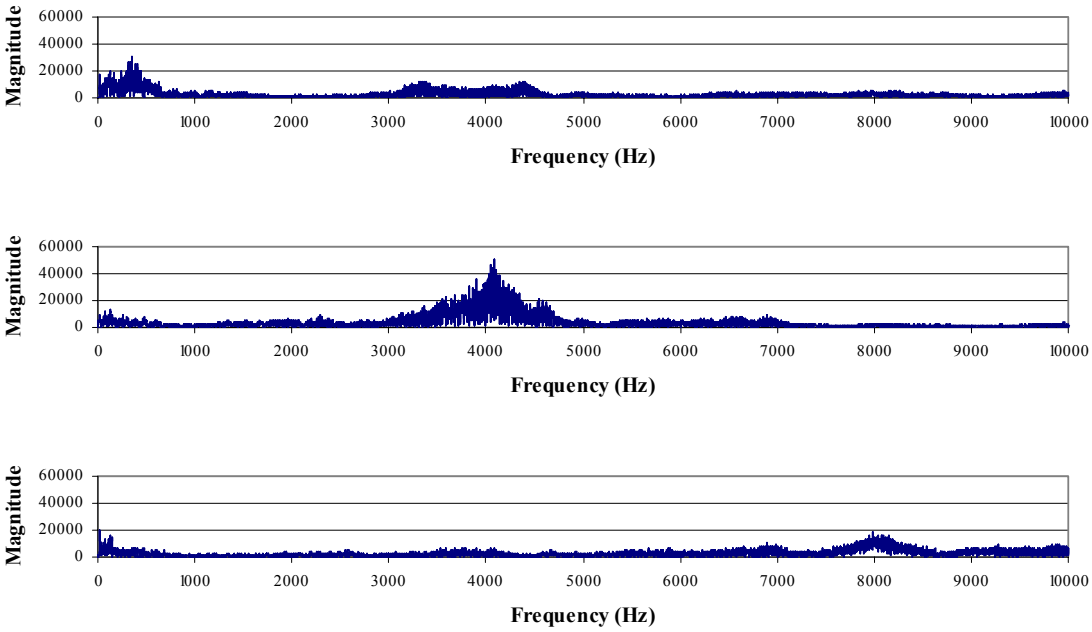

Figure A-169. FFT data from the greater trochanter accelerometer for a ceramic-on-ceramic THA, subjected to a 1730 Newton impact load. The signals are for the D1-axis (upper), D2-axis (middle) and D3-axis (lower).

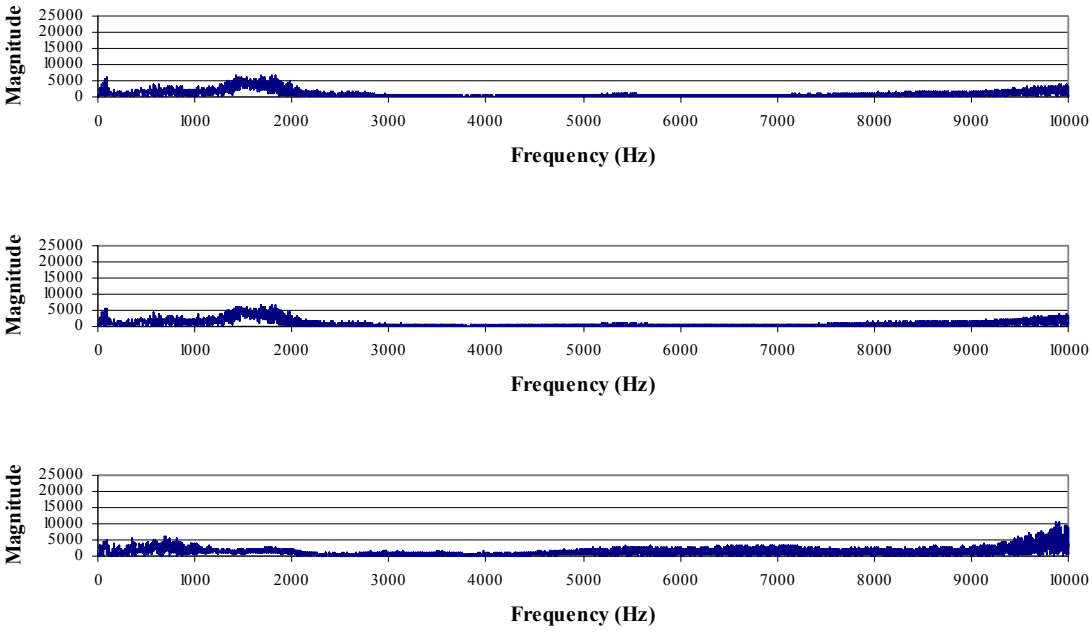

Figure A-170. FFT data from the pelvis accelerometer for a metal-on-polyethylene THA, subjected to a 1900 Newton impact load. The signals are for the A1-axis (upper), A2-axis (middle) and A3-axis (lower).

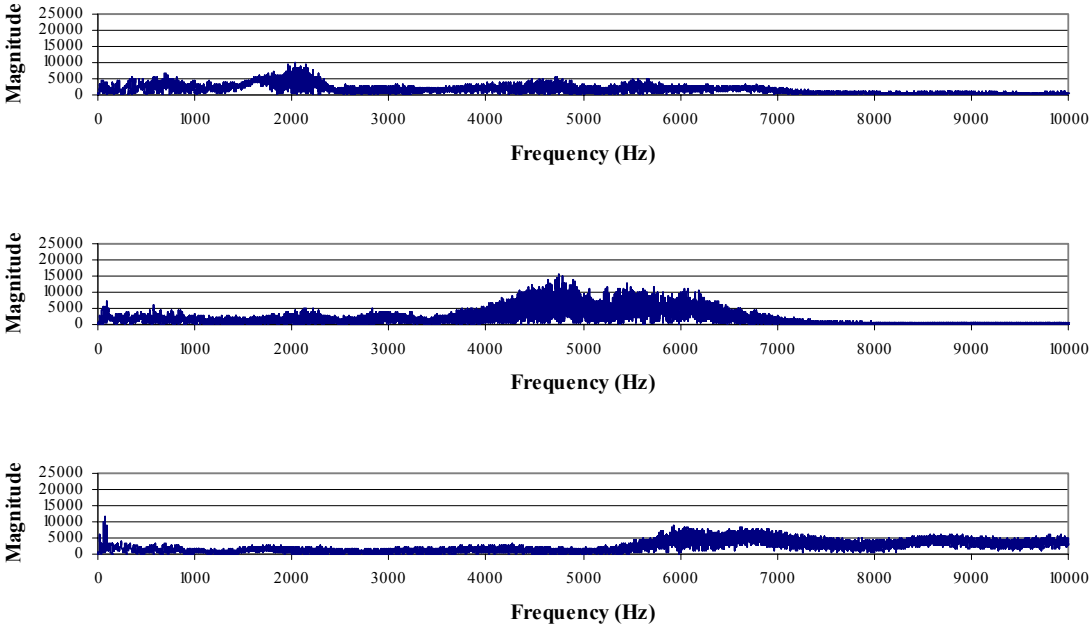

Figure A-171. FFT data from the acetabular cup accelerometer for a metal-on-polyethylene THA, subjected to a 1900 Newton impact load. The signals are for the B1-axis (upper), B2-axis (middle) and B3-axis (lower).

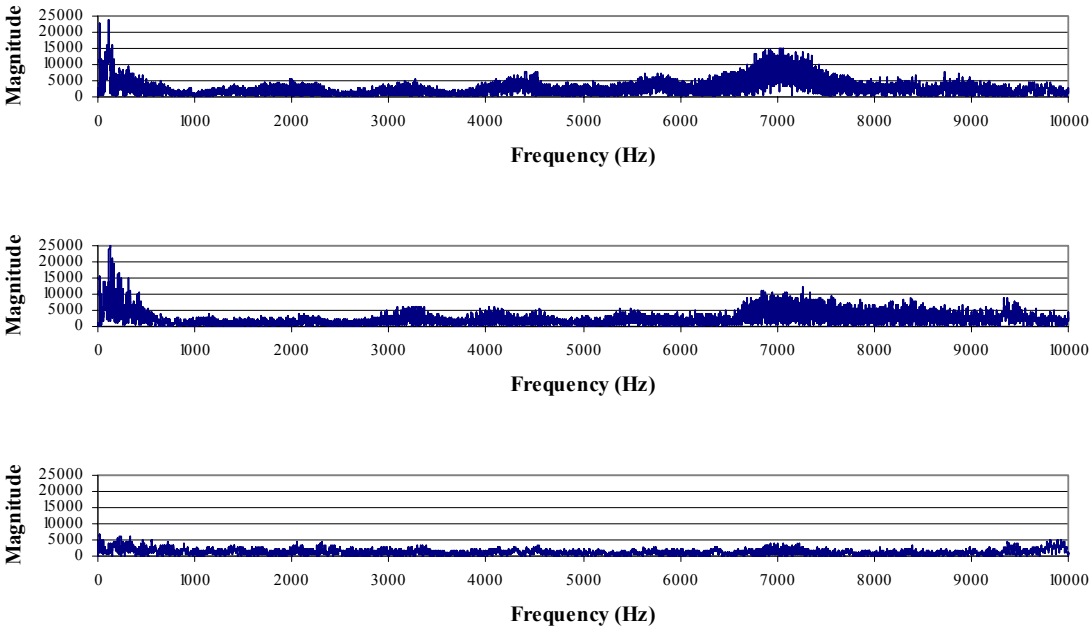

Figure A-172. FFT data from the femoral stem accelerometer for a metal-on-polyethylene THA, subjected to a 1900 Newton impact load. The signals are for the C1-axis (upper), C2-axis (middle) and C3-axis (lower).

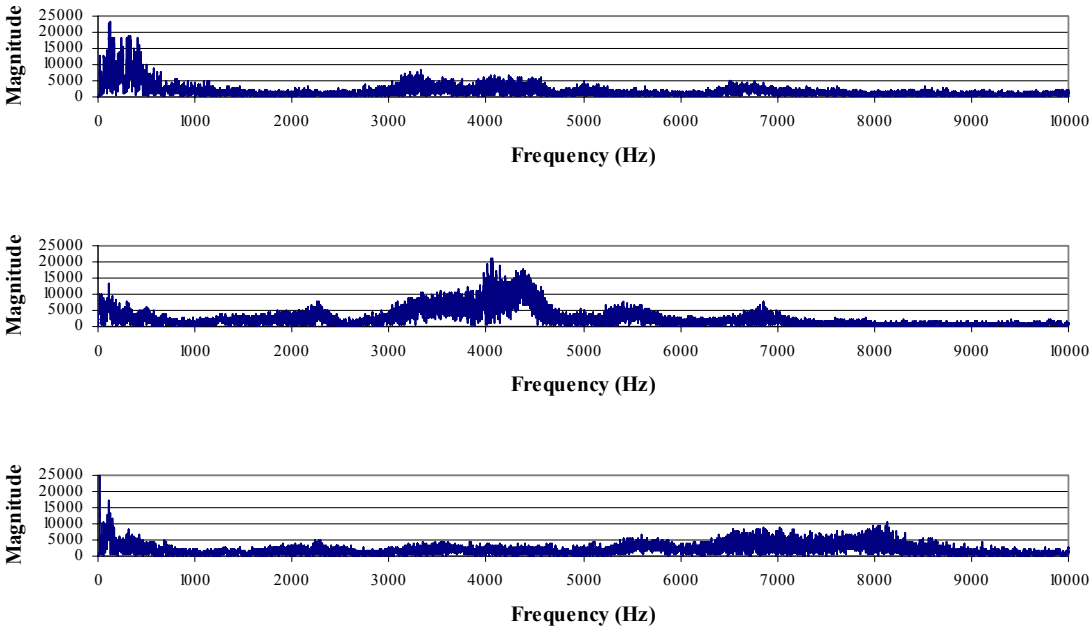

Figure A-173. FFT data from the greater trochanter accelerometer for a metal-on-polyethylene THA, subjected to a 1900 Newton impact load. The signals are for the D1-axis (upper), D2-axis (middle) and D3-axis (lower).

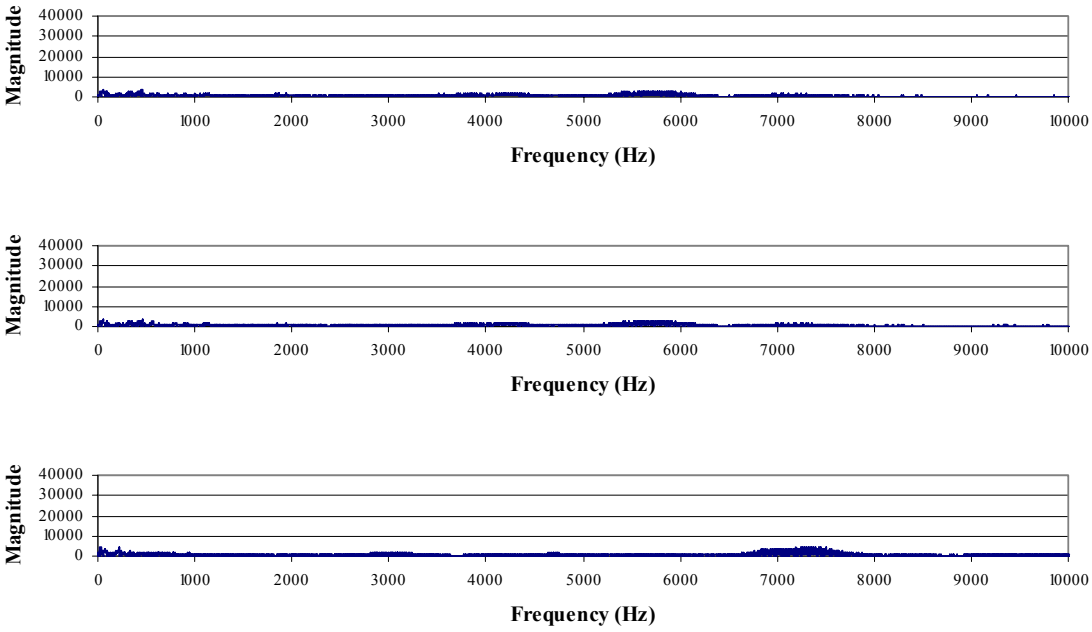

Figure A-174. FFT data from the pelvis accelerometer for a metal-on-metal THA, subjected to a 1900 Newton impact load. The signals are for the A1-axis (upper), A2-axis (middle) and A3-axis (lower).

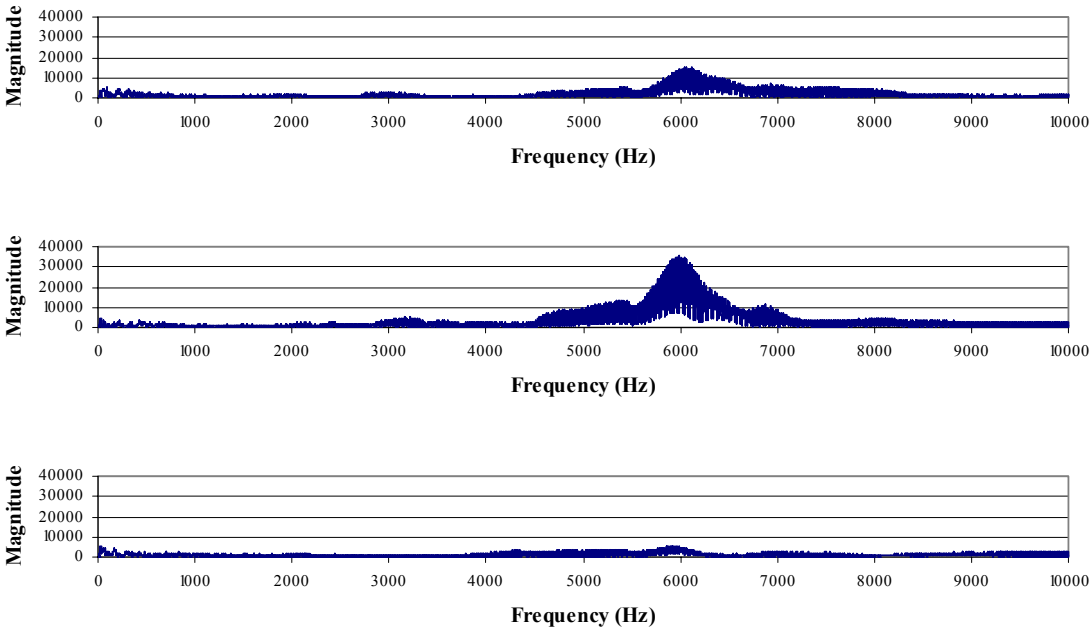

Figure A-175. FFT data from the acetabular cup accelerometer for a metal-on-metal THA, subjected to a 1900 Newton impact load. The signals are for the B1-axis (upper), B2-axis (middle) and B3-axis (lower).

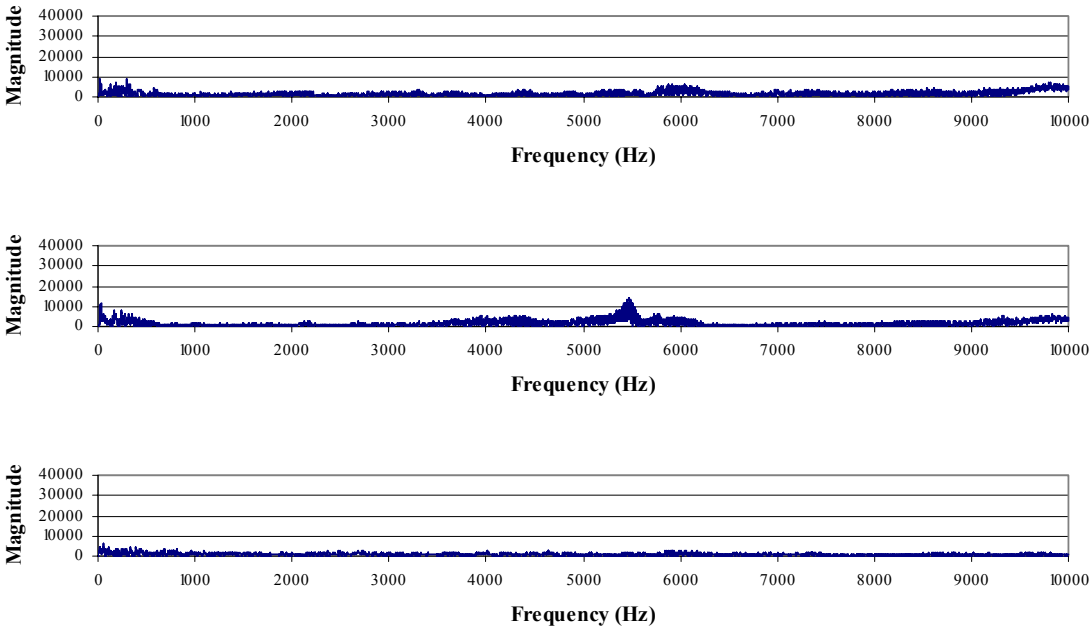

Figure A-176. FFT data from the femoral stem accelerometer for a metal-on-metal THA, subjected to a 1900 Newton impact load. The signals are for the C1-axis (upper), C2-axis (middle) and C3-axis (lower).

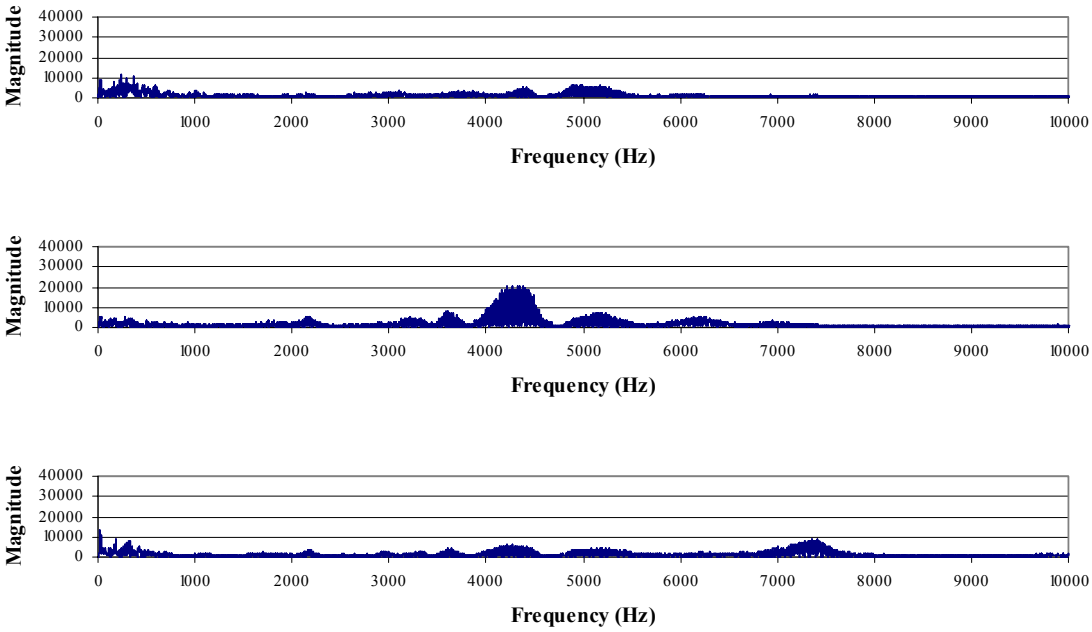

Figure A-177. FFT data from the greater trochanter accelerometer for a metal-on-metal THA, subjected to a 1900 Newton impact load. The signals are for the D1-axis (upper), D2-axis (middle) and D3-axis (lower).

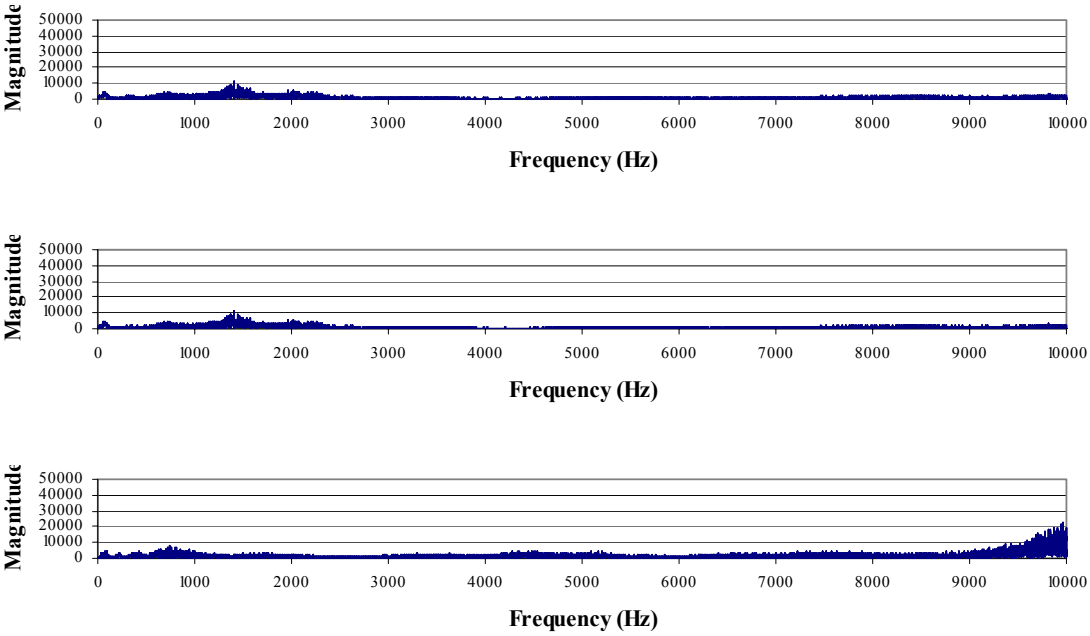

Figure A-178. FFT data from the pelvis accelerometer for a ceramic-on-ceramic THA, subjected to a 1900 Newton impact load. The signals are for the A1-axis (upper), A2-axis (middle) and A3-axis (lower).

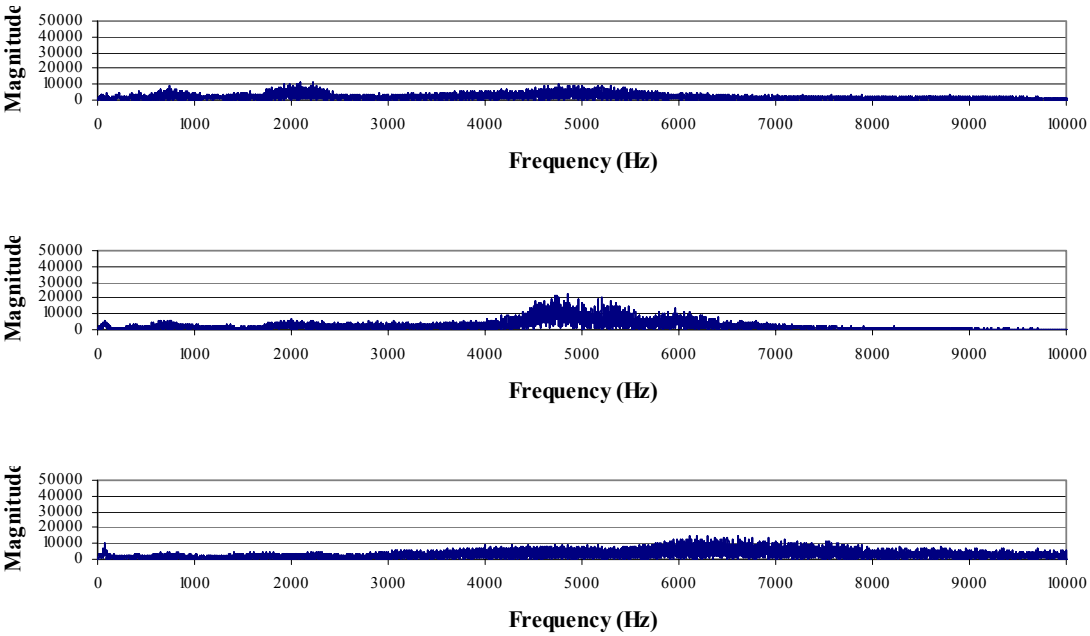

Figure A-179. FFT data from the acetabular cup accelerometer for a ceramic-on-ceramic THA, subjected to a 1900 Newton impact load. The signals are for the B1-axis (upper), B2-axis (middle) and B3-axis (lower).

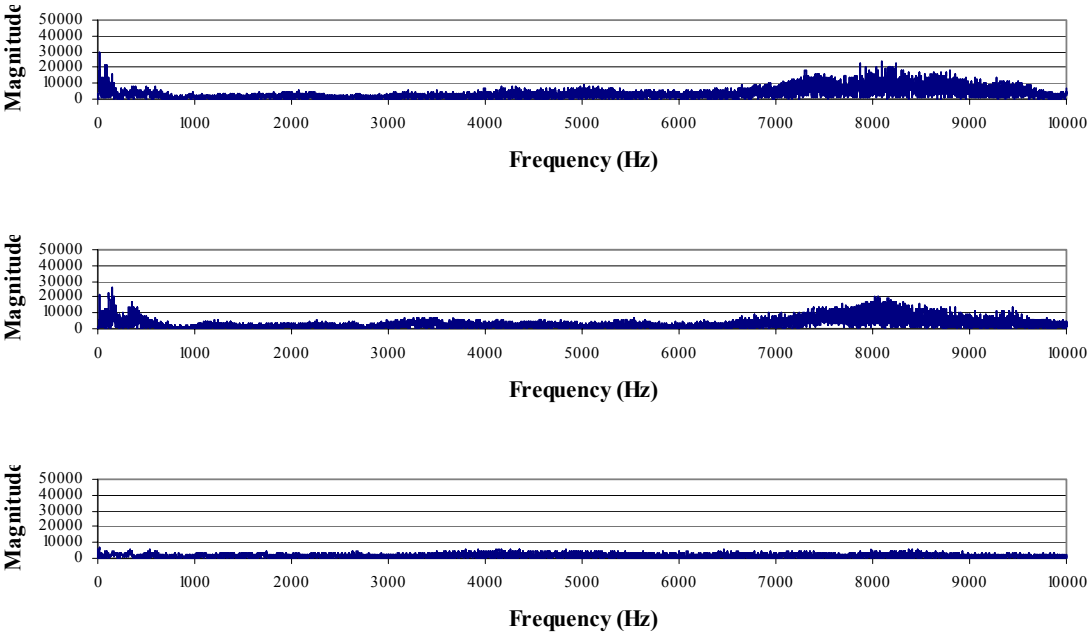

Figure A-180. FFT data from the femoral stem accelerometer for a ceramic-on-ceramic THA, subjected to a 1900 Newton impact load. The signals are for the C1-axis (upper), C2-axis (middle) and C3-axis (lower).

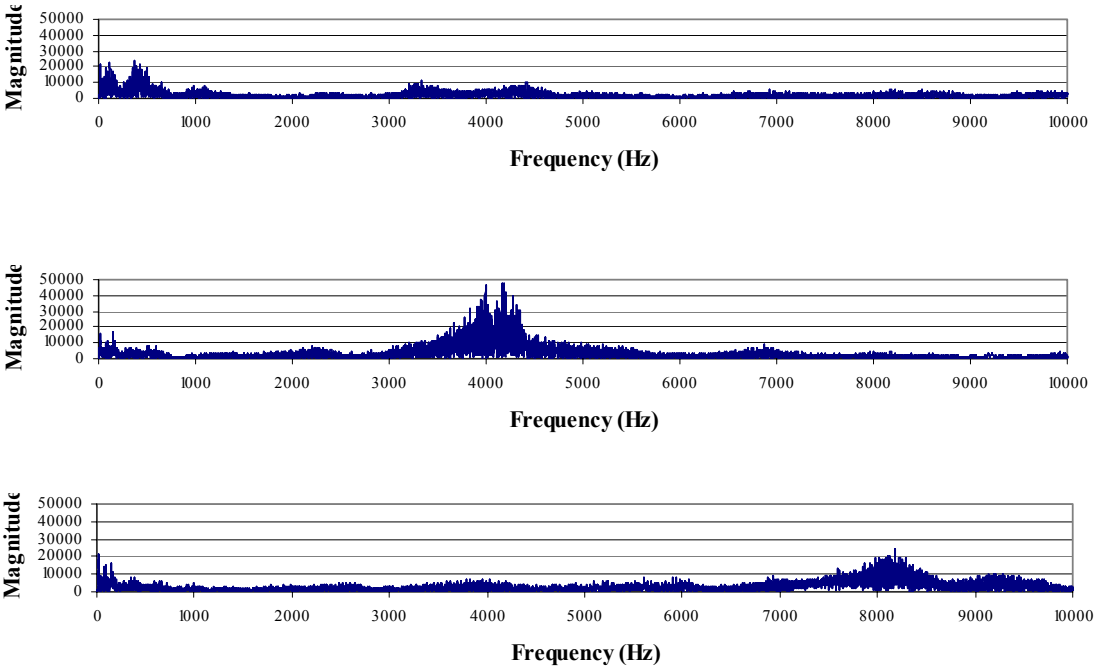

Figure A-181. FFT data from the greater trochanter accelerometer for a ceramic-on-ceramic THA, subjected to a 1900 Newton impact load. The signals are for the D1-axis (upper), D2-axis (middle) and D3-axis (lower).

VITA

Joseph Bader was born in Baton Rouge, LA on June 8,1979. His family moved to Murfreesboro, TN in 1987 where he went attended Oakland High School. He graduated from Oakland in 1997. In fall of 1997 he matriculated to the University of Tennessee, Knoxville and received a B.S. in biomedical engineering in 2003 and a M.S. in mechanical engineering in 2005.

Joseph is currently pursing his doctorate in biomedical engineering at the University of Kentucky, Lexington, KY.